ABSTRACT

Title of Document: **LOCAL AND GLOBAL DRYOUT IN TWO-PHASE MICROGAP COOLING**

Jessica R. Sheehan, Ph.D., 2012

Directed By: Distinguished Professor, Dr. Avram Bar-Cohen, Mechanical Engineering

Limitations in advancements in electronic technology and further development of new technology are due to inadequate thermal management. As Moore's Law continues to drive semiconductor technology, the capabilities of conventional thermal management methods are falling behind the constantly changing and increasing needs of the electronic industry. Roadmap projections for the high-performance chip category suggest that the maximum chip power dissipation will exceed 500 W, and the chip heat flux will exceed 150 W/cm^2 within the next few years. Research currently focuses on two-phase cooling techniques due to their potential to meet the thermal management needs of leading-edge electronic technology. Potential solutions currently being studied include spray cooling, immersion cooling, micro heat pipes, and microgap cooler. Unlike many current thermal management devices, microgap cooler eliminate the high and problematic thermal contact resistance, by allowing direct cooling of an electronic component by the flow of dielectric liquid across the back surface of the chip or substrate. The heat dissipation capability of such microgap coolers is further enhanced by two-phase flow that develops in the microgap channel, producing higher heat transfer coefficients than achievable by single-phase forced convection with that same fluid. In addition, due to the potential utilization of the intrinsic gaps between chips and within the packaging enclosures in both 2.5D (using

interposers) and 3D configurations, microgap coolers provide a promising solution to the challenging problem of high-density heat removal. Despite the many advantages of two-phase microgap coolers, much is still not understood about the physics that governs this thermal management technique and the phenomena that limit its performance.

LOCAL AND GLOBAL DRYOUT IN TWO-PHASE MICROGAP COOLING

By

Jessica R. Sheehan

Dissertation submitted to the Faculty of the Graduate School of the
University of Maryland, College Park, in partial fulfillment
of the requirements for the degree of
Doctor of Philosophy
2012

Advisor Committee:
Professor Avram Bar-Cohen, Chair
Professor Marino DiMarzo
Professor Michael Ohadi
Professor Gary Pertmer
Professor Amir Riaz

TABLE OF CONTENTS

LIST OF FIGURES

LIST OF TABLES

CHAPTER 1

INTRODUCTION

Implementation of advances in electronic technology and successful exploitation of further development of new technology are limited by inadequate thermal management. As Moore's Law continues to drive semiconductor technology, the capabilities of conventional thermal management methods are falling behind the constantly changing and increasing needs of the electronic industry. Roadmap projections for the high-performance chip category suggest that the maximum chip power dissipation will exceed 500 W, and the chip heat flux will exceed 150 W/cm^2 within the next few years [1]. Aggressive two-phase cooling techniques are being researched, due to their potential to bridge the gap between stat-of-the-art convective solutions and the thermal management needs of leading-edge electronic technology. Potential solutions currently being studied include spray cooling, immersion cooling, micro heat pipes, and microgap cooler. Spray cooling, shown in Figure 1, uses a dielectric liquid for direct cooling of a component. The evaporation of thin liquid films, created by spraying liquid on the component

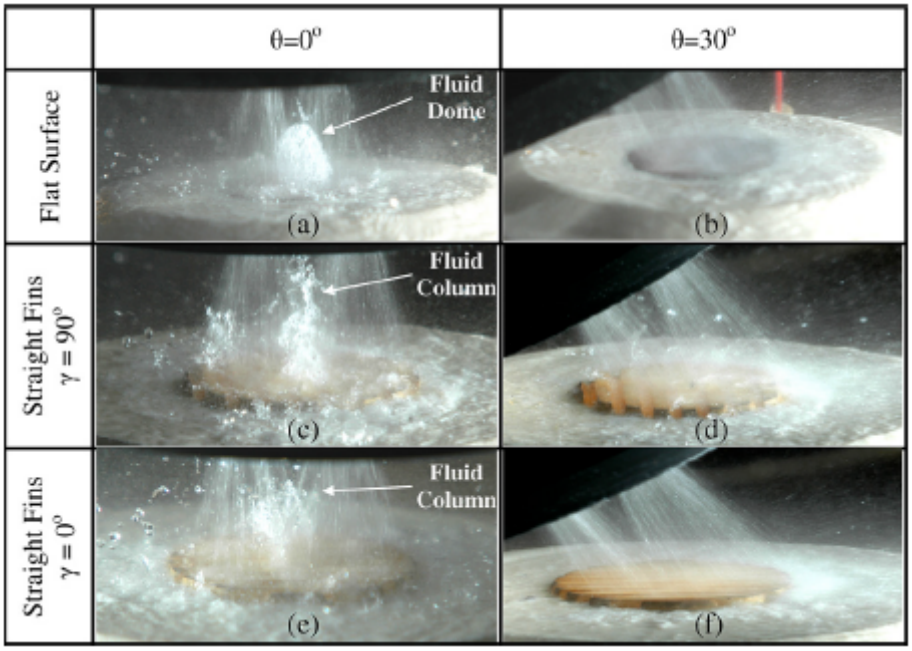

Figure 1: Spray cone stagnation zone phenomena; (a) h = 0 flat surface, (b) h = 30 flat surface, (c) h = 0 , transverse straight fins (c = 90), (d) h = 30 [2].

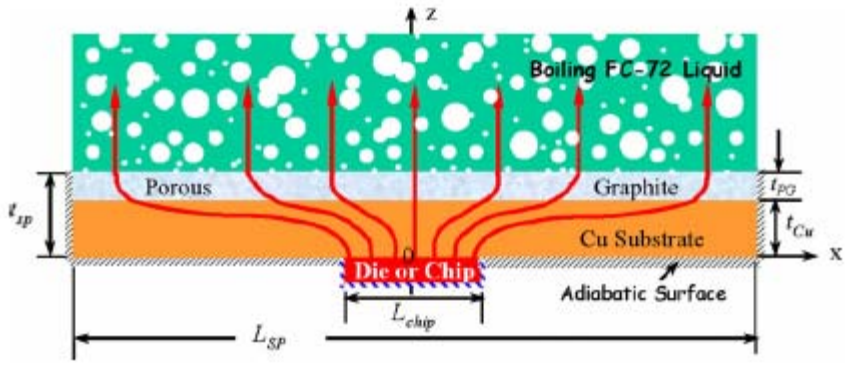

Figure 2: Schematic of A PG–Cu composite spreader for removing dissipated thermal power by underlying 10X10 mm chip using nucleate boiling of dielectric liquid [3].

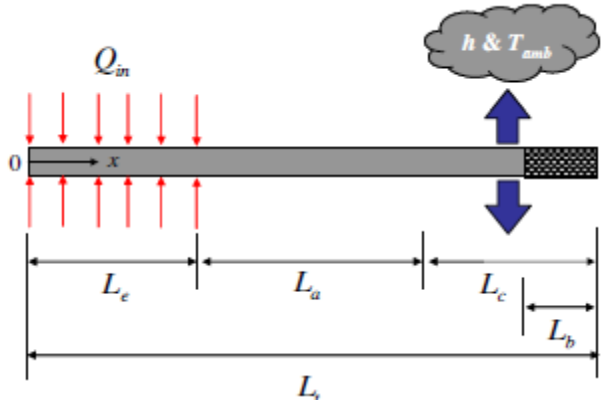

Figure 3: Schematic diagrams of the flat heat pipe considered with a rectangular grooved wick [4].

surface, can manage heat fluxes of 100 W/cm^2 [2]. Figure 1 shows various impingement angles of this jet (θ) and h (distance of the nozzle from the surface) that were studied to determine parametric sensitivities and optimum conditions for this heat transfer mode [2]. Although this method can yield high heat transfer coefficients, it requires relatively high liquid flow rates and, as may be seen in Figure 1, a considerable fraction of the liquid goes unused. Figure 2 shows a spreader-enhanced immersion cooling approach utilizing FC-72 to reach a maximum cooling load of 30 W/cm^2 [3]. Figure 3 shows a schematic of a micro flat heat pipe, which can be efficient in heat spreading but, as an indirect cooling mode, requires attachment to the chip and often involves expensive and arduous fabrication methods.

Unlike many current thermal management devices, microgap cooler eliminate the high and

problematic thermal contact resistance, by allowing direct cooling of an electronic component by the flow of dielectric liquid across the back surface of the chip or substrate. The heat dissipation capability of such microgap coolers is further enhanced by two-phase flow that develops in the microgap channel, producing higher heat transfer coefficients than achievable by single-phase forced convection with that same fluid [1]. In addition, due to the potential utilization of the intrinsic gaps between chips and within the packaging enclosures in both 2.5D (using interposers) and 3D configurations, microgap coolers provide a promising solution to the challenging problem of high-density heat removal. Despite the many advantages of two-phase microgap coolers, much is still not understood about the physics that governs this thermal management technique and the phenomena that limit its performance.

Microgap coolers were first studied by the TherPES Laboratory at the University of Maryland to determine the flow regimes encountered in such devices, evaluate the two-phase heat transfer coefficients at various qualities, and identify the two-phase heat transfer correlation providing adequate predictions for this two-phase cooling configuration [5-10]. This lead to the examination of the reported two-phase heat transfer coefficients with respect to quality, revealing an intrinsic M-shaped curve for the axial variation of the two-phase heat transfer coefficients [8, 9]. Prediction of such two-phase heat transfer coefficients was found to depend greatly on the prevailing flow regime and – when classifying the data by the predicted flow regime, macro correlations (i.e. Chen, Shah, etc) resulted in good agreement with experimental microgap results [8,9]. Interestingly, annular flow was found to be dominant in devices of this size [5-10].

Initial results obtained in the present dissertation, using infrared imaging of the heated surface through a sapphire window on the opposing wall of the channel, revealed previously undetected spatial and temporal temperature variations, as large as 20K, in Annular flow [5,6]. It has been hypothesized that local dryout and recovery of the thin liquid film, with ever larger dry spots as the quality increases, could explain this behavior. Moreover, the local dryout and recovery may initially increase the average heat transfer coefficient, due to the rapid evaporation of the ultra-thin film, but as quality increases and a larger fraction of the area experiences dryout, the average heat transfer coefficient decreases - yielding the parabolic segment of the M-shaped curve. The present dissertation seeks to substantiate, understand, and interpret the effects of local dryout as the limiting mechanism on the thermal performance of microgap coolers by studying the impact of microgap channel geometry (gap size, width, and aspect ratio) on the wall

temperature fluctuations and the heat transfer coefficients associated with thin film evaporative cooling in microgap channels. The study relies on the previously-validated two-phase regime mapping methodology for microgap channels along with IR imaging of the heated surface and the inverse determination of the local wall heat flux based on numerical simulation, to study the thermofluid characteristics of various microgap channels.

Interestingly, while the center of the microgap channel generally displays consistent temperature magnitudes and temporal behavior, this is not always the case for channel edge locations, especially at low and modest mass fluxes. Such a lateral temperature distribution could reflect the potentially significant role played by the edges of the microgap channel in controlling and directing the axial flow of liquid and its availability for evaporative cooling of the entire channel. The sensitivity of the lateral temperature distribution to gap size, microgap width, and microgap length was be explored to further understand the edge effect on overall performance of the microgap channel [7, 23, 26].

CHAPT ER 2

BACKGROUND

2.1 Two-Phase Flow in Miniature Channels

Two-phase mixtures flowing in a miniature or conventional channel are known to aggregate into four distinct flow regimes: bubbly, intermittent, annular and stratified [18-20]. Figure 4 shows these four flow regimes as they might occur in a horizontal pipe. Bubbly flow is

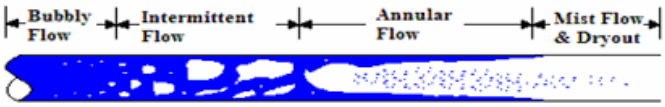

Figure 4: Diagram of a developing flow in a horizontal heated pipe [19].

distinguished by a small volumetric fraction of bubbles within the liquid flow. In Intermittent flow the bubbles begin to coalesce and form "slugs" in the flowing liquid. Annular flow, the dominant flow regime for microgap coolers and other miniature channels [20], is associated with a thin liquid layer flowing along the outer walls of the channel and vapor flowing in the center. The advantage of this thin-film flow regime lies in the high heat transfer rates associated with the liquid layer that traverses the heated walls of the microgap cooler. The low resistance to thermal diffusion posed by such a thin liquid layer and the ease of evaporation into the vapor core aid the film to remove substantial thermal energy from the walls. The thinner this layer of liquid becomes the higher the heat transfer coefficient that can be obtained. However, if the layer becomes too thin, local dryout can occur and propagate to complete dryout.

Recent research on two-phase flow and heat transfer in microchannel coolers has included: the observation and classification of flow regimes [12, 15, 17], development of pressure drop correlations [12, 16, 18], and heat transfer correlations [14, 15]. An extensive review of the recent and more historic literature [33, 34] revealed a characteristic M-shaped variation of the heat transfer coefficient, shown in Figure 5. The inflection points in this M-shaped curve were found to equate approximately with flow regime transitions, including a first

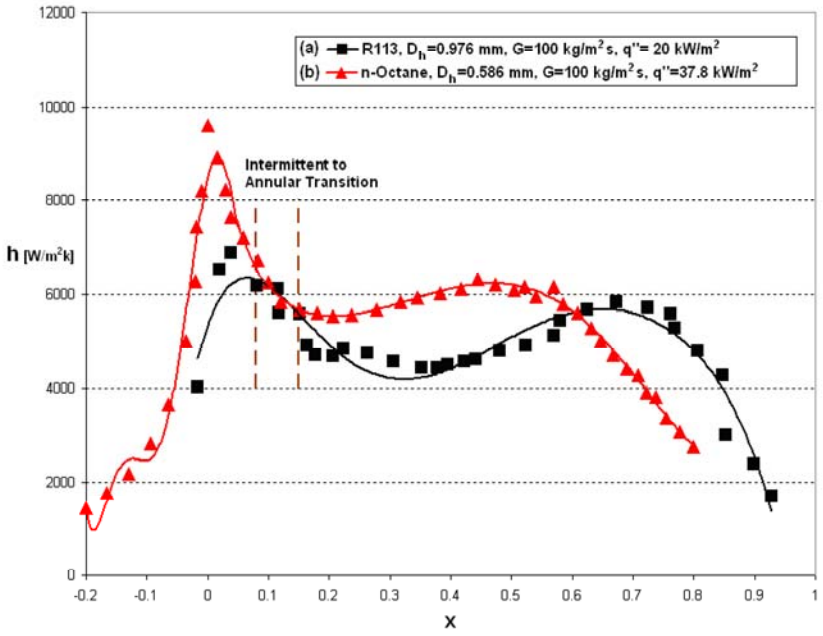

Figure 5: Two-phase flow characteristic M-shaped variation of the heat transfer coefficient [19].

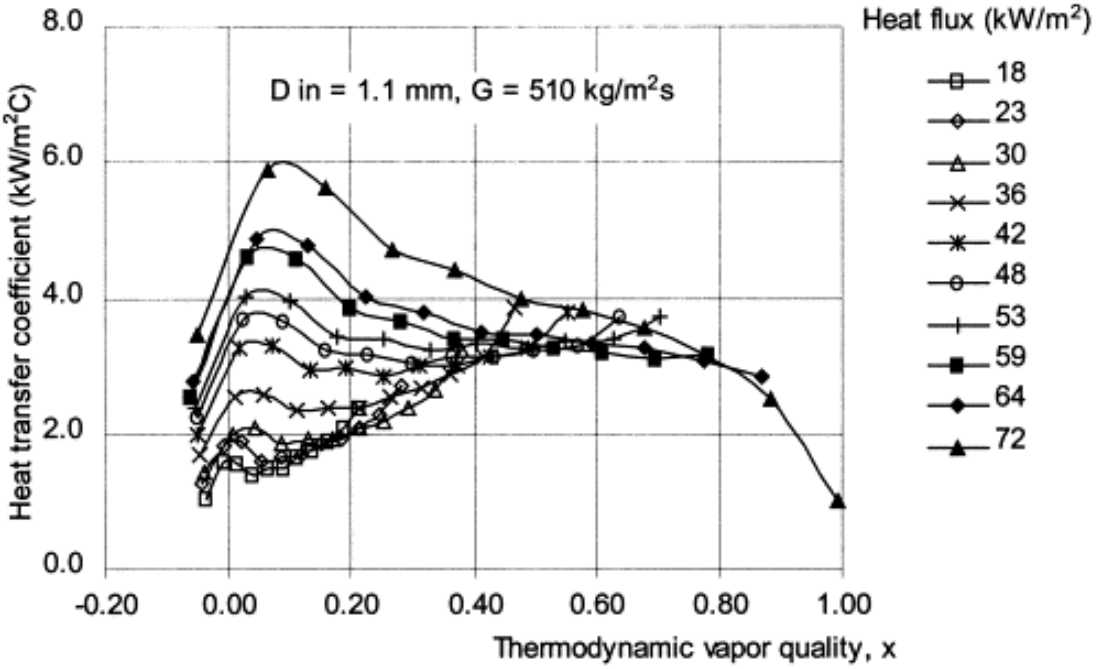

Figure 6: Lin et al (2001) R141b flow boiling map at d_{in} =1.1 mm and G=510 kg/m^2 s, q=18–72 kW/m^2.

maximum at the transition from Bubble to Intermittent flow, a decreasing heat transfer coefficient in the Intermittent regime, followed by a sharp increase on transition to Annular flow, and a second maximum, at relatively high qualities.

The up-sloping segment of this M-shaped curve was found to yield relatively high heat transfer coefficients in the moderate-to-high quality sections of such channels, in contrast with the oft observed inverse dependence of the heat transfer coefficient on quality, as seen in the Lin et al (2001) data displayed in Figure 6. It thus appears that in the moderate-to-high quality region, miniature channels may possess a significant heat transfer coefficient advantage relative to more traditional macrochannels. However, the progressively thinner liquid films encountered in annular flow could be expected to yield ever higher heat transfer coefficients at qualities approaching unity. The failure to observe this monotonic increase was attributed to the onset of local dryout of the thin film.

In their analysis of microgap refrigerant data, Bar-Cohen et al (2009) determined that the classic Chen correlation, Chen, (1966) gave the best agreement with the data that was associated with the up-sloping locus encountered in annular flow, yielding an MAE of just 24% for the heat transfer coefficients falling on the up-sloping branch of the M-shaped locus.

2.2 Flow Regime Mapping

The various flow regimes have been outlined previously, but it is important to properly determine the flow regime when analyzing a data set. A traditional Taitel-Dukler flow regime map (with Ullmann-Brauner correction) is shown in Figure 7. It is apparent that the correction greatly changes the transition between intermittent and annular flow, since the transition previously was a uniform 12% for all mass fluxes and is corrected to a range of 12%-36%. These mappings, done for all subsequent channels, will aid in determining the correct flow regime so phenomena occurring can be properly understood.

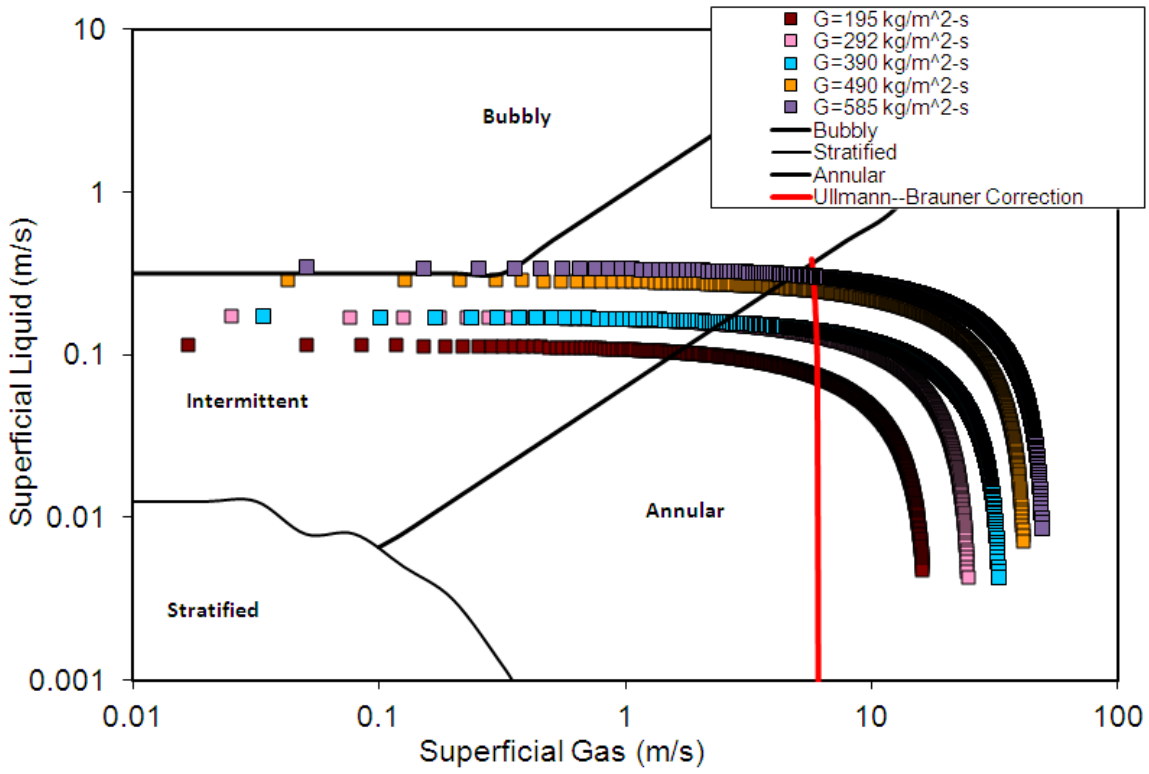

Figure 7: Taitel-Dukler with Ullmann-Brauner Correction (200 microns)

2.3 IR Radiation from Heated Wall

Despite the large fluctuations in temperature observed in the IR images, the thermocouples placed even 0.5 mm below the surface cannot detect such changes. Typical readings from Type E, bare wire thermocouples with 0.076 mm diameter; butt welded inside the copper plate with a 0.004 s response time, demonstrated no fluctuations of temperature (Figure 8). However, accounting for the propagation of the heat through the copper to the thermocouples, it becomes obvious that such high frequency fluctuations are dampened by heat capacity of the wall. Equation 1 was used to calculate the exponential decay in the amplitude of the periodic temperature fluctuations, at various depths below the surface. In this relation, ΔT_{obs} is the observable temperature fluctuation at the thermocouple, ΔT_{surf} is the amplitude of the surface fluctuation, x is the distance below the surface of the heated plate, α is the thermal diffusivity of the plate and τ is the period of the temperature oscillation on the surface [12]. Figure 9 shows the strong amplitude suppression experienced in the copper plate for three distinct fluctuations amplitudes – i.e. 20 K, 15 K, and 10 K for a period of 1s. These results reveal that thermocouples

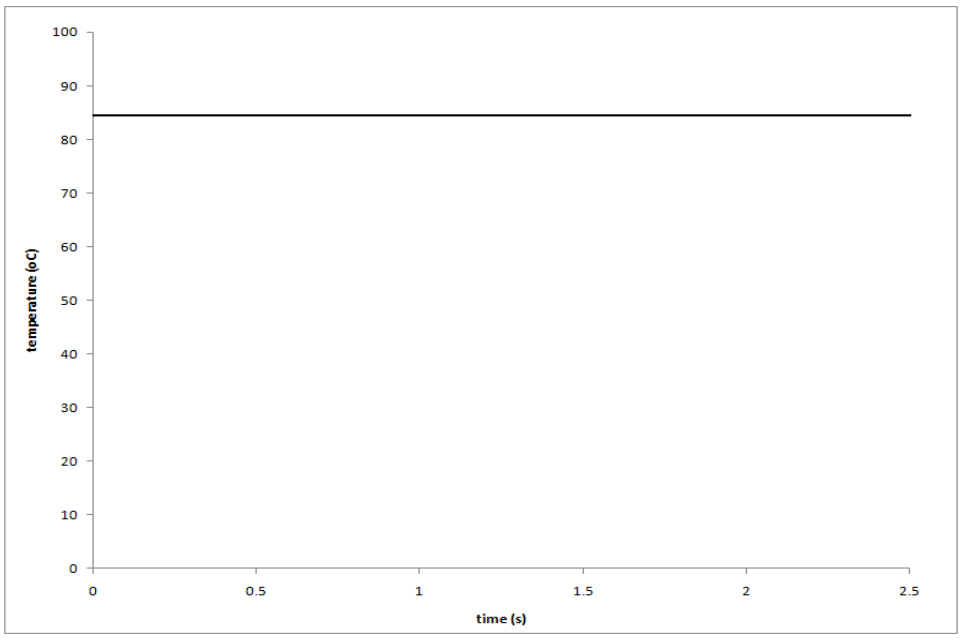

Figure 8: Measured Wall Temperature in Copper Wall of Microgap Channel in Two-Phase Flow (10 mm X 35 mm X 210 μm, G= 195.2 kg/m^{2}s, and q"= 26 W/cm^2).

$$\Delta T_{obs} = \Delta T_{surf} e^{-x\sqrt{\frac{\pi}{\alpha\tau}}} \qquad \text{Equation 1}$$

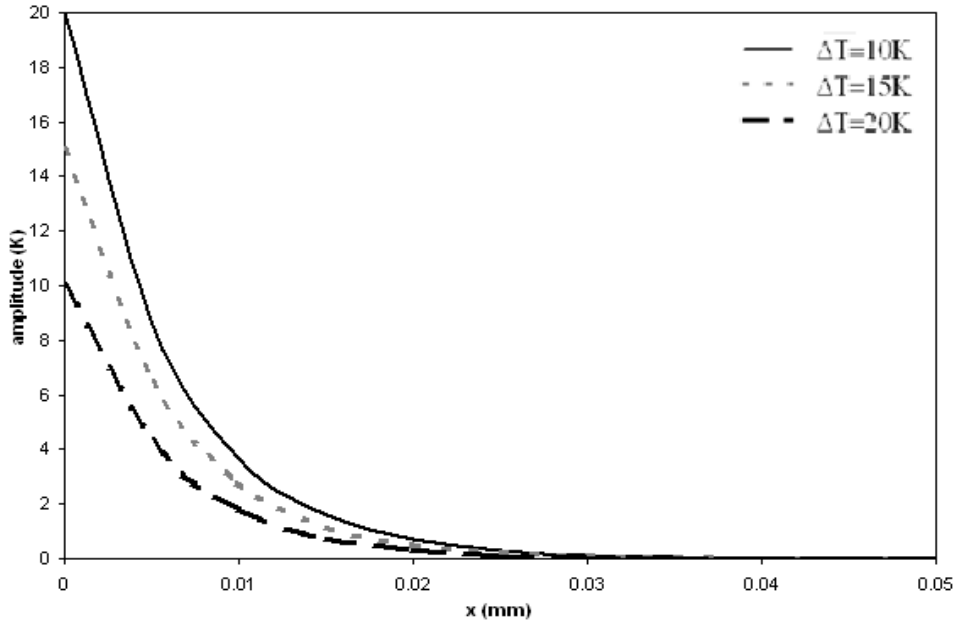

Figure 9: Amplitude Suppression of Copper Plate Subjected to Periodic Surface Temperature Fluctuation (τ=1s)

placed just 0.5 mm below the surface are incapable of detecting such rapid surface fluctuations. Thus, if such fluctuations are to be correctly captured and serve to more precisely characterize two-phase thermofluid behavior in microgap channels, IR surface imaging must play a substantial role in two-phase flow measurements. However, if precise surface temperatures are to be obtained from IR thermography, it is necessary to methodically account for the generation and propagation of thermal radiation from the heated wall to the IR camera lens.

The spectral distribution of the radiation generated by the microgap cooler wall can be expected to follow Planck's law for a "black" surface (emissivity equal to unity), represented by the equations

$$e_{b_\lambda} = \frac{C_1}{\lambda^5 (e^{[C_2/(\lambda T)]} - 1)} \tag{1}$$

$$C_1 = 2\pi hc^2 = 37413 \ \frac{W\mu m^4}{cm^2} \tag{2}$$

$$C_2 = \frac{hc}{k_b} = 14388 \ \mu mK \tag{3}$$

where $e_{b\lambda}$ is the spectral hemispherical blackbody flux, h is Planck's constant (6.624×10^{-34} erg s), c is the speed of light, and k_b is Boltzmann's constant (1.38×10^{-23} J/K) [22]. Equation 1 is plotted in Figure 10, where it can be observed that the emissive power at each wavelength, as well as the total energy emitted by the surface (i.e. the integral under the curve) increases with temperature and that at each temperature the emissive power rises somewhat steeply with wavelength, reaches a peak value, and then decreases more gently with further increases in wavelength.

For a "gray" surface, for which the emissivity is less than unity but independent of wavelength and temperature, i.e. $\varepsilon_{\lambda,T} = \varepsilon < 1$, the magnitude of the irradiance will fall below the values shown in Figure 10 but follow the indicated spectral distribution. For a surface whose emissivity varies in an arbitrary manner with wavelength and temperature, a detailed spectral irradiance map must be created before any conclusions can be drawn.

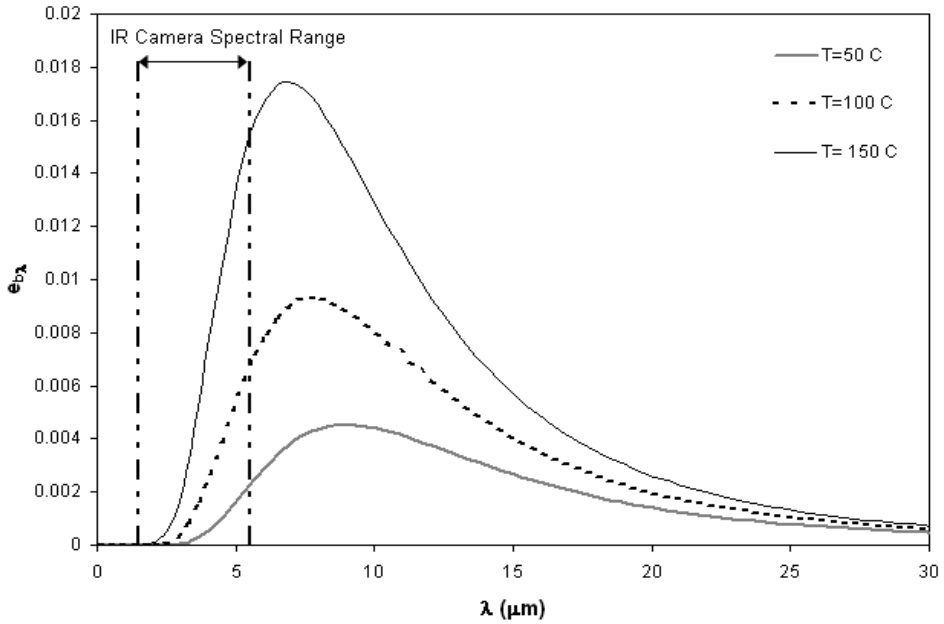

Figure 10: Planck's blackbody function using temperatures of interest to this study, T= 50 ^{o}C, T= 100 ^{o}C, and T = 150 ^{o}C.

For black and gray surfaces, Wien's law (Eq. 4) can be used to calculate the wavelength at which the peak irradiance, λ_{max}, occurs, as

$$(\lambda_{\max} T) = 2897.7 \mu mK \tag{4}$$

where T is the absolute temperature. Thus, the peak irradiance wavelength, λ_{max}, is found to equal 7.8 μm [22] for a surface temperature of 373 K (100 ^{o}C) and 9 μm for a surface temperature of 323 K (50 ^{o}C) – spanning the range of interest in this study.

Integration of Planck's equation, across any range of wavelengths, makes it possible to determine the net radiation emitted by a heated surface in a spectral range of interest. Thus, using Equation 3-5 and anticipating the later discussion on thermal imaging with the FLIR IR camera, it is instructive to note that for a 100C black/gray surface, 6.7% of the radiation falls between 1.5 and 5.5 μm, while for a 50 ^{o}C surface, 3.4% falls in this spectral band [23]. Since integrating Planck's equation is not trivial, tables of the fraction of radiation emitted by a blackbody have been created for easy reference. Thus, using the values from the Table 1 obtained from [22] the above percentages were determined.

Table 1: Fractional Radiation Values [14]

λT (μm x K)	$E_{b,\Delta\lambda}$
1.5 μm *323.15 K =484.7	0
5.5 μm *323.15 K =1777.3	0.034
1.5 μm *373.15 K =559.7	0
5.5 μm *373.15 K =2052.3	0.067

Radiation traversing a series of translucent layers, each with distinct radiation properties - as may occur in the passage of radiation from the heated microgap wall, through the thin liquid layer and a vapor core, then through a second liquid layer, and finally through a window in the opposite channel wall, as shown in Figure 11 - experiences absorption in each layer

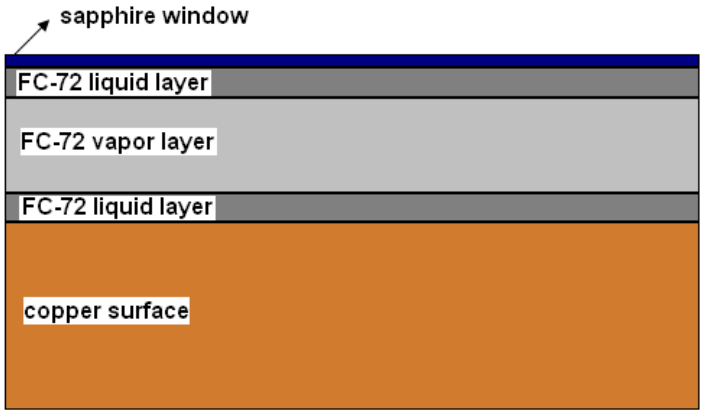

Figure 11: Diagram of various layers within microgap cooler.

and reflection and refraction at each interface. For the analysis conducted on the microgap cooler to determine radiation losses through the various surfaces, calculations of losses from multiple reflections were performed using the refractive indices and absorptivities.

For directional-hemispherical spectral specular reflectivity, the Fresnel equations, Eq. 5, can be used to determine the reflection at each interface, where $\rho'_{\lambda||}$ and $\rho'_{\perp}$ are the average reflectance for the combined parallel and perpendicular polarizations in the incident radiation. Since the incident radiation into the IR camera has a low solid angle from the experimental

setup, it can be considered normal, cosϑ=cosX=1 [27]. This simplification combined with Snell's Law, shown in Eq. 6, results in the normal directional-hemispherical spectral specular reflectivity, as in Eq. 7

$$\begin{aligned}\rho'_{\lambda}(\lambda,\theta) &= \frac{\rho'_{\lambda}\parallel(\lambda,\theta)+\rho'_{\lambda}\perp(\lambda,\theta)}{2} \\ &= \frac{1}{2}\left[\frac{\tan^2(\theta-\chi)}{\tan^2(\theta+\chi)}+\frac{\sin^2(\theta-\chi)}{\sin^2(\theta+\chi)}\right] \\ &= \frac{1}{2}\left[\frac{\sin^2(\theta-\chi)}{\sin^2(\theta+\chi)}\left[1+\frac{\cos^2(\theta+\chi)}{\cos^2(\theta-\chi)}\right]\right]\end{aligned} \tag{5}$$

$$\frac{\sin(\chi)}{\sin(\theta)} = \frac{n_1}{n_2} \tag{6}$$

$$\rho'_{\lambda}(\lambda) = \left[\frac{(n_1-n_2)}{(n_1+n_2)}\right]^2 \tag{7}$$

where n_1 and n_2 are the respective indices of refraction for the two materials traversed by the radiation [18]. Equation 7 was used to calculate the spectral reflectivity in each layer.

2.4 Determination of Wall temperature

As previously noted, the radiation reaching the IR camera sensors originates in the heated microgap channel wall and – for assumed annular two-phase flow - must traverse the thin liquid layers on both walls, the vapor core, and the sapphire window before reaching the IR detectors.

Figure 12 shows a schematic representation of the microgap channel's radiation path, assuming FC-72 as the working fluid (one of the two dielectric liquids that will be tested). While the heated surface radiates hemispherically into the surrounding space, the near normal incidence of the IR radiation on the Merlin optics, allows us to use the simplified Fresnel equations to determine the reflections at each interface. As can be seen by a few representative ray tracings,

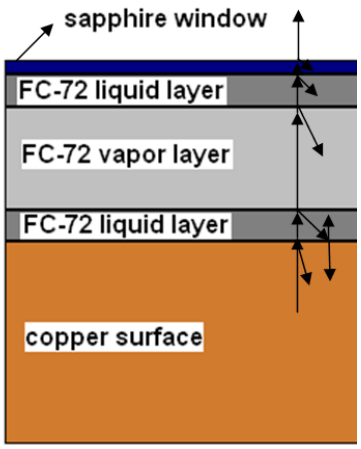

Figure 12: A representation diagram of the experimental setup seen by the IR camera.

the radiation travels through the various media with multiple reflections occurring between the surfaces. All the interfacial reflections and losses through absorption were accounted for by series multiplication of the interface transmissivities (1-reflectivity) and layer transmissivities of the various media, with a radiational contribution of less than 0.01% considered negligible when examining multiple reflections.

The IR radiation leaving the heated wall of the microgap channel – cooled by annular flow of FC-72 – experiences the following sequence of radiational interactions: copper to thin liquid layer of FC-72 (back reflections), passage through the thin layer of FC-72 (absorption. emission), thin liquid layer of FC-72 to vapor FC-72 (back reflections), passage through the FC-72 vapor core (absorption, emission), vapor FC-72 to thin liquid layer of FC-72 (back reflections), thin liquid layer of FC-72 (absorption, emission), and thin liquid layer of FC-72 to sapphire (back reflections), passage through sapphire window (absorption, emission). Equation 11 is a mathematical representation of the ray tracing that was used to account for the various radiation transmissions and losses:

$$q_{obs} = \varepsilon\sigma T^4 \times \left[\tau_{FC-72\_liq} \times \tau_{FC-72\_vap} \times \tau_{FC-72\_liq} \times \tau_{sapphire} \times \tau_{air} + \sum_{copper}^{air} \sum q_m \rho_n \rho_{n-1} \tau_n \right] \qquad (11)$$

where τ_n is the layer transmittance, ρ_n is the layer reflectance, and q_m is the portion of the radiation reflected back through the system. The model will be further refined to include the re-

emission of radiation from the various layers within the channel. Despite absorption being minor, the addition of re-emission will further minimize the effects, or could be assumed negligible if the film and wall temperature are nearly equal. If the film and wall are of nearly equal temperature, the emissivity of the liquid layer and the absorptivity to radiation originating at the wall would be equal; thus the radiation contributions – of the emission and absorption (since the exponential decay is small and almost linear) – essentially will be negating effects.

The radiational properties of the various layers and derived quantities are shown in Table 3 for the spectral range of 1.5-5.5 μm (or as indicated) assuming FC-72 as the dielectric liquid.

Table 2: Properties of the Microgap Cooler Layers [24-26]

	λ (μm)	n	α (cm^{-1})	thickness	ε
Copper	3	1.56	--	--	0.65
FC-72 (liq)	0.546	1.251	0.001	0.065 mm	0.0000065
FC-72 (vap)	0.546	1.1	0.001	0.13 mm	0.000013
Sapphire	3	1.71	0.00005	3.2 mm	0.00002
Air	--	1	--	--	--

Since FC-72 has a bulk absorptivity of 10^{-3}/cm and the "optical thickness" of a nominal 130μm thick layer of FC-72 vapor and 65 μm thick layer of FC-72 liquid are exceedingly small, the absorption in the liquid and vapor can be neglected up to 200 microns or 10% absorption (half of the largest gap being studied). The initial path of radiation, with absorption and reflection losses at each layer, results in an overall transmissivity of 87.6% for this and all gap sizes studied (due to minimal losses due to absorption)**.** Further careful accounting for the multiple reflections and absorption in the various layers results in a slight increase in the total radiation seen by the IR camera to an effective transmissivity of 87.8%. This less than perfect transparency of the microgap channel reduces the net radiation exiting the channel at a specified wall temperature and can be captured in an effective emissivity, defined as

$$\varepsilon_{eff} = \varepsilon_{surface} \times \tau \tag{12}$$

Equation 12 displays the variation in the effective emissivity of the two-phase microgap channel

with the liquid layer thickness. It may be seen that – except for the extremes of no liquid and full liquid - the effective emissivity is nearly constant and even at the extremes, the changes are rather modest. Thus, for preliminary results a constant effective emissivity was applied across the surface. Use of a single effective emissivity across the full field of view – including any dryout regions – may, thus, overestimate the peak temperatures by no more than 1-2 K.

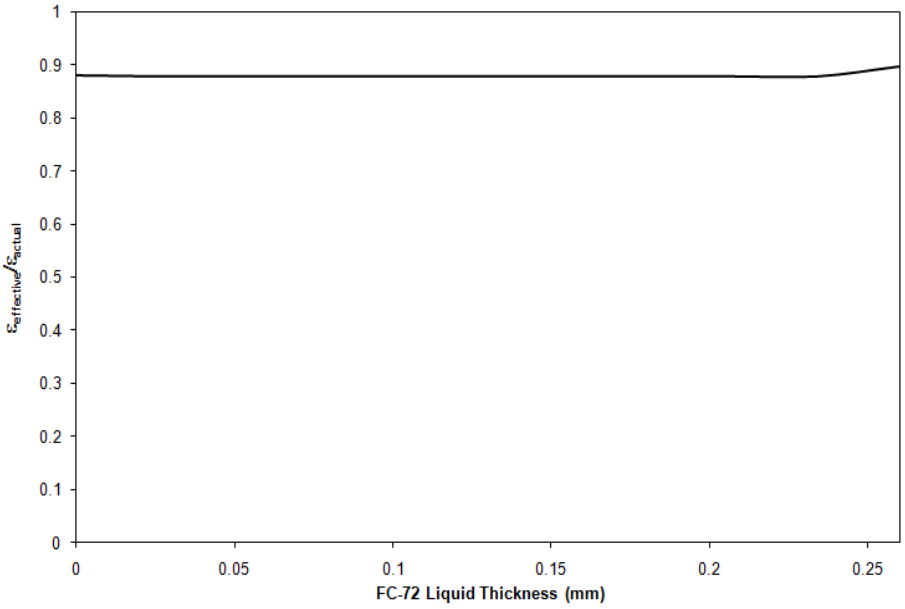

Figure 13: Effective Emissivity of a 210μm Microgap Channel with FC-72 Liquid.

2.5 Wall Temperature Fluctuations

Observations of wall temperature fluctuations in two-phase flow have generally shown relatively low amplitude, high-frequency fluctuations in Bubble flow and time-invariant values for annular flow [22]. However, intermittent or slug flow has been known to yield significant fluctuations in pressure and wall temperature. The frequency of these fluctuations can be calculated using the correlation shown in Eq 9

$$f_s = 0.0226\left[\frac{V_{SL}}{gd}\left(\frac{19.75}{V_{ns}} + V_{ns}\right)\right] \tag{9}$$

where f_s is slug frequency, V_{SL} is superficial liquid velocity, d is pipe diameter, g is gravity, and

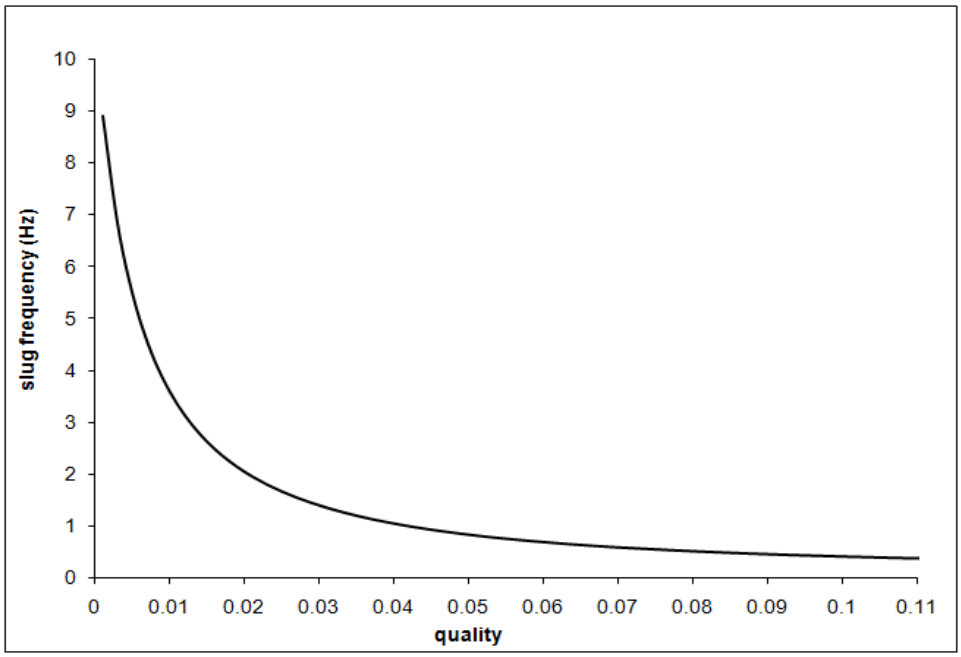

Figure 14: Slug frequency plotted against quality for 210 micron pipes with FC-72 working fluid.

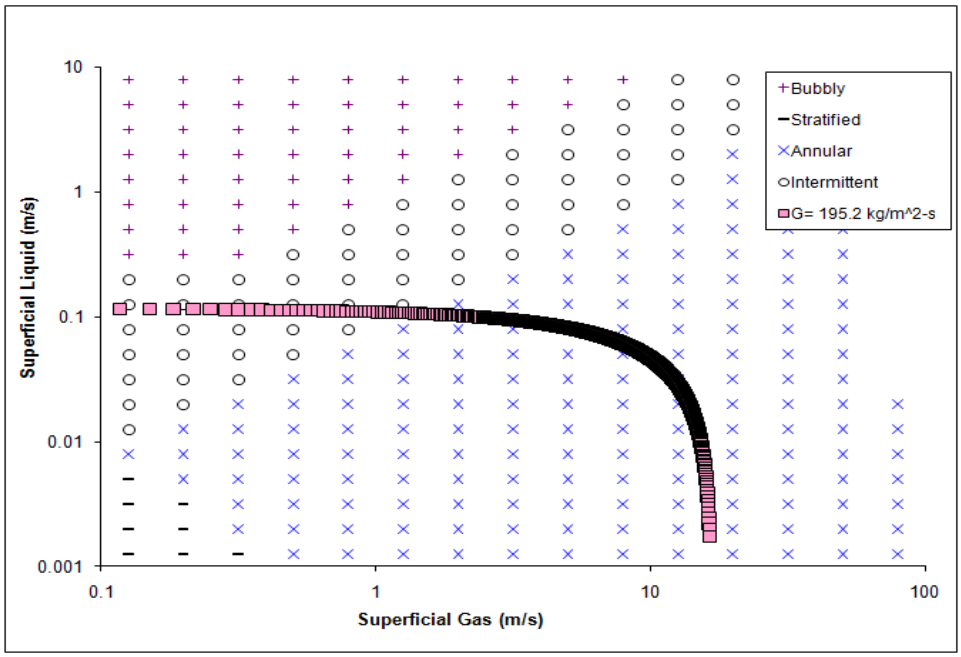

Figure 15: Flow regime map for G=195.2 kg/m^2-s, for 210 micron microgap cooler with FC-72 working fluid.

V_{ns} is no-slip velocity [23-24]. The correlation shown in Eq 9 was developed for small pipes with an air/water flow. Figure 14 shows the slug frequency for typical flow conditions, G=195.2 kg/m^2-s, for FC-72 in a 210 micron channel, as depicted in the flow regime map in Figure 15. The slug frequency is seen to fall with increasing quality and, for slug flow in the specified microgap channel the slug frequency is seen to fall below 1 Hz for qualities greater than 5%. Thus, frequency magnitudes higher than this value would be attributed to other phenomena occurring inside the channel (i.e. instabilities). The discovery of previously undetectable high frequency, large magnitude fluctuations necessitates further investigation to understand what underlying phenomena are occurring.

2.6 Local Dryout in Annular Flow

While the temperature fluctuations so clearly visible in the IR images are large and repeatable, they are generally unexpected in the conventional view of the annular flow regime, in which spatially uniform film thickness and temperature is assumed. However, in the detailed analysis of the thermofluid characteristics of refrigerants flowing in microgap channels, Bar-Cohen and Rahim [19] observed significant deterioration in the heat transfer coefficient at thermodynamic qualities in the range of 40% to 70%, well below the anticipated channel dryout condition. It was postulated that local dryout, associated with flow instabilities and/or the formation of rivulets, could be responsible for this deterioration.

The frequency and amplitude of the observed temperature variations, displayed uniquely by the IR imagery presented in this study, appear to provide evidence of incipient and actual, local dryout in moderate quality annular flow. Moreover, this view is reinforced by the observation that high instantaneous heat transfer coefficients, resulting in surface temperatures nearly equal to the saturation temperature, precede the observed temperature spikes. It would, thus, appear that such behavior could be attributable to the rapid thinning of the liquid layer, leading to very high heat transfer coefficients, just before complete evaporation and local dryout occurs, driving the temperature to elevated levels.

CHAPTER 3

EXPERIMENTAL SETUP

The study will rely on the previously-validated two-phase regime mapping methodology for microgap channels along with IR imaging of the heated surface and the inverse determination of the local wall heat flux based on numerical simulation, to study the thermofluid characteristics of various microgap channels.

3.1 Microgap Channel Design

Microgap coolers with a dielectric liquid as a working fluid are instrumented with thermocouples and pressure transducers for testing, with a 210 micron gap channel was used to obtain initial findings, and addition research data was collected for a full parametric range of gaps, widths, heat fluxes, mass fluxes, and orientation angles. All microgap coolers are instrumented with thermocouples and a sapphire viewing window for temperature measurements. The thermocouples are used to calibrate the infrared camera by matching the average infrared temperature to that of the thermocouple. Figure 16 and Figure 17 show a depiction and digital image of the general

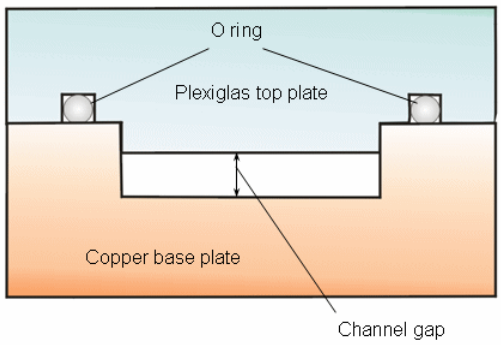

Figure 16: Diagram of microgap cooler.

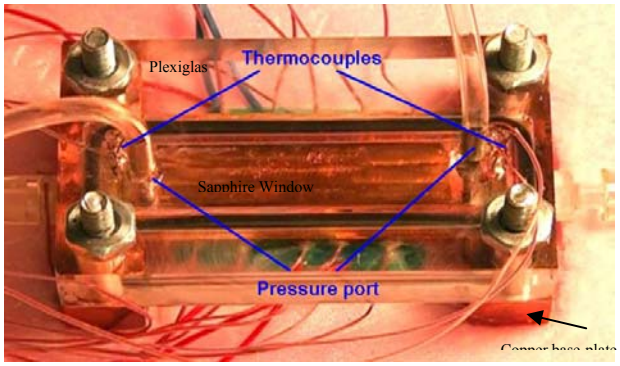

Figure 17: Digital picture of 35 mm X 10 mm X 210 μm microgap cooler.

microgap cooler design used for experimentation. The cooler has a translucent sapphire viewing window fitted into a Plexiglas top plate that is placed on top of the copper base plate with embedded thermocouples.

The embedded thermocouples are Type E butt welded located 0.5 mm below the imaged surface. To simulate the heat from an electronic component, ceramic leaded chip resistors (LR3413737T0100J; American Technical Ceramics) are soldered directly to the bottom of the copper base plate. The heaters can dissipate 100% of the power under 100 ^{o}C, and have dimensions of 1 cm x 1 cm with the ability to generate 250 W (250W/cm^2).

3.2 FLIR Merlin IR camera

An infrared camera captures radiation from a prescribed field of view using a sensor(s), sensitive to a specified spectral range. Figure 18 shows a digital image of the experimental setup, with near-normal incidence. Appropriate radiation relations are used to convert the absorbed radiation to a thermal image of the radiating surface. The camera has a calibrated voltage drop for the electrical current induced by the absorbed radiation over this range. By using Eq. 10 and parameters provided by the user,

$$U_{obj} = \frac{1}{\varepsilon\tau}U_{tot} - \frac{1-\varepsilon}{\varepsilon}U_{refl} - \frac{1-\tau}{\varepsilon\tau}U_{atm} \qquad (10)$$

Figure 18: Digital Image of infrared camera setup and digital image of experimental configuration.

the total radiation detected is converted into the object radiation, where U_{obj} is the object blackbody output voltage calculated from measurements and input parameters, U_{tot} is the measured output voltage of the device, U_{relf} is the theoretical camera output voltage for a blackbody of a specified input temperature, U_{atm} is the theoretical camera output voltage for a blackbody temperature based on atmospheric input temperature, and ε is object emittance [30]. As shown in the Background section, the percent of radiation emitted in this band is between 3.4%-6.7% for operation temperatures of 50 ^{o}C – 100 ^{o}C. Embedded software allows the Merlin to make the necessary corrections and accurately determine the surface temperature to within +/- 2 K in the range of 0-273.15 K [30].

The FLIR Merlin IR camera used for the present experiments has a 1.5 μm -5.5 μm range, with a sampling period of 0.016 s (60 Hz) [30]. The experimental setup is shown below in Figure 19, and the near normal incidence is apparent. The emissivity was empirically determined for each experimental run by matching the average IR temperature to each thermocouple temperature. The empirically determined emissivity on average was 0.50, which varied slightly (+/- 0.02) but was noted for each experimental trial.

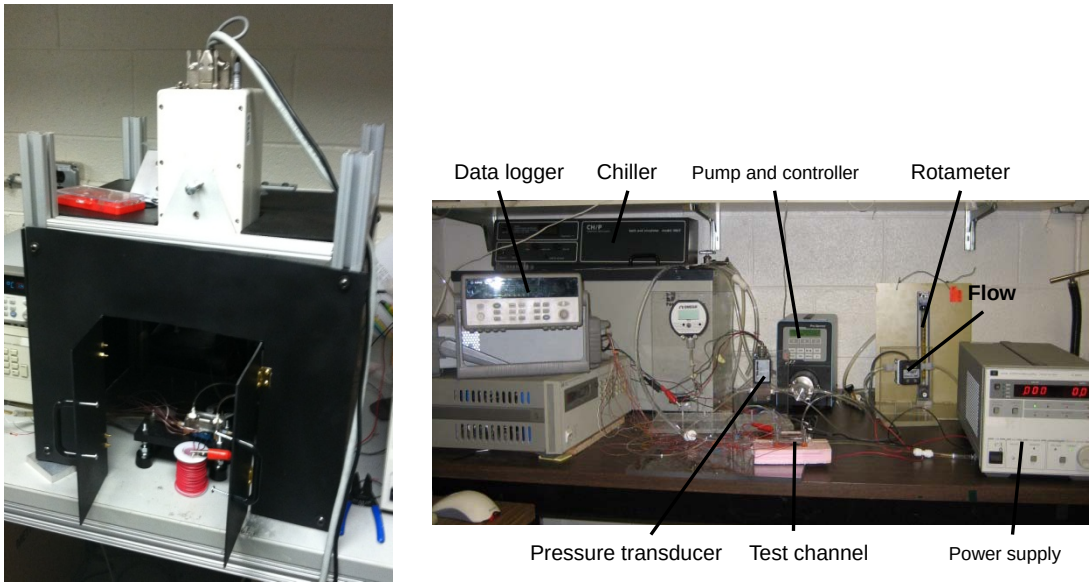

Figure 19: Digital Image of infrared camera setup and digital image of experimental configuration.

3.4 Determination of Heat Transfer Coefficient

Finite Element modeling software (ANSYS ver. 12.1) was used in a previous study to determine the heat losses from the heater and the net heat flux entering the microgap during experimentation. The numerical results were achieved through iterative runs of the ANSYS model, varying the average heat transfer coefficients until very good agreement was attained with the measured surface temperatures [35]. Following this procedure, but using eight local rather than average heat transfer coefficients, in the present study the experimental and numerical results were found to deviate less than 1.0°C on average for 210 μm gap channel at mass flux 195.2 kg/m^2-s. Figure 20 displays the inversely-determined, two-phase heat transfer coefficients for the 210 μm gap channel, operating at G=195 kg/m^2-s, and q”=31 W/cm^2, reported in Sheehan and Bar-Cohen (2011), and compares these empirical values to those predicted from the Chen

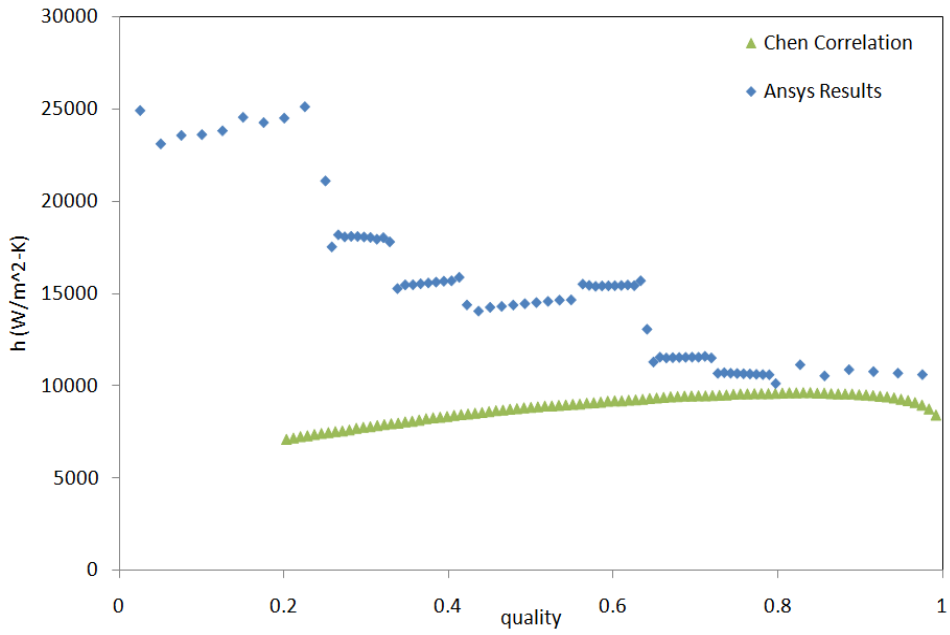

Figure 20: Inversely-Calculated, Axial, Two-Phase Heat Transfer Coefficient Variation for FC-72 [q"=31 W/ cm^2; 210 micron gap; G=195 kg/m^2-s], Sheehan and Bar-Cohen (2011).

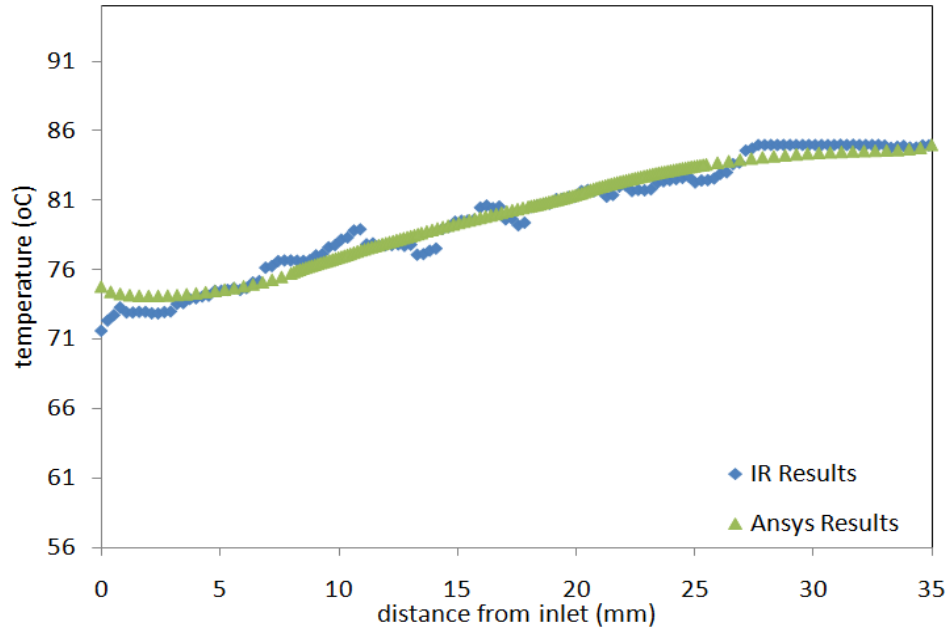

Figure 21: Experimental and Numerical Axial Microgap Wall Temperature Distribution for FC-72 – [210 µm gap; G=195 kg/m^2-s; q"=31 W/cm^2], Sheehan and Bar-Cohen (2011).

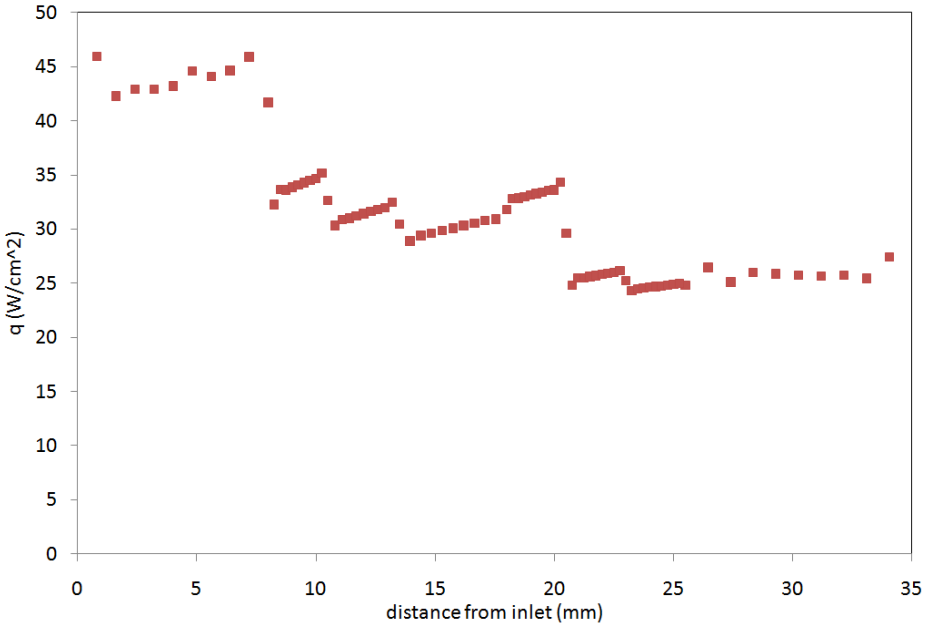

Figure 22: Inversely Determined Axial Heat Flux Distribution [FC-72, 210 micron channel; G=195 kg/m^2-s; q"=31 W/cm^2], Sheehan and Bar-Cohen (2011).

correlation. It is notable that the inversely-determined two-phase heat transfer coefficients exhibit many elements of the characteristic M-shaped curve, observed in earlier studies, Bar-Cohen and Rahim (2009), with a first peak reaching 25kW/m^{2}K at low qualities and a second peak of 15kW/m^{2}K at intermediate qualities, followed by a drop as the quality increases further. The comparison to the values predicted by the Chen correlation reveals the expected discrepancy in the low-quality, Bubble flow region of the channel and improving agreement as the quality reaches and exceeds approximately 65%. Flow in this region is expected to be distinctly Annular and the discrepancy between the inversely-determined heat transfer coefficients and the Chen correlation values is in the range of 17% to 25%.

Figure 21 demonstrates the close agreement achieved (+/- 1 C) between the numerically determined and the IR measured temperatures for this channel. The numerically determined heat flux distribution along the length of this microgap channel is shown in Figure 22 and seen to vary from a peak of 46 W/cm^2 near the inlet, thru several spatial oscillation, before reaching a plateau of approximately 25 W/cm^2 near the outlet of the channel, highlighting the importance of using local heat flux values in determining the local heat transfer coefficients.

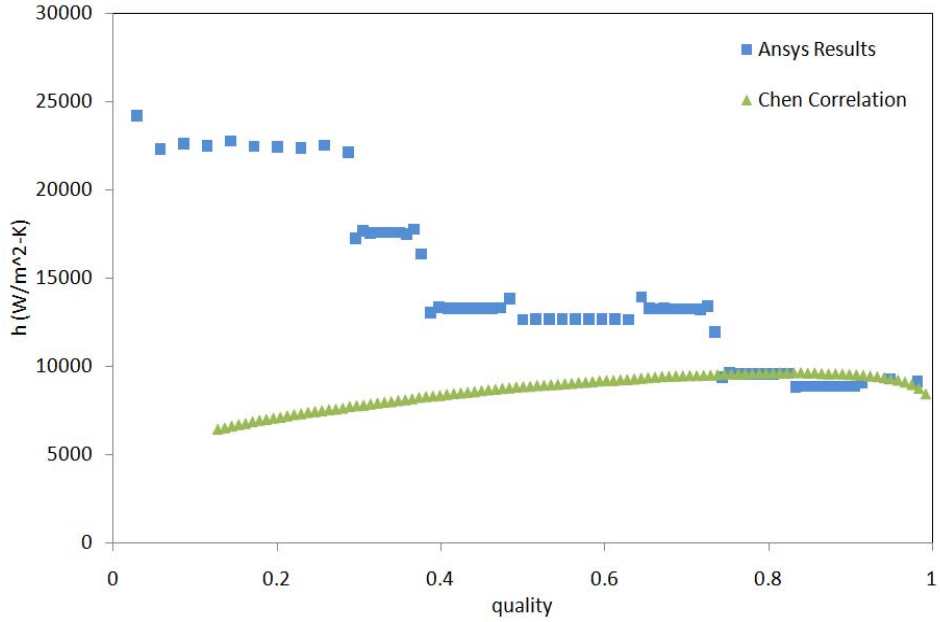

Figure 23: Inversely-Calculated, Axial, Two-Phase Heat Transfer Coefficient Variation for FC-72 [q"=35 W/ cm^2; 210 micron gap; G=195 kg/m^2-s], Sheehan and Bar-Cohen (2011).

Similar heat transfer coefficient results are shown in Figure 23 for the 210 μm gap channel operating at an FC-72 mass flux of 195 kg/m^2-s and a marginally higher heat flux of 35 W/cm^2. The salient elements of the characteristic M-shape curve are again in evidence in these results, with a low quality peak (in this case more of a plateau) of approximately 22kW/m^{2}K, followed by a down-sloping branch, which stabilizes at a lower plateau of approximately 13kW/m^{2}K, and a further drop to approximately 9kW/m^{2}K as the quality approaches unity. Remarkable agreement between the inverse-calculated values and the Chen predictions, for qualities in excess of 70%, is visible in Figure 23. Overall agreement with the Chen correlation for data presumed to fall in the Annular flow regime is, however, still in the previously observed range of approximately 25%.

To achieve further refinement the parametric study the local zones was increased from eight to ten, with ten being the maximum number of zones for which manual iteration could be used to successfully reach conversion without resorting to process automation through software. To perform these simulations use was made of a free mapped mesh in ANSYS, with mesh conversion verified with 600,000 elements. The model built in ANSYS included the base of the

channel (i.e. gap and supporting copper structure), using the two-phase heat transfer zones to represent the complicated physics of the evaporating liquid on the surface.

3.5 Uncertainty Analysis

Measurement errors can be grouped into two categories: bias-those that remain constant during fixed parameter experiments and precision-the repeatability. These errors can be combined to determine the overall uncertainty of measured quantities using the root-sum-square method,

$$u = \sqrt{e_1^2 + e_2^2 + \cdots + e_k^2} \tag{14}$$

where u is the uncertainty in measurement and e is the elemental error of equipment.

Applying this method to the pressure drop measurement, the elemental errors are the accuracy of the pressure transducer (± 0.25% FS) and the uncertainty in the measurement of flow rate (consisting of visual and data logger errors). Thus, the overall uncertainty of the pressure drop measurement is

$$\frac{\delta \Delta p}{\Delta p} = \sqrt{\left(\frac{\delta Q}{Q}\right)^2_{flow\ rate} + \left(\frac{\delta Q}{Q}\right)^2_{read\ out} + \left(\frac{\delta \Delta p}{\Delta p}\right)^2_{t}} \tag{15}$$

where Δp is pressure drop and $\delta\ \Delta p$ is the uncertainty of pressure drop measurement and $(\delta\ \Delta p)t$ *is* error of the pressure transducer. With a data logger error of 0.05%, flow rate measurement error of ± 3% (for a rotameter), and 5% error in the read out, the maximum error for pressure drop measurements is found to equal 6.5%.

Similar analysis shows that the elemental errors for the heat transfer coefficient are: power supply error (±0.1%), wall temperature measurement error (±2%), and error due to ANSYS model prediction of heat flux (±2.6%). ANSYS error was determined by variation of heat transfer coefficients until 2 C agreement on average was found between experimental and modeling temperature, then calculating the error in net heat flux prediction compared to the 1 C

(or acceptable difference) results Equation 16 shows the mathematical expression for the overall uncertainty associated with the heat transfer coefficient

$$\frac{\delta h}{h} = \sqrt{\left(\frac{\delta q}{q}\right)^2 + \left(\frac{\delta \Delta T_{wall}}{\Delta T_{wall}}\right)^2 + \left(\frac{\delta q}{q}\right)^2_{Ansys}} \tag{16}$$

where h is the heat transfer coefficient and δh is the uncertainty of the heat transfer coefficient. Thus, the resulting overall uncertainty is 3.3%.

CHAPTER 4

EXPERIMENTAL METHODOLOGY AND INITIAL RESULTS

To determine the validity of experimental methods using in this dissertation, a preliminary series of experiments was conducted on a 210 micron gap using FC-72 as the working fluid with mass flux of 195.2 kg/m^{2}s. The channel was subjected to heat fluxes of 10.3-26 W/cm^2, which were found to produce temperature fluctuations with variable dominant frequencies and maximum observed amplitude (maximum for all experimental trials being approximately 30 K). Comparisons among various locations within the channel with different heat fluxes, as well as various qualities, were conducted.

The heated wall of the microgap channel was imaged by the IR camera while being asymmetrically heated from the bottom of the copper base plate. Appropriate radiation corrections can be made to recognize the contribution of radiation absorption and reflection by the liquid, vapor, and sapphire window traversed by the radiation reaching the eye of the IR camera.

4.1 Wall Temperature Map

Figure 24 shows typical results of one frame from an infrared video taken for each set of test conditions. Figure 24 shows a "snapshot" from the video taken for q=10.3 W/cm^2 and G=195 kg/m^2-s, with flow from left to right in a 10mm x 37mm with a 210 micron high channel. From this image it may be seen that significant axial and lateral temperature variations exist, for example in the vicinity of the 20% and 34% quality lines, respectively. From a series of such images, the temporal thermal behavior of the microgap channel can be determined and analyzed. Figure 25 shows a sequence of four IR images taken 1 s apart through the sapphire window in the microgap channel. The temperature non-uniformity and the high frequency of temperature fluctuations are clearly visible in these images, for example comparison of the right side of each snapshot shows the fluctuation from purple (73C) to orange (83C) a variation of 10 C.

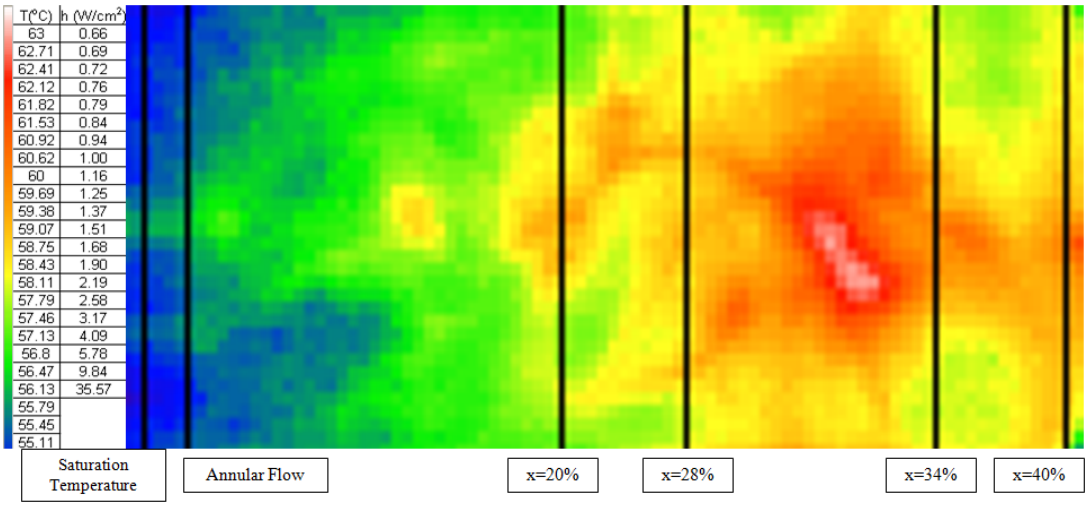

Figure 24: Infrared image for q=10.3 W/cm^2 and G=195 kg/m-s^2.

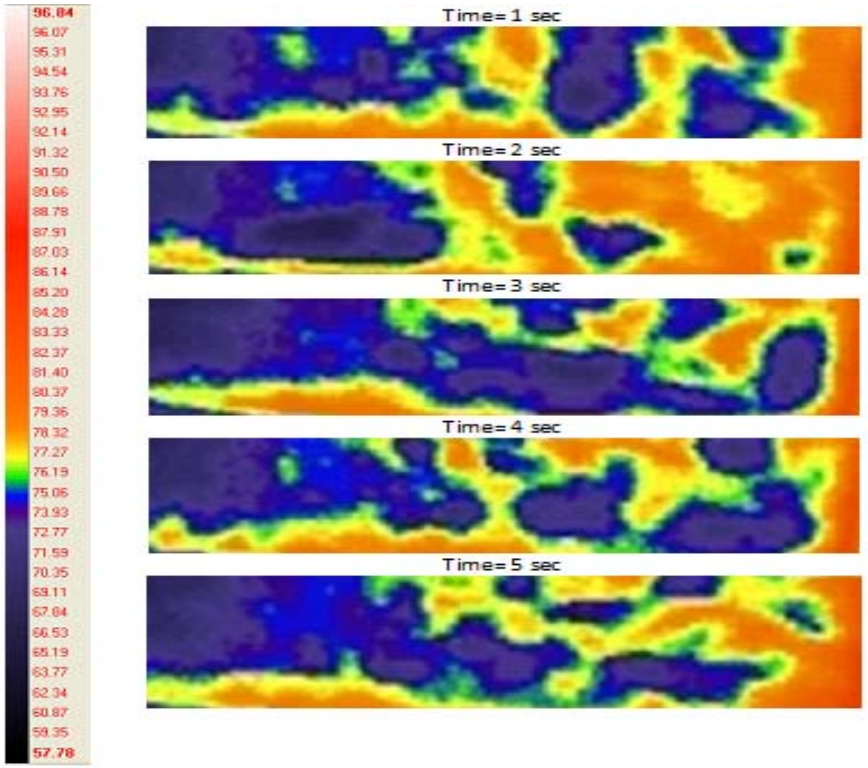

Figure 25: Thermography of 37 mm x 10 mm 210 μm, G= 195 kg/m^{2}s, and q"= 18W/cm^2.

4.2 Axial Temperature Profiles

Figure 26 shows the instantaneous axial temperature variation from the inlet to the outlet of the 35mm microgap channel, for four different heat fluxes. It is to be noted that in this "snapshot" the wall temperatures at all four fluxes increase from the inlet to the outlet, though

more strongly with the highest heat flux, accompanied by modest spatial temperature fluctuations. Since the thermodynamic quality of the two-phase mixture depends on the total heat addition to the flow, the quality at each location varies with the surface heat flux, reaching dryout for the highest heat flux of 26W/cm^2 and just 40% quality for q" = 10.3W/cm^2, for the stated conditions. It should, nevertheless, be realized – from the flow regime map of Figure 3 – that Annular prevails for nearly the entire length of the channel for all but the lowest heat flux. Figure 26 also reveals that, as expected, the wall temperatures for the highest heat flux are significantly higher than for the lowest heat flux. However, due to the dynamics of liquid film thinning with quality, the wall temperatures for the two middle heat fluxes converge to each other. Despite modest axial temperature variations, preliminary data for a higher heat flux shows a distinct difference between temperature fluctuations at two axial locations, as seen in Figure 27. This shows that a 9 mm difference can create a 16K difference in fluctuation amplitude.

Since traditional thermal measurement methods did not previously reveal high wall temperature fluctuations, comparison between average IR heat transfer coefficients along the channel with theory and thermocouple measurements was done. Figure 28 shows a skewed, but

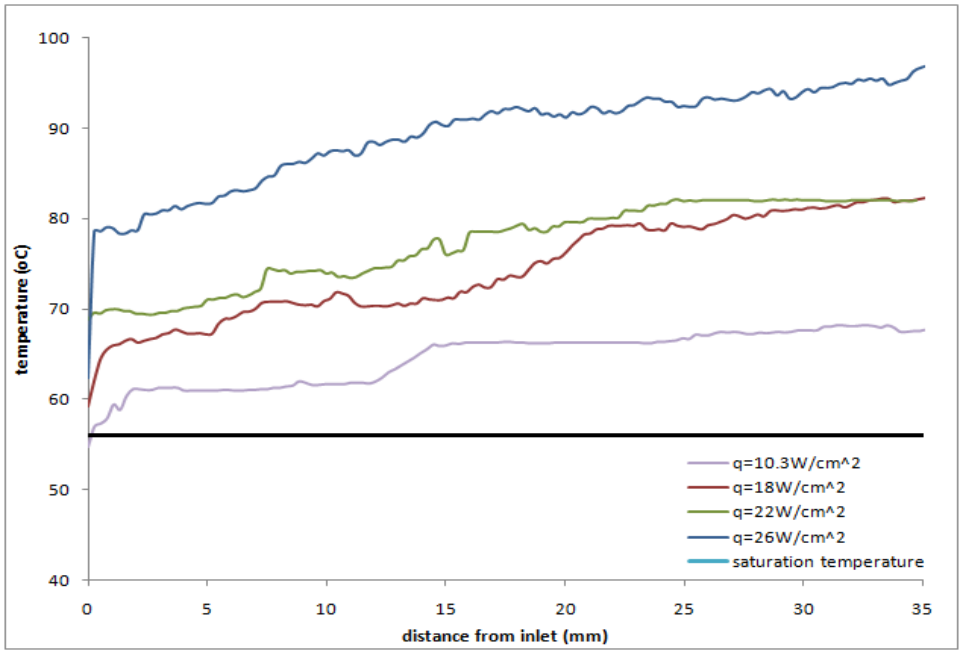

Figure 26: Temperature variation axially in 210 micron microgap cooler with G=195 kg/m^2-s with FC-72 working fluid.

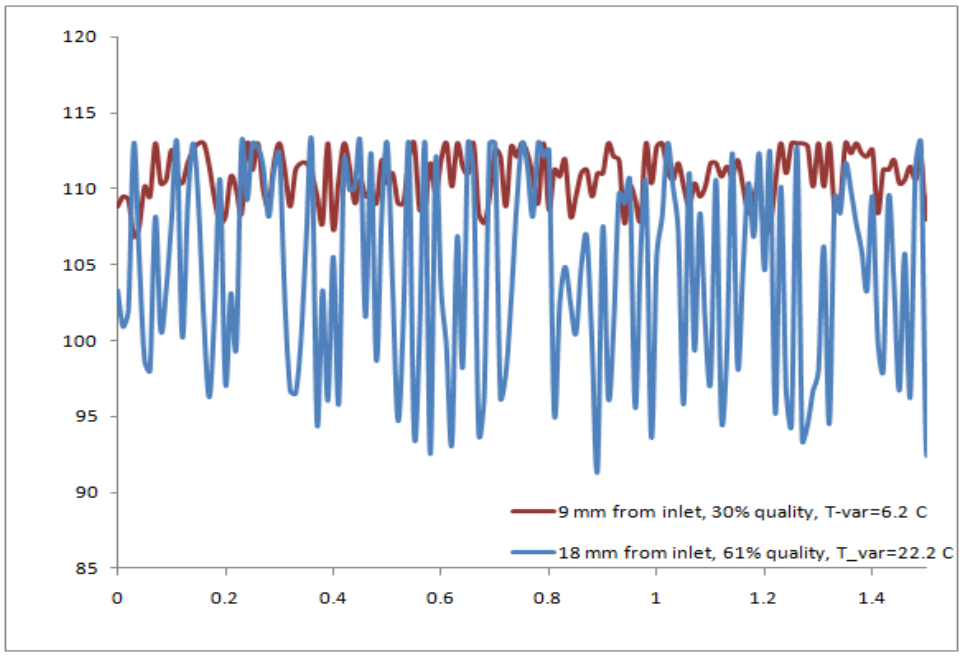

Figure 27: Comparison of two fixed locations within a 210 micron microgap cooler using FC-72 with G=195.2 kg/m^2-s and q=30W/cm^2.

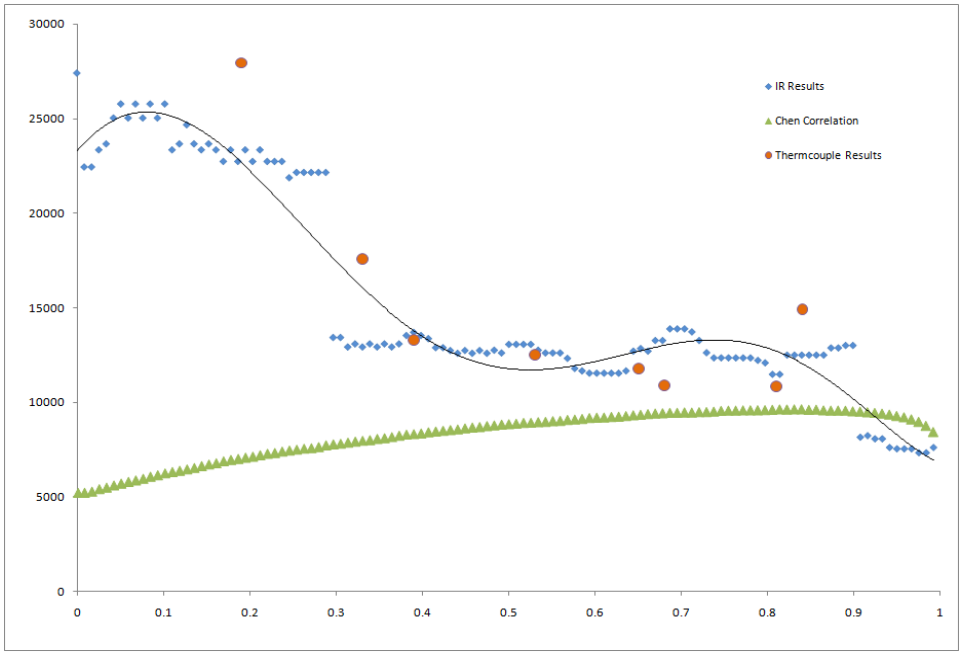

Figure 28: Heat transfer coefficient curve for q=26 W/cm^2 in 210 micron microgap cooler with G=195 kg/m^2-s with FC-72 working fluid.

nonetheless recognizable characteristic M-shape curve for the axial variation of the two-phase heat transfer coefficient from both IR imagery and thermocouple measurements in this experimental configuration. This favorable comparison, along with the observed proximity to the predicted values of the Chen correlation for the higher qualities, lends support to the validity of the measurement technique and, consequently, to the existence of the wall temperature fluctuations.

4.3 Temporal Temperature Variations – Fixed Locations

Figure 29-Figure 31 show the temporal temperature fluctuations for three different locations and four different fluxes, with a fixed mass flux of G=195 kg/m^2-s. Figure 29 reveals results for lower qualities (i.e. closer to the inlet) and demonstrates the high fluctuations occurring at q=26W/cm^2 while modest variations at the other heat fluxes. It is notable that the amplitude of the temperature fluctuations for q=10.3W/cm^2 and q=18W/cm^2 are quite similar – though of somewhat different character -, which can be attributed to similar qualities. Since the quality determines the flow regime, it could be postulated that the prevailing flow regime is the primary factor in the development of these previously unobserved fluctuations.

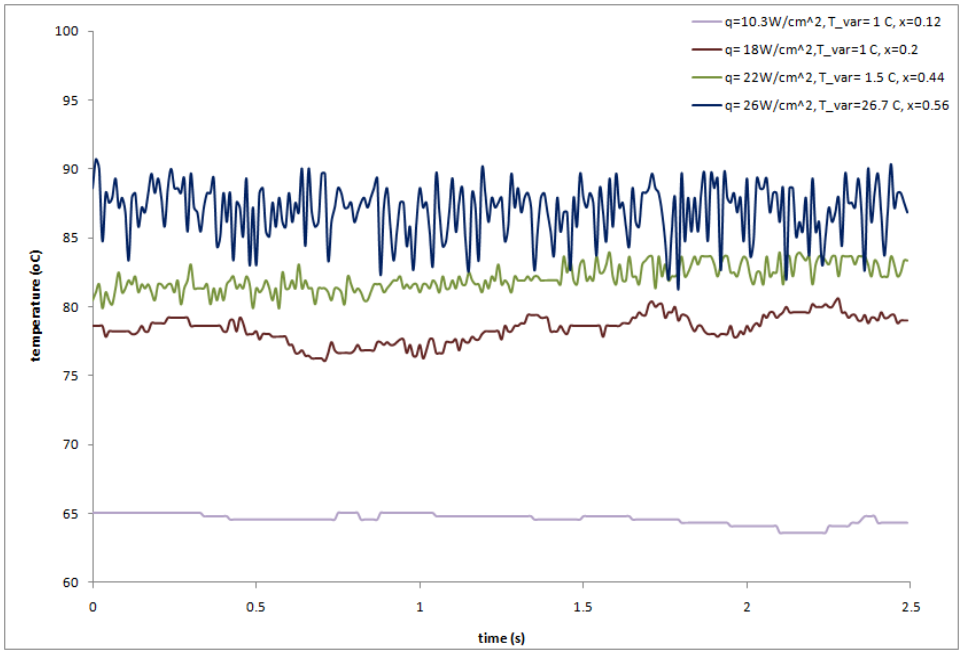

Figure 29: 20 mm location from inlet (T_var is maximum temperature variation) for a 210 micron channel with G=195 kg/m^2-s.

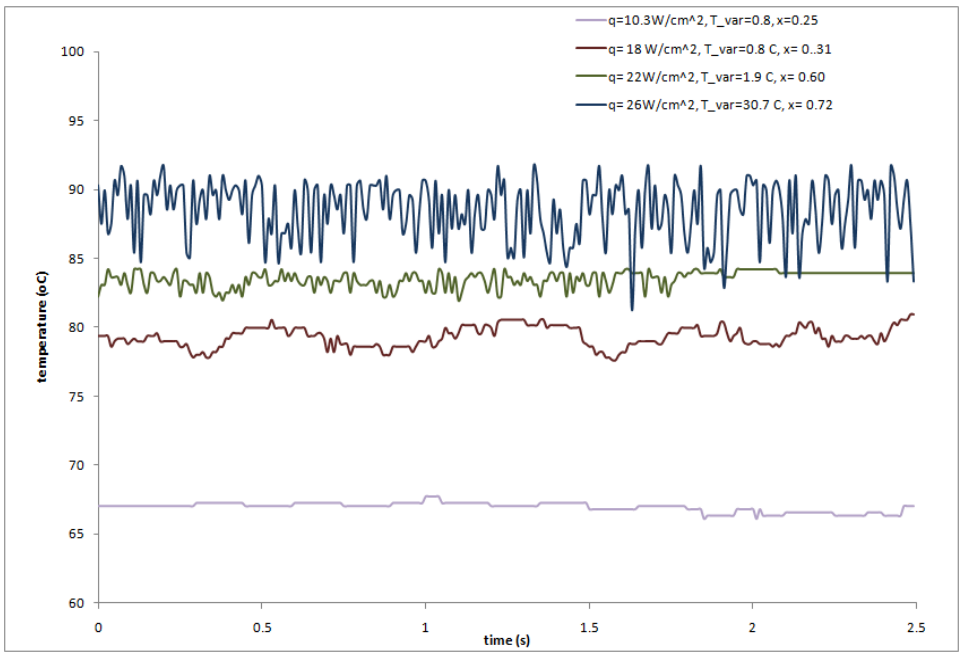

Figure 30: 25 mm location from inlet (T_var is maximum temperature variation) for a 210 micron channel with G=195 kg/m^2-s.

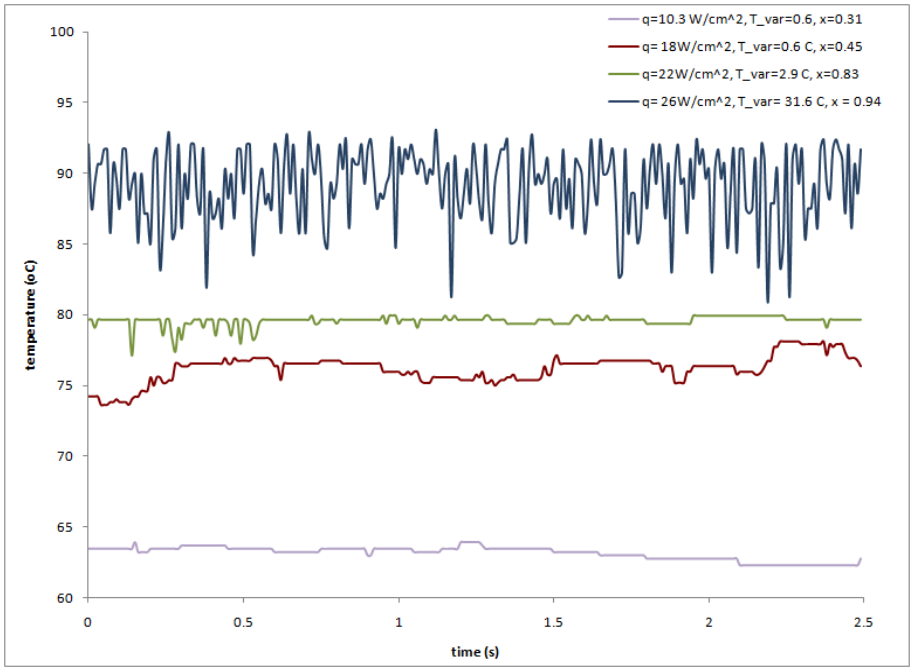

Figure 31: 31 mm location from inlet (T_var is maximum temperature variation) for a 210 micron channel with G=195 kg/m^2-s.

Figure 30 shows results further from the inlet in the axial direction, and interestingly displays somewhat lower (than at x=20mm) average temperatures for the two intermediate heat fluxes and a reduced amplitude in the temperature fluctuation, while the wall temperature for the highest q" remained nearly the same, but the amplitude of the fluctuations markedly increased. This could be due to a "stable" annular thin film regime that precedes the onset of a more "unstable" domain with periodic dryout and re-wetting. For the highest heat flux this transition might have occurred prior to the 20mm location studied and, thus, only increasing temperature fluctuations are observed. For the lowest heat flux, which displays nearly uniform temperature, this transition may only occur at far longer downstream distances.

It would, thus, appear that, contrary to initial expectations, it is both the flow regime and heat flux that influence the wall temperature fluctuations and that such fluctuations can extend over much of the operating envelope of a microgap channel. In addition to this finding, it has been determined that these fluctuations are not due to an artifact (i.e. scratch, groove, protrusion on the surface) on the channel wall at a specific location but caused by a physical phenomenon occurring in the channel. This is checked for all subsequent channel geometries.

4.4 Temporal Temperature Variation – Fixed Quality

Reflecting the effect of flow regime on the wall, Figure 32-Figure 34 display several seconds of temperature history for fixed quality points, at several distinct heat fluxes, in the 210μm channel, cooled by a mass flux of 195 kg/m^{2}s of FC-72 operating fluid within the annular flow regime. The highest heat flux generally has the greatest magnitude temperature variations, and the variations increase in amplitude with increasing quality as shown before. The temperature variation was determined by the peak to peak value of the data, and where appropriate statistical analysis is performed for further understanding. Interestingly, the three other heat fluxes did not continue to follow this trend. Figure 32 demonstrates modest temperature variations for all heat fluxes, since the quality is low and this is at the beginning of annular flow, it can be proposed that "stable" annular flow is occurring. Figure 34 shows these

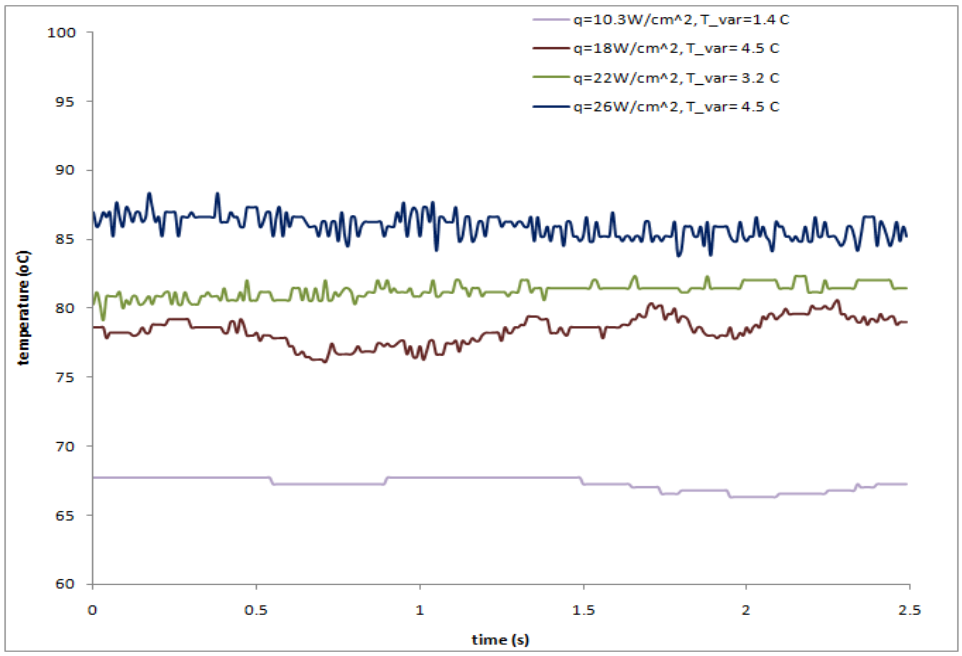

Figure 32: Comparison for 20% quality (T_var is maximum temperature variation) for a 210 micron channel with G=195 kg/m^2-s.

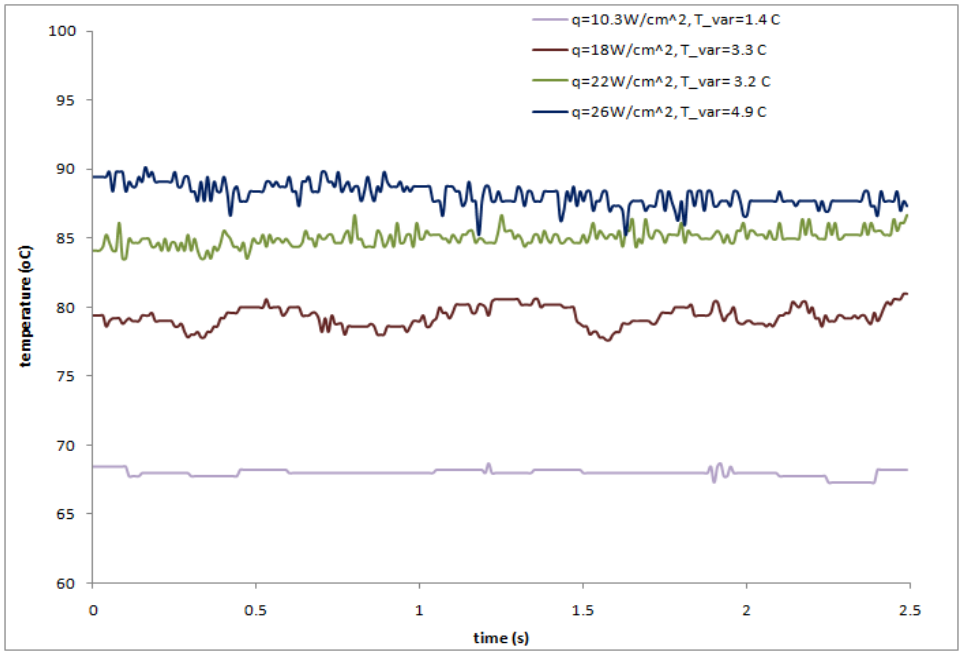

Figure 33: Comparison for 31% quality (T_var is maximum temperature variation) for a 210 micron channel with G=195 kg/m^2-s.

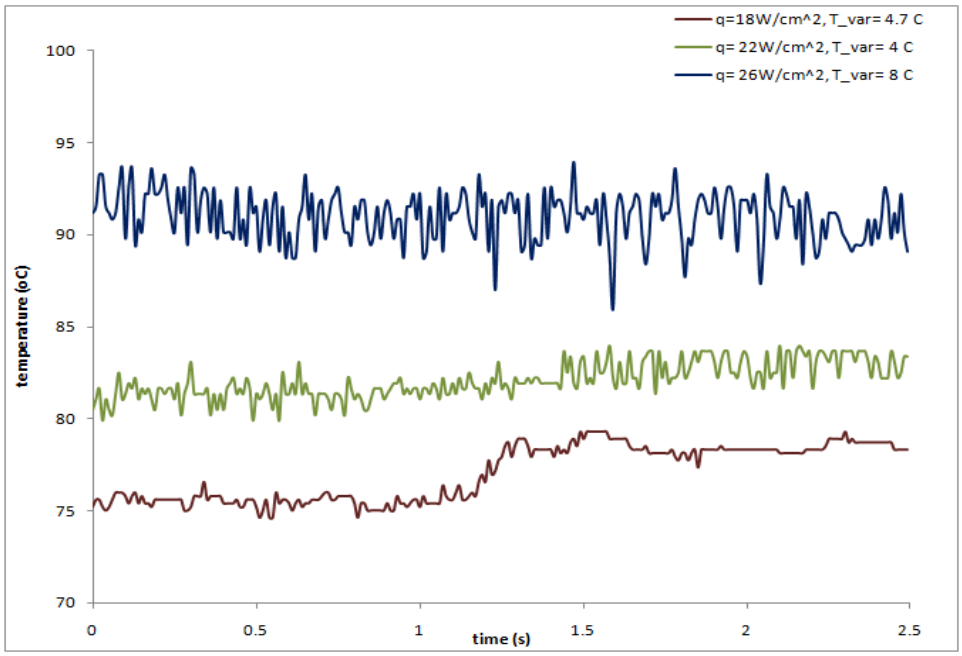

Figure 34: Comparison for 44% quality (T_var is maximum temperature variation) for a 210 micron channel with G=195 kg/m^2-s.

three heat fluxes at higher qualities, and it is apparent that the amplitude of fluctuation increases with the quality but that at the highest heat flux and highest quality, the temperature variations are starting to become chaotic. This further supports the coupled effect of flow regime (developing annular versus ultra-thin-film annular) and heat flux to generate the high frequency high amplitude temperature fluctuations.

4.6 Lateral Temperature Variations

While much of the emphasis thus far has been on the axial temperature variations in the microgap channel, the previously observed two- and three-dimensional waves on a shear-driven liquid film motivate an exploration of the lateral variation in wall temperature in the subject microgap channel [16]. Figure 35-Figure 37 compare the temperature histories of several distinct lateral locations at three fixed axial locations for the imposed 26W/cm^2 heat flux. Interestingly, while the locations in the center of the microgap channel generally display similar

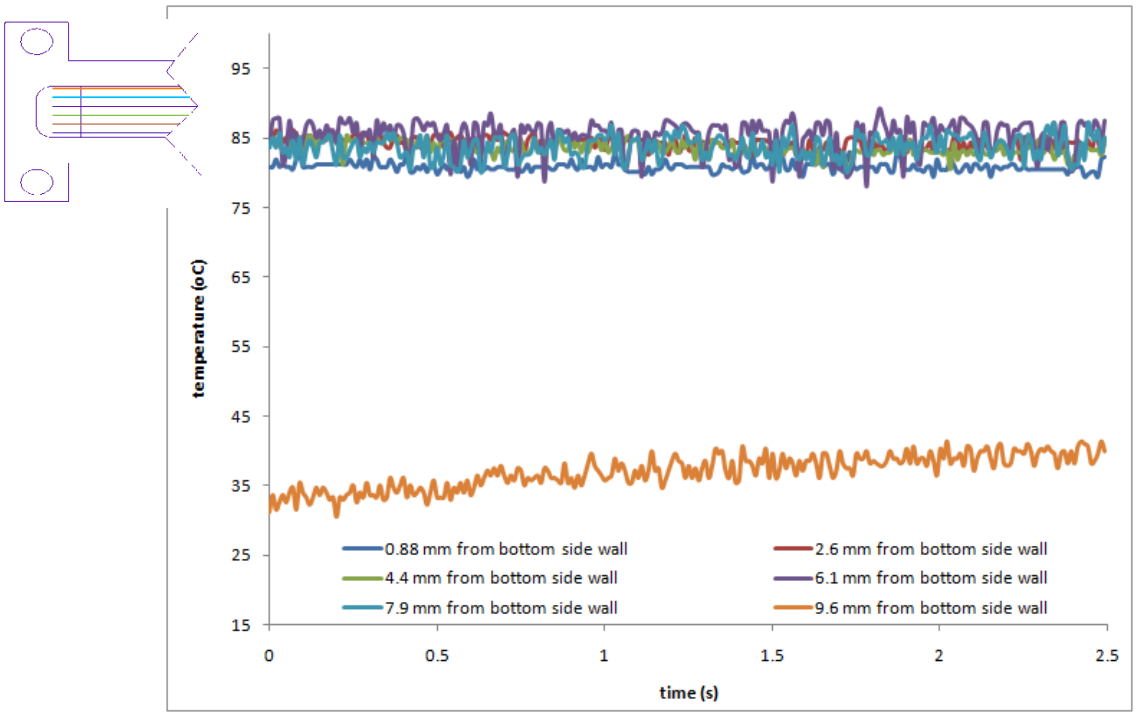

Figure 35: Lateral comparison at 12.75 mm (x=0.32) from inlet for q= 26 W/cm^2.

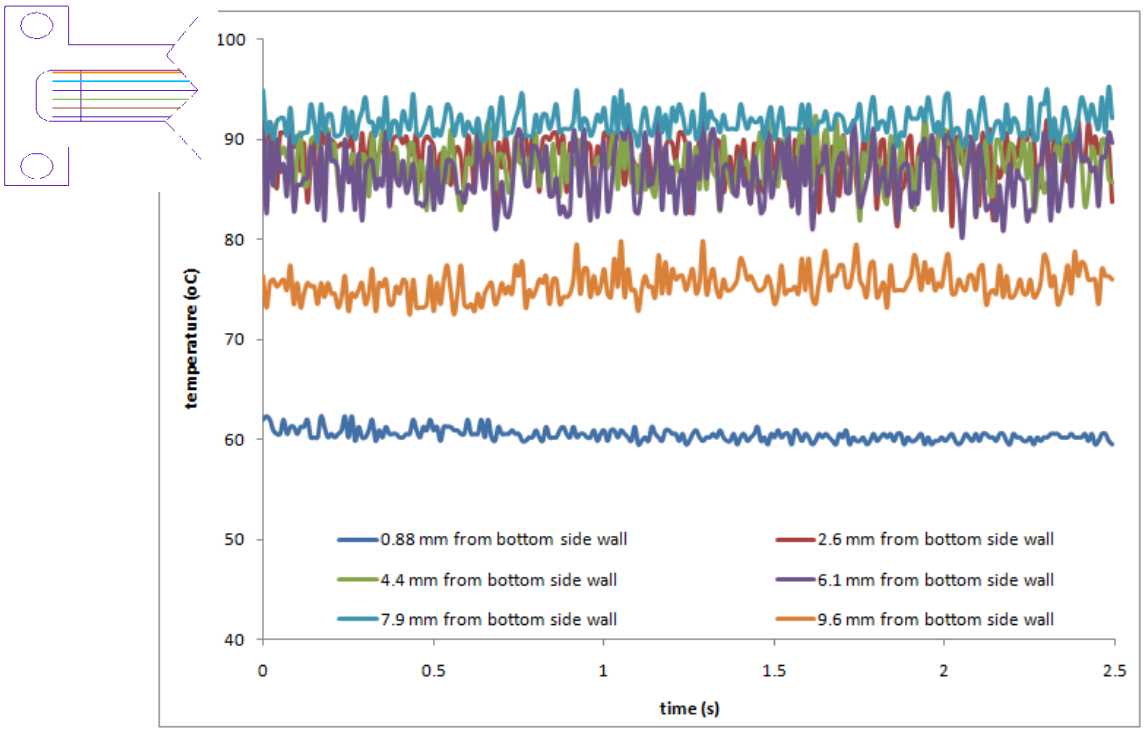

Figure 36: Lateral comparison at 25.5 mm (x=0.73) from inlet for q= 26 W/cm^2.

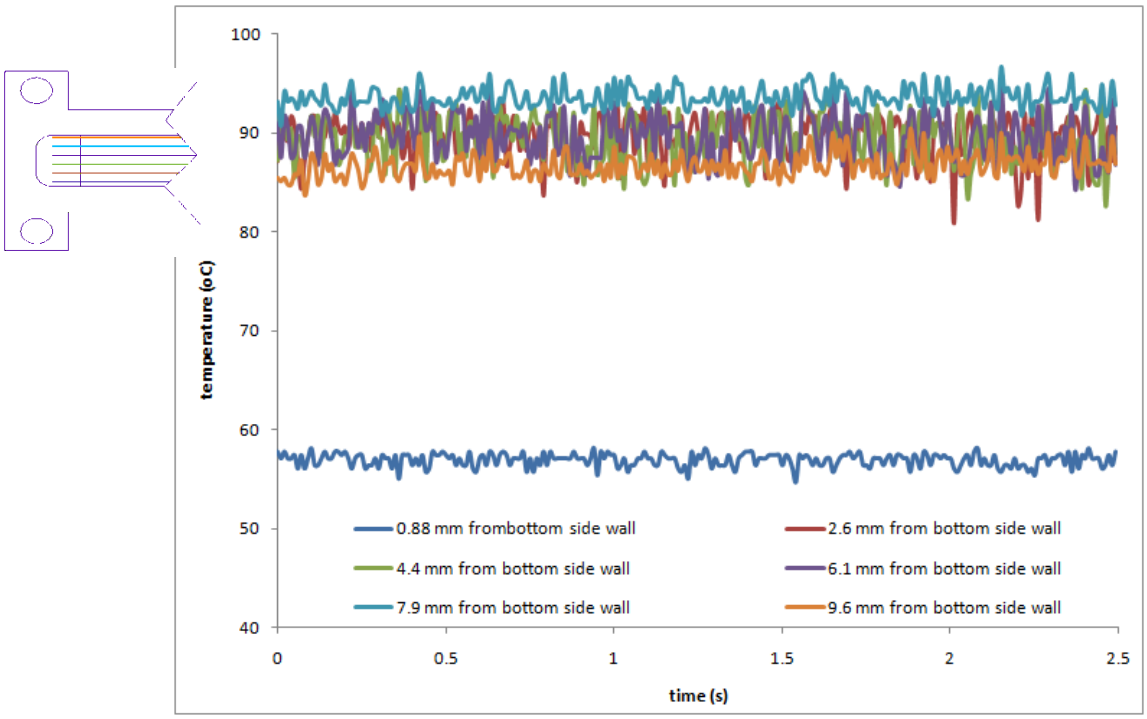

Figure 37: Lateral comparison at 35 mm (x=0.93) from inlet for q= 26 W/cm^2.

temperature magnitudes and temporal behavior, this is not always the case for channel edge locations. Thus, for the conditions of Figure 36 and Figure 37, the location just 0.88mm from the edge of the channel displays a nearly time invariant temperature, just several degrees above saturation and 30K below the center of the channel. At the 25.5mm axial location a point 0.4mm from the opposite edge of the microgap channel, displays a 15K lower temperature than the center with more modest amplitude fluctuations. This lateral temperature distribution would appear to reflect the potentially significant role played by the edges of the microgap channel in controlling and directing the axial flow of liquid and its availability for evaporative cooling of the entire channel.

Further exploration of the significance of liquid flow along the microgap edge, on the prevailing flow pattern and channel behavior, was conducted by varying the orientation, as in Figure 38. Such orientation changes could simulate the consequences of implementing microgap coolers in handheld devices or in vehicles operating on inclined surfaces and might exaggerate the edge effect.

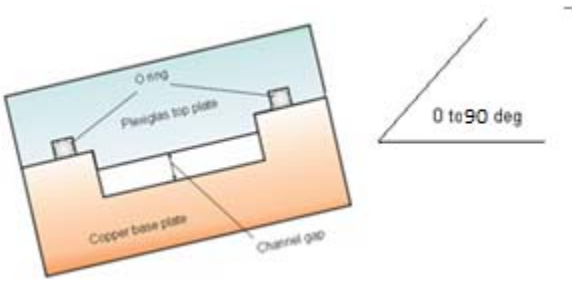

Figure 38: Rotation of Microgap Cooler

4.7 Temporal Temperature Variations – Frequency Domain

To further investigate the characteristics of these temperature fluctuations, the data obtained for the highest flux channel, displaying the largest amplitude fluctuations, was subjected to a Fourier spectral analysis using Matlab [32]. Figure 39-Figure 41 show the variation of energy density with frequency for three distinct locations (and three distinct qualities) in the 26W/cm^2 channel cooled by a mass flux of 195 kg/m^{2}s flow of FC-72. For the

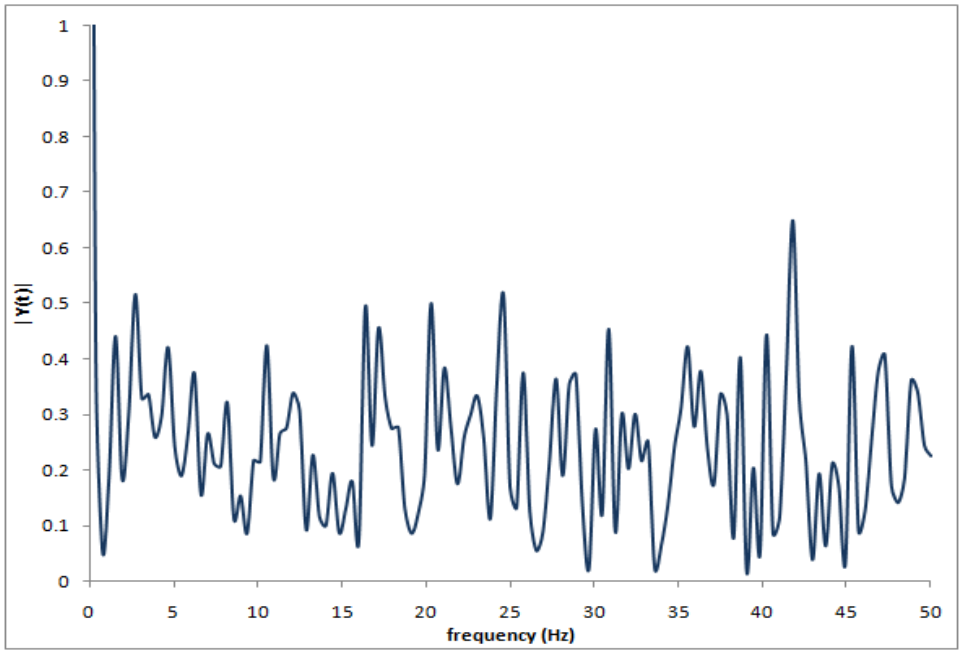

Figure 39: Temporal FFT at 20 mm (56% quality) location from inlet for a 210 micron channel with G=195 kg/m^2-s and q=26W/cm^2.

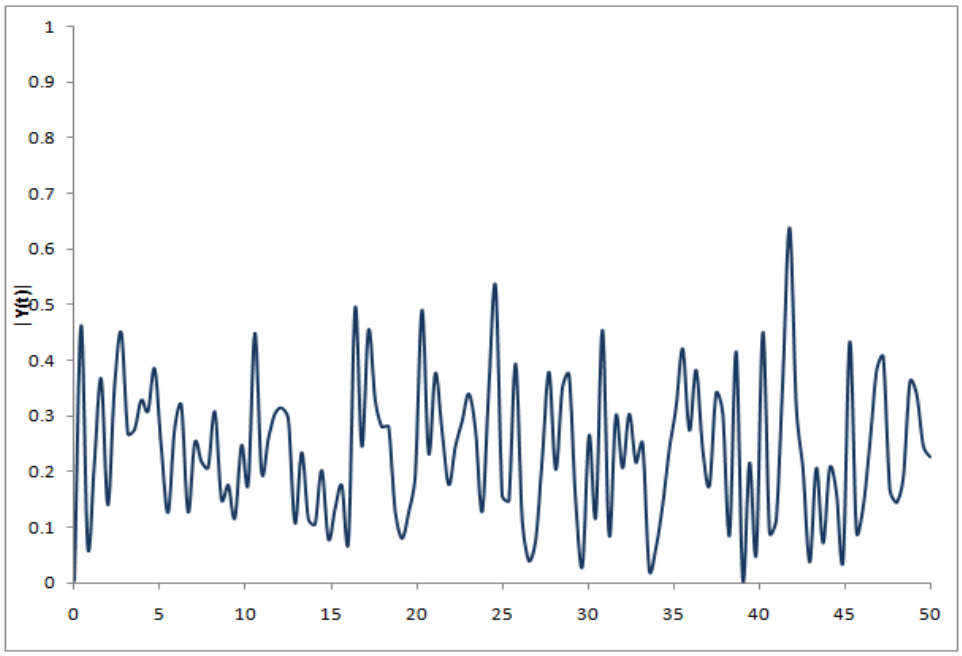

Figure 40: Temporal FFT at 25 mm (72% quality) location from inlet for a 210 micron channel with G=195kg/m^2-s and q=26W/cm^2.

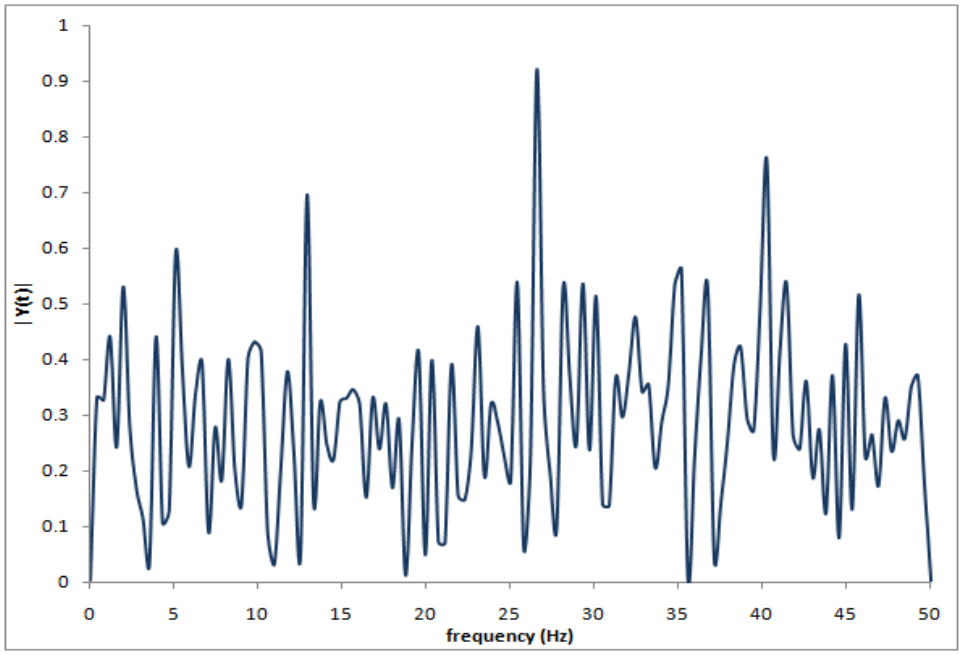

Figure 41: Temporal FFT at 31 mm (94% quality) location from inlet with dominant frequencies at 12.9 Hz, 26.6 Hz, and 39.8 Hz, for a 210 micron channel with G=195 kg/m^2-s and q=26W/cm^2.

conditions of Figure 39 and Figure 40, with a quality of 0.56 and 0.72, respectively, a large number of "dominant" frequencies appear, creating almost a "white noise" condition. However, at the highest quality of 0.94 the spectral analysis reveals a more distinct frequency distribution, with a clear dominant frequency of 26.6Hz and clearly discernible, though lower, peaks at 5Hz, 13Hz, and 39.8Hz. Interestingly, a peak, though not "dominant," frequency close to 40Hz can also be seen in the spectral distribution at the two lower quality maps, though - at these operating conditions - the 40Hz peaks are masked by the presence of a large number of peaks. The high qualities at which these temporal temperature fluctuations occur and the relatively high dominant frequencies appear to support the assertion that mechanisms other than periodic slug flow, and possibly related to thin film instabilities and intense, though non-uniform, local evaporation, are responsible for these fluctuations.

4.8 Spatial Temperature Variations – Frequency Domain

Spatial temperature fluctuations were analyzed to characterize channel behavior for these sets of parameters. As may be seen in Figure 42 and Table 3, spatial FFT for all four heat fluxes for this particular 210micron channel revealed dominant wavelengths close to the Kelvin-Helmholtz "most dangerous wavelength" [22], with the peak spectral power density occurring at 9.1mm for an imposed heat flux of 26 W/cm^2 and 8.7mm for 10.3W/cm^2. Disturbances with wavelengths near the most dangerous wavelength are expected to dominate in the beginning stages of instability within the channel. The most dangerous wavelength is liquid dependent and can be calculated using the below equation

$$\lambda_D = 2\pi \left\{ \frac{3\sigma}{(\rho_l - \rho_v)g} \right\}^{1/2} \qquad (16)$$

where σ is surface tension, ρ_l is vapor density, and ρ_v is liquid density [22]. For FC-72, this wavelength, λ_D, is found to equal 6.85 mm, remarkably close to the spectral power density peaks observed. It may, thus, be possible to speculate that the previously unobserved spatial temperature fluctuations are due, at least in part, to the onset of the Kelvin-Helmholtz or a related instability occurring in the channel.

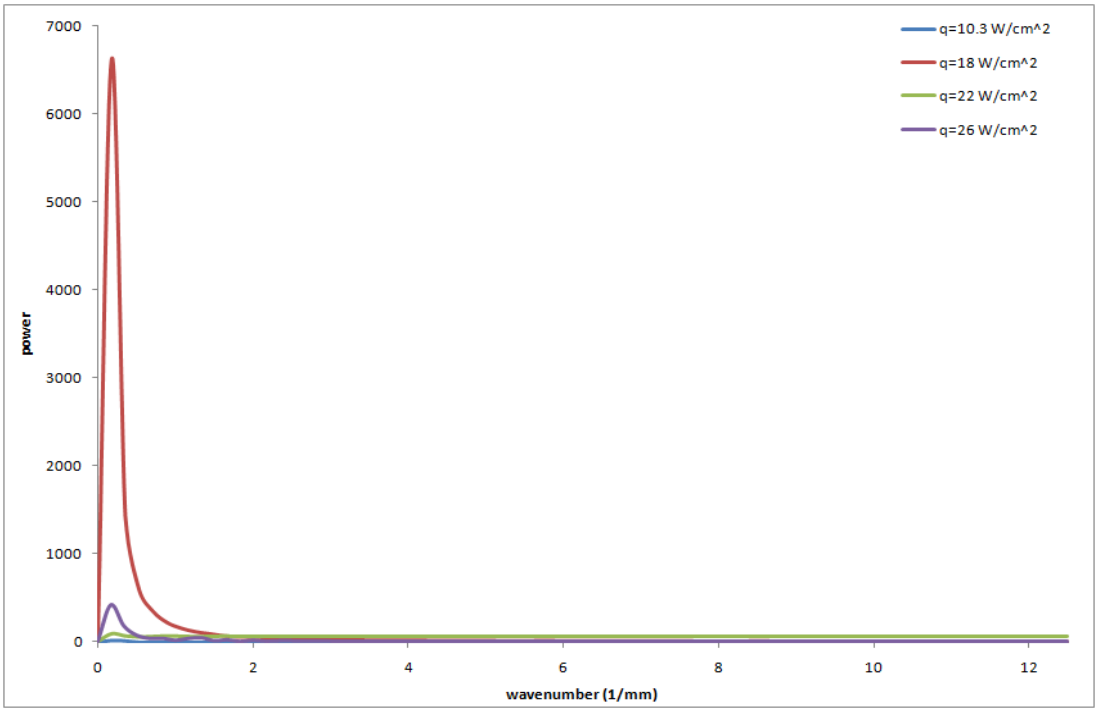

Figure 42: Spatial FFT for four heat fluxes and G=195 kg/m^2-s for 210 micron gap using FC-72 working fluid.

Table 3: Dominant wavelengths from Spatial FFT of IR Images in Microgap Channel using FC-72 - G=195.2 kg/m^2-s, Various q"

Heat Flux (W/cm^2)	Wavelength (mm)
10.3	8.7
18	8.8
22	8.8
26	9.1

CHAPTER 5

RESULTS AND ANALYSIS: MICROGAP CHANNEL WALL THERMOGRAPHY

This section outlines the results of the parametric study performed on microgap coolers of 200, 300, and 400 micron gap height with various channel widths, heat fluxes, mass fluxes, and angle orientation. Table 4 lists the various parameters varied for experimentation, as well as the range of new heat flux that impinges the channel. A range exist because of the variation of other parameters (i.e. width, mass flux, etc), thus for comparison the gross heat flux is listed since on average 93% conversion rate was found but the corrected ANSYS determined heat flux is used for all calculations.

Table 5 shows the various combinations used for experimentation to represent the parametric space and determine trends. The data selected to be presented represents the general trends seen in the results with any outlying data sets presented for completeness.

Table 4: Parameters Varied for Experimentation

Gap Height (µm)	Channel Width (mm)	Gross Heat Flux (W/cm^2)	Range of Net Heat Flux (W/cm^2)	Mass Flux (kg/m^2-s)	Orientation Angle (degs)
200	5	23	21-22	195	0
300	10	28	25-27	292	45
400	20	37	32-35	390	90
		40	36-38	490	
		45	40-43	585	
		70	63-67		

Table 5: Experimental Conditions

		Full				
		200		300	300 (HFE-7100)	400
q (W/cm^2)	G (kg/m^2-s)	Experimented	Angle	Experimented	Experimented	Experimented
23	195	X	X	X	-	-
23	292	X	-	X	-	-
28	195	X	X	X	X	X
28	292	X	X	X	X	X
28	390	X	-	X	X	X
37	390	X	-	-	-	-
40	390	X	-	X	X	X
45	390	X	-	-	-	-
52	780	X	-	-	-	-
70	488	X	X	X	-	-
70	585	X	-	X	-	-

		half			
		200	300	300 (HFE-7100)	400
q (W/cm^2)	G (kg/m^2-s)	Experimented	Experimented	Experimented	Experimented
23	195	X	X	X	X
23	292	X	X	X	X
28	390	X	X	X	X
40	390	X	X	X	X

		Double			
		200	300	300 (HFE-7100)	400
q (W/cm^2)	G (kg/m^2-s)	Experimented	Experimented	Experimented	Experimented
23	195	X	X	X	X
23	292	X	X	X	X

5.1 Axial Temperature Profiles

.The axial temperature profiles show the temporal and spatial variations that occur throughout the length of the channel. The figures in this section show the temperature profile along the center line of the channel plotted against quality (with channel length as reference), with the black line representing the average of 100 frames (for a total elapsed time of 1.7 s) which are shown in various colors. The channel data is shown to quality of 1 to easily compare various conditions and channels, since this research is focused on the behavior in the Annular flow regime. The spread of the temperature variation is analyzed to determine through standard deviation since visually some cases have shown large variation for a small portion of the data shown. The data in this section demonstrates, through the complexity of the previously unobserved temperature fluctuations, occurring mainly in the high quality regions of the channel but sometimes initiating before the onset of Annular flow and often occurring at low and modest quality regions of the microgap channel.

5.1.1 Microgap Channel Height at 200 microns

Microgap Cooler: 200 microns, FC-72, and width=5mm

Figure 43- Figure 46 show the channel data from the 200 micron gap, 5mm width, and 35 mm channel length with FC-72 as the working fluid under various experimental conditions. Figure 43 shows the thermographoically derived axial temperature profiles for q=23 W/cm^2 and G=195 kg/m^2-s, displaying the locii of 100 runs under identical operating conditions and consists of data for low heat flux and mass flux experimental conditions. The onset of fluctuations, at approximately 15% quality occurs earlier than the transition into the annular flow regime, which is predicted to occur at a quality of 36%, and the magnitude of these fluctuations is significant (14 C) The peak to peak temperature variation is large with a standard deviation for this set is 4 C, revealing a smaller core temperature value for the data set. Figure 44 shows the axial temperature profile for q=23 W/cm^2 and G=292 kg/m^2-s, which transitions to the annular regime at 24% quality. Interestingly the onset of strong temperature variations along the center line again occurs before the annular transition band, as appears to occur for almost all channel profiles and experimental conditions. The amplitude variations, at 9 C with standard deviation of

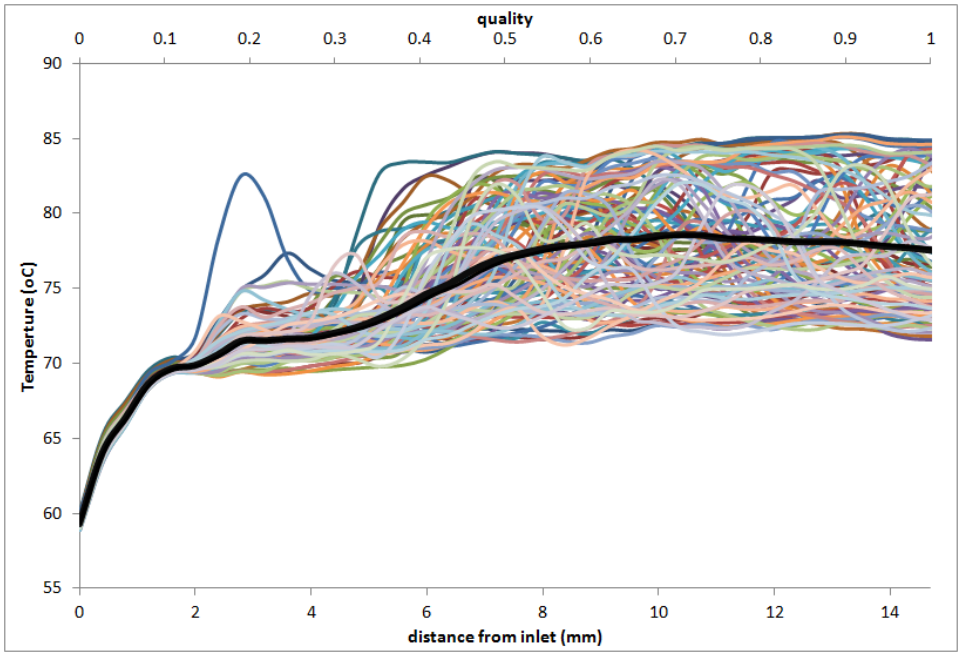

Figure 43: Axial temperature profile for 200 micron channel, 5mm width, FC-72, q=23 W/cm^2 and G=195 kg/m^2-s.

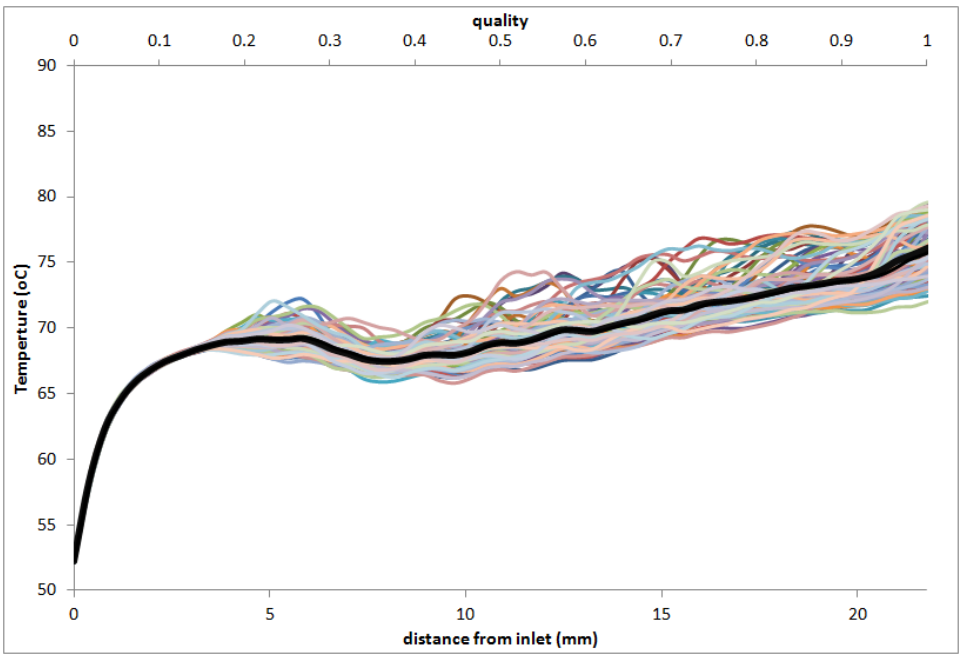

Figure 44: Axial temperature profile for 200 micron channel, 5mm width, FC-72, q=23 W/cm^2 and G=292 kg/m^2-s.

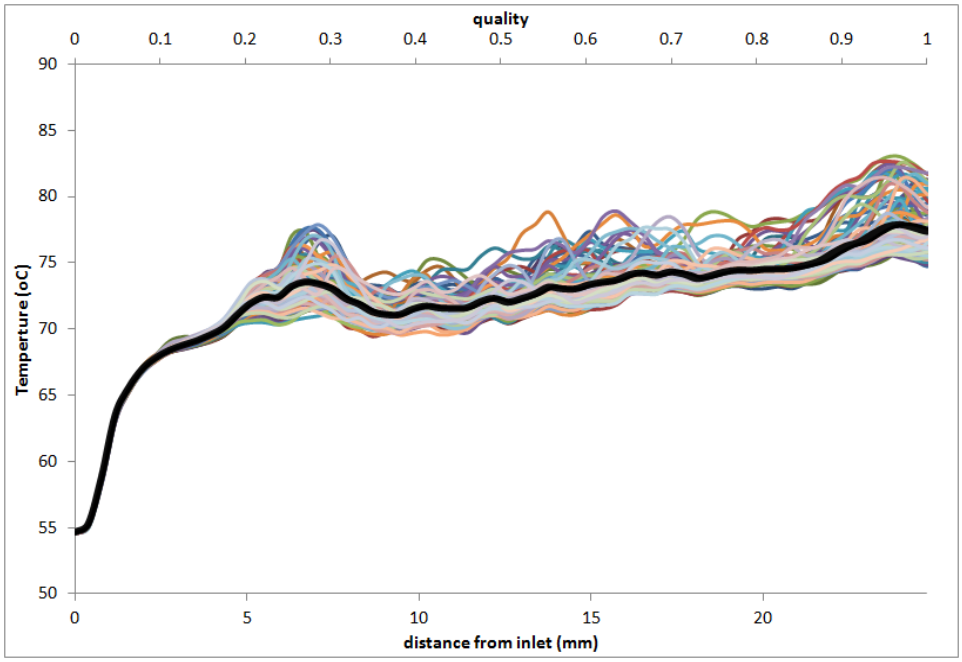

Figure 45: Axial temperature profile for 200 micron channel, 5mm width, FC-72, q=28 W/cm^2 and G=390 kg/m^2-s.

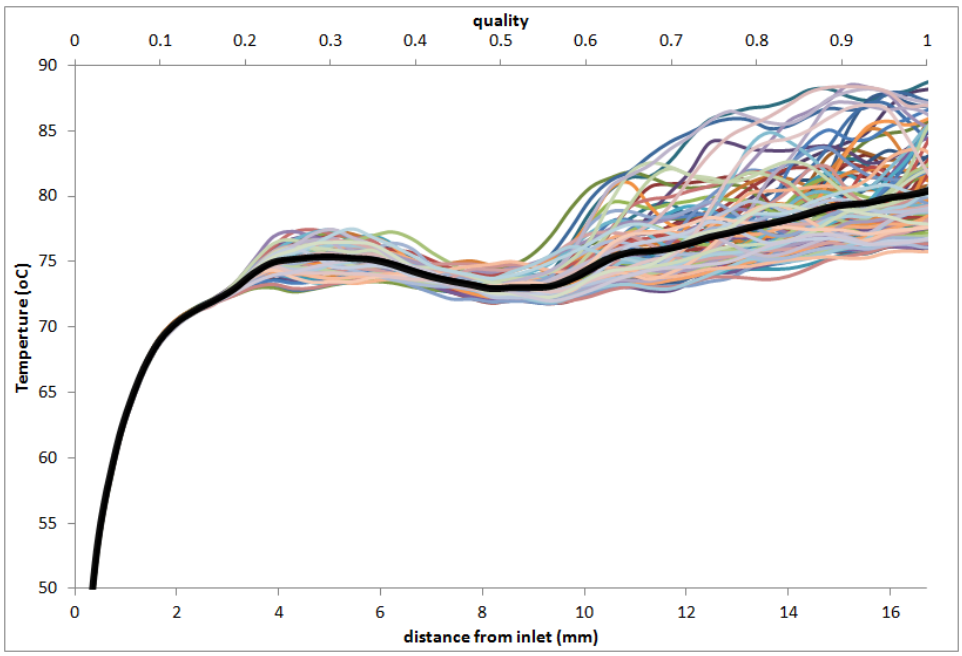

Figure 46: Axial temperature profile for 200 micron channel, 5mm width, FC-72, q=40 W/cm^2 and G=390 kg/m^2-s.

3 C, are also more modest than for the other experimental conditions. Comparing Figure 43 and Figure 44 the relationship can be observed between channel behavior and mass flux since it is only the mass flux that varies between these two cases. The fluctuations, as expected, are larger for the lower mass flux case due, perhaps, to the weaker shear forces introduced by the lower velocity flows.

Figure 45 is the axial temperature profile for q=28 W/cm^2 and G=390 kg/m^2-s transitioning to significant temperature fluctuations at 18% quality. The onset of these fluctuations again occurs before the predicted annular transition band and displays modest temperature variations of 8 C with a standard deviation of 2 C. Intuitively, due to the higher wall heat flux, the channel temperature is higher than seen in Figure 44; however the amplitude of temperature variation is again lower than for the baseline mass flux of 195 kg/m^2-s but essentially unchanged from the lower mass flux of 292 kg/m^{2}s. Figure 46 shows the axial temperature profile with a significantly increased heat flux while fixing the mass flux from the previous case. For these experimental conditions the magnitude of the temperature fluctuations is 14 C with standard deviation of 4 C, and the transition to the annular flow regime occurs at 18% quality. At fixed qualities, for example 50% and 95%, respectively, the data shown in Figure 45

and Figure 46 display distinctly different fluctuation amplitudes, further supporting the previously discussed dependence of wall temperature fluctuations on more than just quality.

Microgap Cooler: 200 microns, FC-72, and width=10mm

The results from the 200 micron gap, 10mm width, and 35mm channel length using FC-72 is shown in this section. Figure 47 is the graphed results for q=23 W/cm^2 and G=195 kg/m^2-s (being the gross heat flux), which begins to experience temperature fluctuations at approximately 36% quality. The temperature fluctuation magnitude is 12 C with standard deviation of 3 C and is slightly lower than the variation seen in channels of similar experimental conditions but with 5 mm channel width. The major distinction between various channel widths when operating under fixed experimental conditions is the delayed onset of the temperature fluctuations. Figure 48 further confirms the delayed onset of temperature fluctuations in a wider channel by showing the data for =28 W/cm^2 and G=195 kg/m^2-s with the transition to annular at 36% quality, the magnitude of fluctuations 9 C, and with standard deviation of 3 C. . In addition, a coupled relationship between width and mass flux is seen in Figure 49, in which interestingly, the

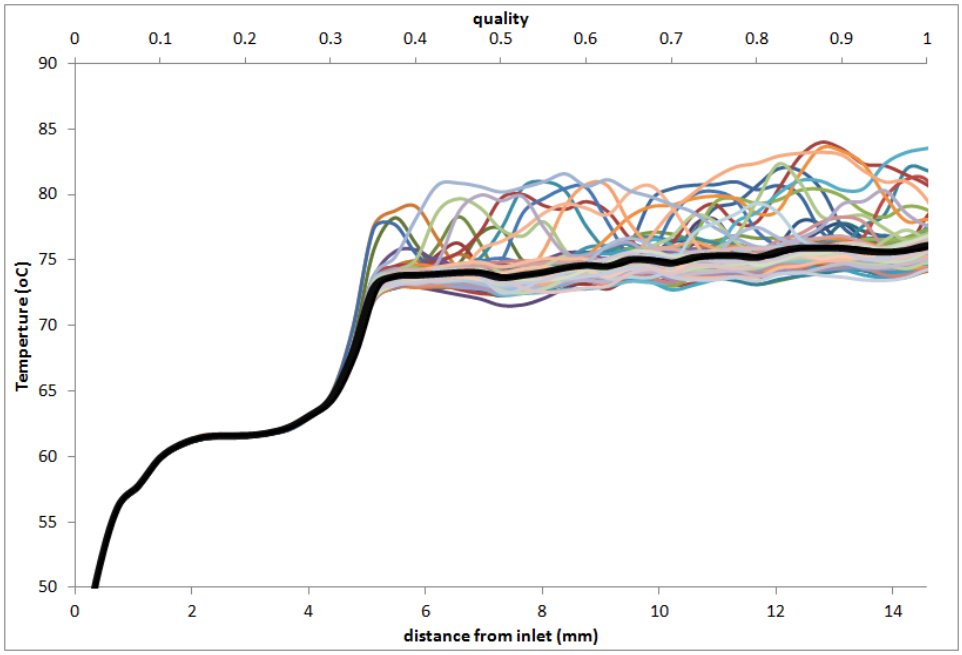

Figure 47: Axial temperature profile for 200 micron channel, 10mm width, FC-72, q==23 W/cm^2 and G=195 kg/m^2-s.

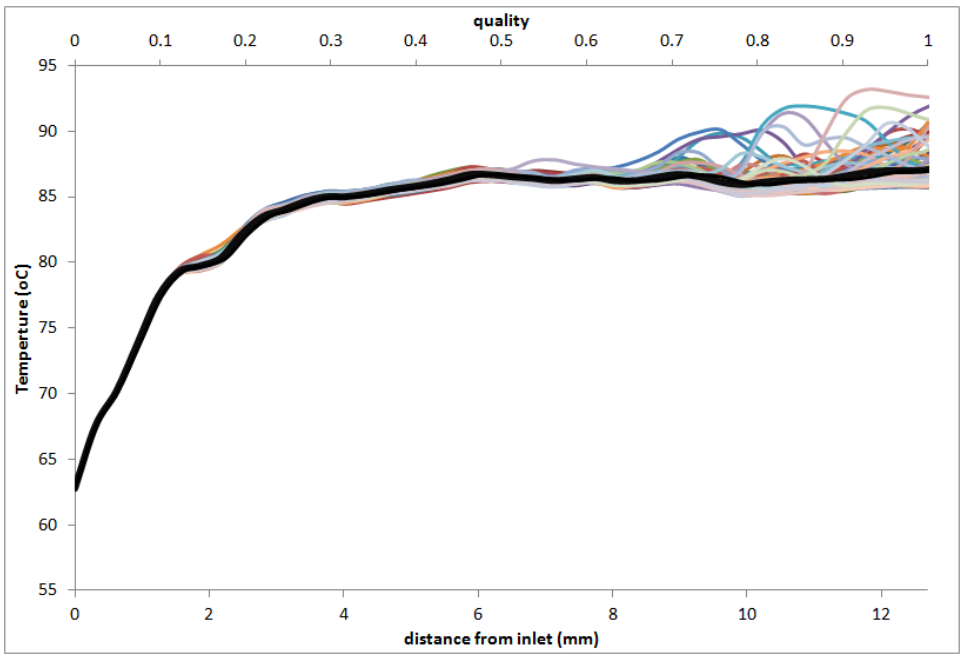

Figure 48: Axial temperature profile for 200 micron channel, 10mm width, FC-72, q=28 W/cm^2 and G=195 kg/m^2-s.

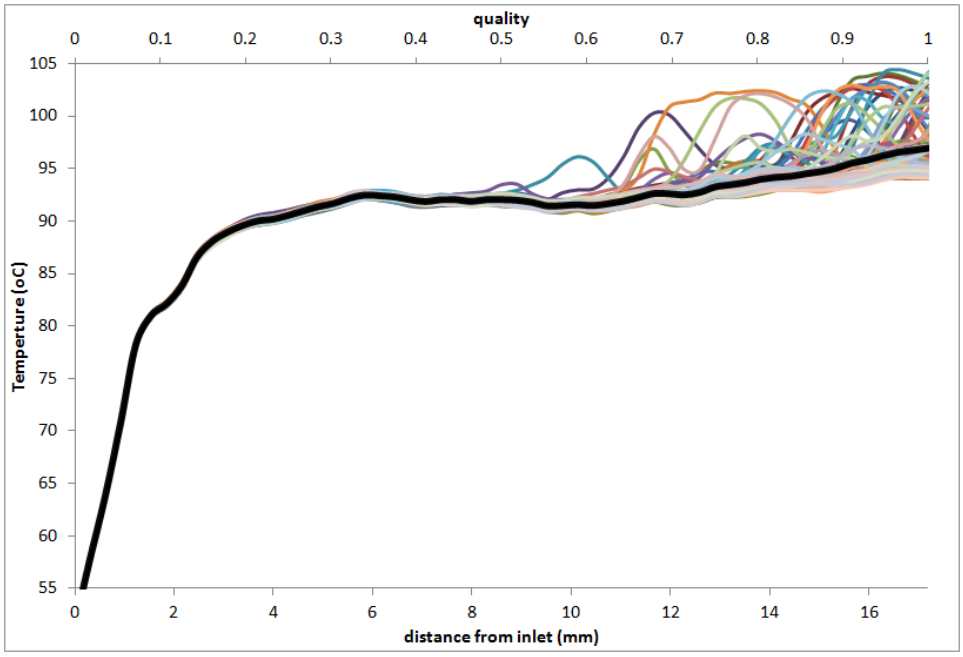

Figure 49: Axial temperature profile for 200 micron channel, 10mm width, FC-72, q"=40 W/cm^2 and G=390 kg/m^2-s.

temperature variation magnitude is also 11 C with standard deviation of 4 C but the onset of the temperature variations for q=40 W/cm^2 and G=390 kg/m^2-s (being the gross heat flux), occurs at approximately 50%, substantially past the annular transition near 18% quality.

Comparison of the data for the narrow, 5mm channel displayed in Figure 444 and for the wider 10mm channel in Figure 47 – both for G=195 kg/m^2-s and q"=23 W/cm^2 - clearly shows the suppression of local dryout and recovery for wider channels due to delayed onset of temperature fluctuations. Similar trends, relative to the ability of wider channels to suppress temperature fluctuations and dryout, are seen in comparing the graphs Figure 46 and Figure 49.

Microgap Cooler: 200 microns, FC-72, and width=20mm

Figure 50 and Figure 51 present the data for 200 micron gap, 20mm width, and 35 mm channel length using FC-72 for various experimental conditions. Figure 50 is the graphed results q=23 W/cm^2 and G=195 kg/m^2-s (being the gross heat flux), which transitions at 36% quality. The magnitude of the temperature fluctuations is 11 C with standard deviation of 3 C, and similarly to the observed behavior of the 10mm channel.

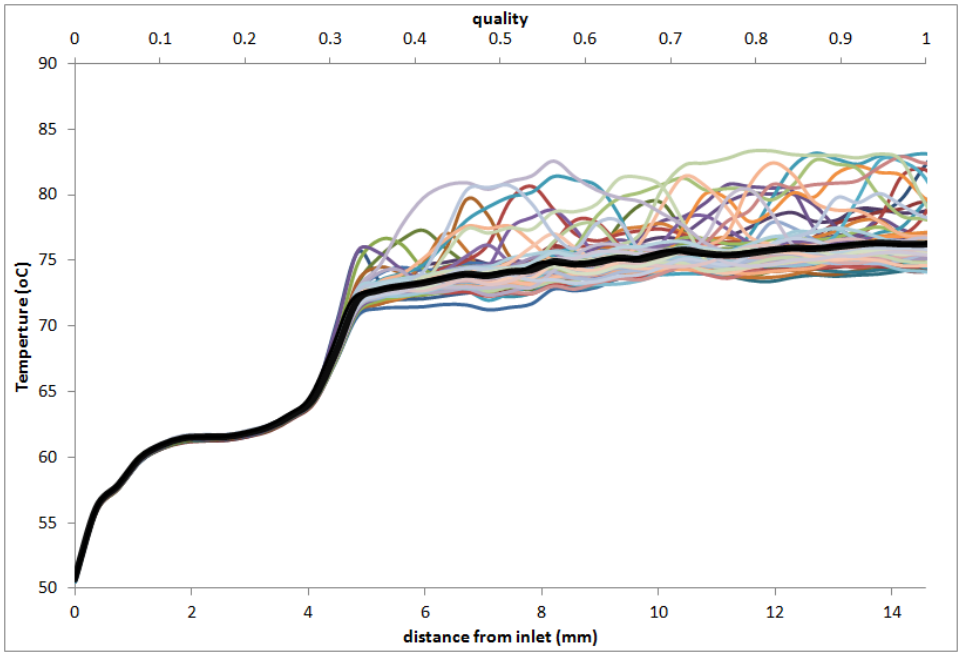

Figure 50: Axial temperature profile for 200 micron channel, 20mm width, FC-72, q=23 W/cm^2 and G=195 kg/m^2-s.

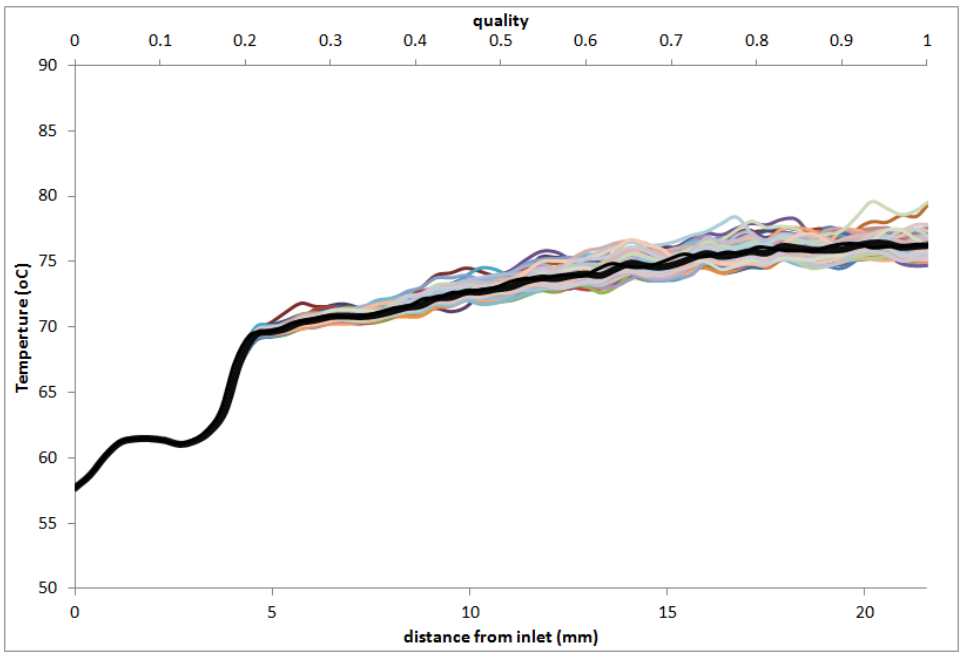

Figure 51: Axial temperature profile for 200 micron channel, 20mm width, FC-72, q=23 W/cm^2 and G=292 kg/m^2-s.

Thus, the additional suppression between 10mm channel and 20mm channel is minimal. Figure 51 shows the axial profile for q=23 W/cm^2 and G=292 kg/m^2-s with transition at 24% quality. The onset of temperature fluctuations is strongly delayed and suppressed when compared to the 5mm channel width, with temperature variations limited to 4 C with standard deviation of 2 C while in the 5mm width data shown in Figure 44 fluctuations of 9 C were observed.

The behavior outlined in this section suggests that increasing the microgap channel width from 5mm to 10mm changes the behavior of the channel, first delaying the onset of fluctuations and then dampening the fluctuations. For the 210 micron microgap channel, further increase of the channel width to 20mm results in only minimal changes in the onset and amplitude of the temperature fluctuations that appear in the channel.

5.1.2 Microgap Channel Height at 300 microns

Microgap Cooler: 300 microns, FC-72, and width=5mm

Heat transfer data for 300 microns height, 5mm width, and 35mm length microgap channel using FC-72 as the working fluid is presented in this section. At identical mass flux (G)

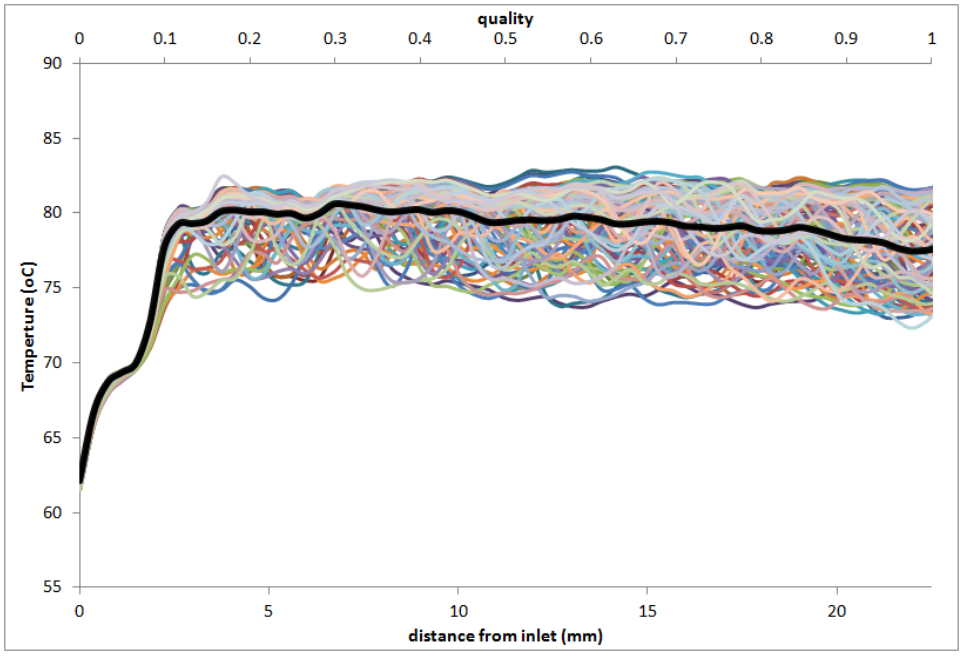

Figure 52: Axial temperature profile for 300 micron channel, 5mm width, FC-72, q=23 W/cm^2 and G=195 kg/m^2-s.

values, the qualities for this section will be lower than those for the 200 micron gap, due to the higher volumetric flow rate in the channel. Figure 52 shows the axial temperature profile for q=23 W/cm^2 and G=195 kg/m^2-s, which transitions at 36% quality. This shows similar behavior to 200 micron channel gap height for fixed experimental conditions, with somewhat more restrained temperature fluctuations of 9 C with standard deviation of 2 C. The onset of these fluctuations occurs early in the channel, following previously discussed trends. Figure 53 shows the graphed data for q=23 W/cm^2 and G=292 kg/m^2-s (being the gross heat flux), which transitions at 24% quality with temperature fluctuations of 12 C with standard deviation of 2 C. Comparison of Figure 52 and Figure 53 reveals the first instance in which the temperature fluctuation amplitudes were higher with increased mass flux at a fixed heat flux. In addition, these fluctuations are distinctly different from those for the comparable conditions in a 200 micron channel. These results point to the role of microgap height in wall temperature fluctuations, in addition to the effect of both heat flux (i.e. evaporation rate) and mass flux (i.e.

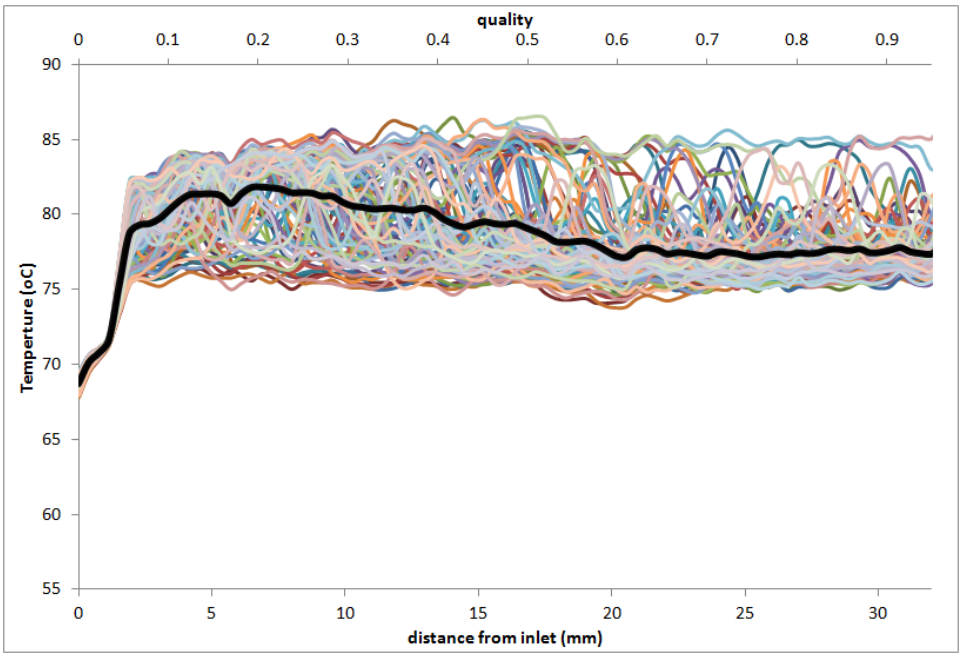

Figure 53: Axial temperature profile for 300 micron channel, 5mm width, FC-72, q=23 W/cm^2 and G=292 kg/m^2-s.

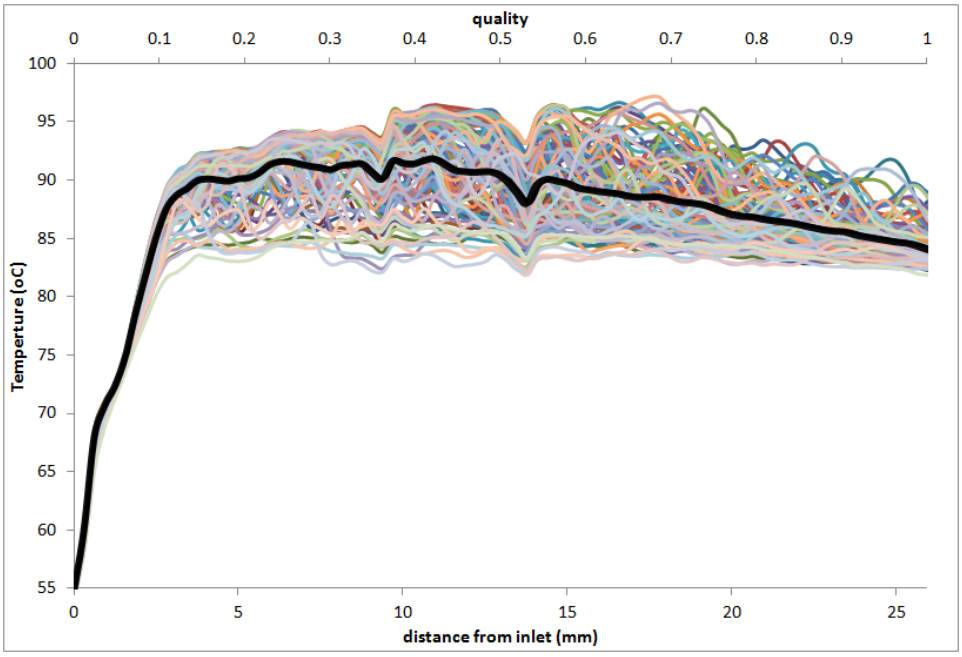

Figure 54: Axial temperature profile for 300 micron channel, 5mm width, FC-72, q=40 W/cm^2 and G=390 kg/m^2-s.

flow regime). For the same experimental conditions, the inherently thicker film for larger gap heights can alter the thermofluid behavior occurring in the channel. Figure 54 shows the axial temperature profile for q=40 W/cm^2 and G=390 kg/m^2-s, which transition at 18% quality. The trend of early onset of temperature fluctuations in the narrower channel is continued in this data set. The magnitude of the fluctuations is significant, 19 C with standard deviation of 3 C, which is comparable to the wall temperature variations observed for the 200 micron gap height under comparable experimental conditions. While the results suggest a minimal role for the gap height in setting the microgap channel behavior, it is likely that geometric effects may have been overcome by the high wall heat flux.

Microgap Cooler: 300 microns, FC-72, and width=10mm

The graphs shown in this section are for 300 micron gap, 10mm width, and 35 mm channel utilizing FC-72 as the working fluid. Figure 55-Figure 58 show the axial temperature profile for several experimental conditions. Some graphs were omitted since no additional insight was gained from their analysis. Figure 55 shows the graphed results for q=23 W/cm^2 and

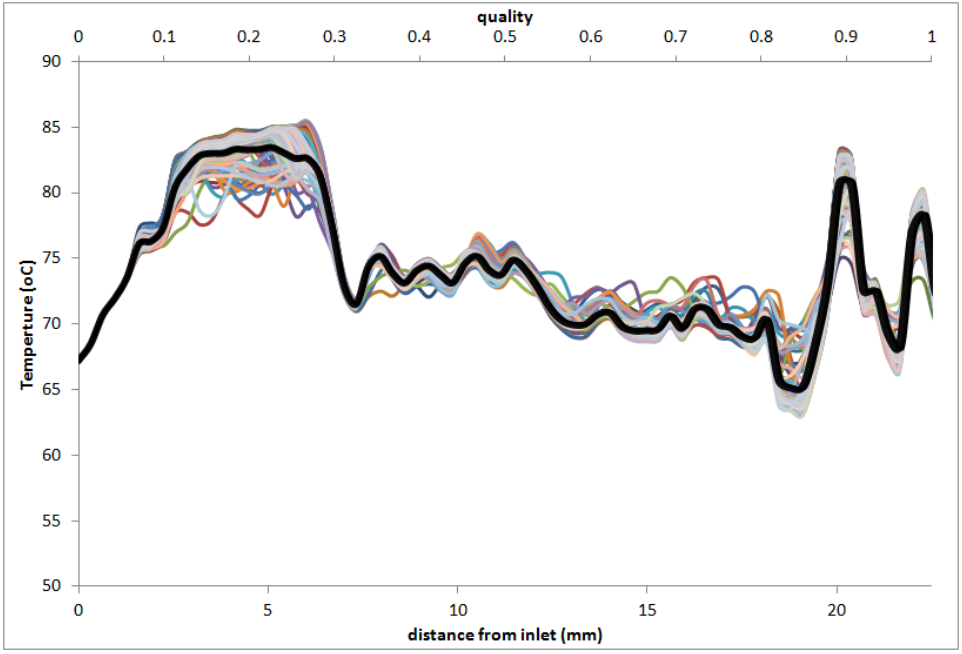

Figure 55: Axial temperature profile for 300 micron channel, 10mm width, FC-72, q=23 W/cm^2 and G=195 kg/m^2-s.

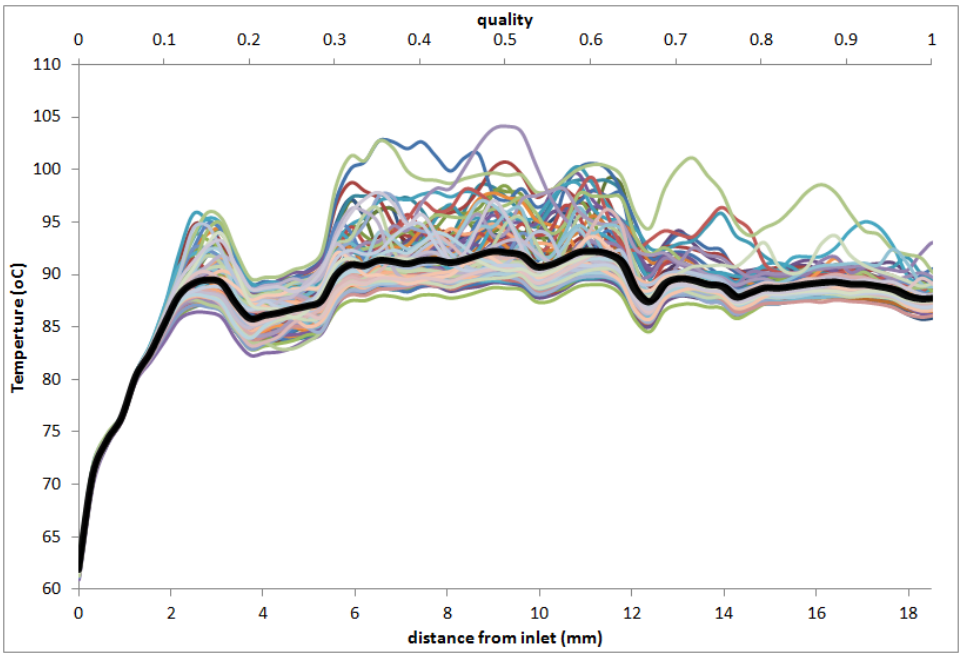

Figure 56: Axial temperature profile for 300 micron channel, 10mm width, FC-72, q=28 W/cm^2 and G=195 kg/m^2-s.

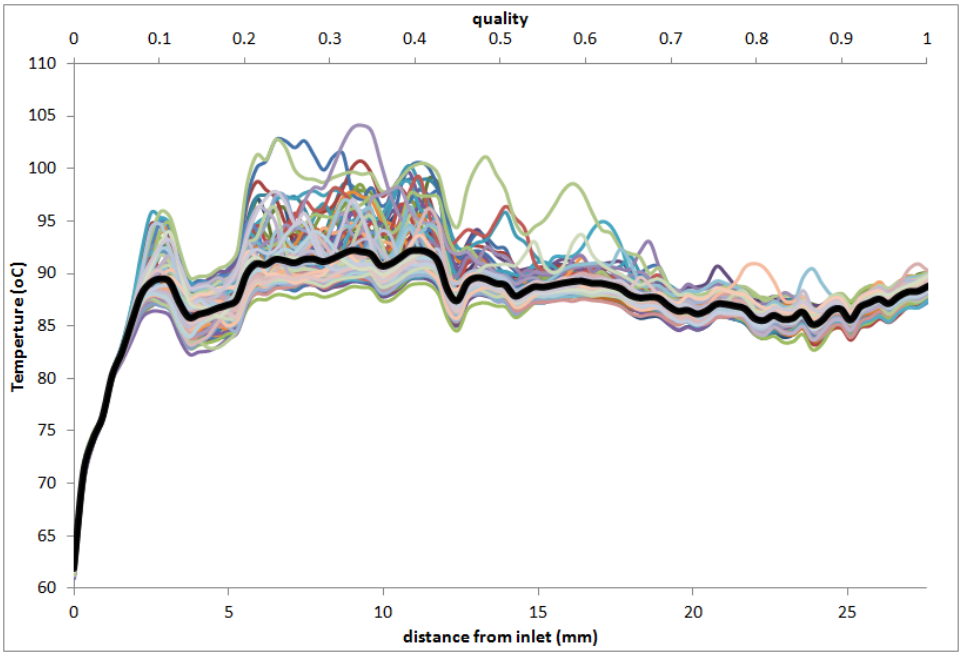

Figure 57: Axial temperature profile for 300 micron channel, 10mm width, FC-72, q=28 W/cm^2 and G=292 kg/m^2-s.

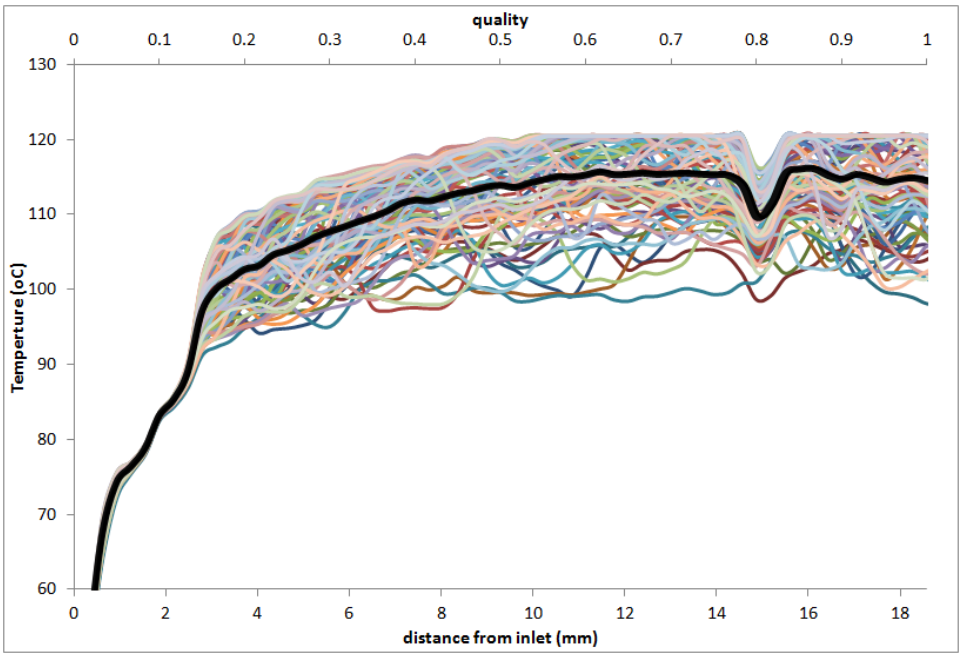

Figure 58: Axial temperature profile for 300 micron channel, 10mm width, FC-72, q=70 W/cm^2 and G=490 kg/m^2-s.

G=195 kg/m^2-s (being the gross heat flux), which transitions to annular at 36% quality and has temperature variations of 9 C with standard deviation of 2 C. This case shows how although the peak to peak over the full range of qualities can results in a instantaneously high temperature variation, overall the variation is minimal as represented through the standard deviation. This case involves low heat flux and mass flux, and demonstrates minimal local temperature fluctuations following previously discussed behavior for similar conditions in the 200 micron gap height channel. Interestingly, these modest local temperature fluctuations appear to initiate at relatively low quality and envelope significant axial temperature variations, thus, in this larger microgap channel the fluctuating wall temperature behavior is no longer delayed. Figure 56 shows the axial temperature profile for q=28 W/cm^2 and G=195 kg/m^2-s, which transitions to annular 36% quality and has temperature variations of 15 C with standard deviation of 4 C. This 10mm wide, 300micron high microgap channel does not demonstrate any suppression of amplitude nor onset of wall temperature fluctuations.

Figure 57 shows the data for q=28 W/cm^2 and G=292 kg/m^2-s again displaying the early onset of temperature fluctuations, with both local variations and significant axial variations in wall temperature. Figure 58 shows the axial temperature profile for q=70 W/cm^2 and G=490

kg/m^2-s, which transitions at 14% quality and temperature fluctuations of 25 C with standard deviation of 6 C. This case shows the highest amplitude wall temperature fluctuations lending further support to the role of the imposed heat flux in the generation of the cyclic local wall dryout and recovery pattern. Comparison of the temperature fluctuation magnitudes of Figure 55-Figure 58 confirms the trend that as the heat flux is increased an increase in temperature fluctuations increases. Thus, again a relationship between local dryout and recovery and heat flux (i.e. evaporation rate) exists.

The 300 micron gap cases examined appear to supports the importance of gap height, in addition to gap width, mass flux, and heat flux to the instabilities that cause the local dryout and recovery on the microgap channel wall. At a comparable width and operating conditions, the thicker microgap channel (i.e. 300 microns vs 200 microns) typically displays stronger and earlier temperature fluctuations than a thinner microgap channel.

Microgap Cooler: 300 microns, FC-72, and width=20mm

This section shows the data for 300 micron, 20mm width, and 35mm channel length, using FC-72 as the working fluid. Figure 59 is the graphed results for q=23 W/cm^2 and G=292

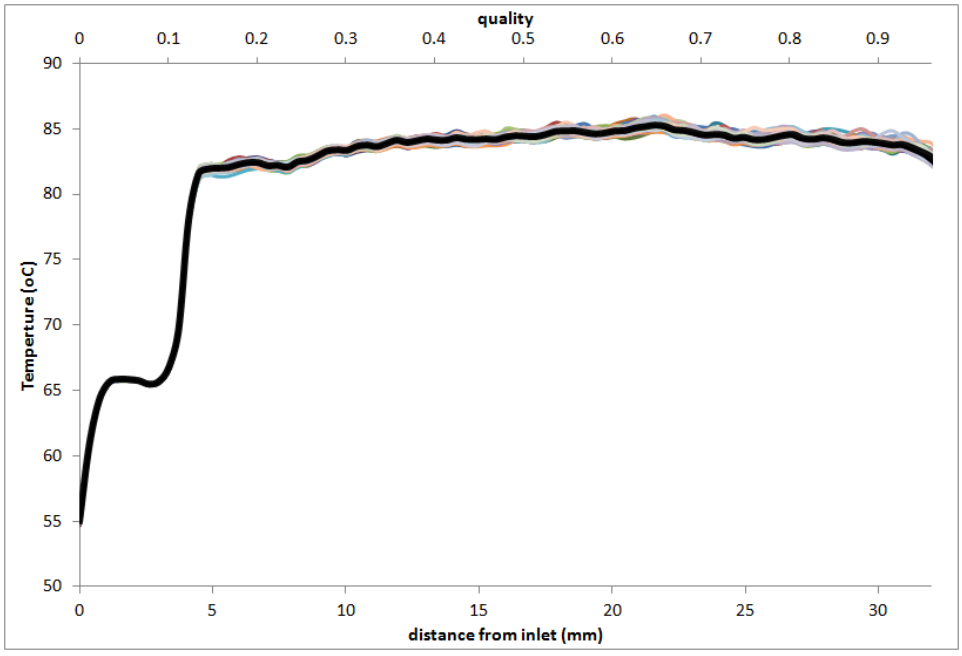

Figure 59: Axial temperature profile for 300 micron channel, 20mm width, FC-72, q=23 W/cm^2 and G=292 kg/m^2-s.

kg/m^2-s, which transitions to annular at 24% quality and temperature variations of 2 C with standard deviation of 0.4 C. It is apparent that there are no significant temperature fluctuations for these experimental conditions, which shows the effect of width on the local dryout and recovery that occurs in the channel. Comparing Figure 57 and Figure 59 shows the drastic change in channel behavior with this further increase in channel width, and emphasizes the relationship between the temperature fluctuations and channel width.

It is significant that the observed suppression of the onset and amplitude of wall temperature fluctuations for the thicker microgap of 300 microns occurred at the widest channel tested, i.e. 20mm, rather than at the 10mm width as observed for the thinner, 200 micron gap.

Microgap Cooler: 300 microns, HFE-7100, and width=10mm

This section outlines the data collected using HFE-7100 as the working fluid for a 300 micron gap, 10mm width, and 35 mm length channel and establishes the fact that the observed

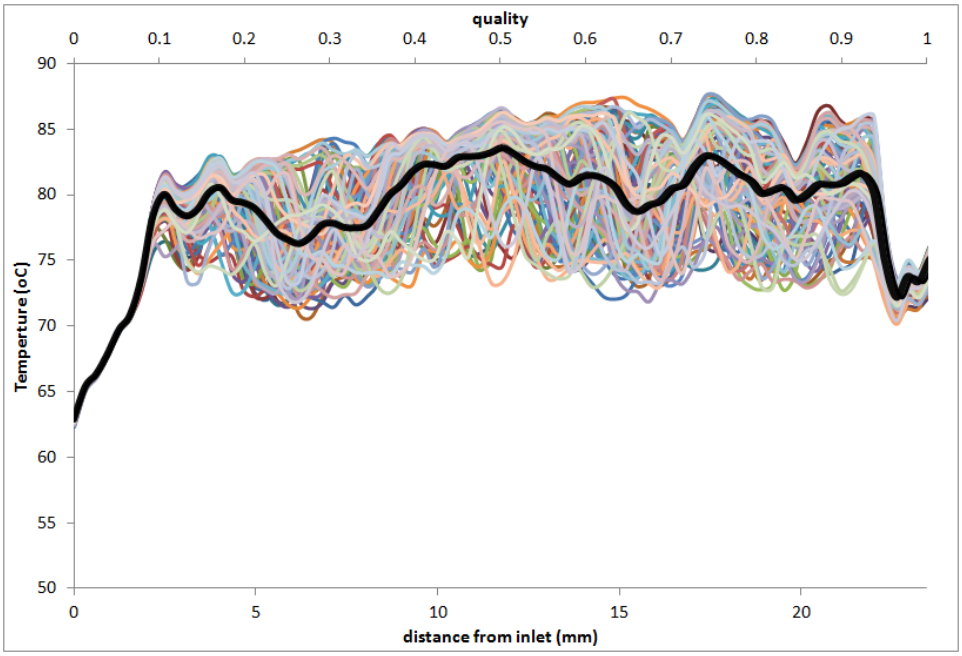

Figure 60: Axial temperature profile for 300 micron channel, 10mm width, HFE-7100, q=28 W/cm^2 and G=195 kg/m^2-s.

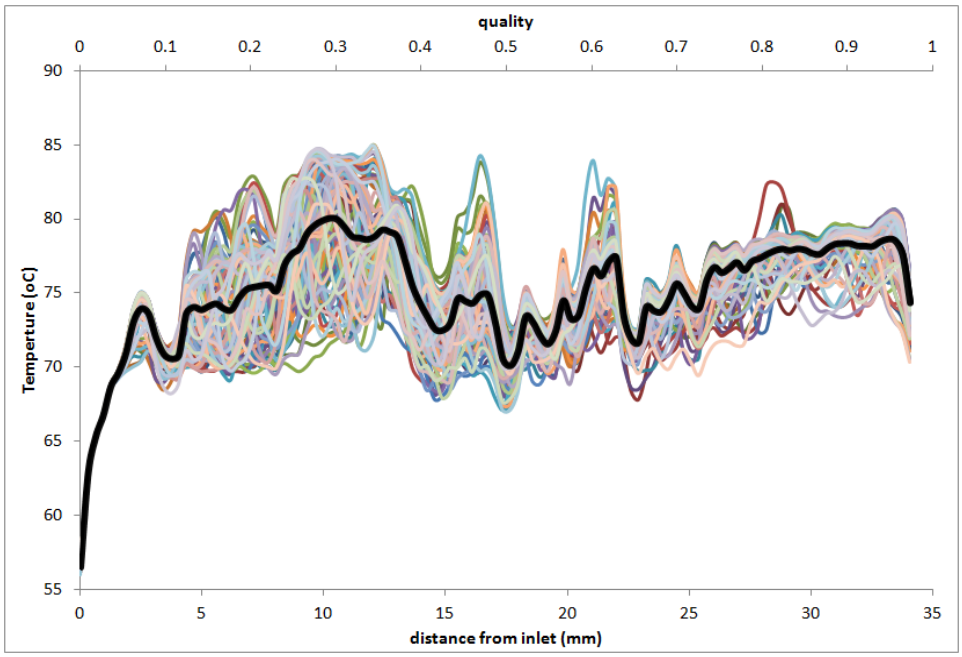

Figure 61: Axial temperature profile for 300 micron channel, 10mm width, HFE-7100, q=28 W/cm^2 and G=292 kg/m^2-s.

wall temperature fluctuations and their parametric sensitivities are not limited to a single working fluid. Figure 60 shows the axial temperature profile for q=28 W/cm^2 and G=195 kg/m^2-s (being the gross heat flux), which transitions at 36% quality and temperature variations of 15 C with standard deviation of 4 C. Since the latent heat for HFE-7100 is nearly twice that of FC-72, it is expected that qualities are significantly lower at comparable axial position in the channel, though – for the operating conditions reported - qualities of unity were attained at the end of the channel. Despite the 61C saturation temperature at atmospheric pressure (vs 56C for FC-72), the superior thermal transport properties of HFE7100 yielded somewhat lower wall temperatures along the microgap channel than observed for FC-72. Nevertheless, as seen in Figure 60 the wall temperature fluctuations were similar in magnitude, though somewhat larger and more chaotic, to those observed for FC-72. Figure 61 shows results for q=28 W/cm^2 and G=292 kg/m^2-s with transition to the annular flow regime at 24% quality and has temperature variations of 14 C with standard deviation of 4 C. As seen with FC-72 cases for the 300 micron high and 10mm wide microgap channel, there is no delay in the onset of local dryout and recovery, with the onset of temperature fluctuations occurring earlier in the HFE7100 channel than any other cases.

Comparison of Figure 60and Figure 61 shows the difference in behavior induced by increasing the mass flux, while keeping the heat flux constant. Examining the wall temperature fluctuations at fixed locations, the distinct difference between these two cases confirms that it is not local imperfections of the channel wall causing the observed phenomena. The benefit of transitioning into annular flow is the heat transfer that results from thin-film evaporation and leads to the second peak in the M-shaped curve. Due to the higher latent heat of HFE-7100, operation in a microgap cooler may be constrained due to lower qualities and increase local dryout and recovery. This will be further explored in the two-phase heat transfer section.

5.1.3 Microgap Channel Height at 400 microns

Microgap Cooler: 400 microns, FC-72, and width=5mm

This section outlines the data collected for 400 micron gap, 5mm width, and 35mm length channel with FC-72 as the working fluid. Figure 62 is the axial temperature profile for q=40 W/cm^2 and G=390 kg/m^2-s, which transitions at 14% quality and has temperature variations of 10 C with standard deviation of 3 C. This shows large temperature fluctuations as

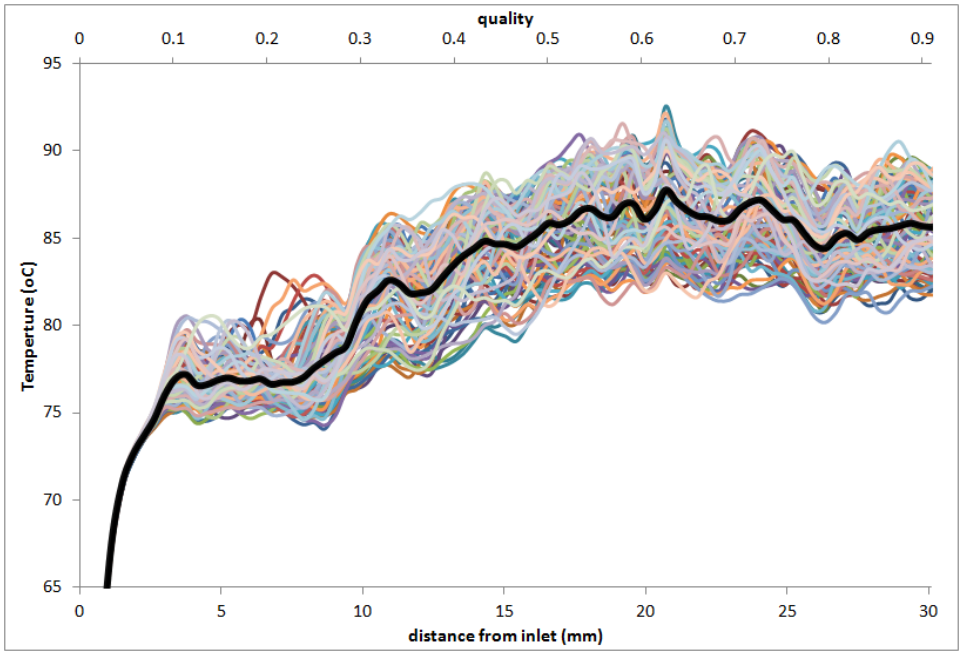

Figure 62: Axial temperature profile for 400 micron channel, 5mm width, FC-72, q=40 W/cm^2 and G=390 kg/m^2-s.

expected from review of previous channel data for these experimental conditions. Comparison with the 200 and 300 micron data shows comparable temperature fluctuations and, thus, in the presence of a high heat flux and narrow channel, the gap height effect appears to be negligible.

Microgap Cooler: 400 microns, FC-72, and width=10mm

Figure 63-Figure 67 show the axial temperature profiles for 400 microns, 10mm width, and 35mm channel length using FC-72 as the working fluid. Figure 63 shows the data for q=28 W/cm^{2}and G=195 kg/m^2-s (being the gross heat flux), which transitions at 36% quality and has temperature variations of 9 C with standard deviation of 2 C. This case is low heat and mass flux, and shows comparably modest temperature fluctuations. Comparison with previous cases with similar experimental conditions reveals a dampening of the local dryout and recovery phenomena. This may be due to the increased film thickness, which would alter the dynamics occurring in the channel. In addition, this gap height and channel width combinations results in the same aspect ratio as 200 micron gap height with 5mm channel width. This permits an aspect

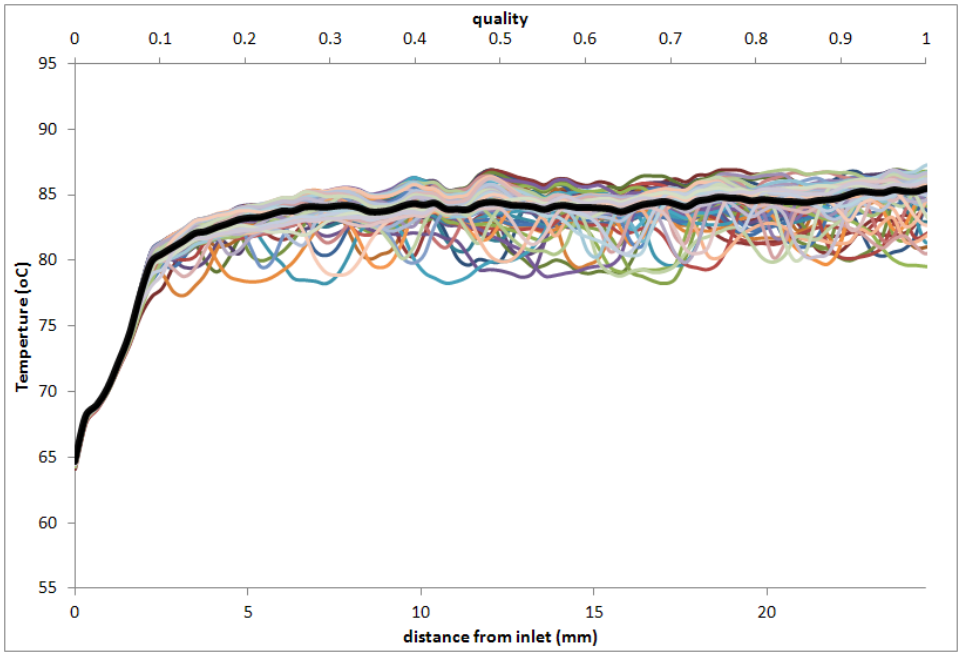

Figure 63: Axial temperature profile for 400 micron channel, 10mm width, FC-72, q=28 W/cm^2 and G=195 kg/m^2-s.

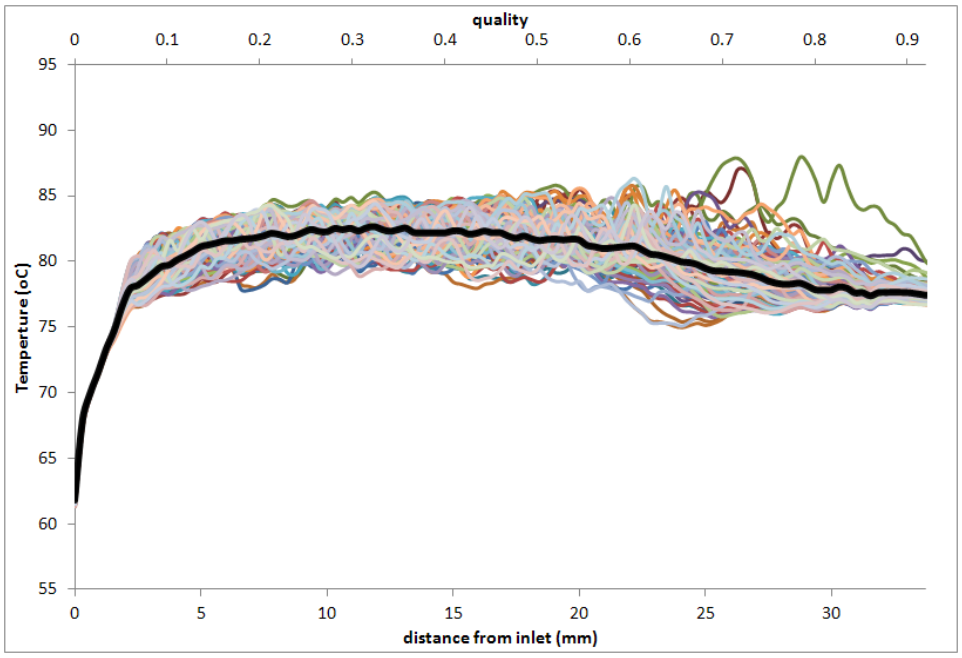

Figure 64: Axial temperature profile for 400 micron channel, 10mm width, FC-72, q=28 W/cm^2 and G=292kg/m^2-s.

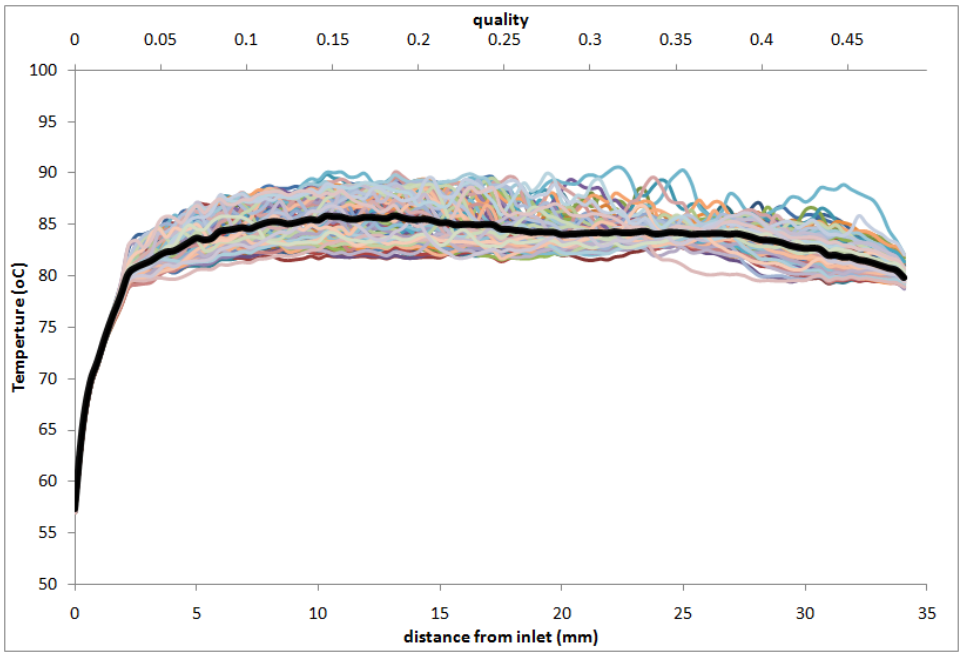

Figure 65: Axial temperature profile for 400 micron channel, 10mm width, FC-72, q=40 W/cm^2 and G=390 kg/m^2-s.

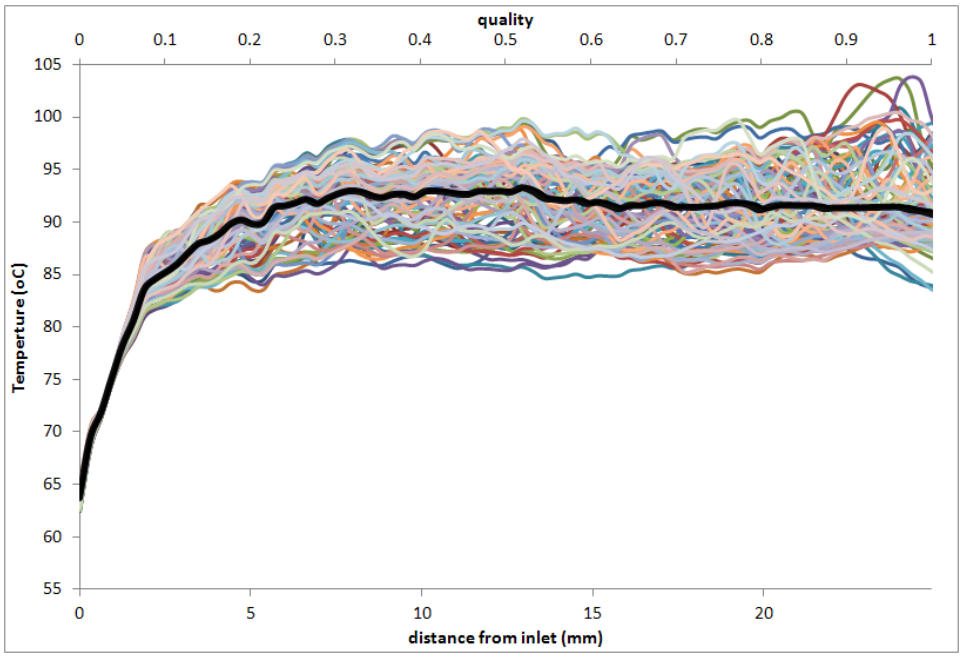

Figure 66: Axial temperature profile for 400 micron channel, 10mm width, FC-72, q=70 W/cm^2 and G=490 kg/m^2-s.

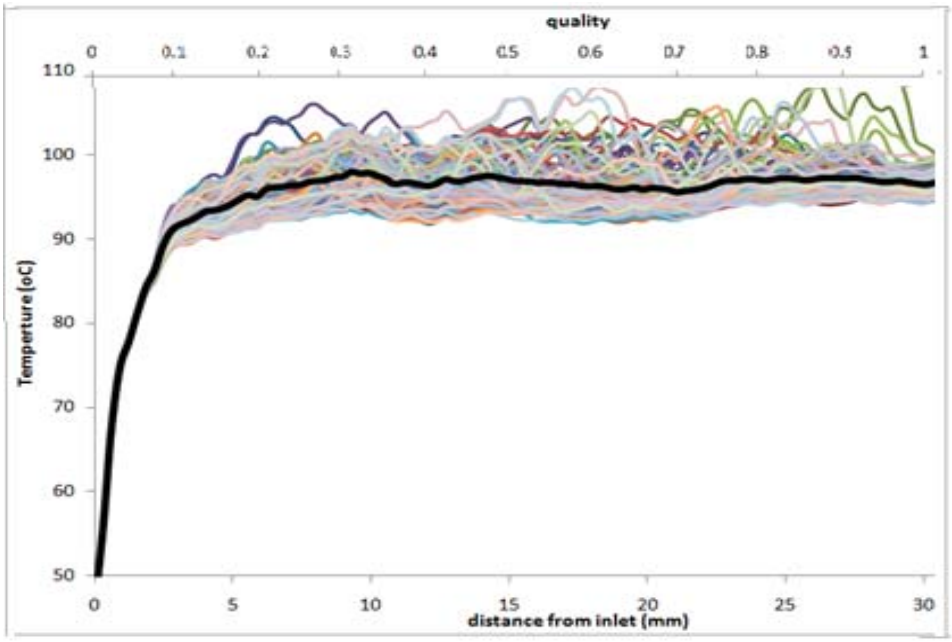

Figure 67: Axial temperature profile for 400 micron channel, 10mm width, FC-72, q=70 W/cm^2 and G=585 kg/m^2-s.

ratio comparison, revealing no distinct relationship between this parameter and channel behavior. Figure 64 is the axial profile for q=28 W/cm^2 and G=292kg/m^2-s, which transitions at 24% quality and has temperature variations of 12 C with standard deviation of 3 C. These cases show

the importance of gap height due to the lack of delayed onset of local dryout and recovery. Figure 66 and Figure 67 are the axial temperature profiles for high heat flux cases, and transition to annular 14% and 11% respectively. These cases support the previously discussed trend of increased heat flux resulting in increase temperature fluctuations, which shows further local and dryout occurring in the channel. In addition, comparing these cases to the previously discussed thinner channels shows overall higher temperatures. This can be related to the lower heat transfer coefficients obtained in annular flow due to the thicker film thickness in the downstream sections of the channel.

Figure 68 shows the axial temperature profile for various experimental conditions for comparison between several cases analyzed for 400 micron gap height with 10mm channel width. This shows the distinct behavior that occurs at fixed locations between all the conditions, confirming that the channel behavior is not due to an artifact within the channel itself. Interestingly, it may also be seen that – due to the complex thermofluid dynamics prevailing in the microgap channel - at comparable qualities, the highest heat flux, of 70W/cm2, does not result in the highest wall temperatures.

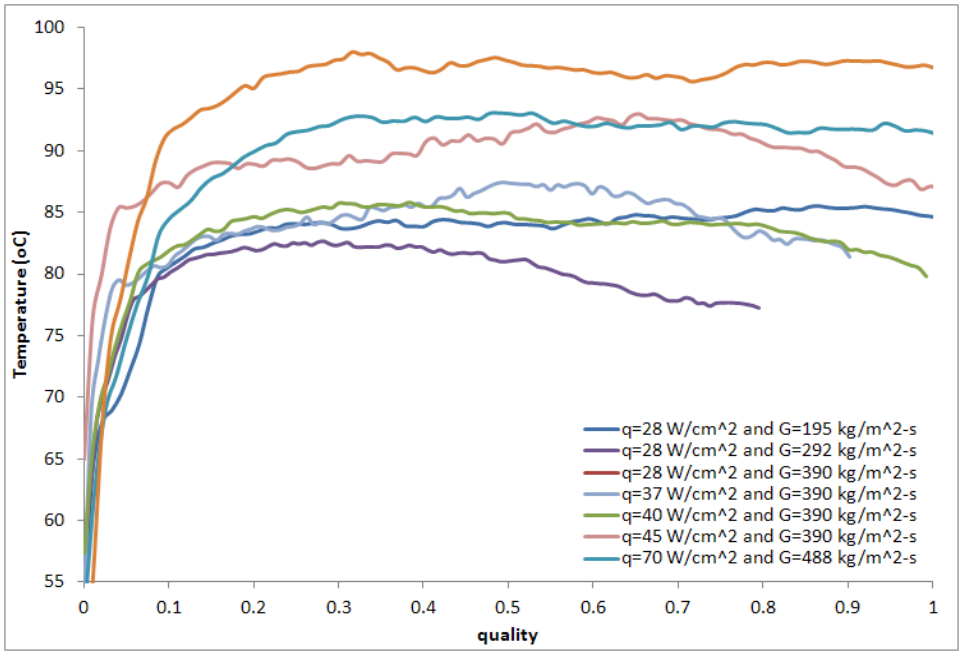

Figure 68: Axial temperature profile for 400 micron channel, 10mm width, FC-72, various experimental conditions

Microgap Cooler: 400 microns, FC-72, and width=20mm

This section outlines the data for 400 micron gap, 20mm width, and 35mm channel length with FC-72 as the working fluid. Figure 69 shows the axial temperature profile for q=23W/cm^2 and G=195 kg/m^2-s, which transitions at 36% quality. This case shows the dampening effect of the 20mm width on the temperature fluctuations, resulting in nearly negligible magnitudes for the full axial length of the channel. It is thus apparent that for the thicker gap channel, amplitude suppression and delay of the onset of temperature fluctuations occurs only at the widest channel geometry. While it is difficult to claim precise quantitative equivalence to the 200 micron gap and 10mm channel width, which yields the identical aspect ratio to this 400micron and 20mm wide channel, it is apparent that there is a qualitative dependence of the suppression mechanisms on the microgap aspect ratio. Consequently, as the channel gap grows significant temperature fluctuations persist to wider and wider geometries.

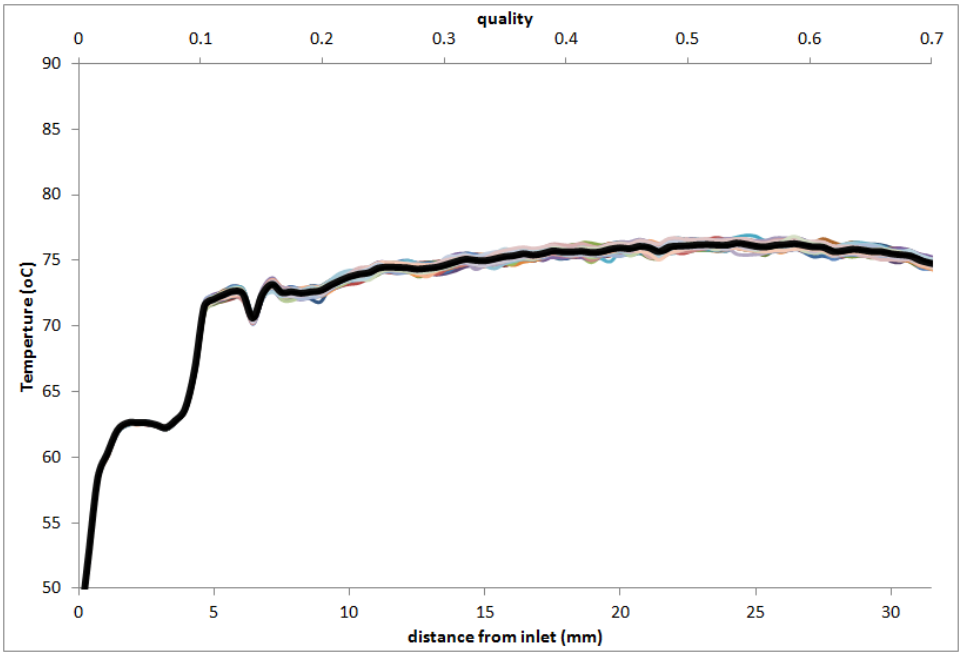

Figure 69: Axial temperature profile for 400 micron channel, 20mm width, FC-72, q=23W/cm^2 and G=195 kg/m^2-s.

CHAPTER 6

6.1 TEMPORAL TEMPERATURE VARIATION – FIXED QUALITY

The data in this section shows the temperature fluctuations that occurs at a fixed quality to further explore the relationship of local dryout and recovery with the magnitude of this phenomenon. In general the increase of the temperature fluctuation magnitude is coupled with the decrease in channel performance, thus as local dryout and recovery becomes more prevalent in the channel thermal capabilities are decreased. This is due to more of the channel being dried out than recovered at any instantaneous moment. As the quality is near unity, the fluctuations tend to decrease or plateau in magnitude due to a lack of liquid to recover to substantiate this behavior in the channel. The graphs of the various temperature fluctuations are separated for ease of examination when appropriate.

6.1.1 Microgap Channel Height at 200 microns

Microgap Cooler: 200 microns, FC-72, and width=5mm

This section overviews the data for 200 micron, 5mm width, and 35 mm length channel using FC-72 for the working fluid. Figure 70 is the temporal temperature variations for q=23 W/cm^2 and G=195 kg/m^2-s for qualities x=0.5, x=0.75, and x=0.95 with transition to annular occurring at x=0.36. The temperature fluctuations occurring at these locations are high in magnitude, and support previous observations discussed. This case shows a flattening of the temperature fluctuations as quality increases. Figure 71 shows the temporal temperature profile

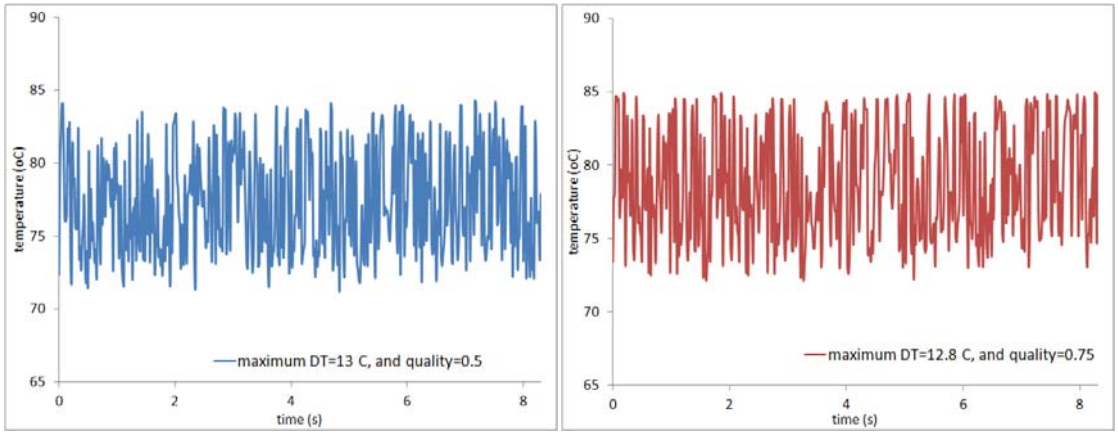

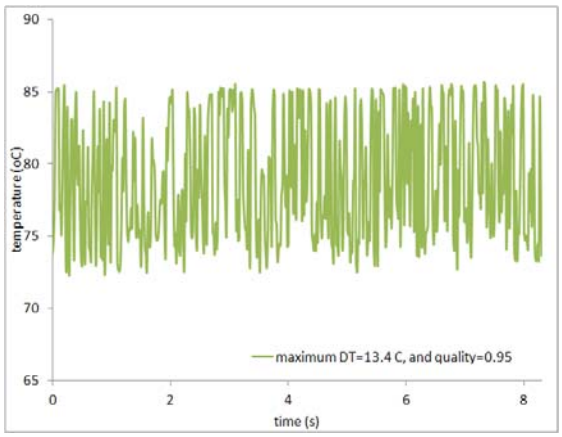

Figure 70: Temporal temperature variation for 200 micron channel, 5mm width, FC-72, q=23 W/cm^2 and G=195 kg/m^2-s.

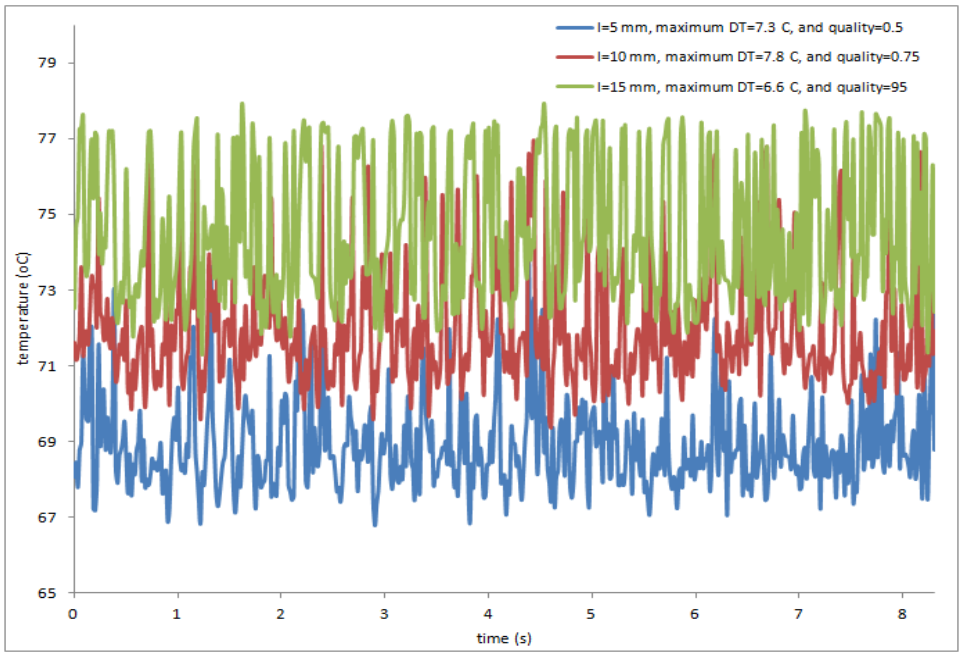

Figure 71: Temporal temperature variation for 200 micron channel, 5mm width, FC-72, q=23 W/cm^2 and G=292 kg/m^2-s.

for q=23 W/cm^2 and G=292 kg/m^2-s, which transitions to annular at 24% quality. This case has the same heat flux as the previous, however, with increased mass flux. This shows the distinct relationship between flow regime and local dryout and recovery since the fluctuations significantly decrease. Figure 72 and Figure 73 confirm the previously discussed dependence of

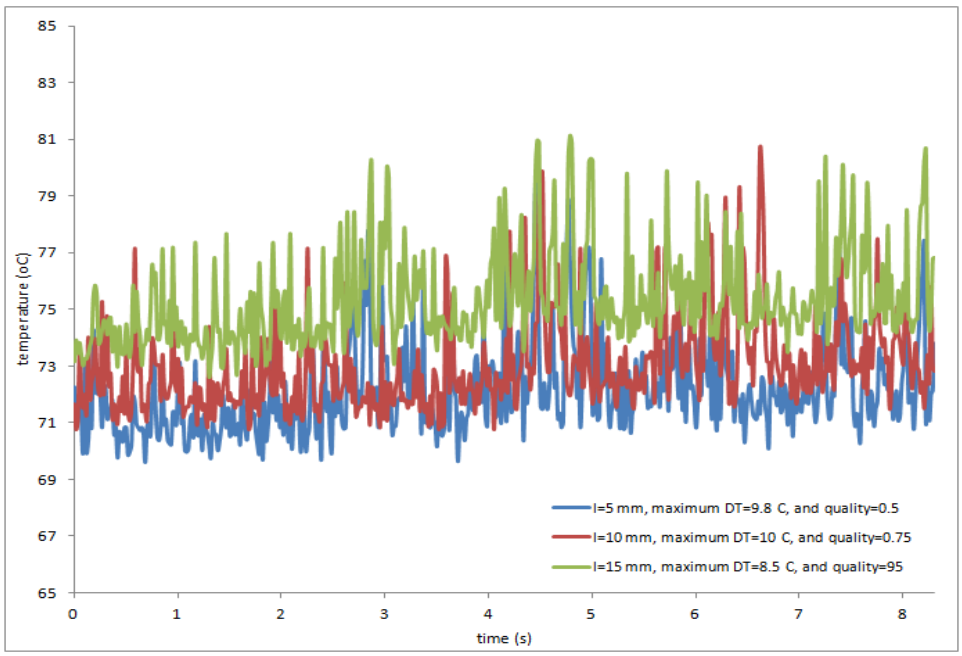

Figure 72: Temporal temperature variation for 200 micron channel, 5mm width, FC-72, q=28 W/cm^2 and G=390 kg/m^2-s.

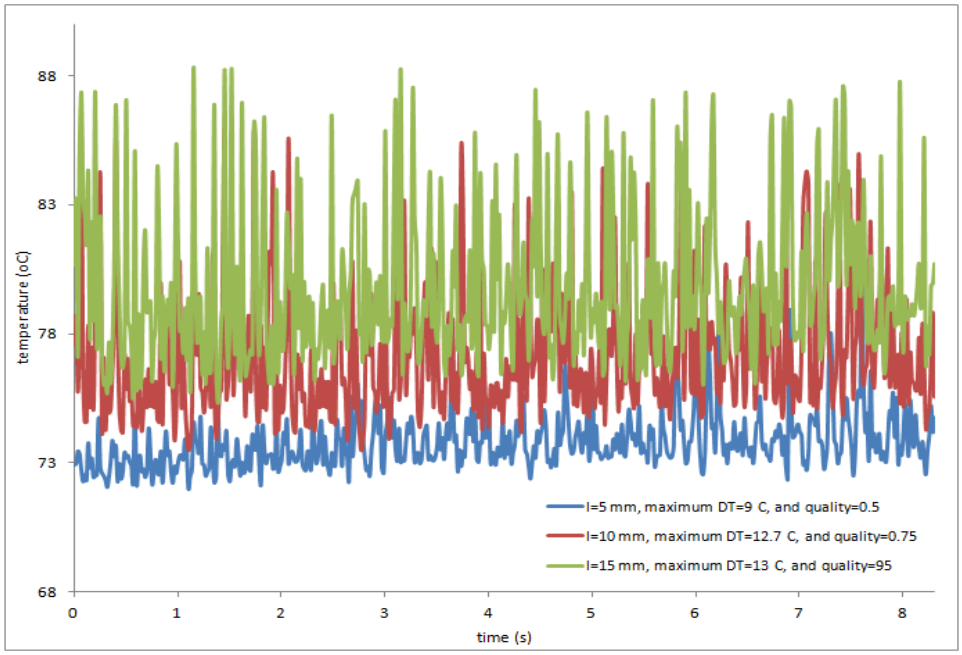

Figure 73: Temporal temperature variation for 200 micron channel, 5mm width, FC-72, q=40 W/cm^2 and G=390 kg/m^2-s.

local dryout and recovery on heat flux, since the temperature fluctuations greatly increase from cases. These cases have the same mass flux with different heat fluxes.

Microgap Cooler: 200 microns, FC-72, and width=10mm

Figure 74 shows the temporal temperature profile for q=40 W/cm^2 and G=390 kg/m^2-s, which transitions at 18% quality. This case is high heat flux with moderate mass flux, and shows increasing temperature locations as quality increases. The fluctuations are only comparable at high qualities between this case and the 5mm channel width case with similar experimental conditions. This confirms the dampening effect seen in the previous section, and demonstrates the channel width importance to local dryout and recovery.

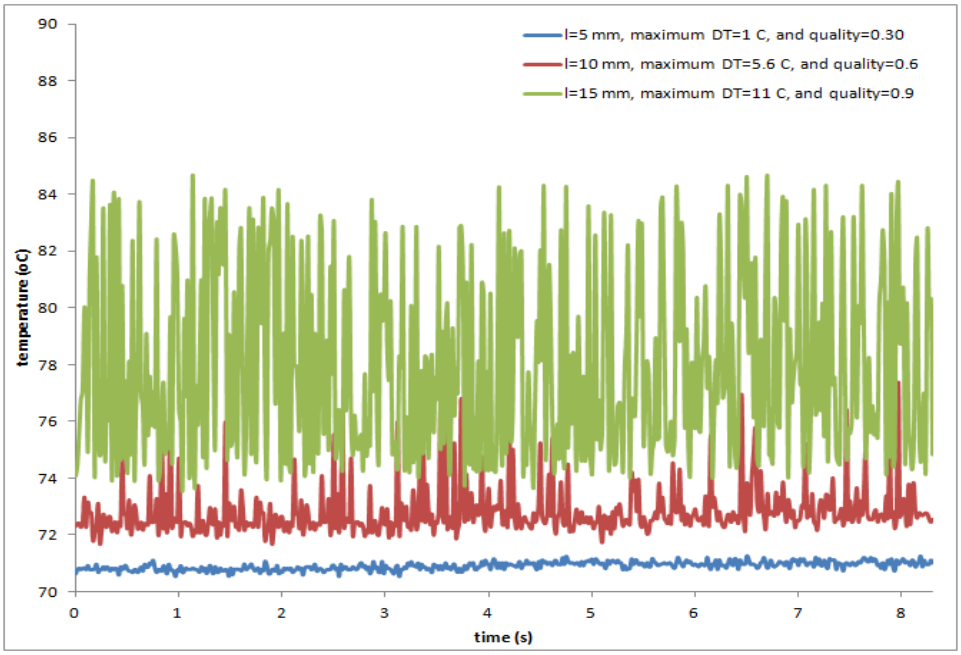

Figure 74: Temporal temperature variation for 200 micron channel, 10mm width, FC-72, q=40 W/cm^2 and G=390 kg/m^2-s.

Microgap Cooler: 200 microns, FC-72, and width=20mm

This section shows the temporal temperature profiles for 200 micron gap, 20mm width, ad 35mm channel length with FC-72 for the working fluid. Figure 75 shows the data for q=23 W/cm^2 and G=195 kg/m^2-s, which transitions to annular at 36% quality and has temperature fluctuations of 11 C. This is comparable to similar experimental conditions with 5mm channel width, and has a flattening out of the temperature fluctuations with increasing quality. Figure 76 shows the temporal temperature profile for q=23 W/cm^2 and G=292 kg/m^2-s, which transitions at 24% quality and has temperature fluctuations of 5 C. Comparison between Figure 75 and

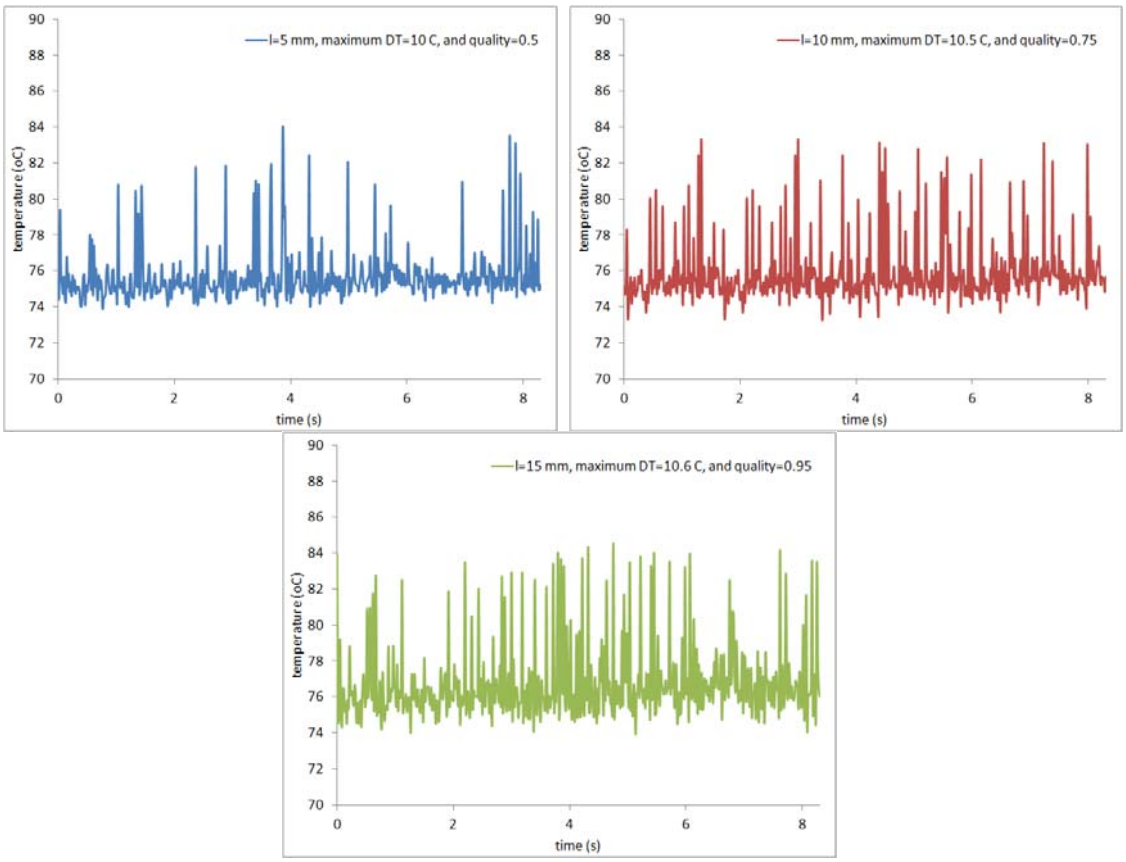

Figure 75: Temporal temperature variation for 200 micron channel, 20mm width, FC-72, q=23 W/cm^2 and G=195 kg/m^2-s.

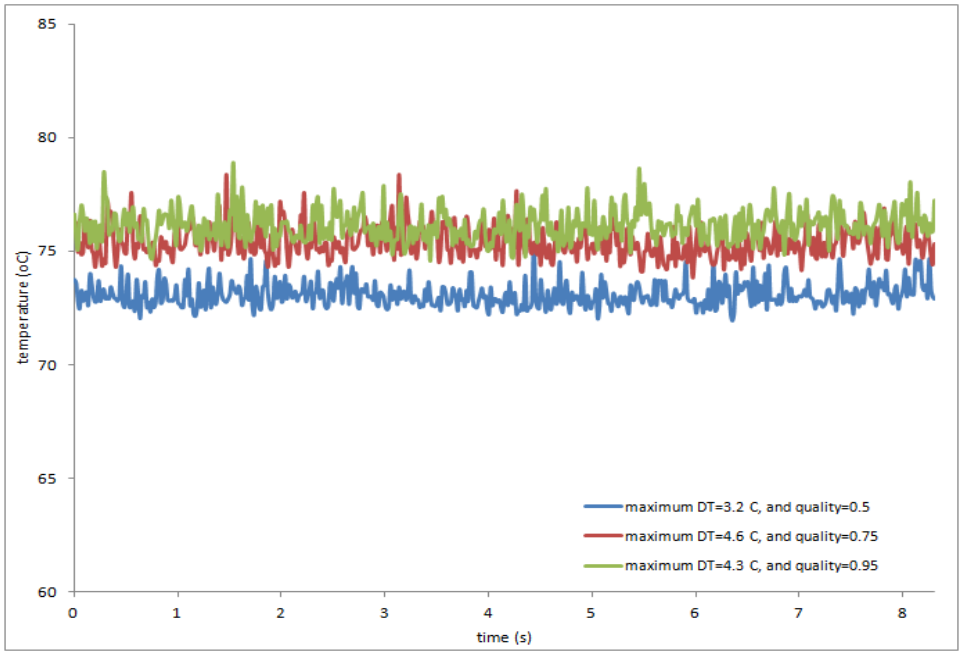

Figure 76: Temporal temperature variation for 200 micron channel, 20mm width, FC-72, q=23 W/cm^2 and G=292 kg/m^2-s.

Figure 76 supports the dampening effect the mass flux (i.e. flow regime) has on the local dryout and recovery. In addition, comparison between Figure 76 and the 5mm channel with shows the dampening effect width has on local dryout and recovery due to the decreased magnitude of temperature fluctuations.

6.1.2 Microgap Channel Height at 300 microns

Microgap Cooler: 300 microns, FC-72, and width=5mm

This sections outlines the temporal temperature variations for 300 micron gap, 5mm

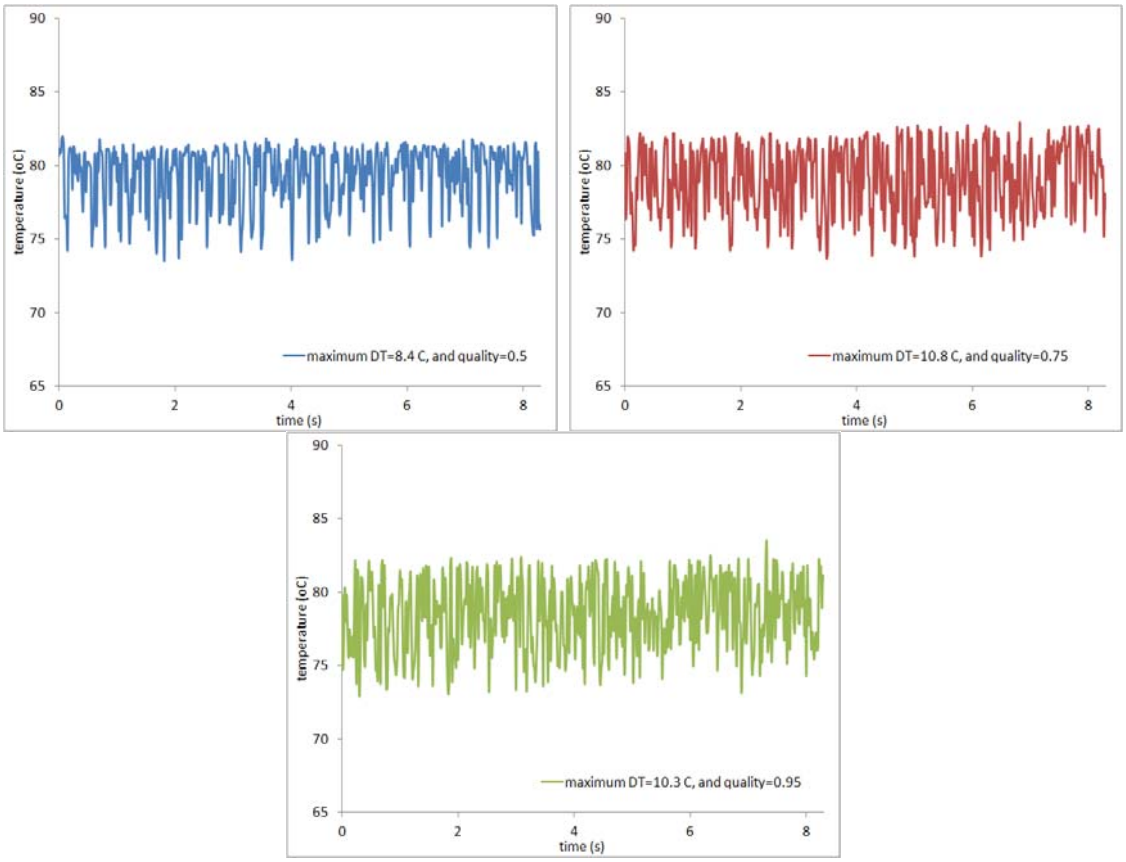

Figure 77: Temporal temperature variation for 300 micron channel, 5 mm width, FC-72, q=23 W/cm^2 and G=195 kg/m^2-s.

width, and 35mm channel length with FC-72 working fluid. Figure 77 shows the profile for q=23 W/cm^2 and G=195 kg/m^2-s, which transitions at 36% quality. This case is low heat and mass flux, and temperature fluctuations that plateau with increasing qualities of 11 C. Comparison of

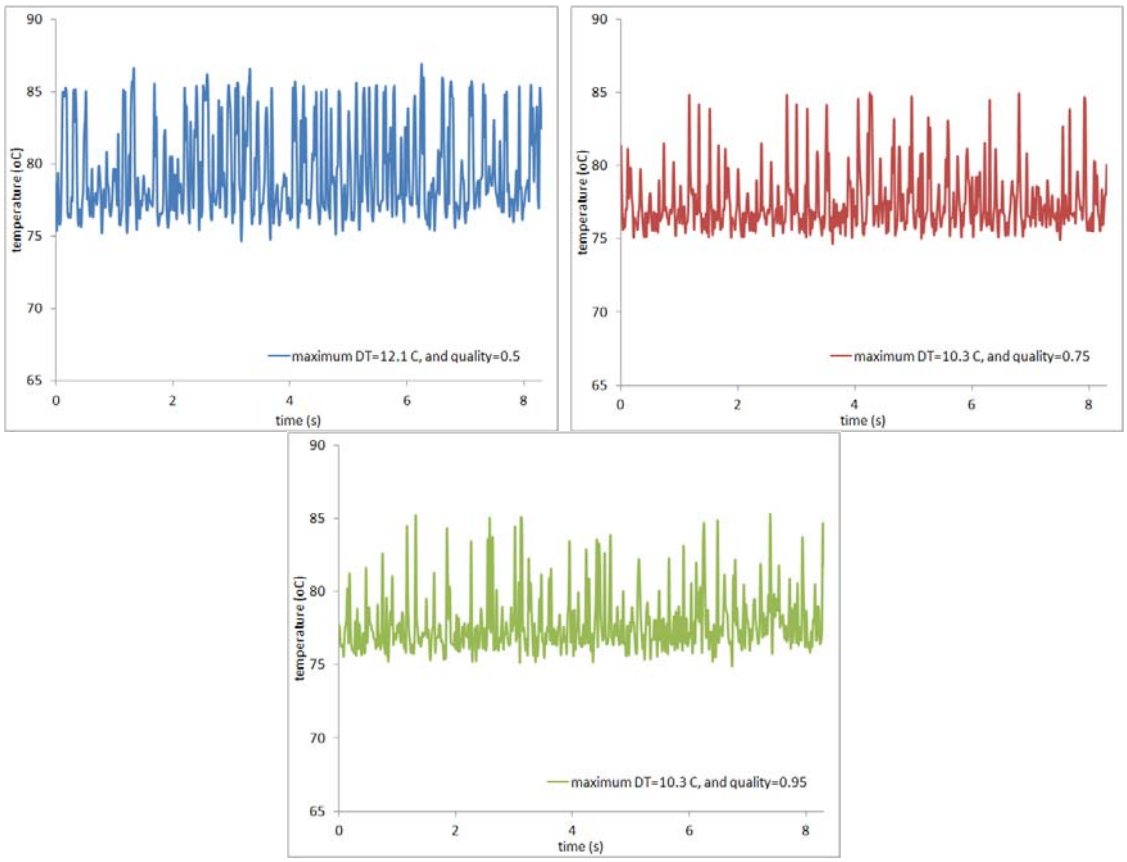

Figure 78: Temporal temperature variation for 300 micron channel, 5 mm width, FC-72, q=23 W/cm^{2}and G=292 kg/m^2-s.

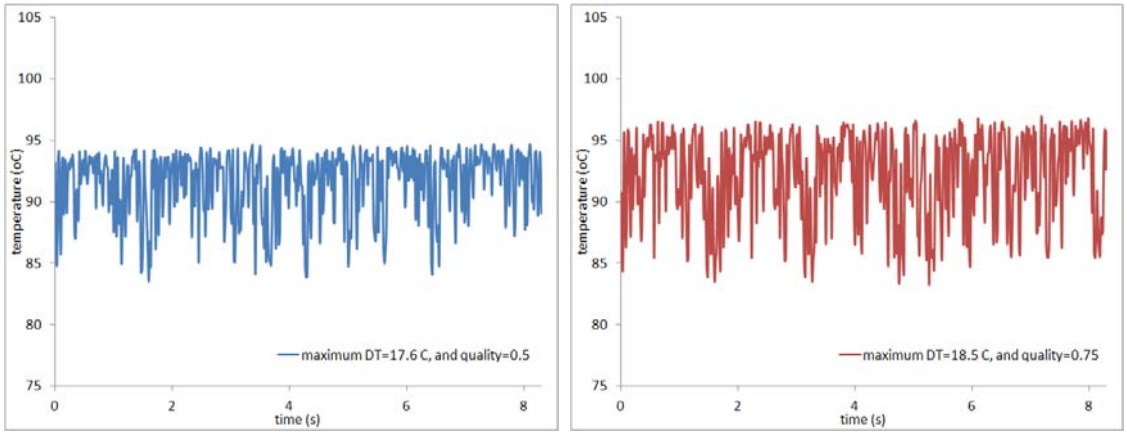

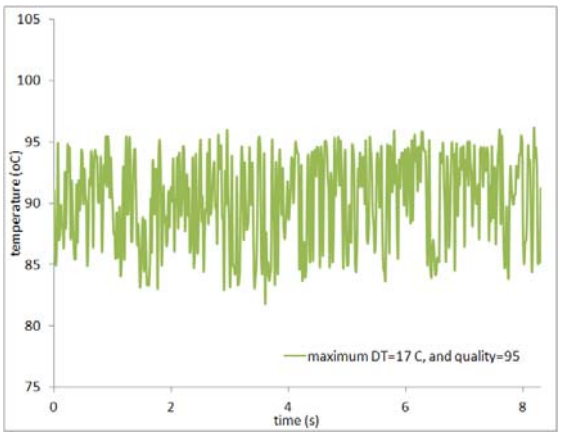

Figure 79: Temporal temperature variation for 300 micron channel, 5 mm width, FC-72, q=40 W/cm^2 and G=390 kg/m^2-s.

this case with the comparable 200 micron gap height case supports the previous discussion of gap height dampening out local dryout and recovery due to film thickness. Figure 78 shows the data for q=23 W/cm^2 and G=292 kg/m^2-s, which transitions at 24% quality. As previously observed, this case does not have diminished temperature fluctuations as expected, but speaks to the complicated combination of effects on local dryout and recovery. This case also plateaus as quality increases, and comparison with 200 micron case shows no dampening of local dryout and recovery supporting theories of mass flux dominating over gap height effects. Figure 79 shows the temporal temperature profile for q=40 W/cm^2 and G=390 kg/m^2-s, which transitions to annular at 18% qualities. This case shows the distinct increase in temperature fluctuations with increased heat flux, and shows that with increased mass flux the gap effect is negligible.

Microgap Cooler: 300 microns, FC-72, and width=10mm

This sections shows the data for 300 micron gap, 10mm width, and 35 mm channel length with FC-72 as the working fluid. Figure 80 shows the temporal temperature fluctuations

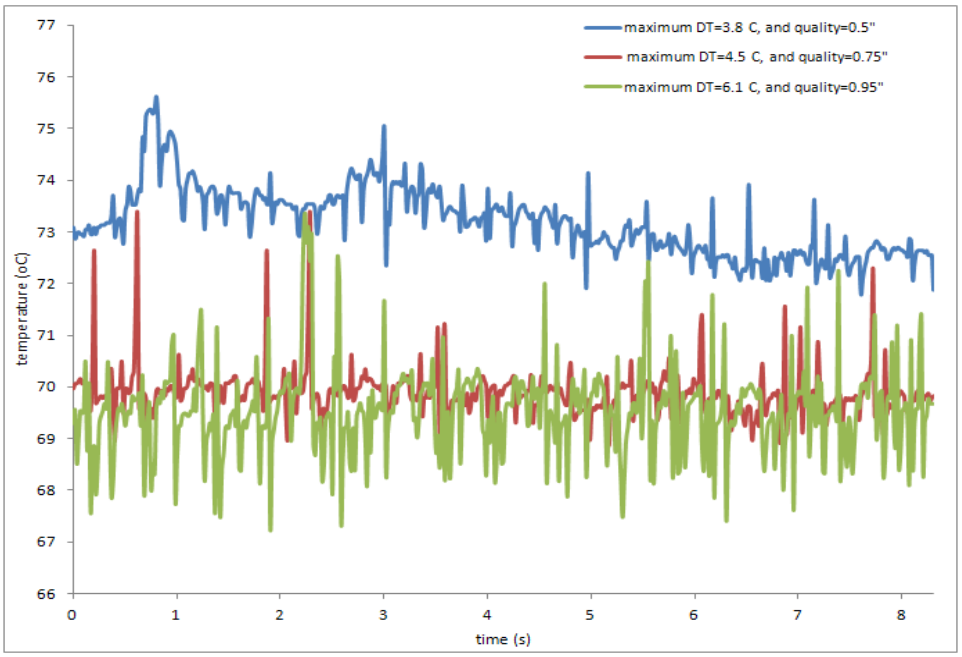

Figure 80: Temporal temperature variation for 300 micron channel, 10mm width, FC-72, q=23 W/cm^2 and G=195 kg/m^2-s.

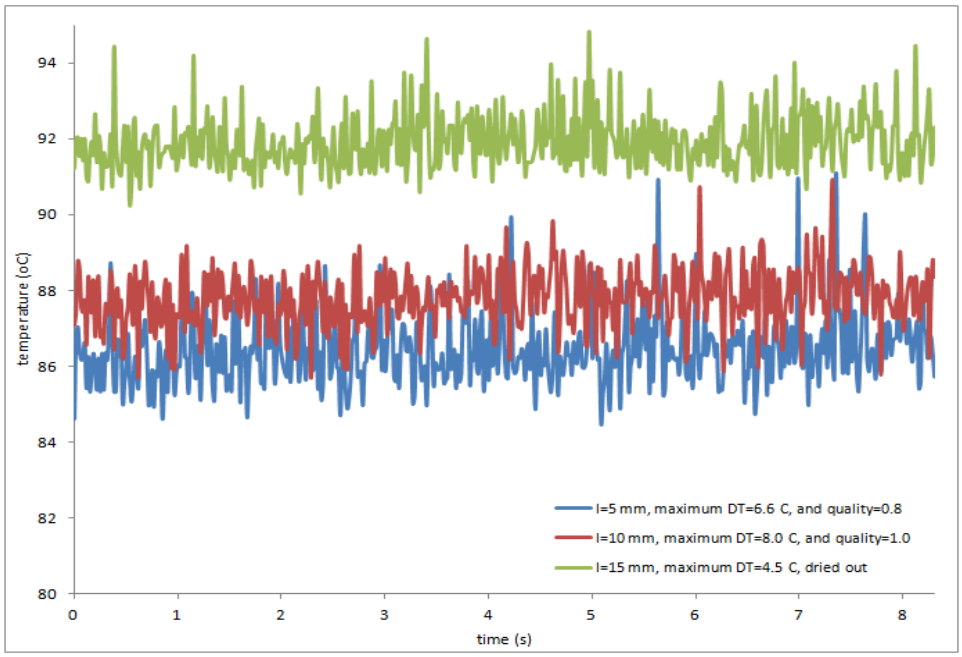

Figure 81: Temporal temperature variation for 300 micron channel, 10mm width, FC-72, q=28 W/cm^2 and G=195 kg/m^2-s.

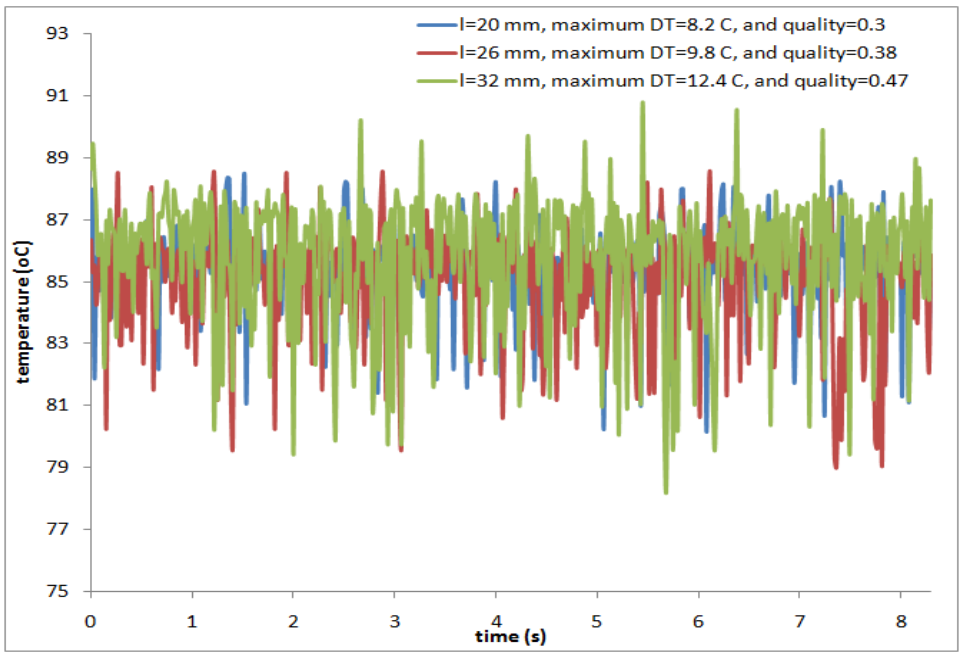

Figure 82: Temporal temperature variation for 300 micron channel, 10mm width, FC-72, q=28 W/cm^2 and G=292 kg/m^2-s.

for q=23 W/cm^2 and G=195 kg/m^2-s, which transitions at 36% quality. The temperature fluctuations are once again dampened between this and the 5 mm case, supporting previous discussion of this relationship. The temperature fluctuations plateau with increasing qualities which is also seen in Figure 82. Figure 82 shows the temperature profile for q=28 W/cm^2 and G=292 kg/m^2-s, and interestingly also has comparable temperature fluctuation magnitudes despite the increased mass flux. This follows with the trend seen for similar experimental

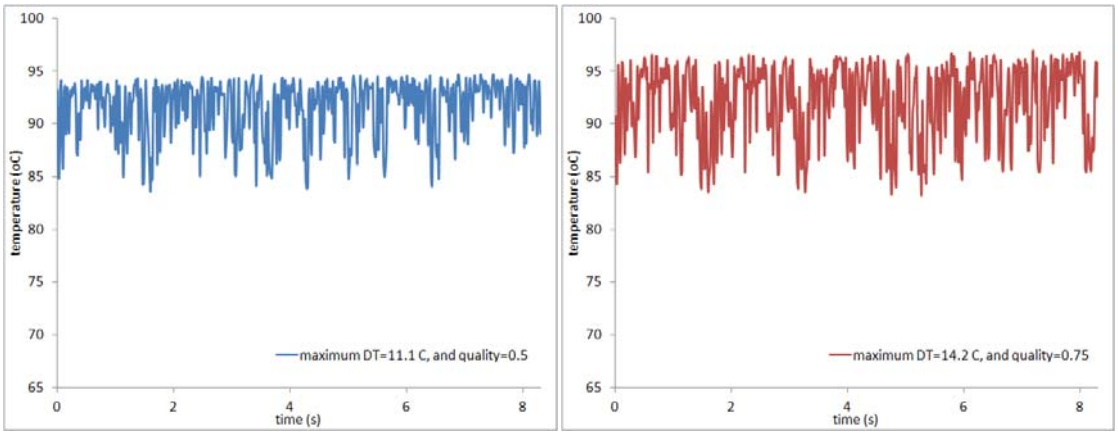

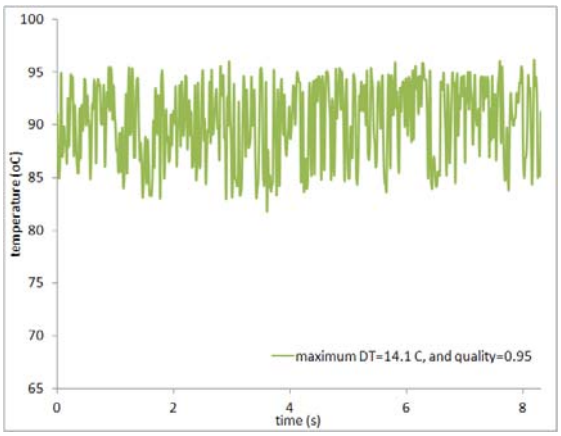

Figure 83: Temporal temperature variation for 300 micron channel, 10mm width, FC-72, q=40 W/cm^2 and G=390 kg/m^2-s.

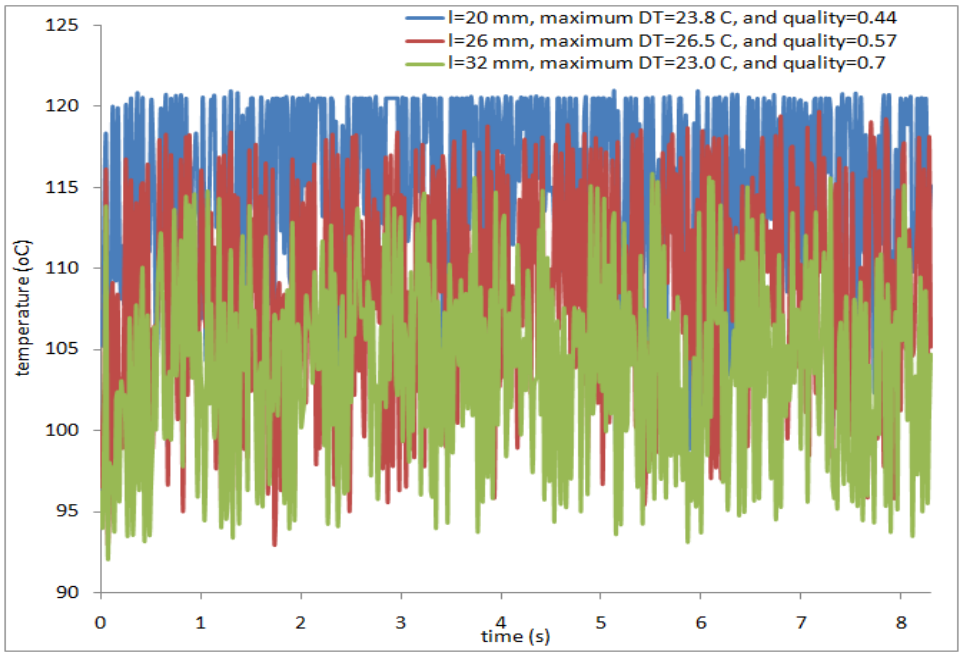

Figure 84: Temporal temperature variation for 300 micron channel, 10mm width, FC-72, q=70 W/cm^2 and G=490 kg/m^2-s.

conditions but 5mm channel width. Figure 83 shows the data for q=40 W/cm^2 and G=390 kg/m^2-s showing the distinct increase in temperature fluctuations from lower heat flux cases, but also confirming the width dampening of local dryout and recovery since the magnitudes are lower than those found for the 5mm case. Figure 84 shows the extreme case of q=70 W/cm^2 and G=490 kg/m^2-s, which transitions to annular at 14% quality. This confirms the trend of increased heat

transfer leads to increased local dryout and recovery, and further support previous discussion of this relationship.

Microgap Cooler: 300 microns, FC-72, and width=20mm

Figure 85 shows the temporal temperature variations for q=23 W/cm^2 and G=292 kg/m^2-s, which transitions to annular at 24% quality. This case follows the previously outlined trend of dampened fluctuations due to width, and shows a plateau trends for temperature fluctuations with increased quality.

Figure 86-Figure 88 shows the comparison of all various experimental conditions for the 300 micron, 10mm width, using FC-72 as the working fluid. These demonstrate the distinctly different behavior at fixed locations, eliminating the possibility of channel behavior being caused by channel structure. In addition, this shows the different behavior of various experimental combinations at fixed qualities. This outlines the complex nature of local dryout and recovery, and its dependence on both heat flux and flow regimes.

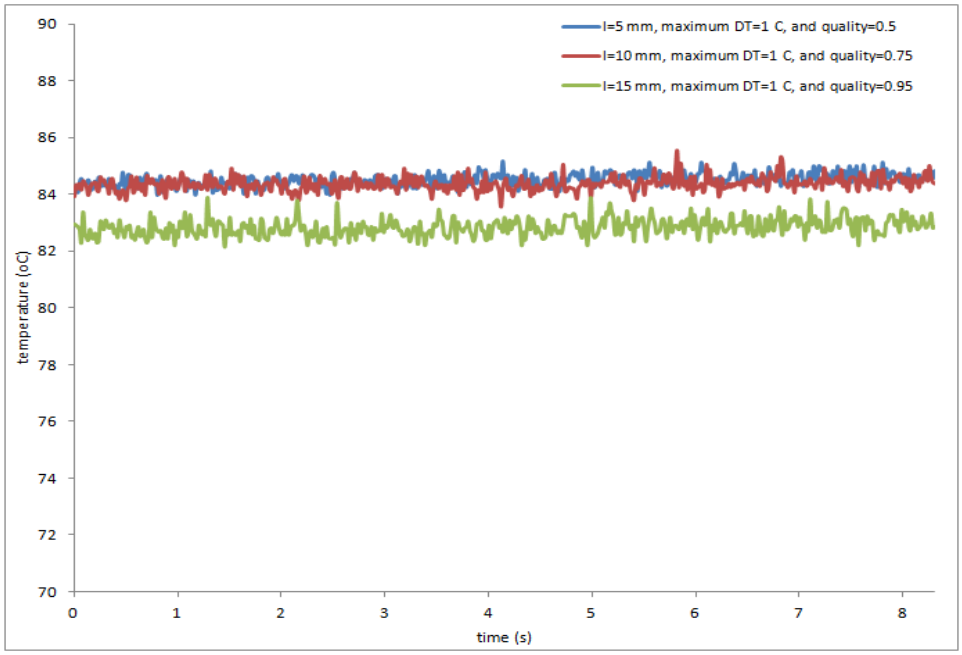

Figure 85: Temporal temperature variation for 300 micron channel, 20mm width, FC-72, q=23 W/cm^2 and G=292 kg/m^2-s.

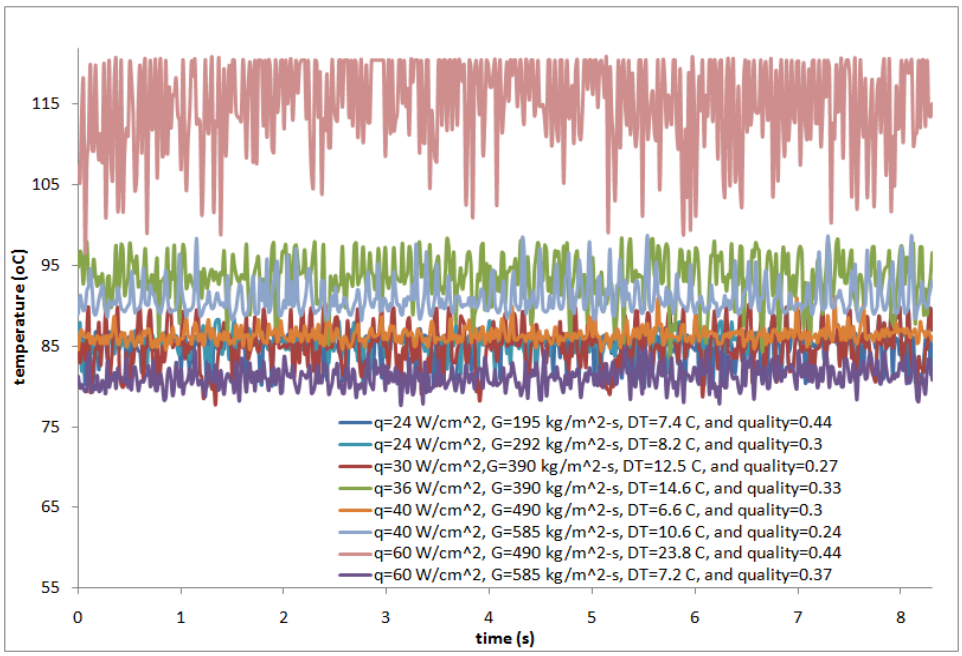

Figure 86: Temporal temperature variation fixed location (20 mm from inlet) for 300 micron channel, 10mm width, FC-72, comparison

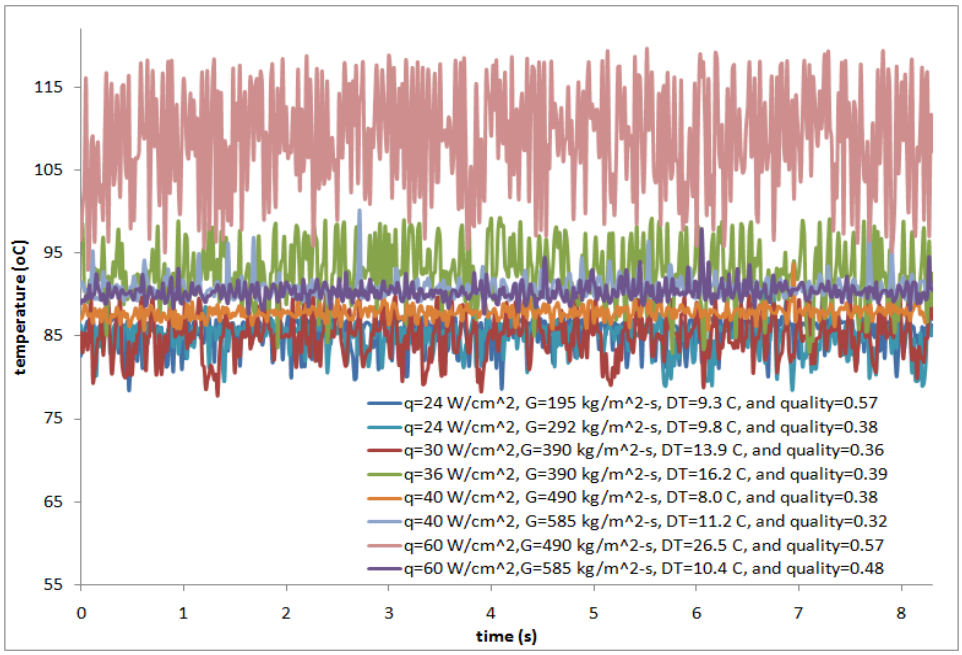

Figure 87: Temporal temperature variation fixed location (26 mm from inlet) for 300 micron channel, 10mm width, FC-72, comparison

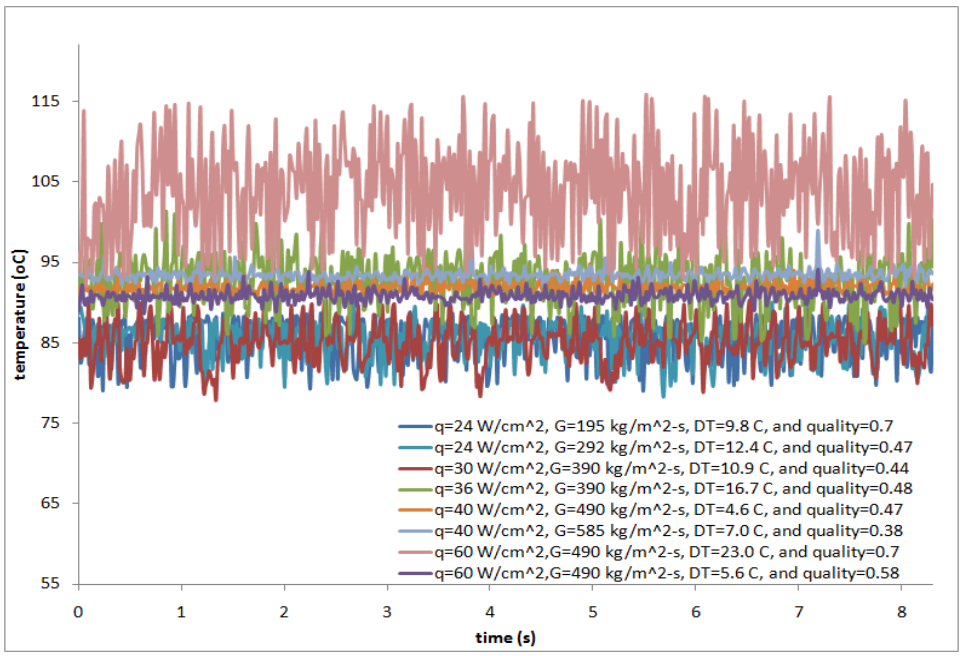

Figure 88: Temporal temperature variation fixed location (32 mm from inlet) for 300 micron channel, 10mm width, FC-72, comparison

Microgap Cooler: 300 microns, HFE-7100, and width=10mm

This section shows the data for 300 micron gap, 10mm width, and 35 mm channel length, with HFE-1700 working fluid. Figure 89 shows the data for q=23 W/cm^2 and G=195 kg/m^2-s, which transitions at 36% quality. Comparison with this case and one utilizing FC-72 reveals comparable temperature fluctuations. This supports the earlier discussion, however these fluctuations occur at lower qualities and no advantage will be gained. Figure 90and Figure 91 confirm this trend, and follow the trend of increased mass flux decreased local dryout and recovery.

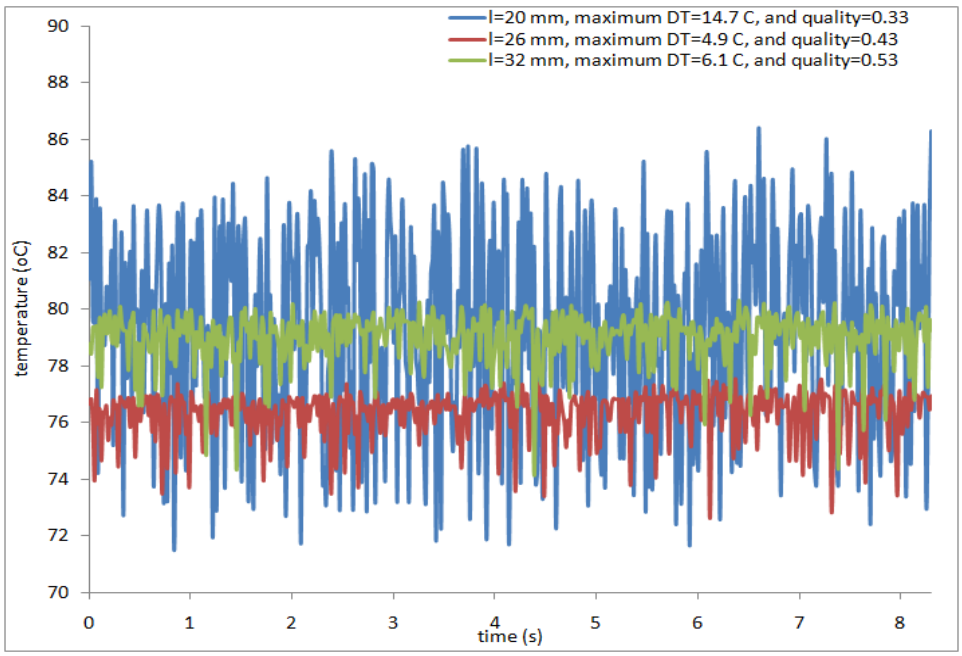

Figure 89: Temporal temperature variation for 300 micron channel, 10mm width, HFE-7100, q=23 W/cm^2 and G=195 kg/m^2-s.

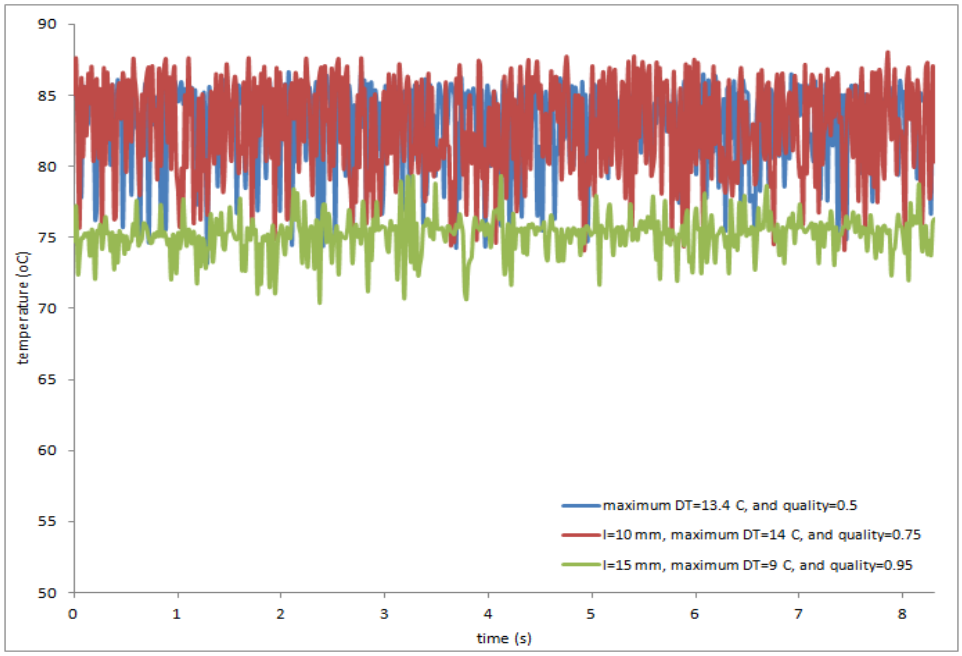

Figure 90: Temporal temperature variation for 300 micron channel, 10mm width, HFE-7100, q=28 W/cm^{2}and G=195 kg/m^2-s.

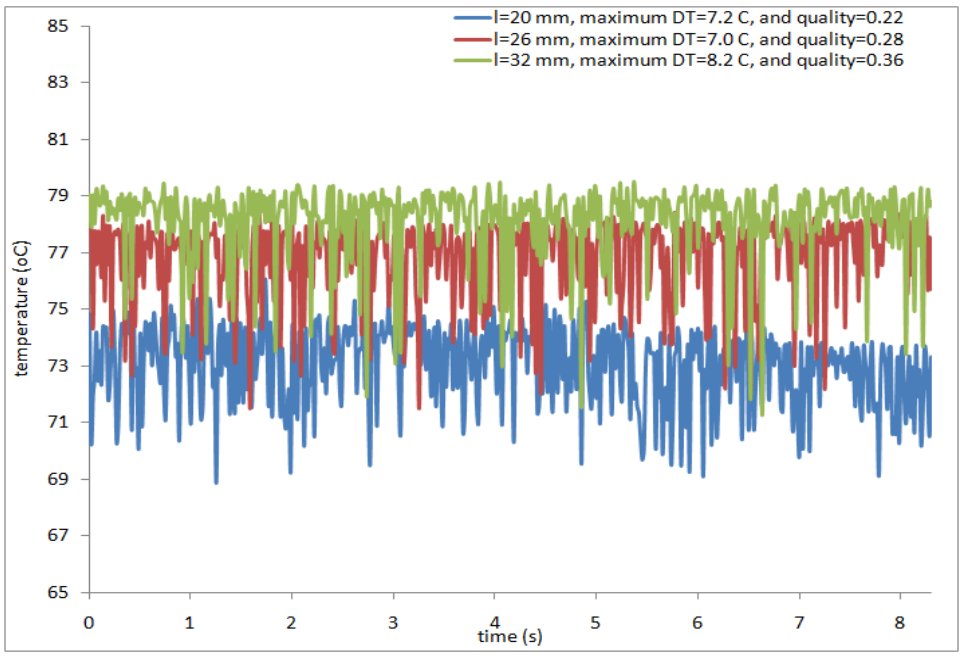

Figure 91: Temporal temperature variation for 300 micron channel, 10mm width, HFE-7100, q=28 W/cm^2 and G=292 kg/m^2-s.

6.1.3 Microgap Channel Height at 400 microns

Microgap Cooler: 400 microns, FC-72, and width=5mm

Figure 92 shows the data for q=40 W/cm^2 and G=390 kg/m^2-s transitioning at 18% quality. This case shows the decreasing temperature fluctuation magnitudes with increasing quality, and follows the general trend of having dampening local dryout and recovery due to width. In addition, the gap effect appears to be dampened out by the mass flux of this particular case.

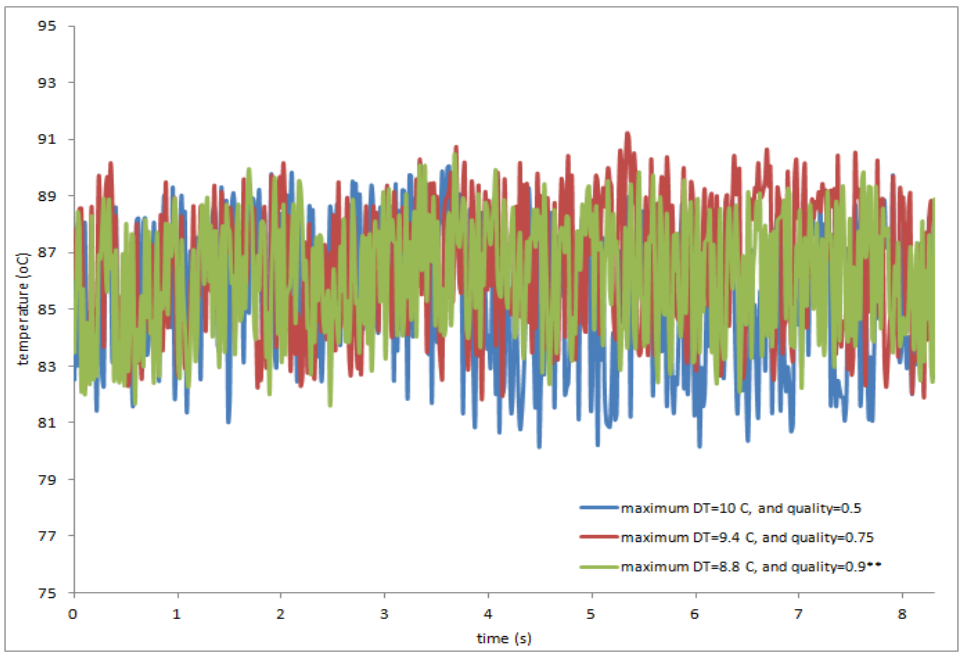

Figure 92: Temporal temperature variation for 400 micron channel, 5mm width, FC-72, q=40 W/cm^2 and G=390 kg/m^2-s.

Microgap Cooler: 400 microns, FC-72, and width=10mm

This section outlines the data for 400 micron gap, 10mm width, and 35mm channel length with FC-72 working fluid. Figure 93 shows the temperature profile for q=28 W/cm^2 and

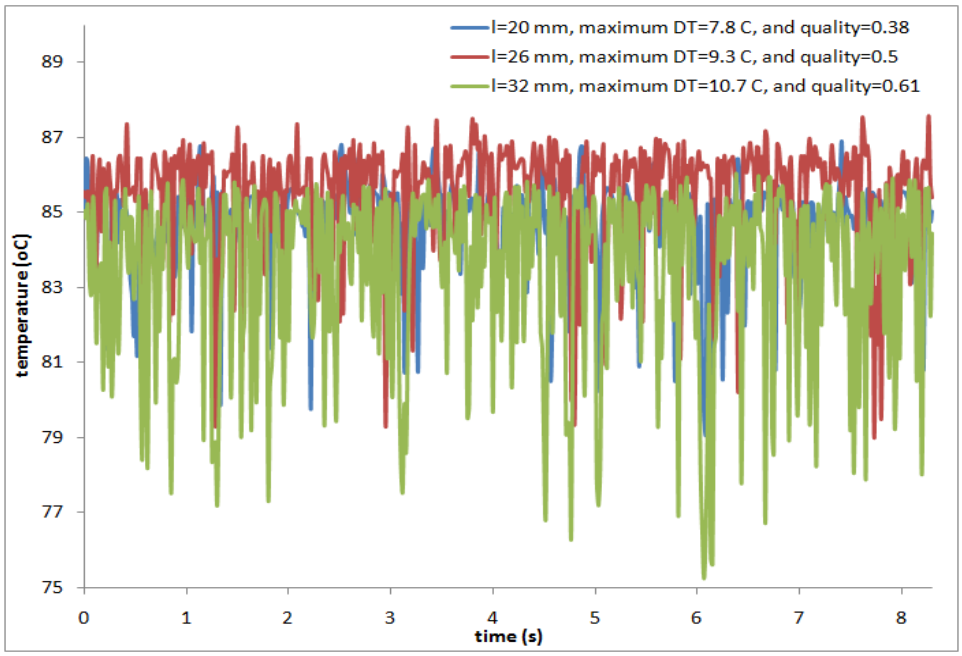

Figure 93: Temporal temperature variation for 400 micron channel, 10mm width, FC-72, q=28 W/cm^2 and G=195 kg/m^2-s.

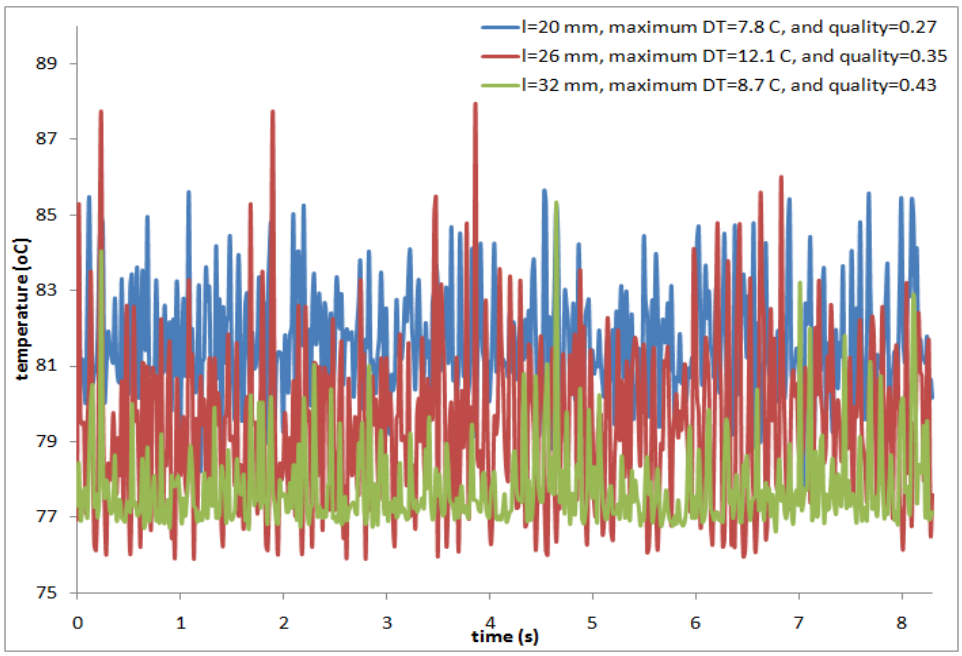

Figure 94: Temporal temperature variation for 400 micron channel, 10mm width, FC-72, q=28 W/cm^2 and G=292 kg/m^2-s.

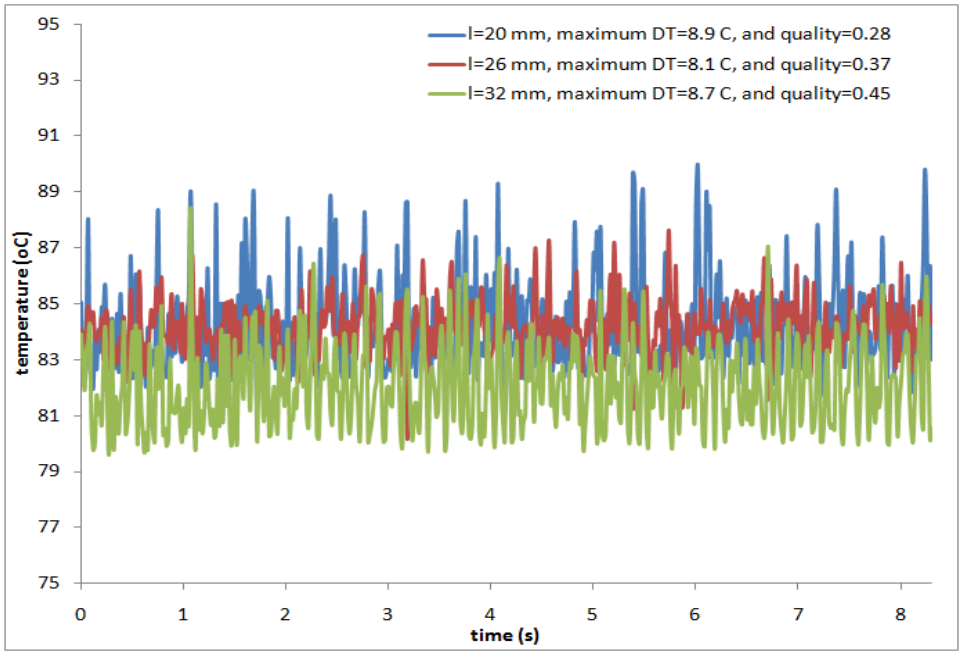

Figure 95: Temporal temperature variation for 400 micron channel, 10mm width, FC-72, q=40 W/cm^2 and G=390 kg/m^2-s.

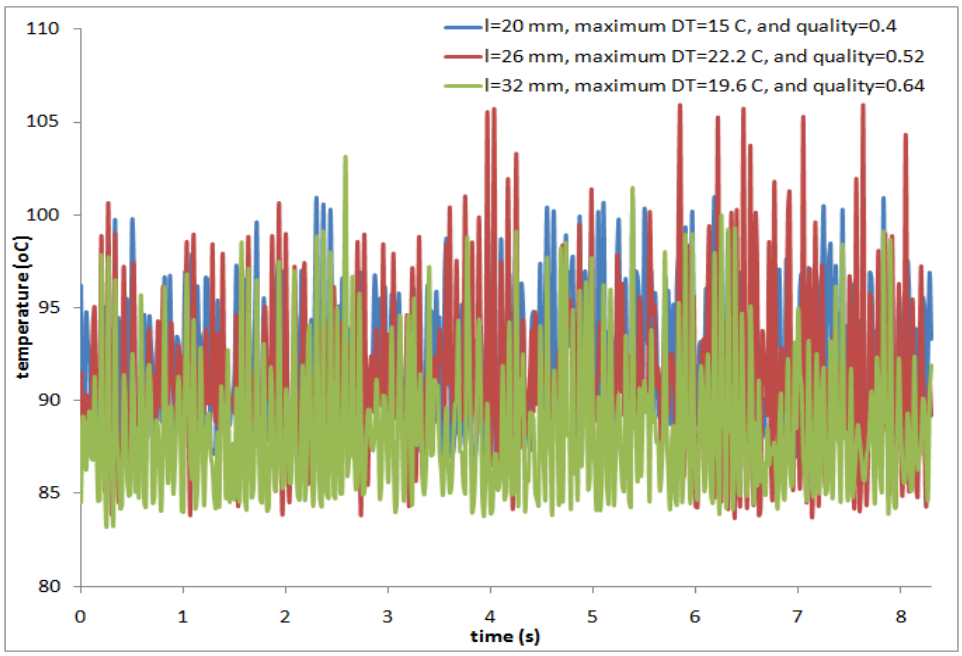

Figure 96: Temporal temperature variation for 400 micron channel, 10mm width, FC-72, q=70 W/cm^2 and G=490 kg/m^2-s.

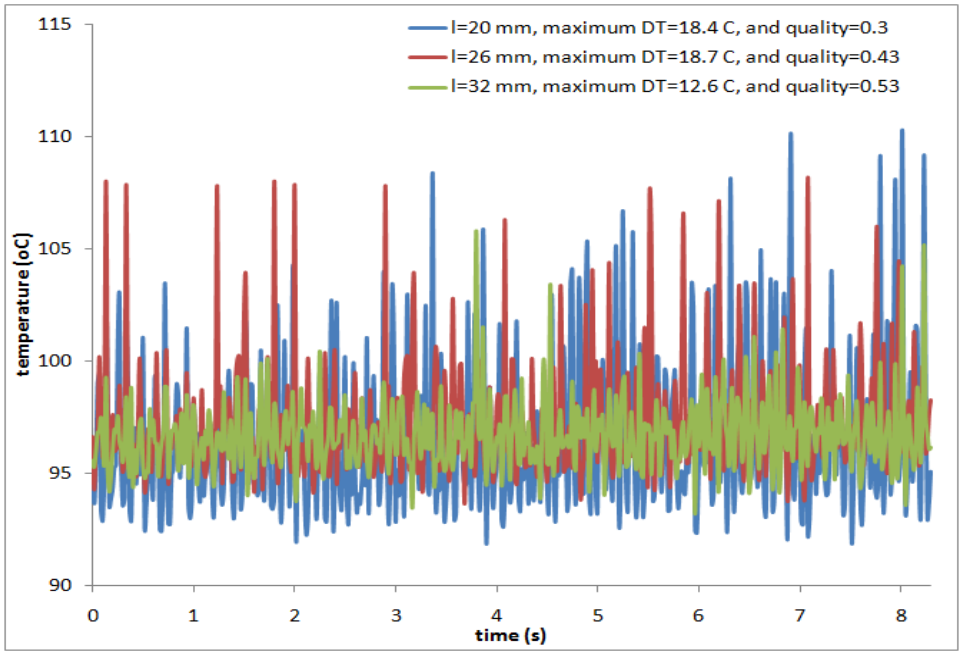

Figure 97: Temporal temperature variation for 400 micron channel, 10mm width, FC-72, q=70 W/cm^2 and G=585 kg/m^2-s.

G=195 kg/m^2-s, which transitions at 36% quality. This case is low heat and mass flux, and shows moderate temperature fluctuations. Comparing this data to Figure 94, the fluctuations are greater with the higher mass flux case contrary to general trends followed by data. This demonstrates the

complex nature of the local dryout and recovery phenomenon and its relationship with many factors. Figure 96-Figure 98 show additional cases showing increasing fluctuations with increasing heat flux, confirming previously discussed trends.

Microgap Cooler: 400 microns, FC-72, and width=20mm

Figure 98 shows the temporal temperature fluctuations for q=23 W/cm^2 and G=292 kg/m^2-s, which transitions at 24% quality. This shows the distinct effect of width on the local dryout and recovery behavior with no significant fluctuations occurring for this case.

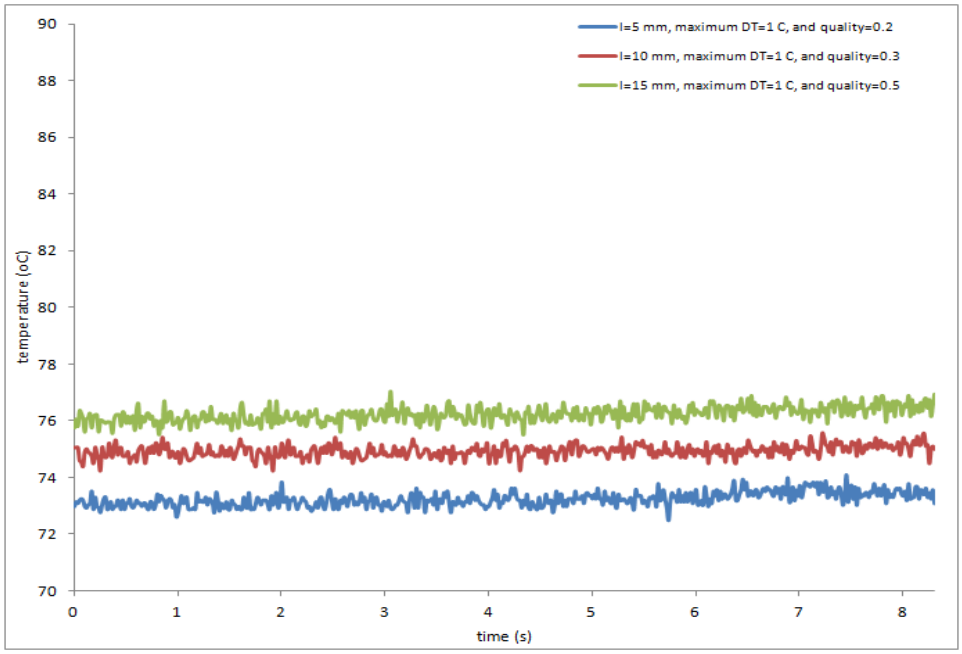

Figure 98: Temporal temperature variation for 400 micron channel, 20mm width, FC-72, q=23 W/cm^2 and G=292 kg/m^2-s.

CHAPTER 7

RESULTS AND ANALYSIS: MICROGAP CHANNEL HEAT TRANSFER CHARACTERISTICS

7.1 Two-Phase Heat Transfer Coefficients

The data presented in this section are two-phase heat transfer coefficients determined by the inverse ANSYS calculation method described in an earlier Chapter 3 and related to the observed temperature fluctuation magnitude where appropriate. The temperature fluctuations were calculated at qualities of 20, 30, 40, 50, 60, 75, 95, and 100 percent to explore the relationship between this parameter and the two-phase heat transfer coefficients. The average heat transfer coefficient, calculated using the gross heat flux and thermocouple temperatures, is represented in red showing the complex heat flow occurring in the channel. It was expected that the intrinsic M-shaped curve would be present throughout the two-phase heat transfer coefficient data, and a potential link could be derived between this trend and the temperature magnitude (i.e. local dryout and recovery).

7.1.1 Microgap Channel Height at 200 microns

Microgap Cooler: 200 microns, FC-72, and width=5mm

This section shows the data for 200 micron gap, 5mm width, and 35mm channel length with FC-72 as the working fluid. Figure 99 shows the two-phase coefficients for q=23 W/cm^2 and G=195 kg/m^2-s, which transitions to annular at 36% quality. The secondary axis shows the temperature fluctuations and reveals a potential relationship between the magnitude of the fluctuation and the two-phase heat transfer coefficient. Figure 99 does not blatantly display the M-shaped curve previously discussed, but shows a maximum of 4100 W/m^2-K at 55% quality. Figure 100 shows the data q=23 W/cm^2 and G=292 kg/m^2-s, which transitions to annular at 24% quality. The performance (i.e. two-phase heat transfer coefficients) is higher for Figure 99 than Figure 100, but the overall average is moderately different. This further supports the complex nature of channel behavior, with relationships to many parameters. Figure 101 shows

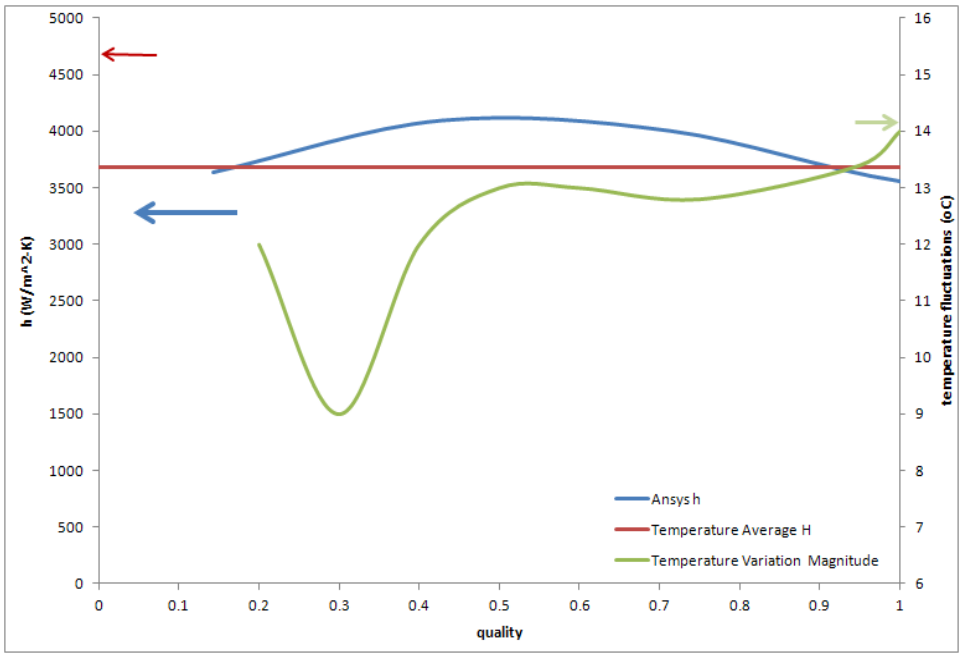

Figure 99: Two-phase coefficient for 200 micron channel, 5mm width, FC-72, q=23 W/cm^2 and G=195 kg/m^2-s.

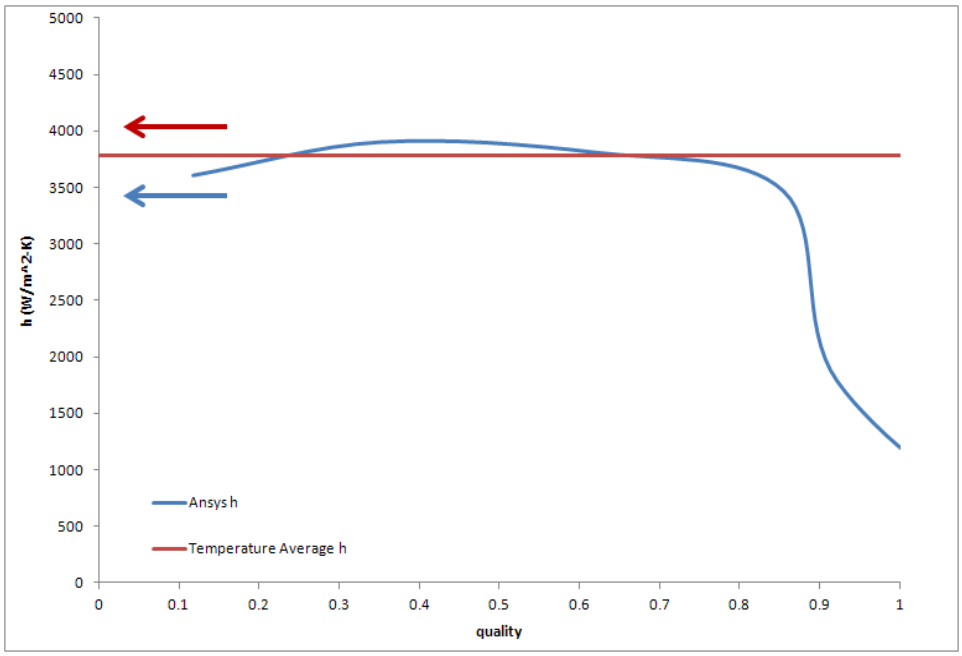

Figure 100: Two-phase coefficient for 200 micron channel, 5mm width, FC-72, q=23 W/cm^2 and G=292 kg/m^2-s.

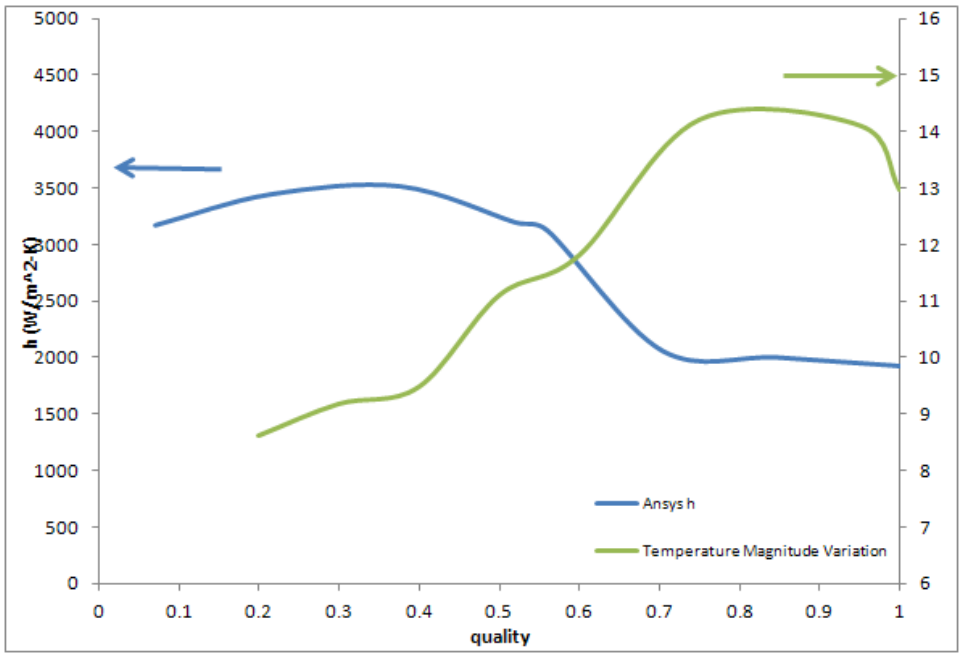

Figure 101: Two-phase coefficient for 200 micron channel, 5mm width, FC-72, q=28 W/cm^2 and G=390 kg/m^2-s.

the data for q=28 W/cm^2 and G=390 kg/m^2-s, which transitions at 18% quality. The dependence of the two-phase heat transfer coefficient on local dryout and recovery is shown for this case. This case shows a skewed version of the characteristic M-shaped curve discussed earlier, and shows how the local dryout and recovery could be one factor driving the distinct M-shape.

Microgap Cooler: 200 microns, FC-72, and width=10mm

Figure 102 is the graphed data for q=23 W/cm^2 and G=195 kg/m^2-s, which transitions at 36% quality. The trend of local dryout and recovery influencing the two-phase heat transfer is not supported by these results and not temperature magnitude is graphed. The intrinsic M-shaped curve is not apparent, but some of the trend of a peak value followed by a decreasing two-heat heat transfer coefficient is present. Figure 103 is the graphed data for q=23 W/cm^2 and G=292 kg/m^2-s, which transitions at 24% quality. The expected M-shaped curve is present, with a degradation of the two-phase heat transfer coefficient occurring at 75% quality. The figure shows the relationship between the magnitude of the fluctuations and the behavior of the two-phase heat transfer potentially being indirect. Comparison with similar experimental conditions with 5 mm width reveals an advantage with increased width on channel performance. Figure 104 shows the general agreement necessary to consider an ANSYS inverse calculation to have converged.

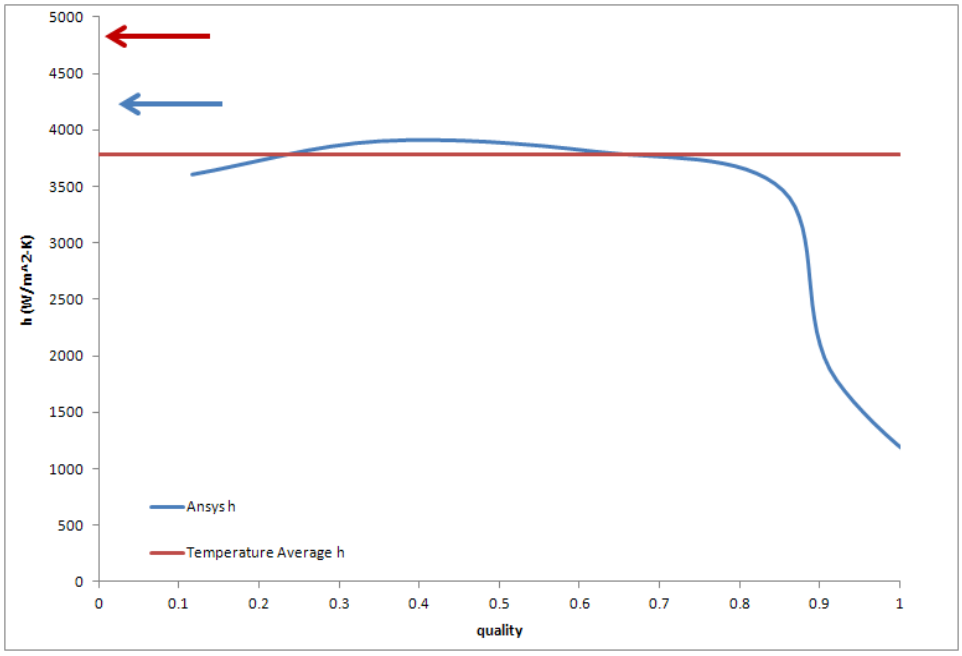

Figure 102: Two-phase coefficient for 200 micron channel, 10mm width, FC-72, q=23 W/cm^2 and G=195 kg/m^2-s.

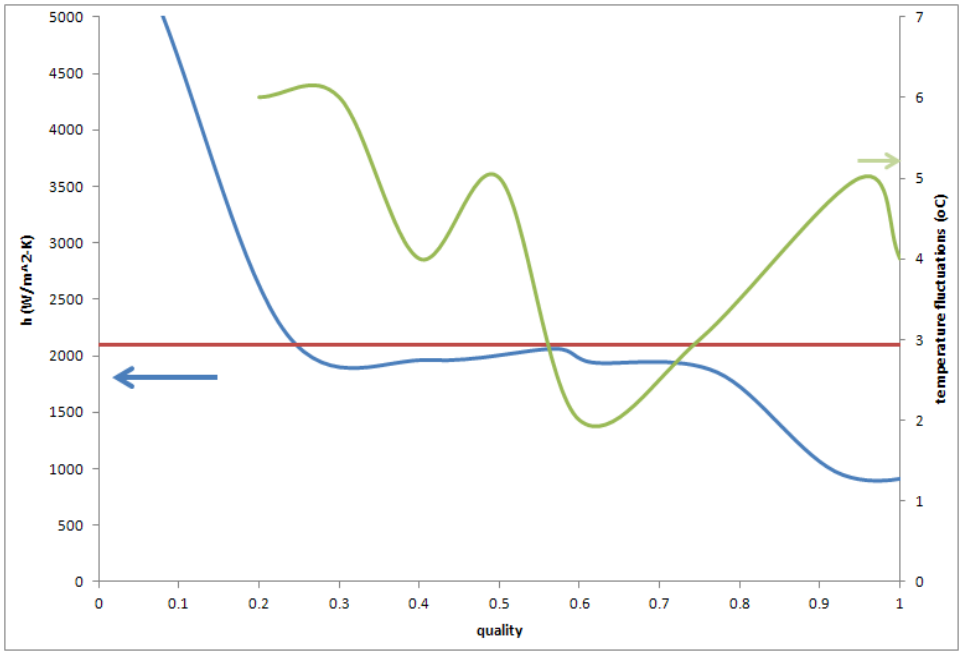

Figure 103: Two-phase coefficient for 200 micron channel, 10mm width, FC-72, q=23 W/cm^2 and G=292 kg/m^2-s.

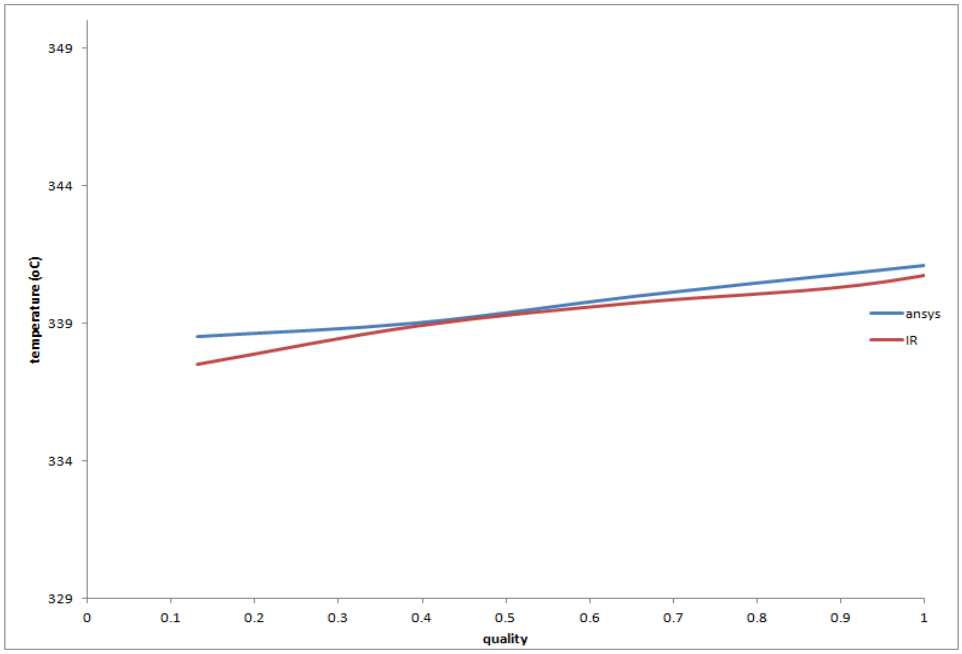

Figure 104: Numerically determined microgap temperatures for 200 micron channel, 10mm width, FC-72, q=28 W/cm^2 and G=195 kg/m^2-s.

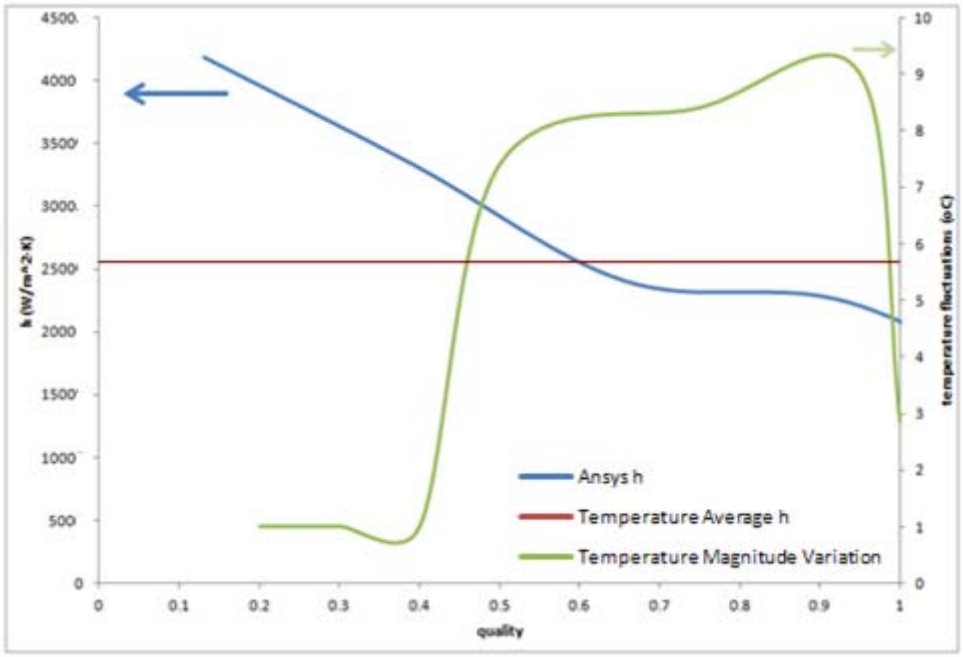

Figure 105: Two-phase coefficient for 200 micron channel, 10mm width, FC-72, q=28 W/cm^2 and G=195 kg/m^2-s.

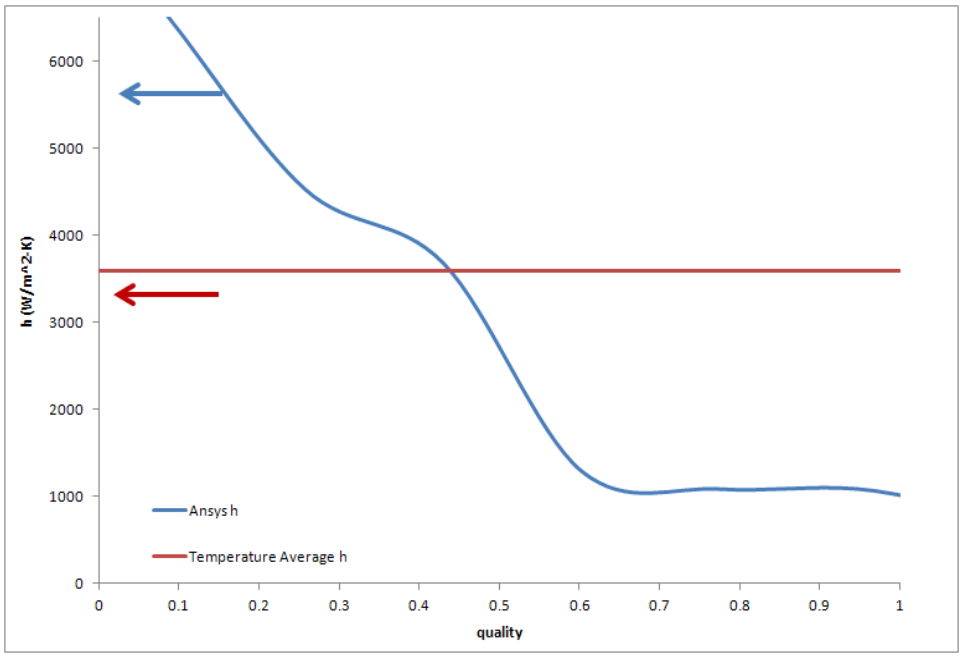

Figure 106: Two-phase coefficient for 200 micron channel, 10mm width, FC-72, q=28 W/cm^2 and G=292 kg/m^2-s.

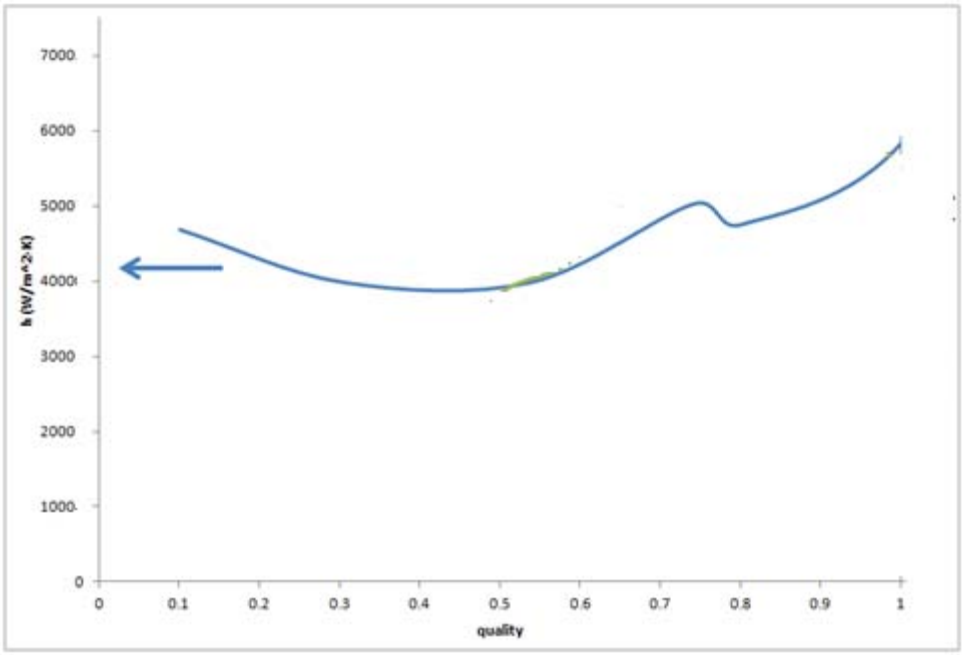

Figure 107: Two-phase coefficient for 200 micron channel, 10mm width, FC-72, q=40 W/cm^2 and G=390 kg/m^2-s.

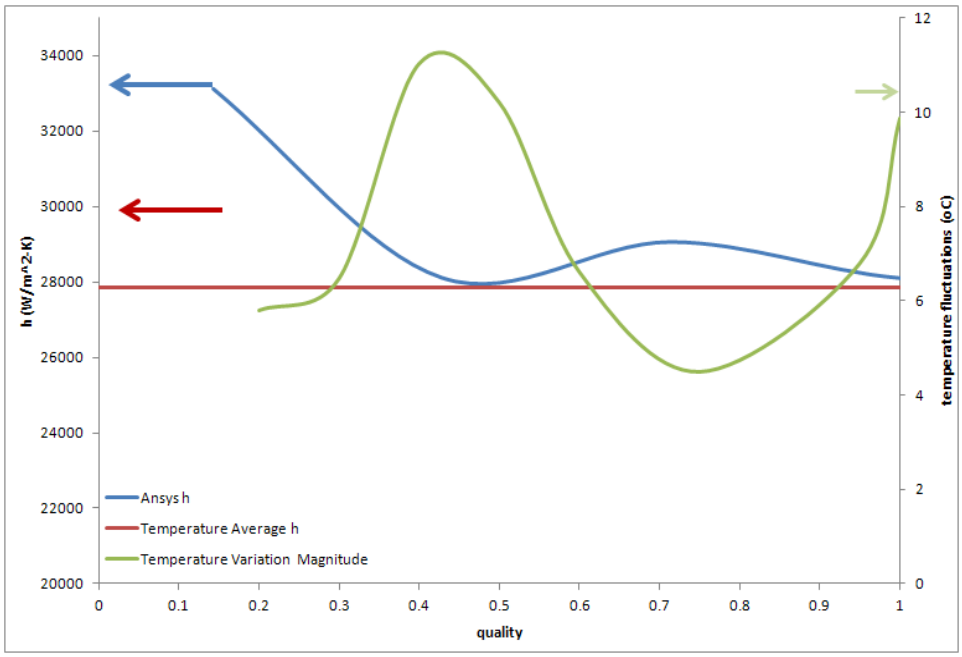

Figure 108: Two-phase coefficient for 200 micron channel, 10mm width, FC-72, q=70 W/cm^2 and G=490 kg/m^2-s.

Figure 105 shows the two-phase heat transfer coefficients for q=28 W/cm^2 and G=195 kg/m^2-s graphed with the temperature fluctuation magnitude versus quality. The intrinsic M-shaped curve is present matching literature, with the transition to the annular regime beginning at 36% quality for these experimental conditions. As the fluctuations increase the two phase heat transfer decreases, thus as the local dryout and recovery is detrimental to the local thermal transport. Figure 106 shows the curve of two-phase heat transfer coefficients in the channel with the same heat flux but increased mass flux from the previous case. The overall heat transfer for the higher mass flux is greater than the previous cause, as expected. Parts of the M-shaped trend of the two-phase heat transfer values is represent, with high initial values degrading until the values plateau at 65% quality versus peaking then degrading further. Figure 107 shows the data for q=40 W/cm^2 and G=390 kg/m^2-s transitioning to annular at 18% quality. This case shows the initial stages of the M-shaped curve that is expected, have a second peak occurring at 73% quality. However, instead of continuing to decrease after 73% this case shows a recovery and eventual increase in the two-phase heat transfer coefficient. Since there is no distinct relationship for this case with the local dryout and recovery, it is most likely that the complex physics of 2-D, 3-D, and lateral waves has generated a situation permitting for increasing h vales. Figure 108 shows the comparative graph with a higher flux case =70 W/cm^2 and G=490 kg/m^2-s, and repeats the M-

shaped trend and the inverse relationship between the temperature fluctuation magnitudes with the two-phase heat transfer coefficients. The magnitude of fluctuations is comparable to those shown in Figure 106, suggesting that a maximum is inherent due to fluid properties.

Microgap Cooler: 200 microns, FC-72, and width=20mm

Figure 109 shows the data for q=23 W/cm^2 and G=195 kg/m^2-s, which transitions to annular at 36% quality. There is no significant temperature fluctuations for this case, thus the relationship between the two-phase heat transfer coefficient and local and dryout recovery is not supported. In general, the two-phase heat transfer coefficient shows the expected M-shaped found in literature, with a secondary peak occurring at unity. Since there are no temperature fluctuations, this shows that natural trends the system. This is more apparent in Figure 110, which also have no significant temperature fluctuations. This would reveal that the system has an initial downturn due to transition between flow regimes, recovers, but is ultimately dampened by instabilities. When such instabilities are driven by local dryout and recovery, it significantly affects the performance.

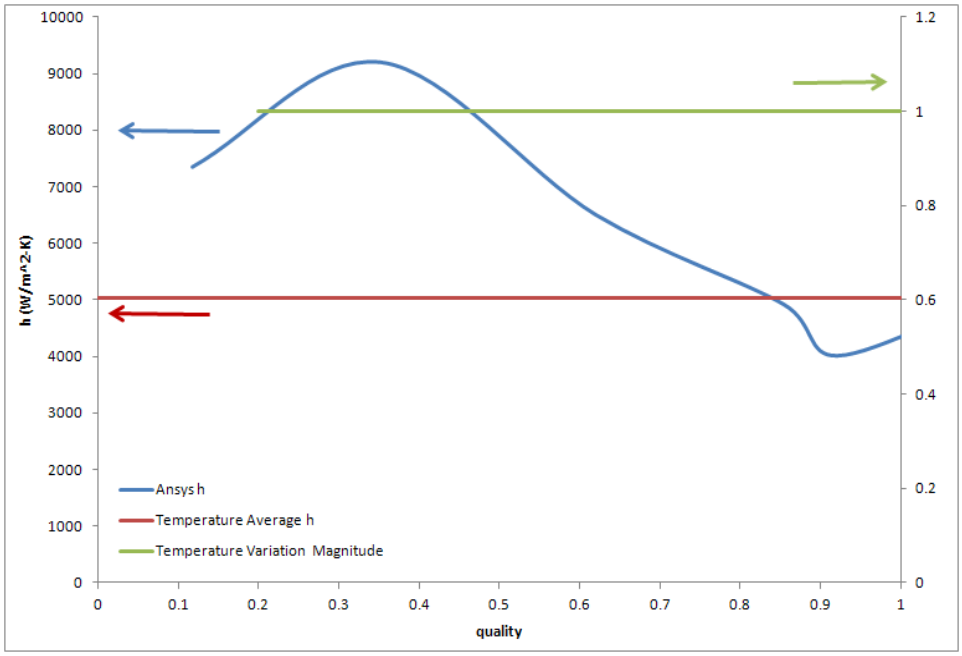

Figure 109: Two-phase coefficient for 200 micron channel, 20mm width, FC-72, q=23 W/cm^2 and G=195 kg/m^2-s.

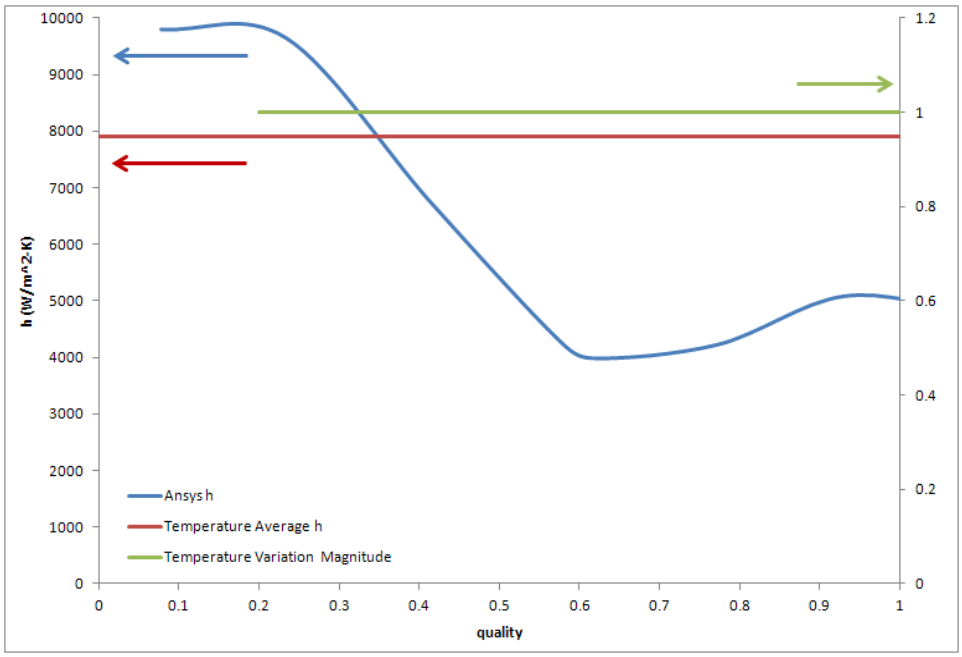

Figure 110: Two-phase coefficient for 200 micron channel, 20mm width, FC-72, q=23 W/cm^2 and G=292 kg/m^2-s.

7.1.2 Microgap Channel Height at 300 microns

Microgap Cooler: 300 microns, FC-72, and width=5mm

Figure 111 shows the two-phase heat transfer coefficients for q=23 W/cm^2 and G=195 kg/m^2-s, which transitions to annular at 36% quality. The intrinsic M-shaped curve is seen, but no distinct relationship between temperature fluctuations and channel performance is observed. Comparison with similar conditions with 200 micron gap shows no distinct advantage for increasing the gap height due to the complex behavior of the channels. Figure 112 shows the data for q=23 W/cm^2 and G=292 kg/m^2-s, which transitions at 24% quality. The M-shaped trend expected is seen in the lower qualities of the channel; however the degradation of the two-phase heat transfer coefficient (starting at 75%) is recovered through natural processes in the channel.

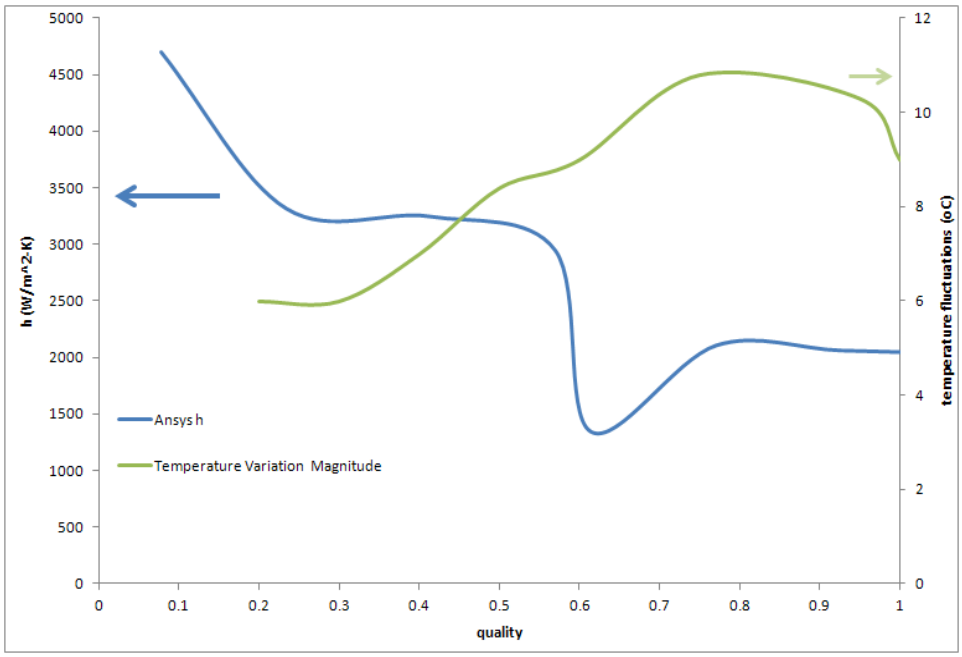

Figure 111: Two-phase coefficient for 300 micron channel, 5mm width, FC-72, q=23 W/cm^2 and G=195 kg/m^2-s

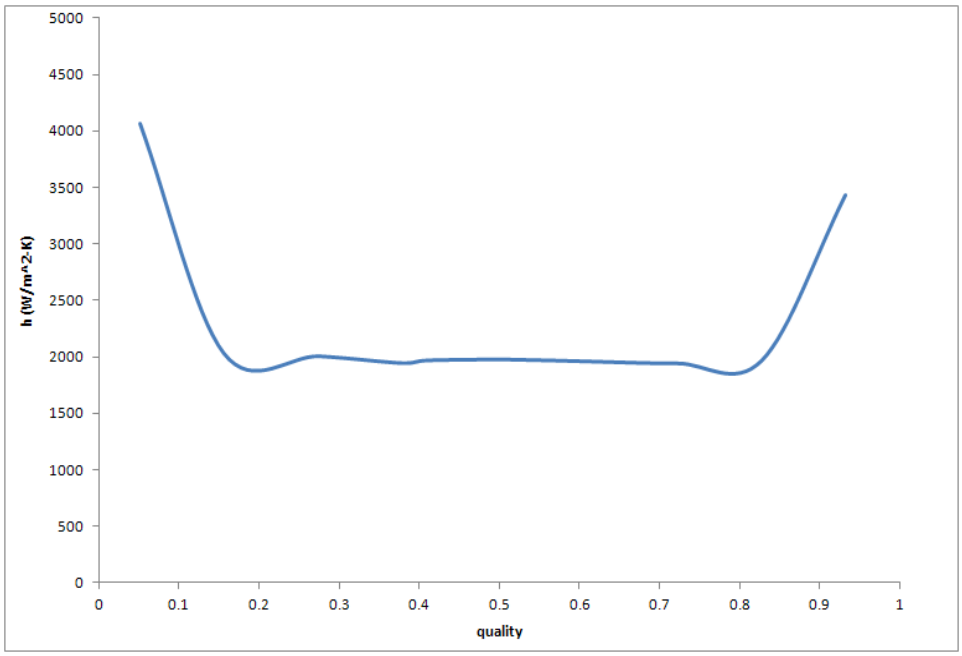

Figure 112: Two-phase coefficient for 300 micron channel, 5mm width, FC-72, q=23 W/cm^{2}and G=292 kg/m^2-s

Microgap Cooler: 300 microns, FC-72, and width=10mm

Figure 113 shows the channel performance for q=23 W/cm^2 and G=195 kg/m^2-s, which transitions at 36% quality. The M-shaped trend of the two-phase heat transfer coefficient is presented with a secondary peak occurring at 75% quality. Overall the performance is improved to the previous case with 5mm, this reveals once again a potential advantage to increased width since it dampens out the fluctuations.

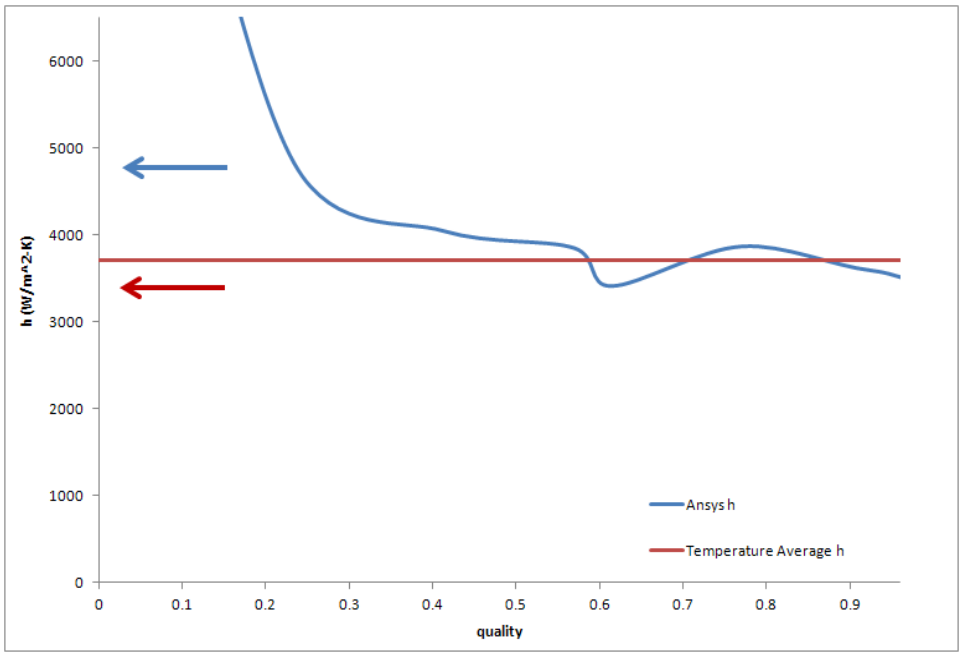

Figure 113: Two-phase coefficient for 300 micron channel, 10mm width, FC-72, q=23 W/cm^2 and G=195 kg/m^2-s

Microgap Cooler: 300 microns, FC-72, and width=20mm

Figure 114 shows the data for q=23 W/cm^2 and G=195 kg/m^2-s transitioning to annular at 36% quality. The intrinsic M-shaped curve appears for this case without any distinct fluctuations occurring within the channel. Figure 115 shows the temperature matching of a typical case that occurs before the two-phase heat transfer coefficients are accepted. Figure 116 shows the performance for q=23 W/cm^2 and G=292 kg/m^2-s, which transitions at 24% quality. This performance is not influenced temperature fluctuations, but displays the desired upturn as quality approaches unity. Comparison with the 10 mm case reveals a distinct advantage in

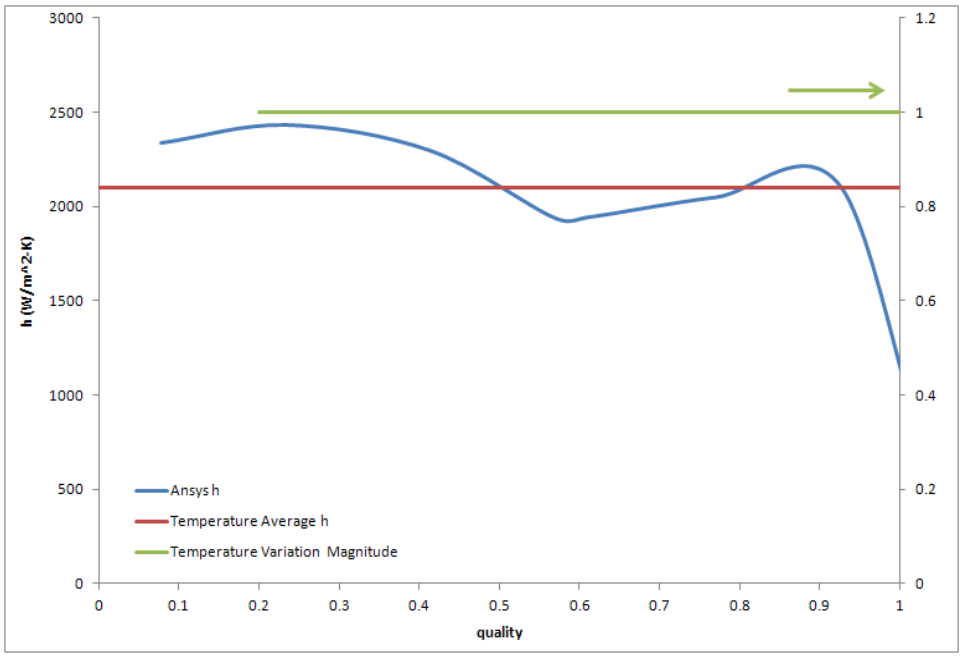

Figure 114: Two-phase coefficient for 300 micron channel, 20mm width, FC-72, q=23 W/cm^2 and G=195 kg/m^2-s

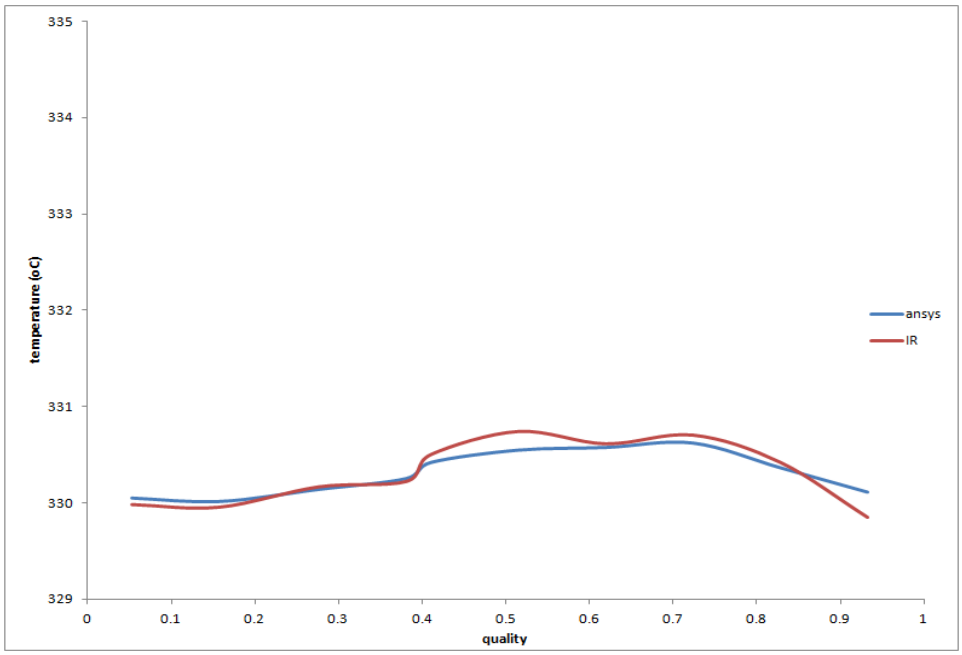

Figure 115: Temperature comparison for 300 micron channel, 20mm width, FC-72, q=23 W/cm^2 and G=292 kg/m^2-s

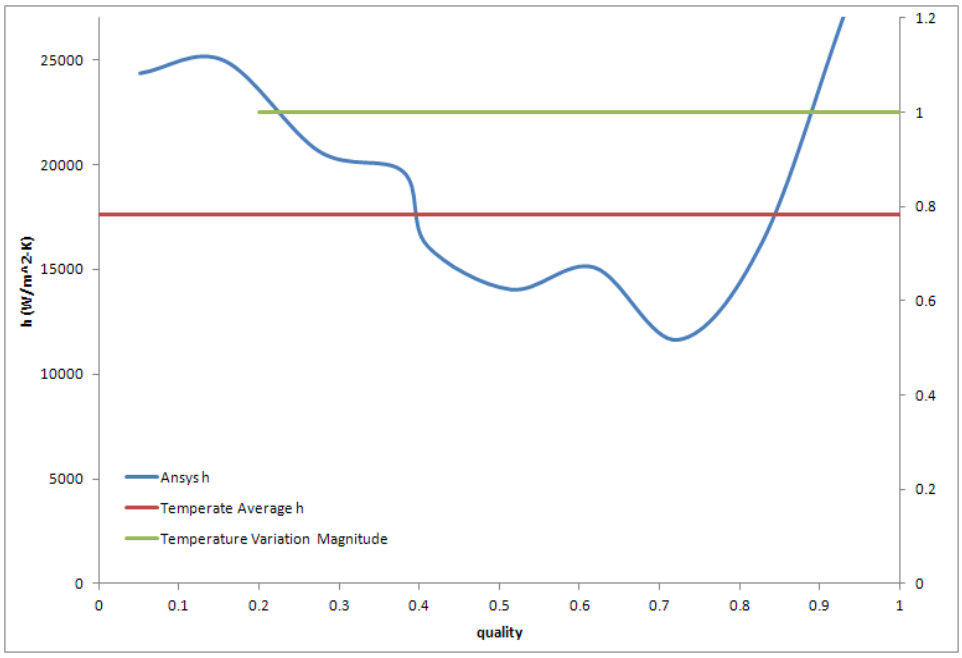

Figure 116: Two-phase coefficient for 300 micron channel, 20mm width, FC-72, q=23 W/cm^2 and G=292 kg/m^2-s

performance with increased width. Further analysis reveals a similar benefit in performance over the 5 mm case with similar experimental conditions. Figure 116 two-phase heat transfer values follow the expected M-shape trend, but are larger than expected due to the low average temperature observed over the ten local zones. The average temperature throughout the zones was only 1 C above saturation, creating large heat transfer values. Although such performance would be desirable, the experimental uncertainty for IR temperature measurements is +/- 2 C, thus Figure 116 is shown for completeness to the study but would have to be further securitized to determine the validity of this particular case.

Microgap Cooler: 300 microns, HFE-7100, and width=10mm

Figure 117 shows the performance for q=28 W/cm^2 and G=195 kg/m^2-s, which transitions at 36% quality. Comparison with the case utilizing FC-72 shows an advantage in using HFE-7100 as the working fluid due most likely to the increased latent heat. The relationship between the performance and local dryout and recovery is more ambiguous for this case.

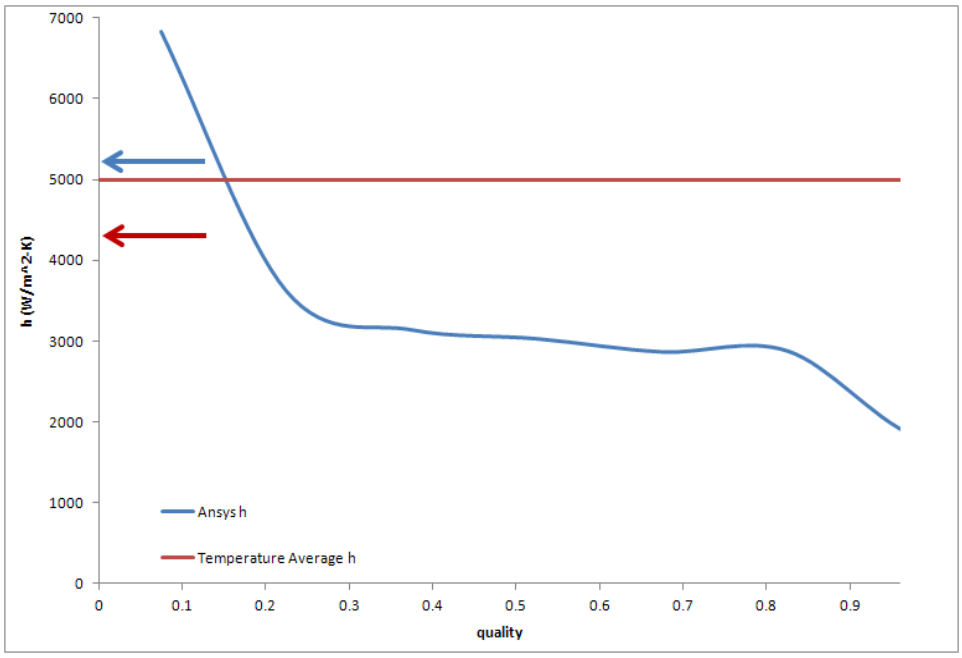

Figure 117: Two-phase coefficient for 300 micron channel, 10mm width, HFE-7100, q=28 W/cm^2 and G=195 kg/m^2-s

7.1.3 Microgap Channel Height at 400 microns

Microgap Cooler: 400 microns, FC-72, and width=10mm

Figure 118 shows the two-phase heat transfer coefficients for q=40 W/cm^2 and G=390 kg/m^2-s, which transitions to annular at 18% quality. The general inverse relationship between performance and local dryout and recovery is observed, further supporting a potential relationship between local dryout and recovery and performance. The desired upturn as quality approaches unity is seen, and the general M-shaped curve is observed. The case shows a secondary peak occurring at 50% quality, with decreasing values being recovered at 70% quality. Although a relationship is observed between the temperature magnitudes and two-phase heat transfer values, the physics governing the channel is complex and not limited to one parameter. Comparison of aspect ratios reveals similar values for two-phase heat transfer coefficients, with different local behavior. As stated in earlier sections, since the effects of width are delayed with larger gaps, some influence due to the aspect ratio is present.

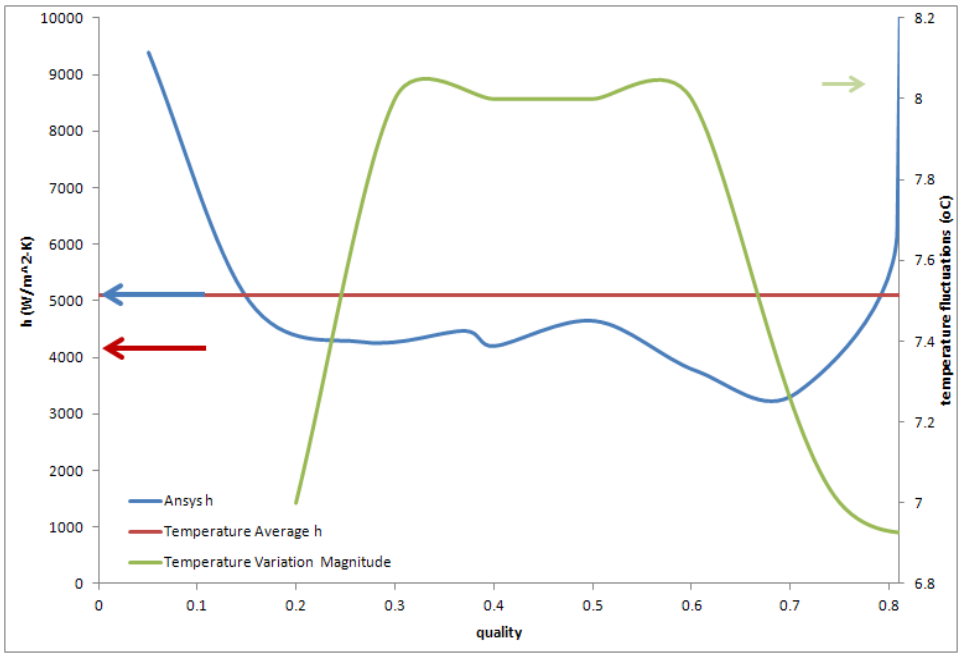

Figure 118: Two-phase coefficient for 400 micron channel, 10mm width, FC-72, q=40 W/cm^2 and G=390 kg/m^2-s very good h and delta T curve but values seem too high

Microgap Cooler: 400 microns, FC-72, and width=20mm

Figure 119 shows the data for q=23 W/cm^2 and G=292 kg/m^2-s, which transition at 24% quality. The relationship between temperature fluctuations and performance is unobservable due to a lack of significant fluctuations in this case. The performance is significantly better than any previous case, and shows the M-shaped curve found in literature, with the secondary peak occurring at 40% quality and being recovered at 52% quality to values comparable to phase change heat transfer values near quality of zero.

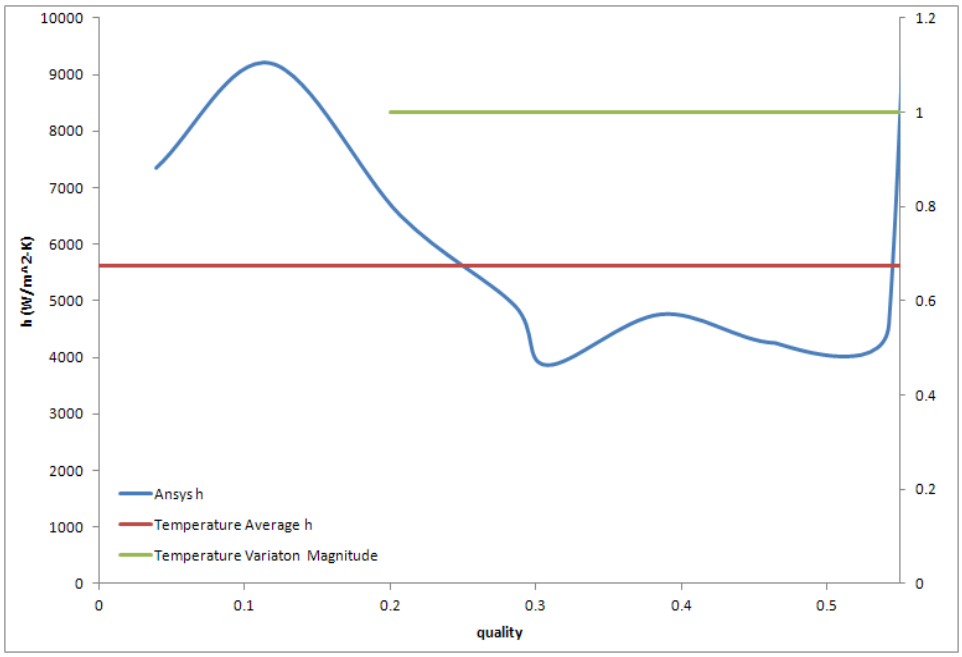

Figure 119: Two-phase coefficient for 400 micron channel, 20mm width, FC-72, q=23 W/cm^2 and G=292 kg/m^2-s

CHAPTER 8

8.1 Lateral Temperature Variation and Edge Analysis

This section outlines the lateral and edge data for all the channels with various experimental conditions. Data was collected at various positions near the edge and away from the center to analyze the behavior of the channel and any effects that may exist. Figure 120 shows the reference edge, bottom edge, used to note the location being examined. Two analyses

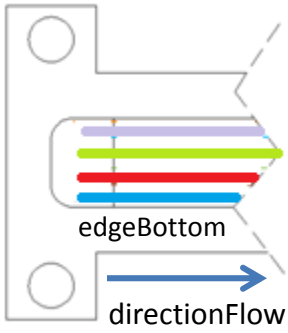

Figure 120: Channel diagram denoting bottom edge reference for lateral variation and edge analysis.

were performed on the various cases presented: (1) examining the axial temperature profile of four locations near the edge and away from the center line and (2) temporal temperature fluctuations at those four lateral locations with 75% quality (where appropriate another quality is used). The axial temperature profile and the temporal temperature variation analyses were performed as previously described. Additionally, for a few cases the orientation effect is examined through comparison of these two analyses for various orientation angles (as seen in Figure 38 and discussed previously).

8.1.1 Microgap Channel Height at 200 microns

Microgap Cooler: 200 microns, FC-72, and width=5mm

This section outlines the lateral temperature variations and edge analysis for 200 micron gap height, 5 mm channel width, and 35 mm channel length using FC-72 as the working fluid. Figure 121 shows the axial temperature profile for q=23 W/cm^2, and G=195 kg/m^2-s at four

locations laterally across the channel. For this low heat flux and low mass flux case, the lateral temperature variations are not significant throughout the channel, and modest when present. Figure 122 is the temporal temperature variations for the previous case with the same lateral locations, but at fixed axial location where 75% quality occurs. Although the inverse calculation of the two-phase heat transfer coefficient averages in the edge effect on the performance, this analysis allows for examination of this behavior. Since the magnitude of the temperature fluctuations is comparable at all four locations, as well as the average temperature, there is no significant edge effect observable for these experimental conditions for this channel. Figure 123 and Figure 124 display the axial temperature profile and the temporal temperature variations for q=28 W/cm^2, and G=292 kg/m^2-s, respectively. The graphs shows the same lack disparities of the lateral axial temperature profiles and temperature fluctuations, supporting the previous conclusions that for this channel the edge has no significant effect. Figure 124 and Figure 125

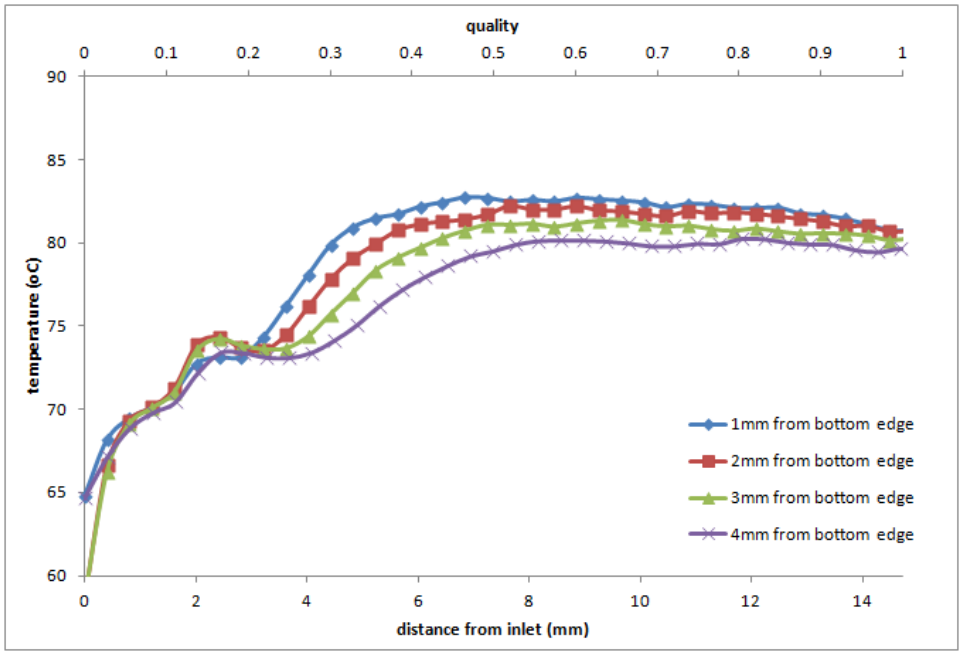

Figure 121: Axial temperature profile for 200 micron, 5mm width, FC-72, q=23 W/cm^2, and G=195 kg/m^2-s.

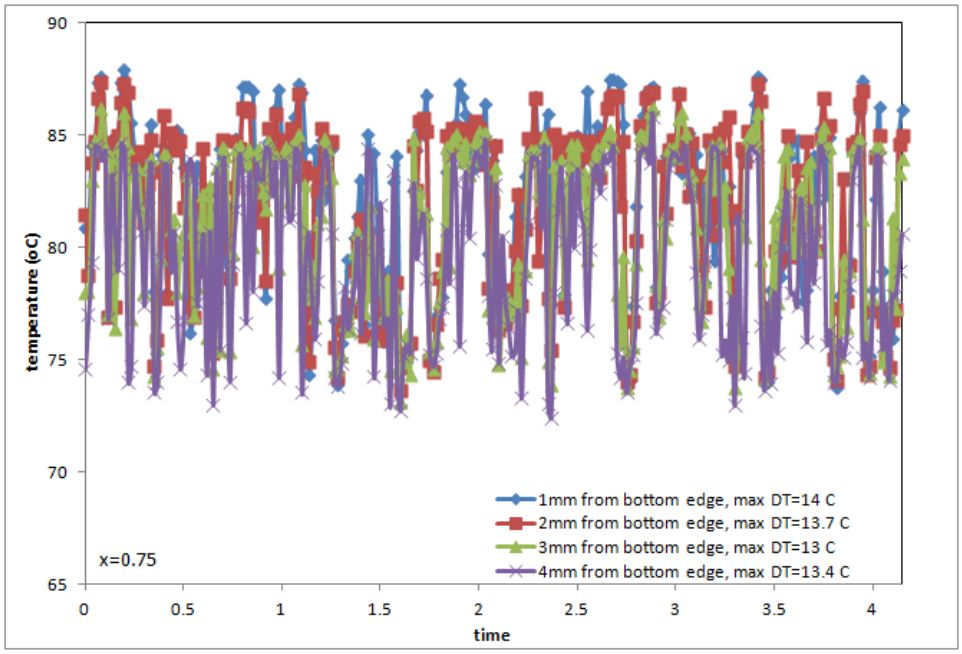

Figure 122: Temporal temperature variations for 200 micron, 5mm width, FC-72, q=23 W/cm^2, and G=195 kg/m^2-s.

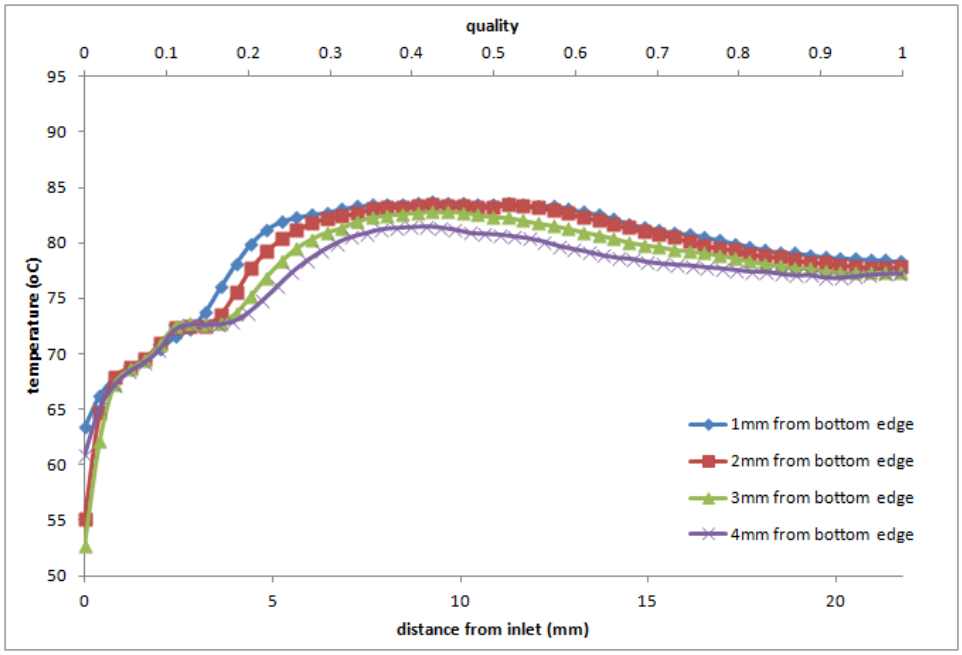

Figure 123: Axial temperature profile for 200 micron, 5mm width, FC-72, q=28 W/cm^2, and G=292 kg/m^2-s.

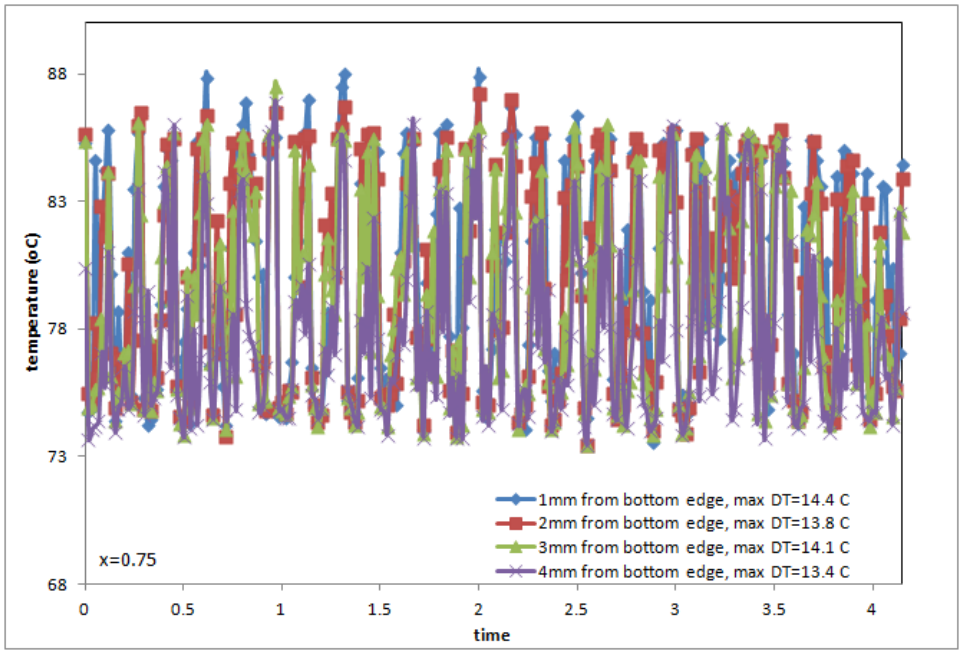

Figure 124: Temporal temperature variations for 200 micron, 5mm width, FC-72, q=28 W/cm^2, and G=292 kg/m^2-s.

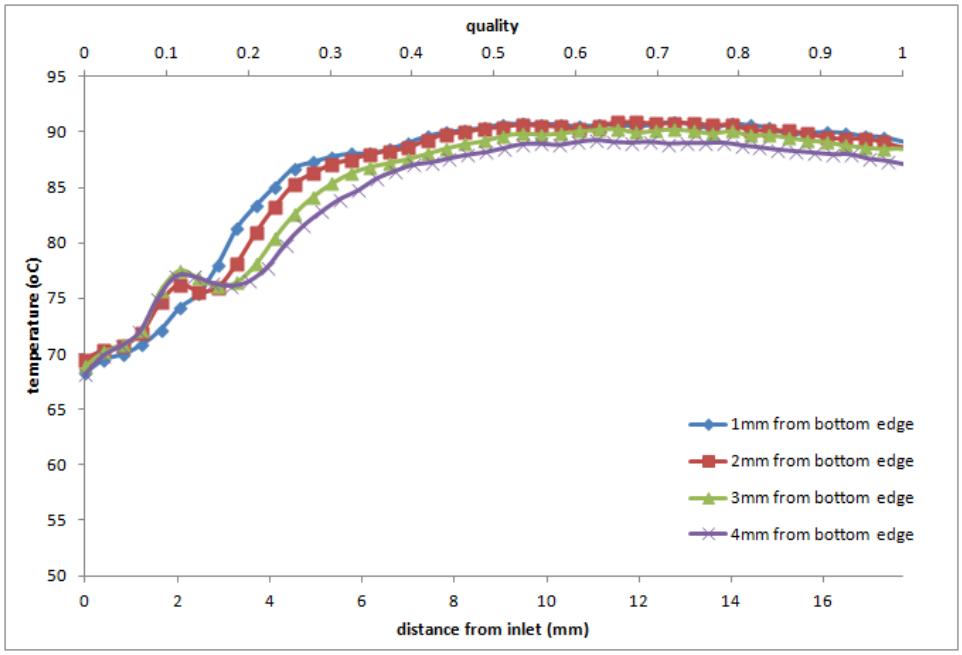

Figure 125: Axial temperature profile for 200 micron, 5mm width, FC-72, q=28 W/cm^2, and G=390 kg/m^2-s.

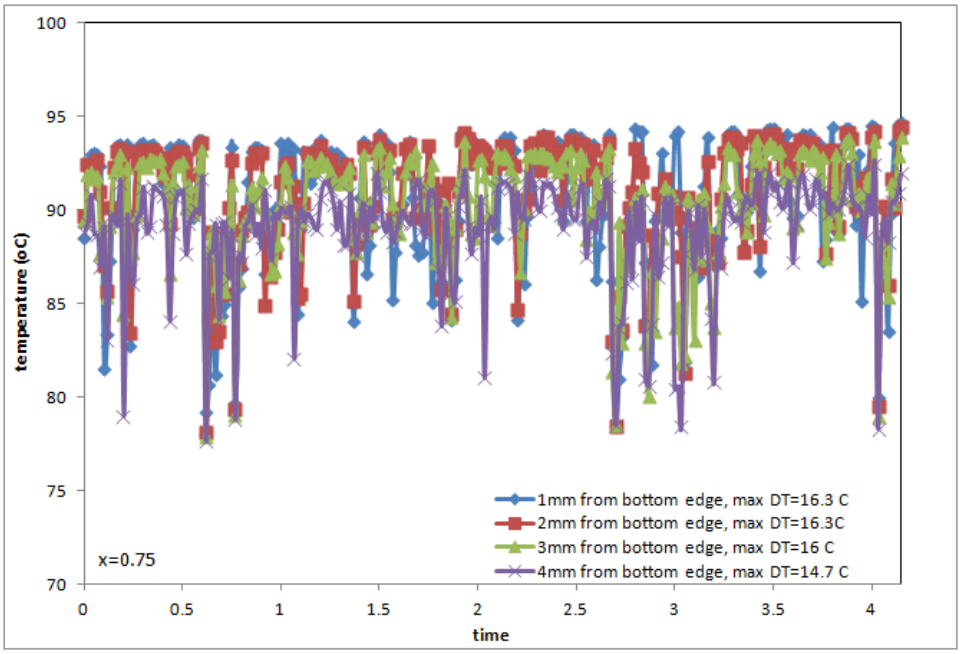

Figure 126: Temporal temperature variations for 200 micron, 5mm width, FC-72, q=28 W/cm^2, and G=390 kg/m^2-s.

show the same analysis performed on data with q=28 W/cm^2 and G=390 kg/m^2-s. Examination of the graphs reveals that the edge does not play a role in lateral axial temperature profiles or the magnitude of the temperature fluctuations. Furthermore, comparison of Figure 121 and Figure 123 demonstrates a potential mass flux dependence since the little discrepancy in lateral temperatures disappears with increased mass flux. Thus, with the temperature magnitudes and the average temperatures being comparable laterally across the channel no change in performance is seen.

Microgap Cooler: 200 microns, FC-72, and width=10mm

Figure 127 shows the lateral axial temperature profile for q=23 W/cm^2 and G=195 kg/m^2-s, which displays some notable discrepancies in lateral temperatures. Figure 128 shows similar disparities in lateral axial temperature profiles, suggesting with increased width the edge becomes significant to the channel behavior. This is supported in Figure 129, which reveals a significant difference in temperature fluctuations in the lateral direction. Thus, locally the two-phase heat transfer coefficient would be different. Figure 130 shows the lateral axial temperature variations for the same experimental conditions as the previous case, but with the orientation angle being 45 degrees. Distinct lateral variations occur as large as 15 C within the channel,

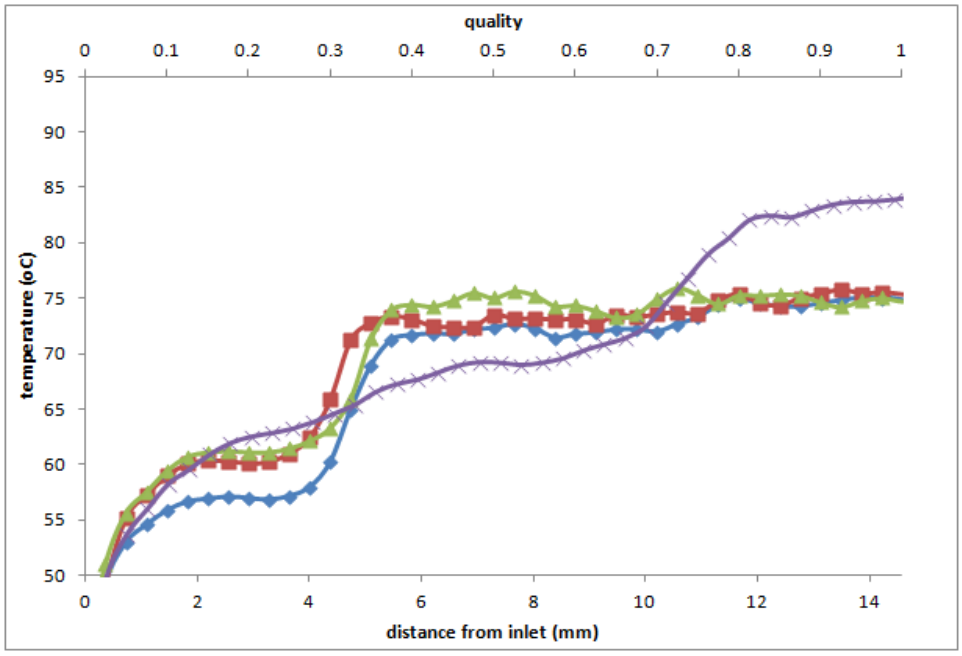

Figure 127: Axial temperature profile for 200 micron, 10 mm width, FC-72, q=23 W/cm^2, and G=195 kg/m^2-s.

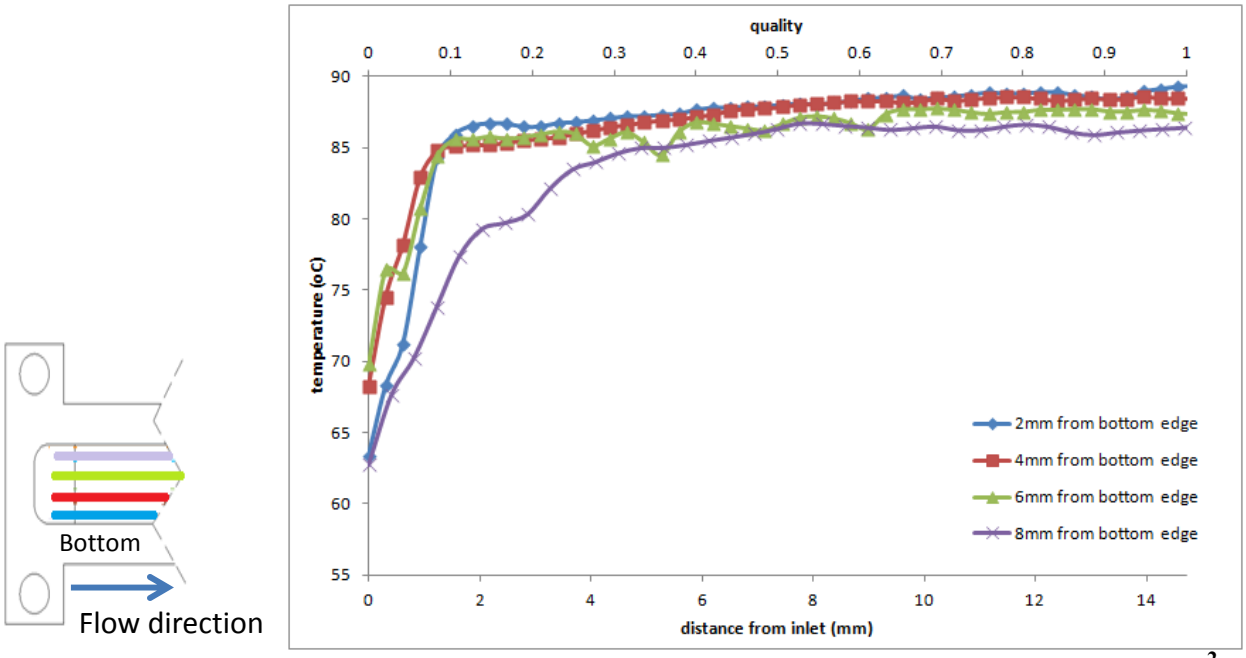

Figure 128: Axial temperature profile for 200 micron, 10 mm width, FC-72, q=28 W/cm^2, and G=195 kg/m^2-s.

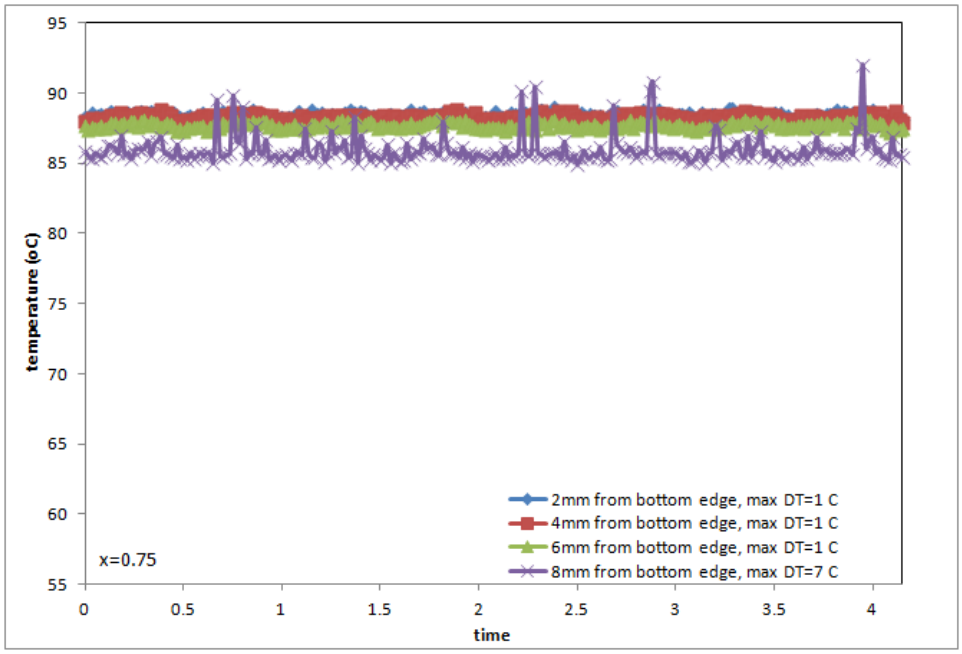

Figure 129: Temporal temperature variations for 200 micron, 10 mm width, FC-72, q=28 W/cm^2, and G=195 kg/m^2-s.

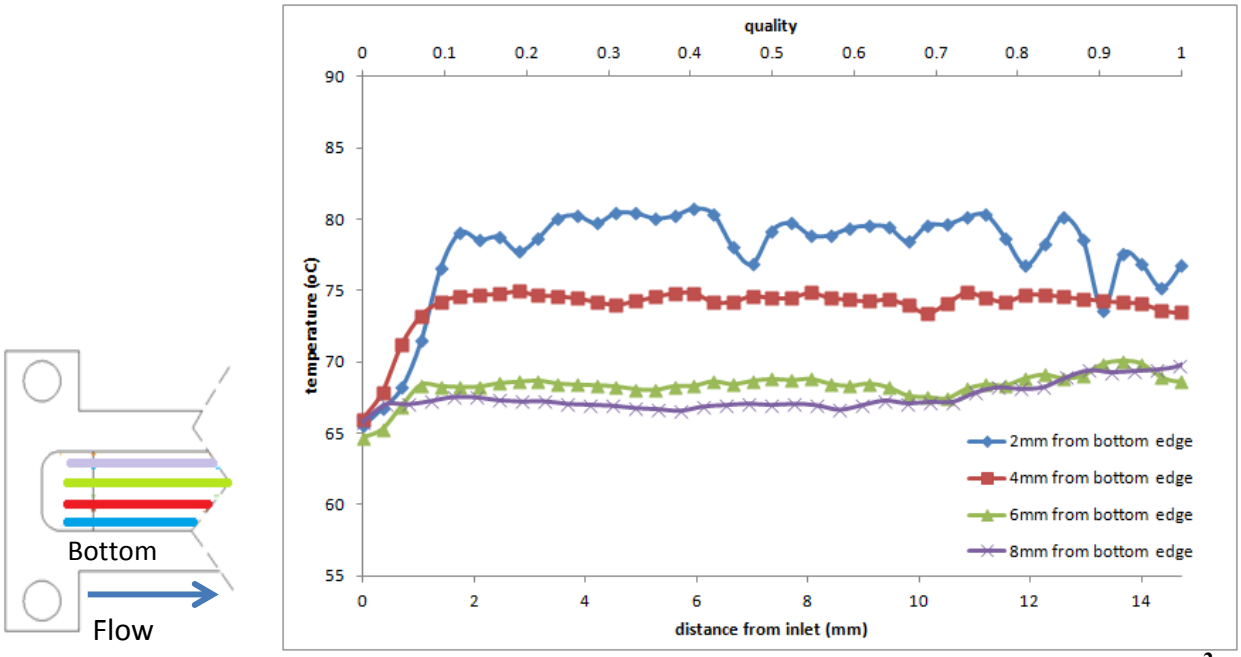

Figure 130: Axial temperature profile for 200 micron, 10 mm width, FC-72, q=28 W/cm^2, G=195 kg/m^2-s, and 45 degrees.

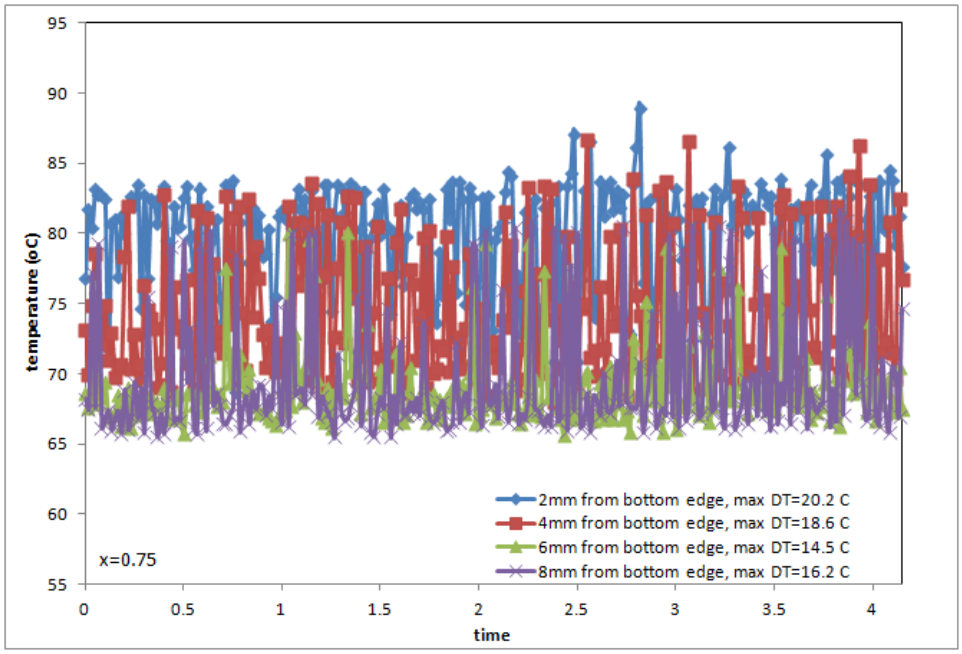

Figure 131: Temporal temperature variations for 200 micron, 10 mm width, FC-72, q=28 W/cm^2, G=195 kg/m^2-s., and 45 degrees.

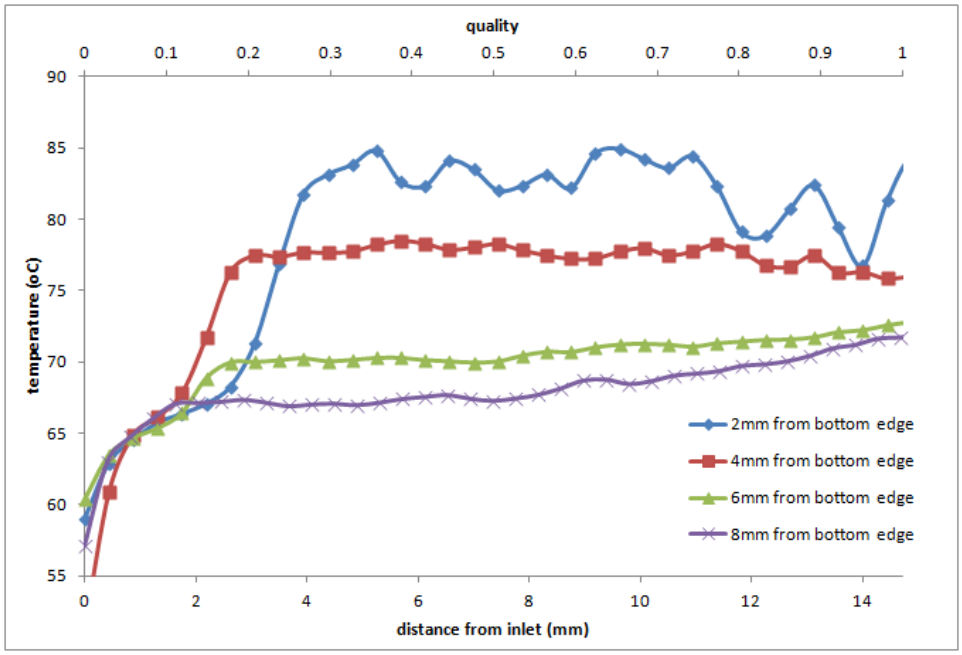

Figure 132: Axial temperature profile for 200 micron, 10 mm width, FC-72, q=28 W/cm^2, G=195 kg/m^2-s, and 90 degrees.

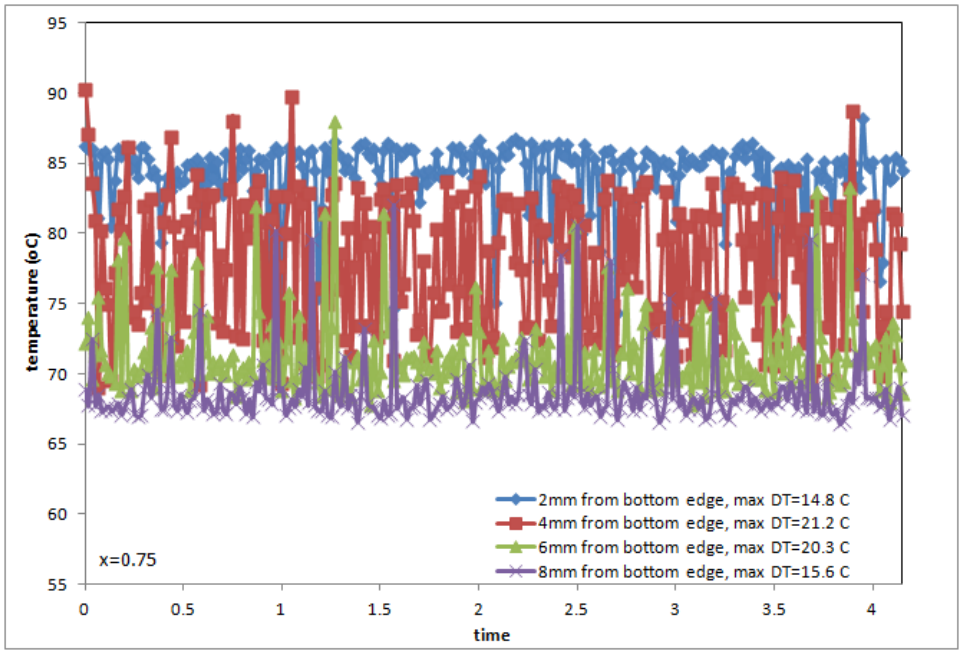

Figure 133: Temporal temperature variations for 200 micron, 10 mm width, FC-72, q=28 W/cm^2, G=195 kg/m^2-s., and 90 degrees.

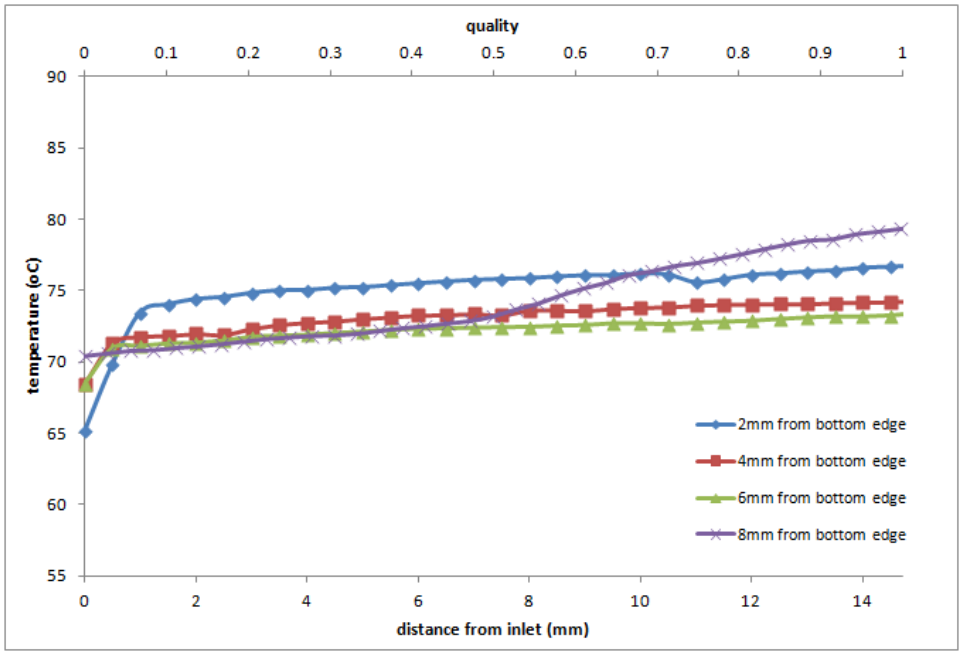

Figure 134: Axial temperature profile for 200 micron, 10 mm width, FC-72, q=28 W/cm^2, G=292 kg/m^2-s, and 90 degrees.

showing that orientation can have a significant effect on channel behavior. This is further supported by Figure 131, which shows differences in the temporal temperature fluctuations.

Thus, the lateral channel behavior at fixed axial location varies greatly with variation of orientation angle. This is even more pronounced for 90 degrees, shown in Figure 132 and Figure 133, where lateral variations of up to 20 C exist. Although the relationship between orientation and channel behavior is notable, with slight increase in mass flux the effect becomes negligible as seen in Figure 134. Figure 134 shows the lateral variations for q=28 W/cm^2, G=292 kg/m^2-s, and 90 degrees with little lateral variations observed. Thus, the mass flux continues to dampen out the edge effect as well as the orientation.

Microgap Cooler: 200 microns, FC-72, and width=20mm

This section shows the lateral temperature variations and temporal temperature fluctuations for 200 micron gap height, 20 mm width, and 35 mm channel length with FC-72 working fluid. Figure 135 shows the lateral temperature variations axially across the channel for q=23 W/cm^2, and G=195 kg/m^2-s, which shows modest lateral differences in the channel. Figure 136 shows the distinct temporal variations discrepancies which would greatly affect the local channel performance. Thus, again it is observed that channel width influences the lateral variations and the edge effect on the channel behavior.

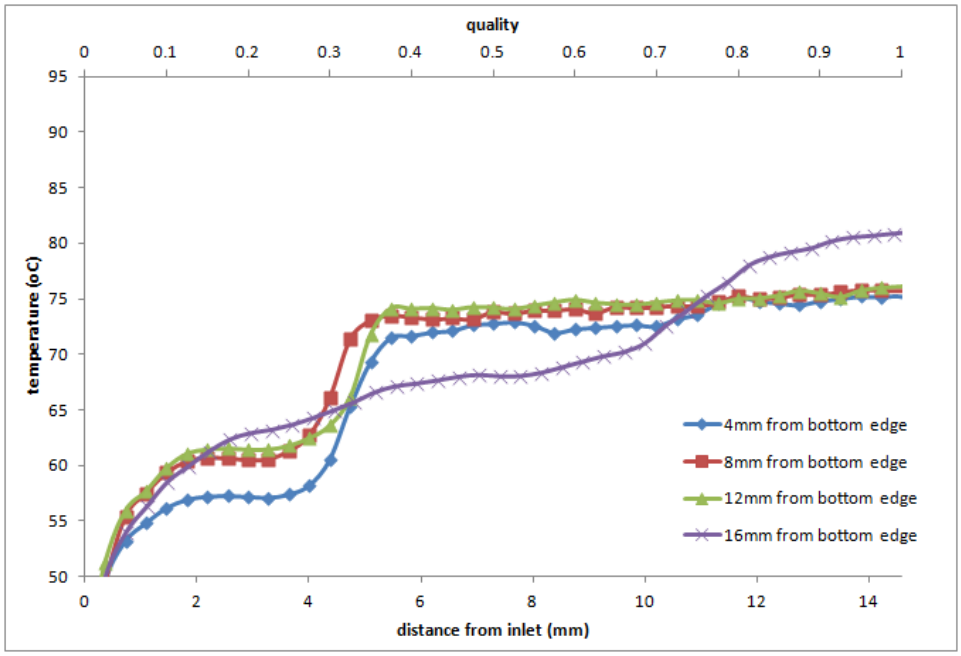

Figure 135: Axial temperature profile for 200 micron, 20 mm width, FC-72, q=23 W/cm^2, and G=195 kg/m^2-s.

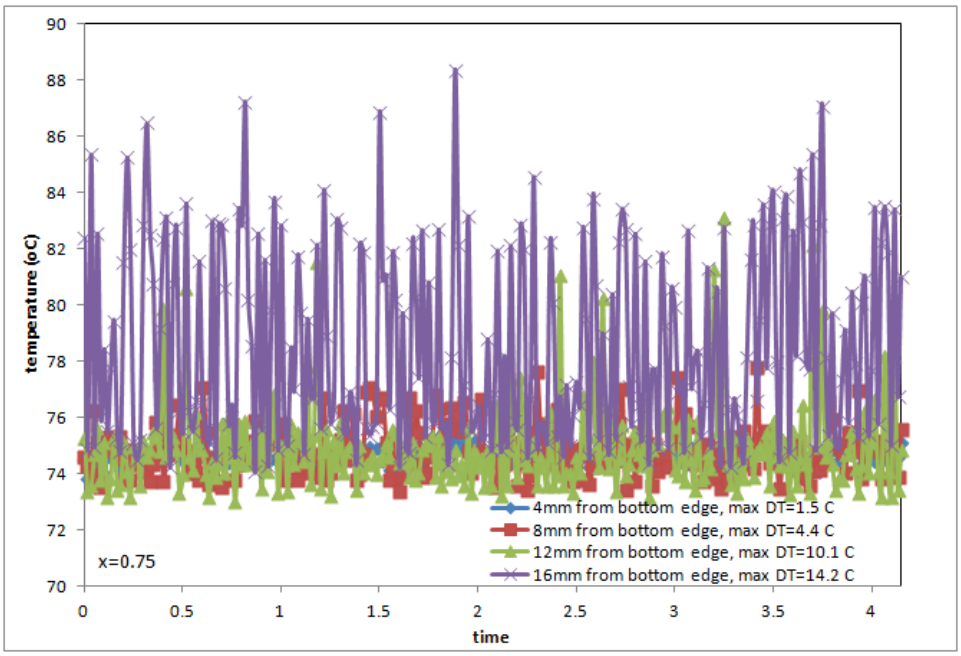

Figure 136: Temporal temperature variations for 200 micron, 20 mm width, FC-72, q=23 W/cm^2, and G=195 kg/m^2-s.

8.1.2 Microgap Channel Height at 300 microns

Microgap Cooler: 300 microns, FC-72, and width=5mm

Figure 137- Figure 140 shows the lateral temperature variations and the temporal temperature fluctuations for q=23 W/cm^2, and G=195 kg/m^2-s and q=23 W/cm^2, and G=292 kg/m^2-s. For either case little or no significant difference in lateral behavior is observed, supporting previous data trends of width influencing the lateral effect. However, the previously discussed dependence on mass flux is not seen for this channel. Figure 141 and Figure 142 show a distinct lateral difference for the location 1mm from bottom edge. This location has distinct lower average temperature and smaller temperature fluctuation magnitude. This would suggest that locally the performance for this part of the channel is significantly better than the lateral counterparts. Since the gap height was increased, the lateral effect would also appear to be influenced by this geometric parameter.

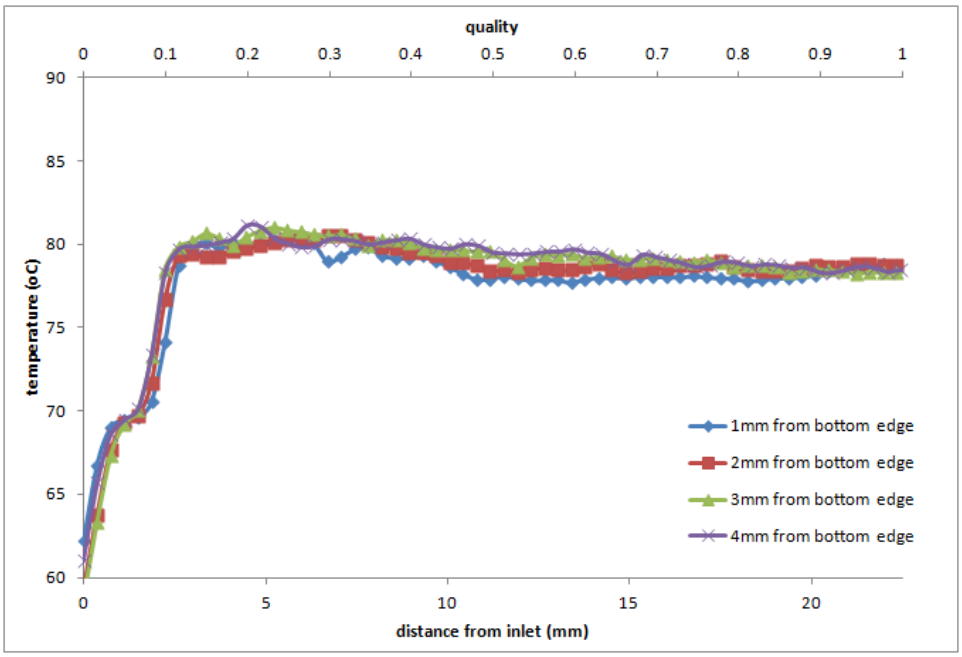

Figure 137: Axial temperature profile for 300 micron, 5 mm width, FC-72, q=23 W/cm^2, and G=195 kg/m^2-s.

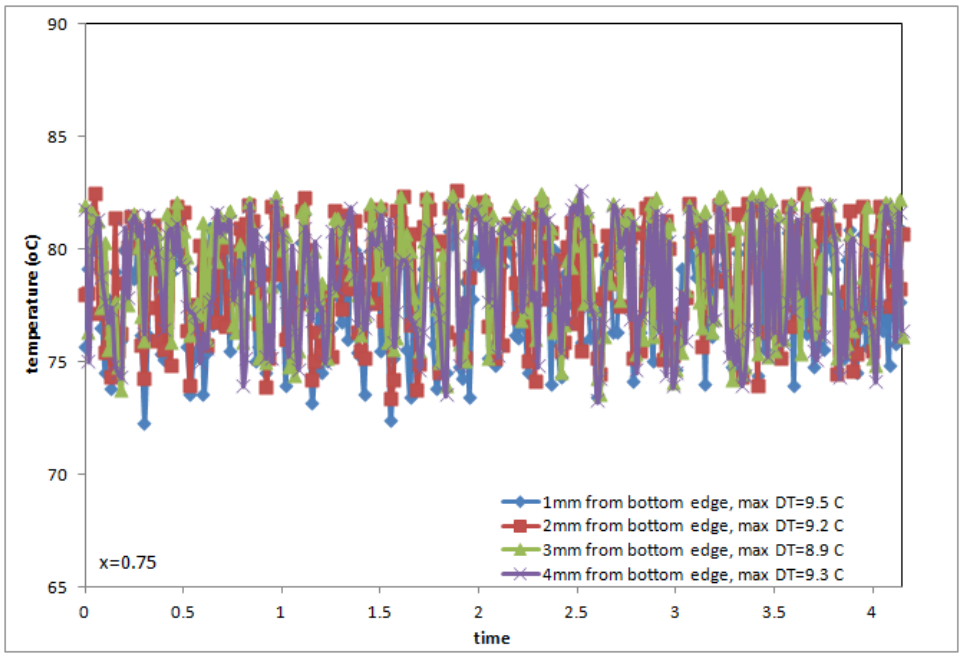

Figure 138: Temporal temperature variations for 300 micron, 5 mm width, FC-72, q=23 W/cm^2, and G=195 kg/m^2-s.

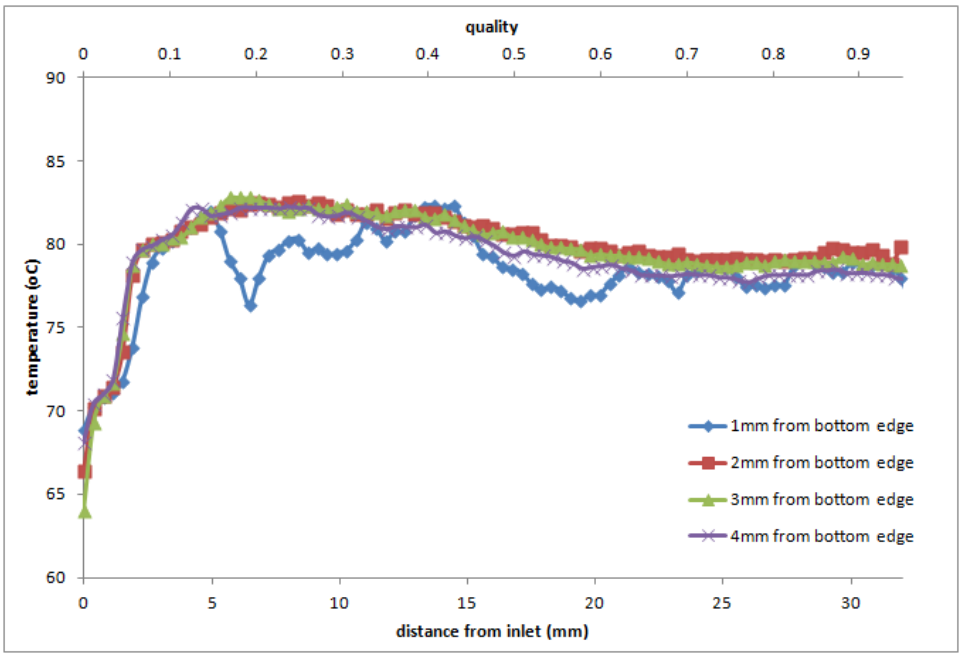

Figure 139: Axial temperature profile for 300 micron, 5 mm width, FC-72, q=23 W/cm^2, and G=292 kg/m^2-s.

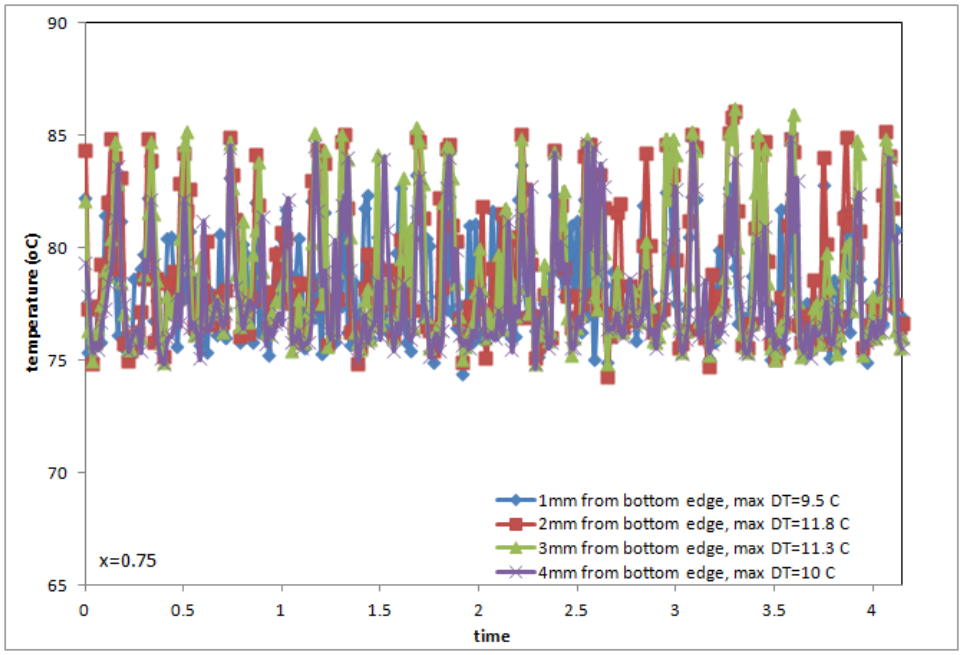

Figure 140: Temporal temperature variations for 300 micron, 5 mm width, FC-72, q=23 W/cm^2, and G=292 kg/m^2-s.

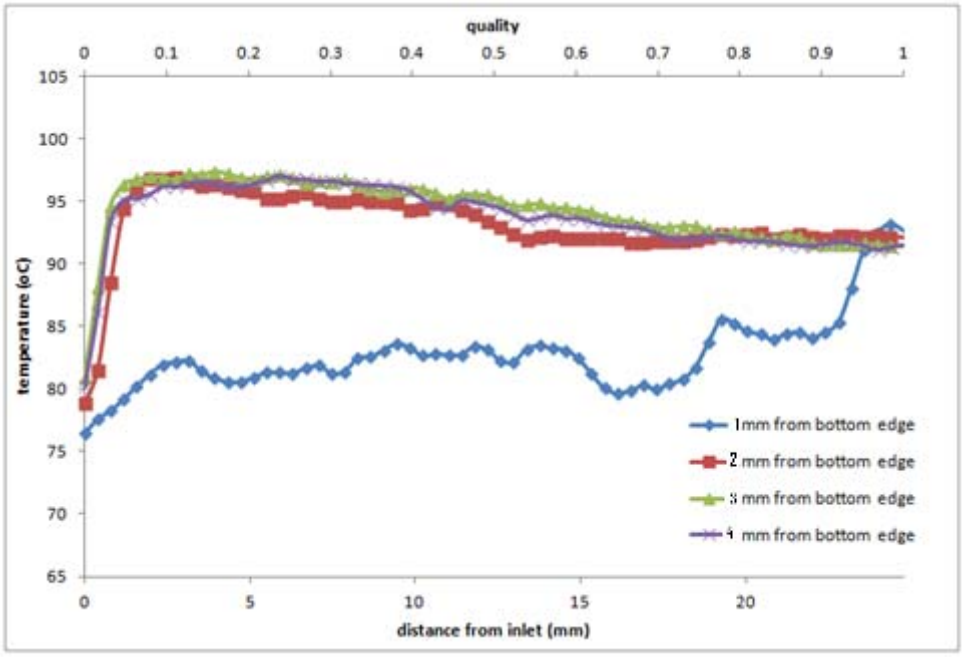

Figure 141: Axial temperature profile for 300 micron, 5 mm width, FC-72, q=40 W/cm^2, and G=390 kg/m^2-s.

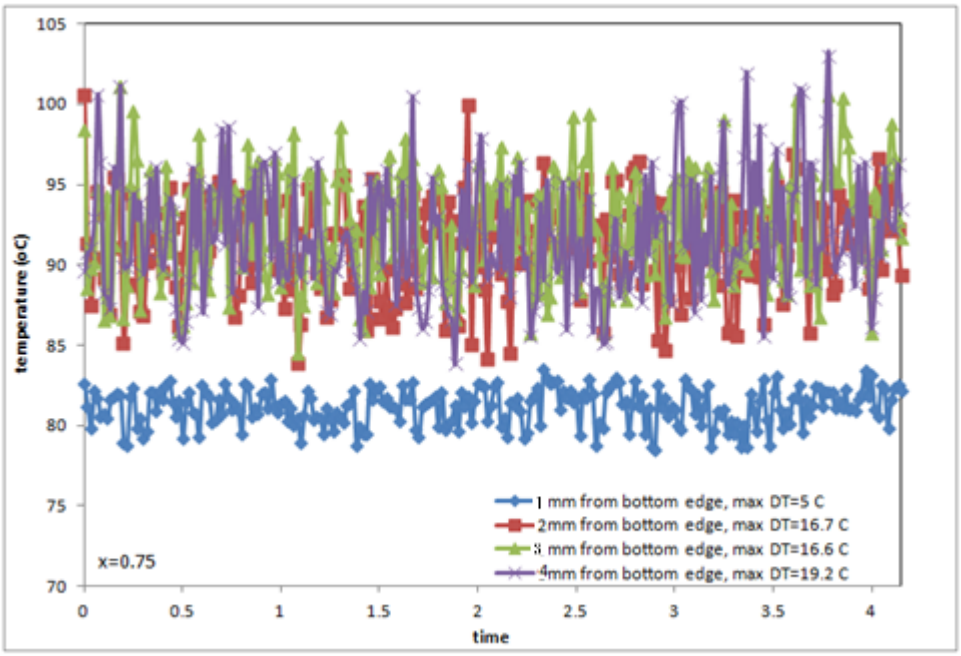

Figure 142: Temporal temperature variations for 300 micron, 5 mm width, FC-72, q=40 W/cm^2, and G=390 kg/m^2-s.

Microgap Cooler: 300 microns, FC-72, and width=10mm

Figure 143 and Figure 144 show the lateral variations for q=23 W/cm^2 and G=195 kg/m^2-s and reveal significant difference in lateral behavior. The difference in behavior does not follow the previously discussed trends seen in the 200 micron gap height data, which would show a dependence on the gap height. This cases also shows a difference at 4mm from the bottom edge, which is not directly along the corner of the channel. The local two-phase coefficients for this lateral location would be distinctly difference, enhanced, as compared to the behavior at the same axial location but different lateral. Although in Figure 144 the magnitude of the variations is comparable, the average temperature would change the local performance of the channel.

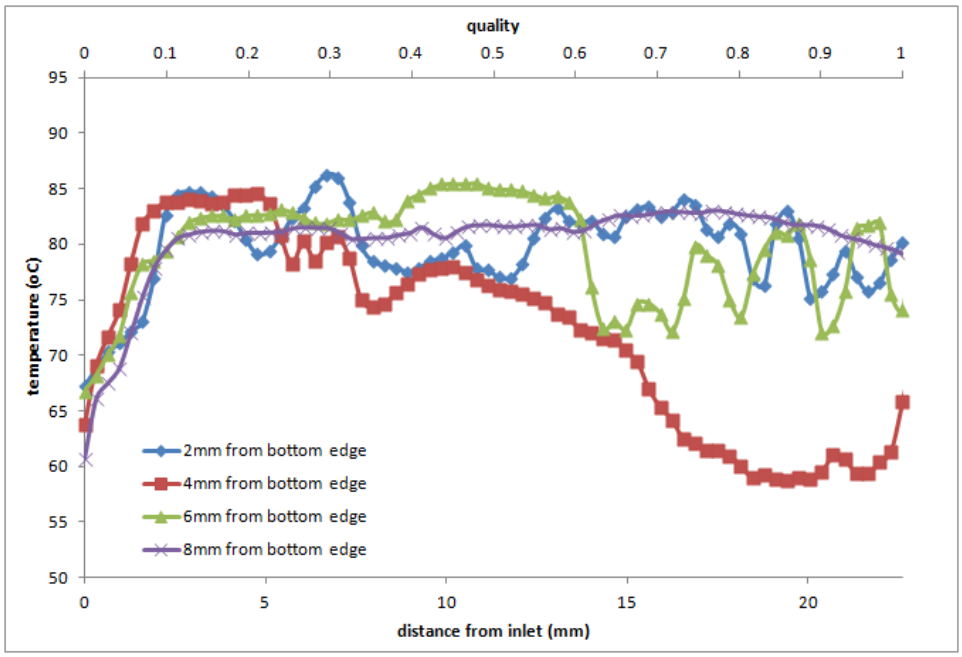

Figure 143: Axial temperature profile for 300 micron, 10 mm width, FC-72, q=23 W/cm^2, and G=195 kg/m^2-s.

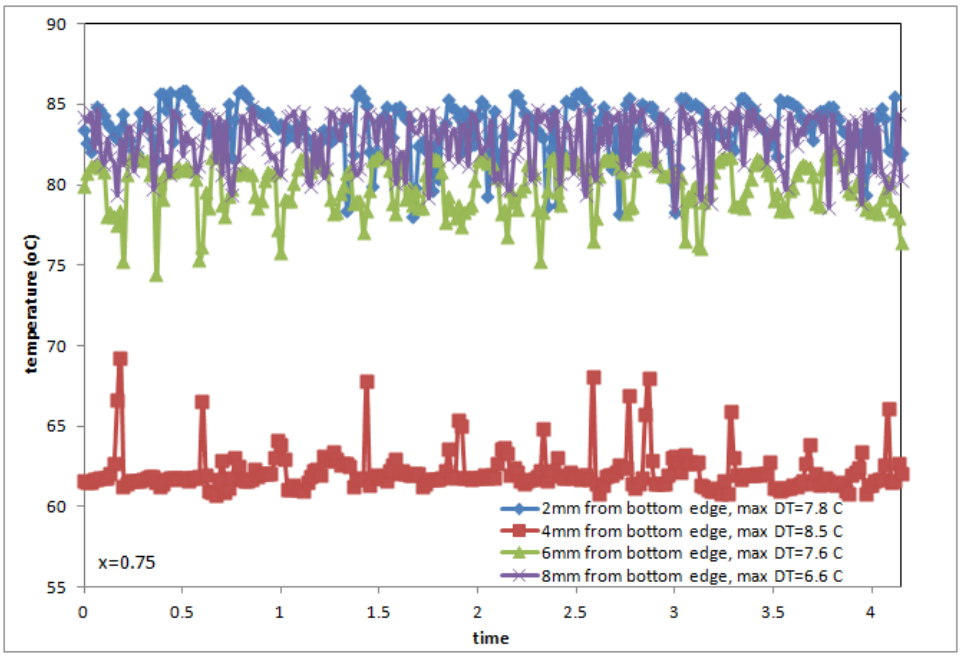

Figure 144: Temporal temperature variations for 300 micron, 10 mm width, FC-72, q=23 W/cm^2, and G=195 kg/m^2-s.

Microgap Cooler: 300 microns, FC-72, and width=20mm

Figure 145 shows the temporal temperature variations for q=23 W/cm^2, and G=292 kg/m^2-s, with distinct lateral differences. The fluctuations furthest from the bottom edge have the greatest magnitude, thus from relationships discussed earlier would have poor local two-phase heat transfer coefficients. Comparison of previous cases with the same gap height show the previously discussed relationship with width is supported by data in this section. However, a stronger dependence on gap height becomes apparent that overrides the effect of mass flux.

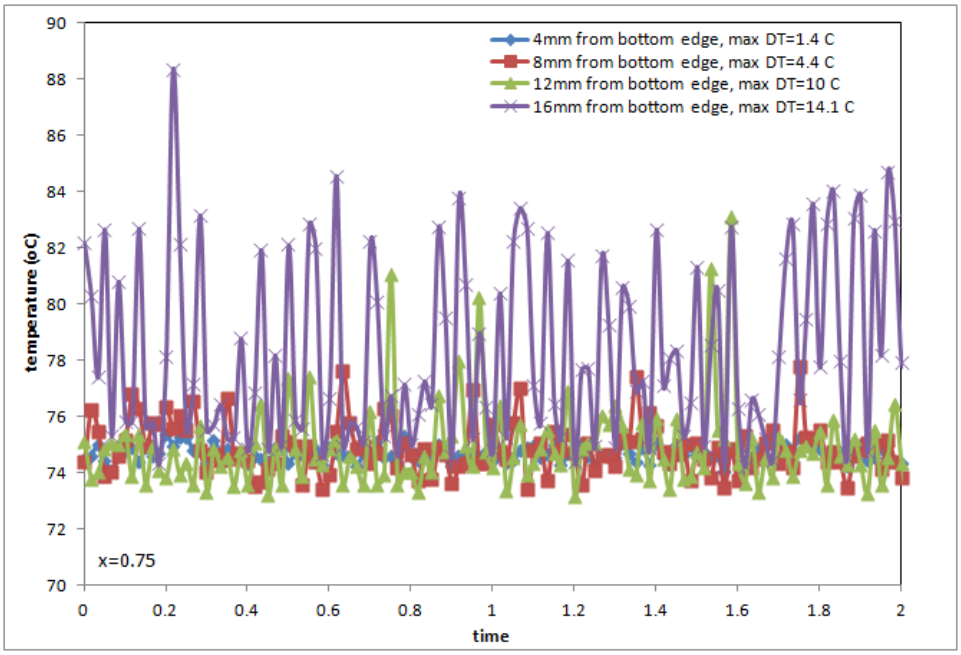

Figure 145: Temporal temperature variations for 300 micron, 20 mm width, FC-72, q=23 W/cm^2, and G=292 kg/m^2-s.

Microgap Cooler: 300 microns, HFE-7100, and width=10mm

This section examines the data for HFE-7100, to determine the effects of varying the working fluid. Figure 146 and Figure 147 show the lateral data for q=28 W/cm^2, and G=195

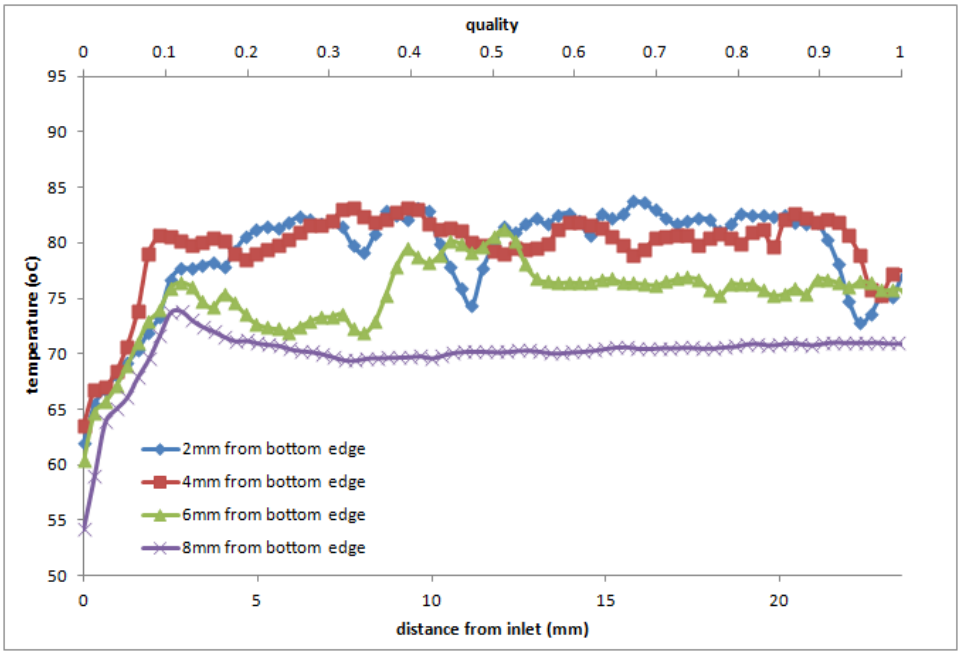

Figure 146: Axial temperature profile for 300 micron, 10 mm width, HFE-7100, q=28 W/cm^2, and G=195 kg/m^2-s.

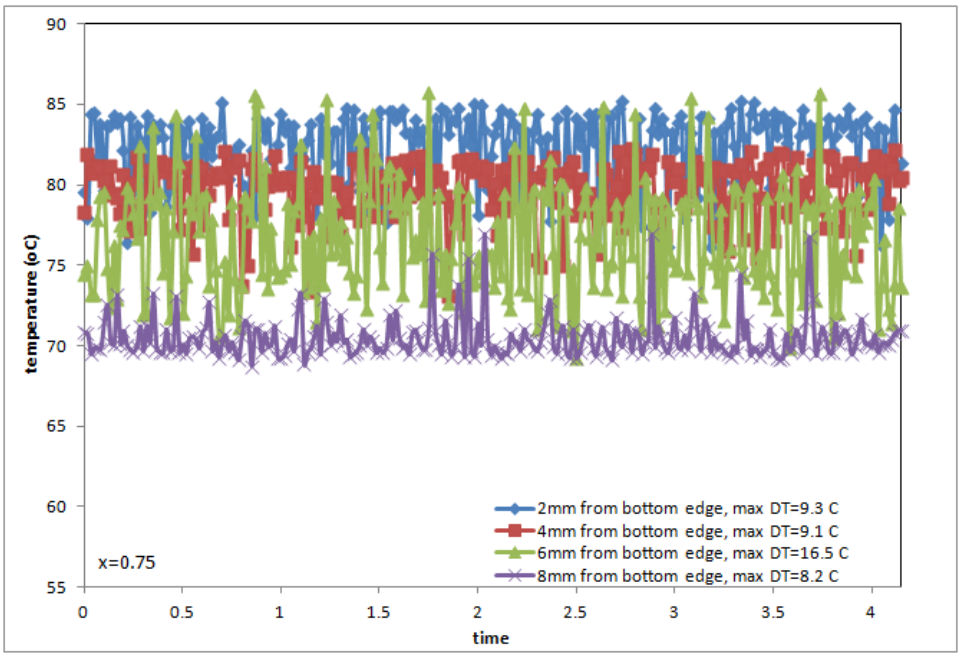

Figure 147: Temporal temperature variations for 300 micron, 10 mm width, HFE-7100, q=28 W/cm^2, and G=195 kg/m^2-s.

kg/m^2-s, which shows distinct lateral variations. Comparison of the behavior shown for these graphs with those of similar conditions using FC-72 reveals comparable trends. Thus, although the actual performance is different the trends and behavior is not significantly affected by the working fluid.

8.1.3 Microgap Channel Height at 400 microns

Microgap Cooler: 400 microns, FC-72, and width=20mm

Figure 148 and Figure 149 show the lateral behavior for q=23 W/cm^2, and G=292 kg/m^2-s, and reveal unique behavior that does not completely match previous trends. Due to the increase in gap height and width, both known to affect channel behavior, this odd channel behavior points to the complexity of the phenomena occurring in the channel. Thus, locally it can be observed first an improvement to heat transfer at 16 mm from the bottom lateral location. However, a decrease in local performance occurs around 1.6 s which could be due to a dried out portion occurring at that location.

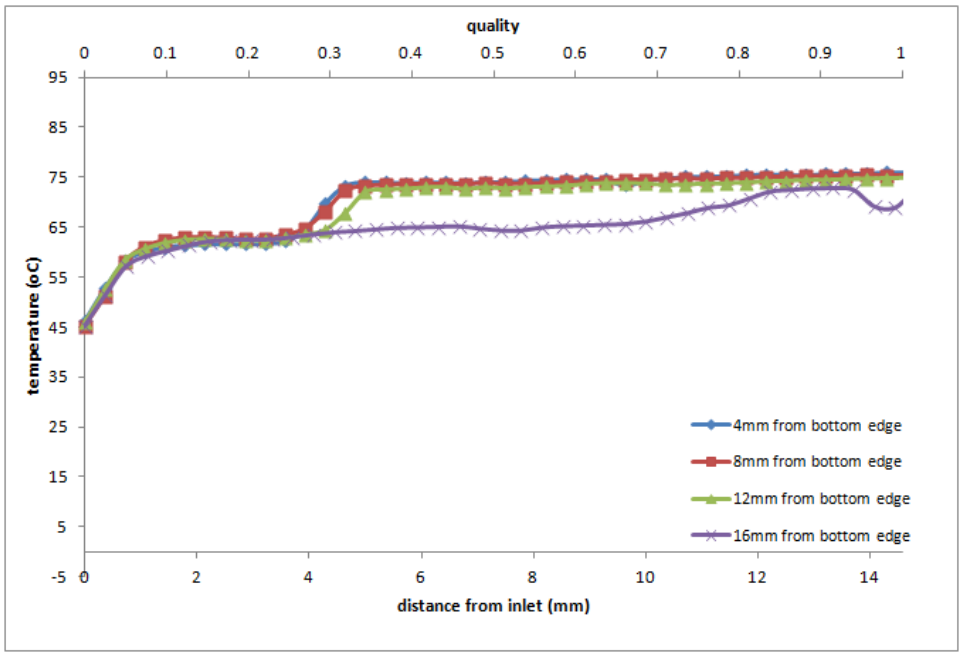

Figure 148: Axial temperature profile for 400 micron, 20 mm width, FC-72, q=23 W/cm^2, and G=292 kg/m^2-s.

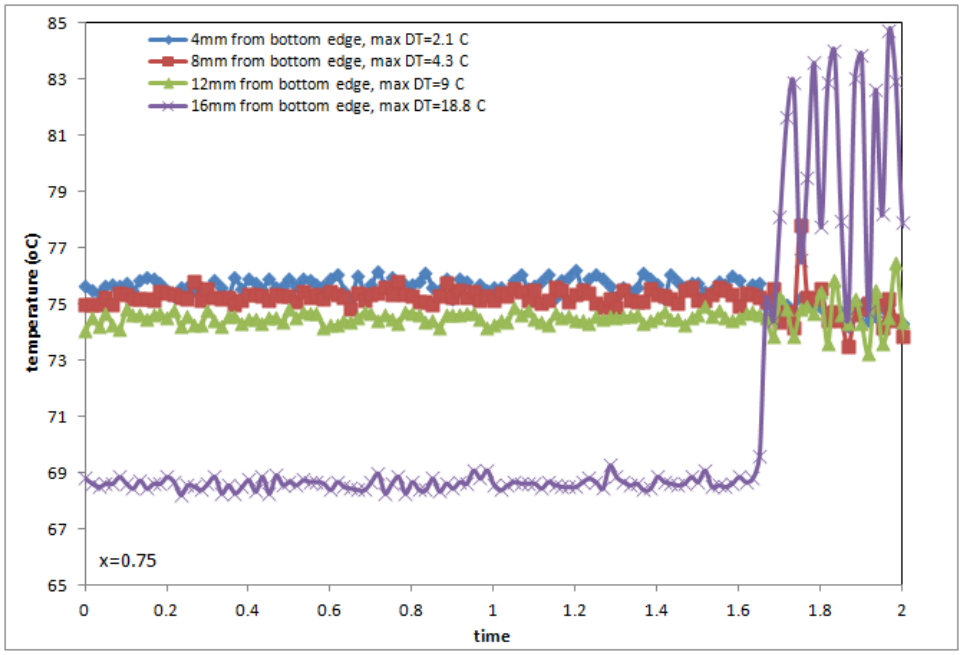

Figure 149: Temporal temperature variations for 400 micron, 20 mm width, FC-72, q=23 W/cm^2, and G=292 kg/m^2-s.

8.2 Temporal Temperature Variations – Frequency Domain

The fluctuations throughout the data have been significant, and analysis to better understand the occurrence of this behavior was conducted. Fast Fourier transforms were performed on all data to determine if a dominate frequency could be linked to the channel behavior. Figure 150 and Figure 151 show typical results for the analysis performed, which show that for various qualities within a data set no dominate frequencies occur. Despite the visual stimulation of a pattern to the fluctuations, analysis shows that the behavior is more chaotic in nature. Thus, no dominate frequency could be linked directly to change behavior or the two-phase heat transfer coefficients.

Microgap Cooler: 300 microns, HFE-7100, and width=10mm

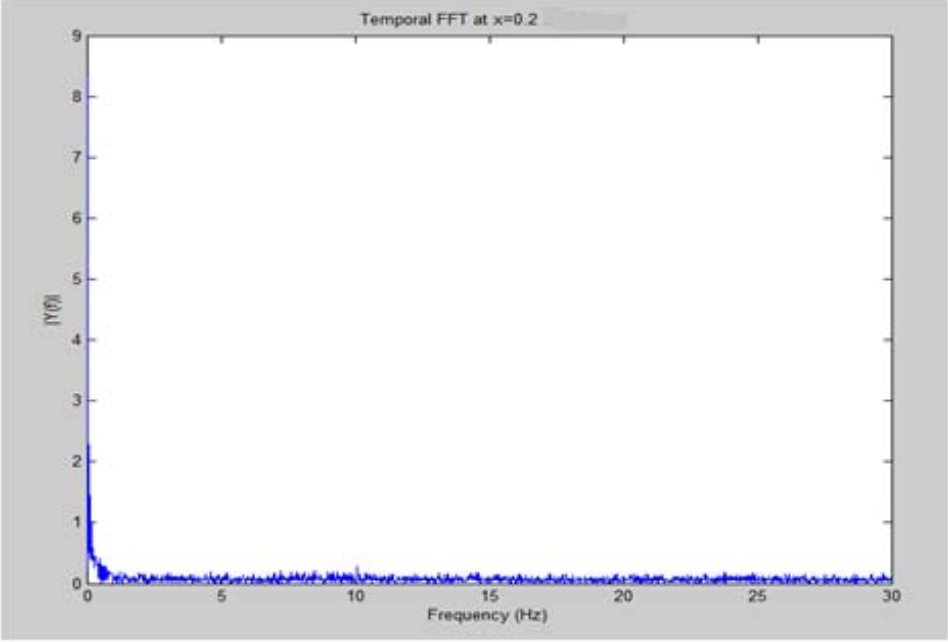

(a)

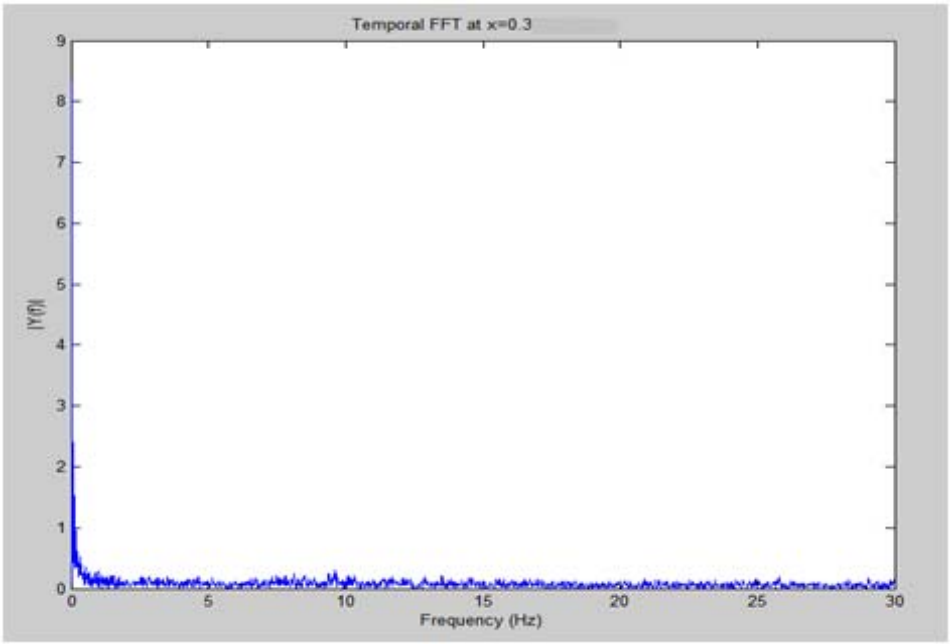

(b)

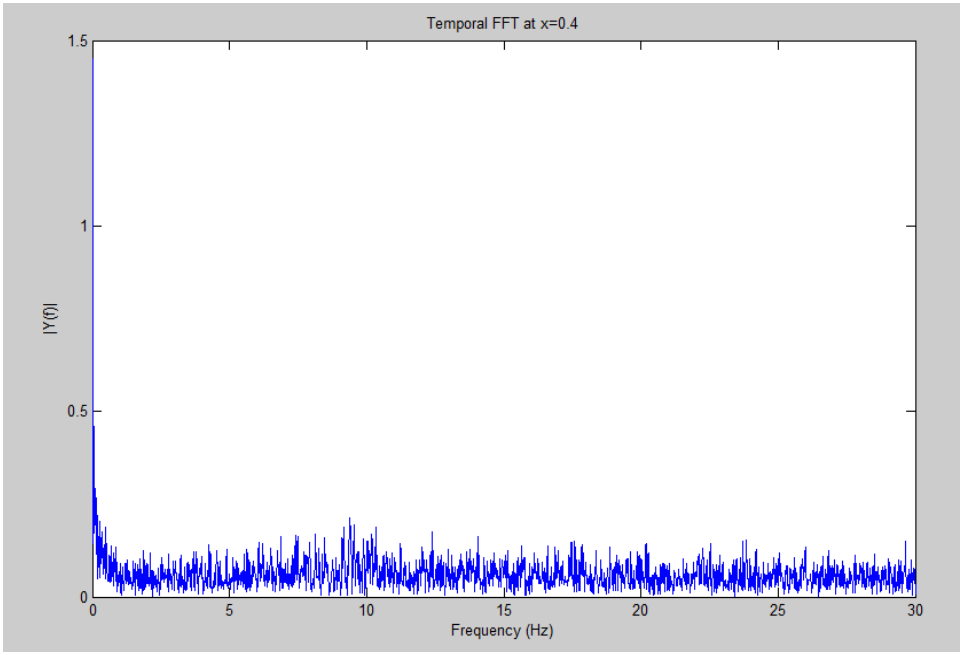

(c)

Figure 150: Temporal temperature variation PSD for 300 micron channel, 10mm width, HFE-7100, q=28 W/cm^2 and G=292 kg/m^2-s, (a) x=0.2, (b) x=0.3, and (c) x=0.4.

Microgap Cooler: 400 microns, FC-72, and width=10mm

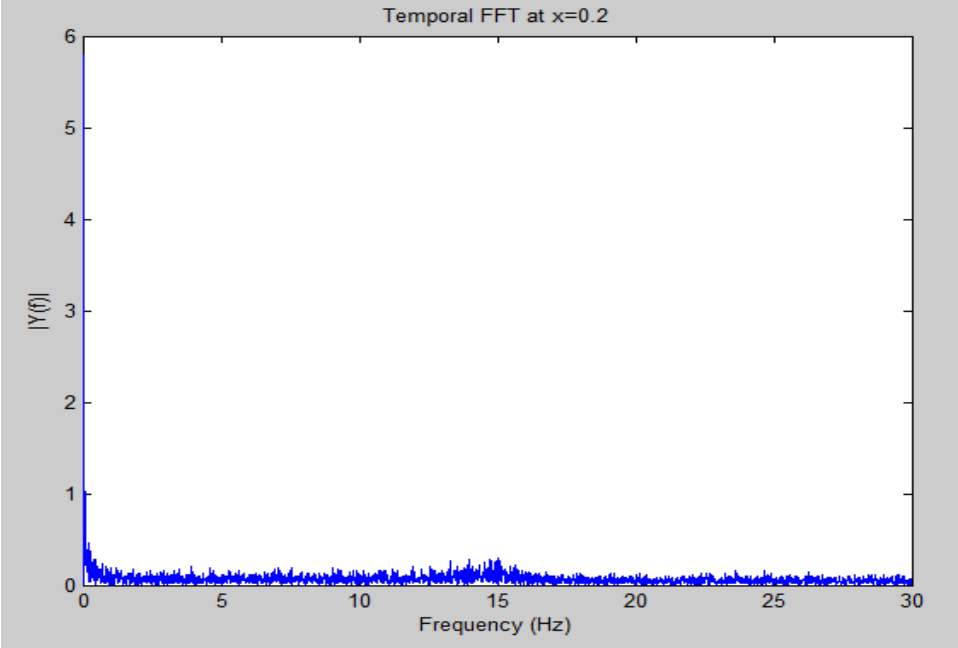

(a)

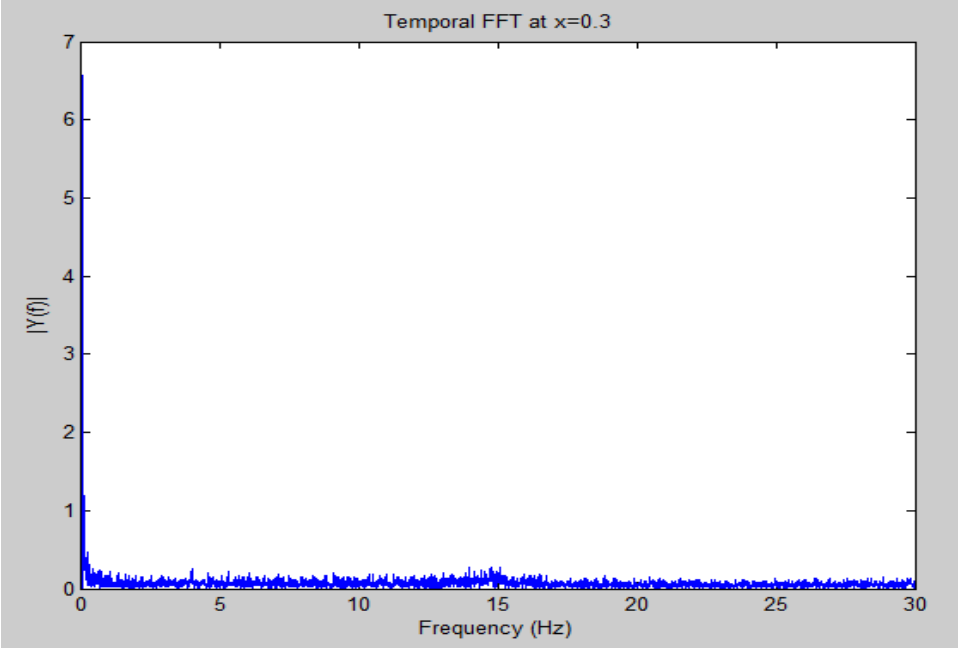

(b)

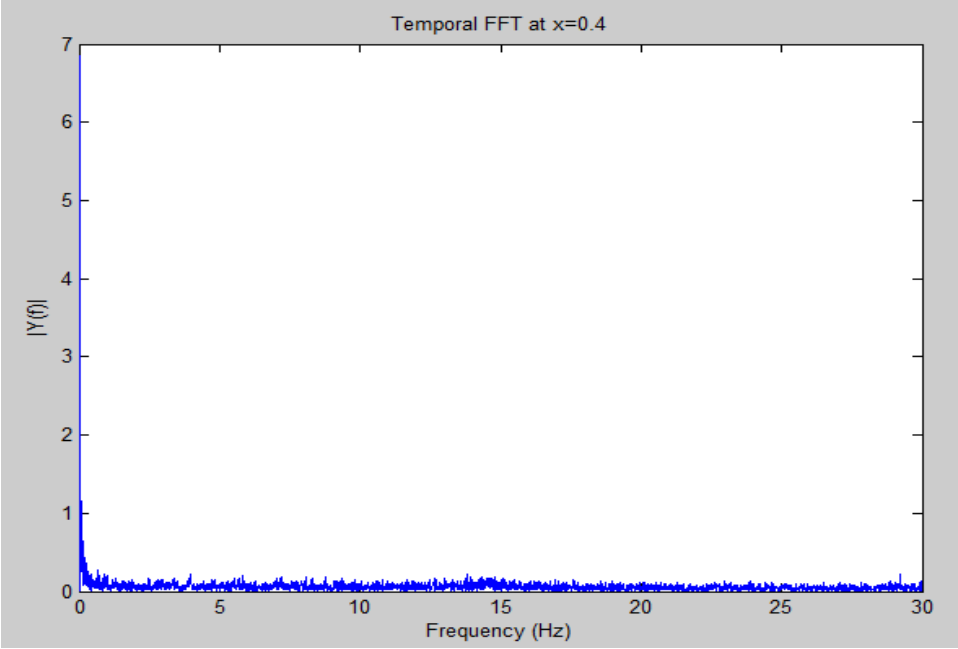
Temporal FFT at x=0.4
|Y(f)|
Frequency (Hz)
0
1
2
3
4
5
6
7
0
5
10
15
20
25
30

(c)

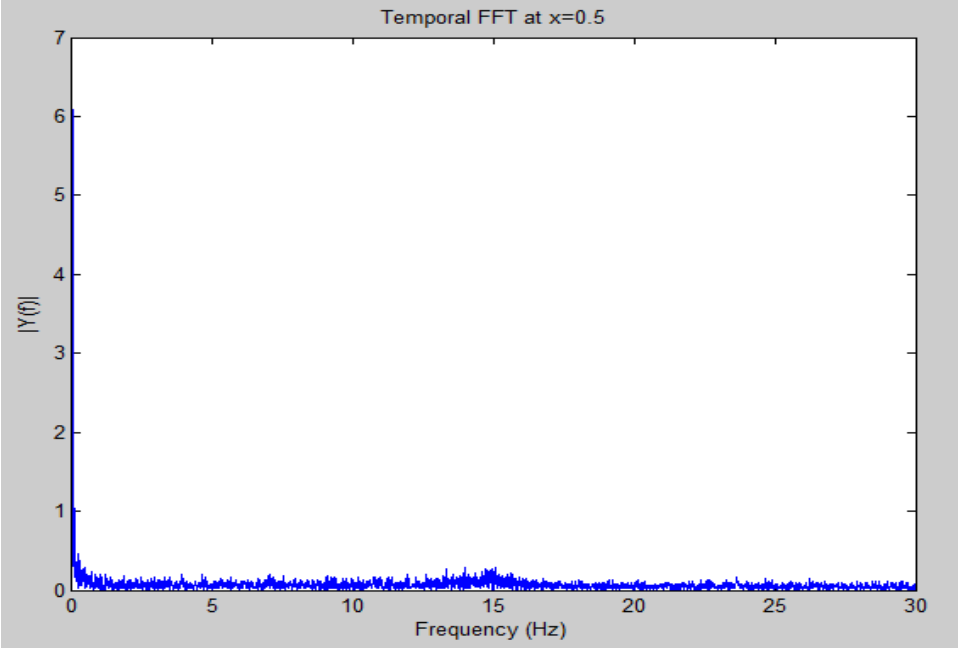
Temporal FFT at x=0.5
|Y(f)|
Frequency (Hz)
0
1
2
3
4
5
6
7
0
5
10
15
20
25
30

(d)

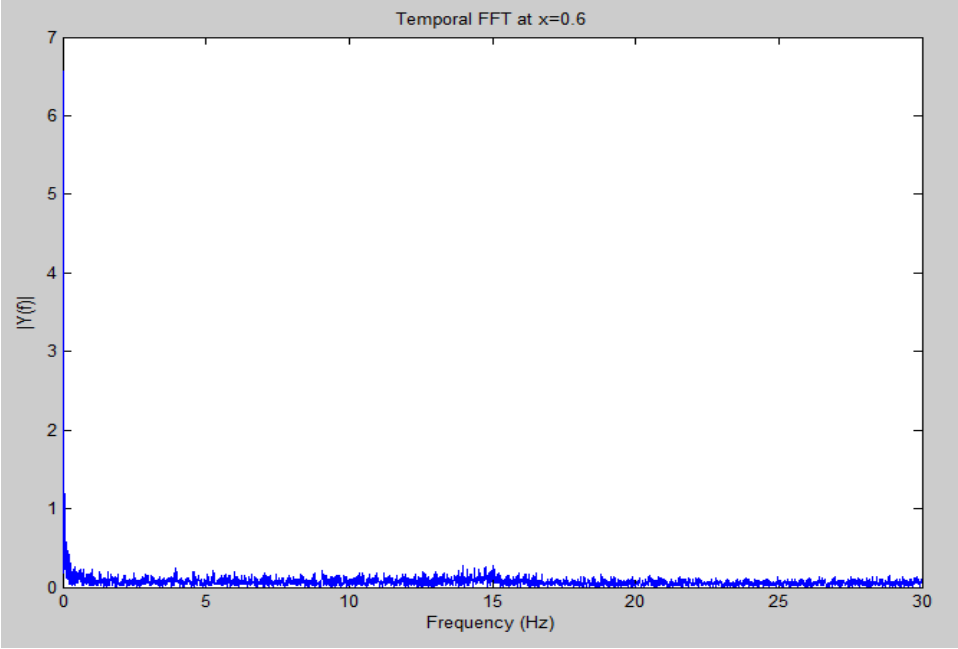
Temporal FFT at x=0.6
|Y(f)|
Frequency (Hz)
0
1
2
3
4
5
6
7
0
5
10
15
20
25
30

(e)

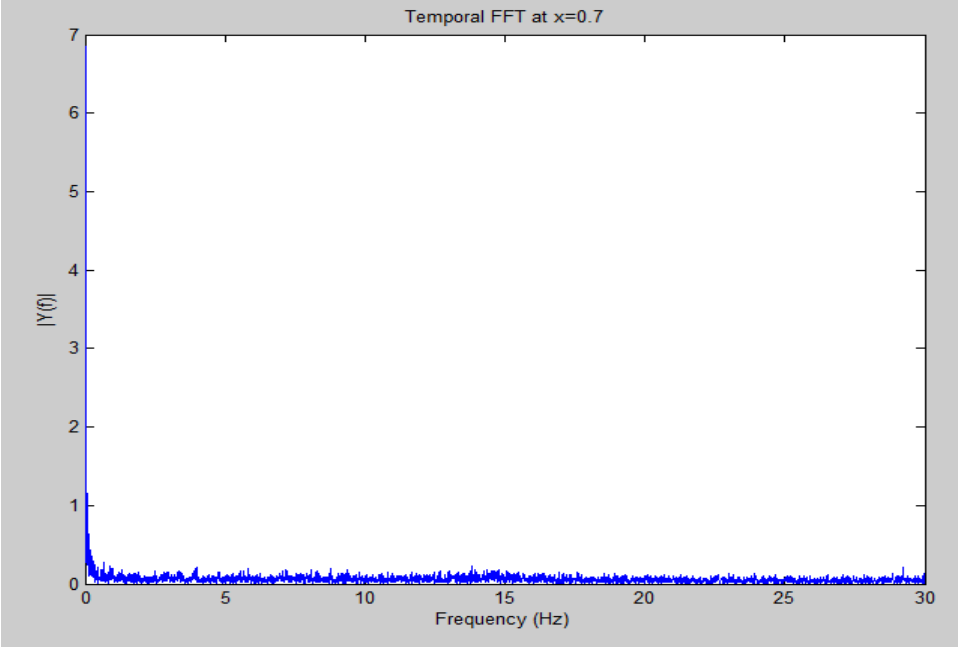
Temporal FFT at x=0.7
|Y(f)|
Frequency (Hz)
0
1
2
3
4
5
6
7
0
5
10
15
20
25
30

(f)

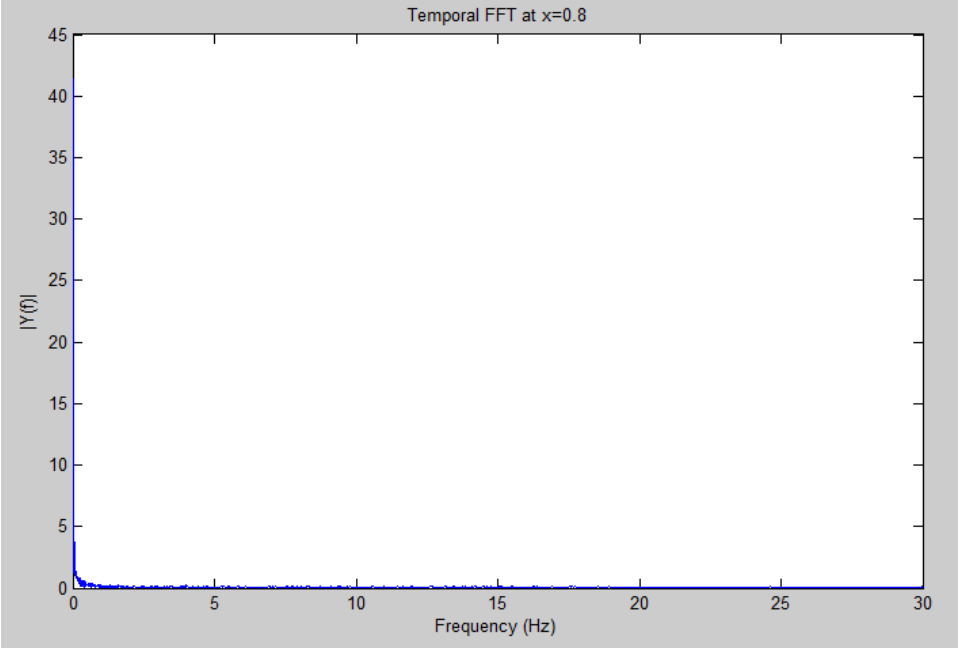

(g)

Figure 151: Temporal temperature variation PSD for 400 micron channel, 10mm width, FC-72, q=70 W/cm^2 and G=490 kg/m^{2}s, (a) x=0.2, (b) x=0.3, and (c) x=0.4, (d) x=0.5, (e) x=0.6, and (f) x=0.7, (g) x=0.8.

8.3 Spatial Temperature Variations – Wavelength Domain

In addition to dominate frequencies, examinations of potential dominate wavelengths that could be compared to RL instabilities were performed on all data sets. Figure 152 and Figure 153 show typical PSD graphs generated from the various data sets, revealing no distinct wavelengths as previously observable. This is most likely due to the chaotic nature of the data, and the increased amount of data that was used to perform the analysis. Due to the complex nature of two-phase flow and the complicated techniques necessary, further research is necessary to glean further spatial domain information.

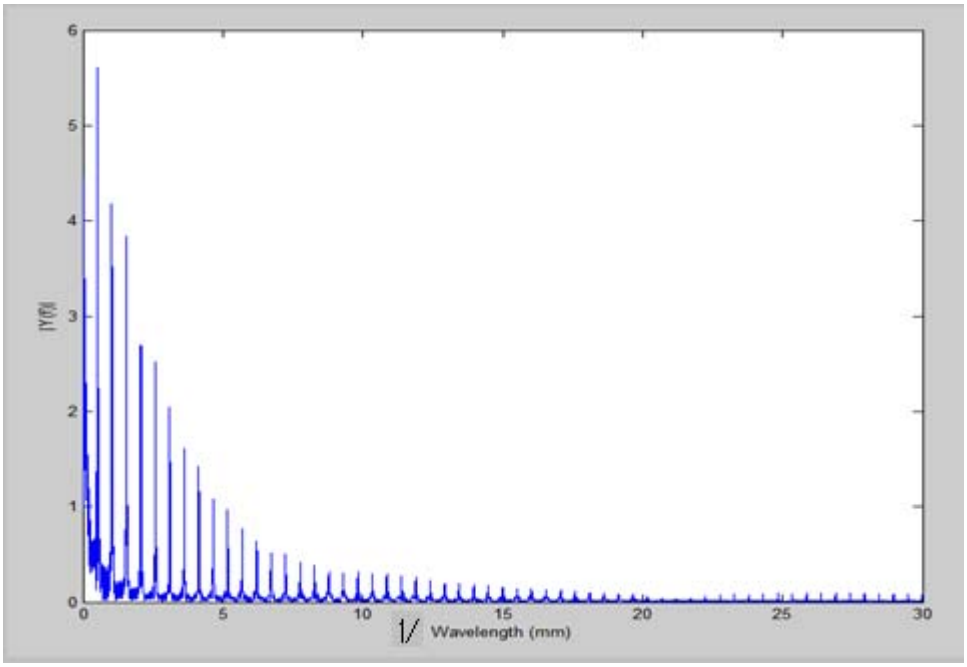

Figure 152: Spatial PSD for 200 micron channel, 10mm width, FC-72, q=40 W/cm^2 and G=390 kg/m^2-s.

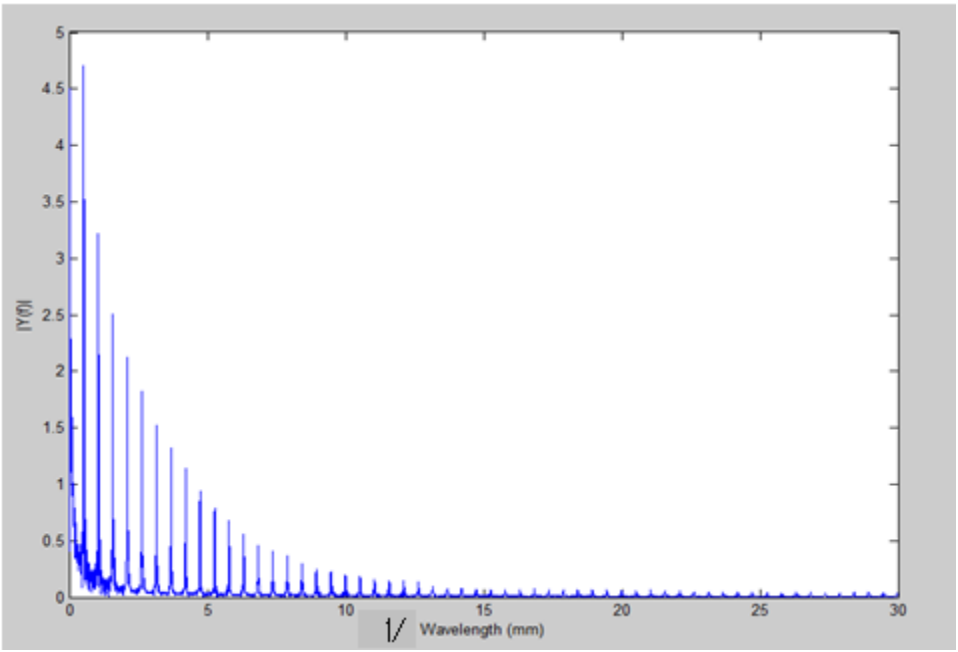

Figure 153: Spatial PSD for 400 micron channel, 10mm width, FC-72, q=40 W/cm^2 and G=390 kg/m^2-s.

CHAPTER 9

CONCLUSIONS AND FUTURE WORK

Conclusions

Two-phase microgap coolers appear to provide unique advantages in the on-chip thermal management of advanced electronic, photonic, and telecommunication modules, eliminating thermal contact resistances and providing very high heat transfer coefficients, by allowing heat flow directly into the dielectric liquid. The research presented here has shown many novel approach, behaviors, trends, relationships, etc. The observation of the intrinsic M-shaped curve has lead to an in-depth study of the phenomena within the microgap channels that causes this trend. Previous methods of analyzing channels utilizing traditional temperature measurement methods failed to obtained sufficient data to explain channel behavior. Advanced measurement techniques are needed to characterize the thermofluid performance and the approach to catastrophic limits of such two-phase cooling techniques. IR imaging is used to obtain the temperature distribution along the heated wall of a microgap cooler channel. Significant spatial and temporal temperature variations, approaching 20 K, were observed. The frequency and amplitude of the observed temperature variations appear to reflect the complexity of the prevailing two-phase flow regimes and provide evidence of incipient, local dryout in moderate quality annular flow. Analysis revealed previously unobserved temperature fluctuations caused by local dryout and recovery that are occurring in the channel. Further examination has linked these fluctuations to the two-phase heat transfer coefficients, and shown that potentially indirect relationship exist between the two. Through a study of geometric parameters, increased gap height and width generally decrease temperature fluctuations. Additionally the temperature fluctuations are influenced by aspect ratio, as seen through the delayed affect of widen the channel when gap height is also increased. Due to the complex physics occurring within the channel, this does not always directly correlate to a decreased performance. In addition, a complex relationship exists between the heat flux (i.e. evaporation rate) and the mass flux (i.e. flow regime/quality) that influences the local dryout and recovery of the channel.

Publications and Presentations

*1.*Bar-Cohen, A., Sheehan, J.R., and Rahim, E. "Two-Phase Thermal Transport in Microgap Channels - Theory, Experimental Results, and Predictive Relations." September 2011. *Microgravity - Science and Technology,* Volume 23**,** pages TBA

2.Sheehan, J.R. and Bar-Cohen, A., "IR Thermography of Two-Phase Microgap Cooler." August 2011. *Journal of Heat Transfer*. Volume 133, pages TBA.

3.Sheehan, J. R. and Bar-Cohen, A., 2011, "IR-Based Inverse calculation of two-phase Heat Transfer Coefficients in Microgap Channels ", *ASME/Pacific Rim Technical Conference and Exhibition on Packaging and Integration of Electronic and Photonic Systems, MEMS and NEMS,* INTERPACK2011-52238.

4.Sheehan, J.R. and Bar-Cohen, A., 2010, "Spatial and Temporal Wall Temperature Fluctuations in Two-Phase Flow in Microgap Coolers", *ASME International Mechanical Engineering Congress and Exposition*, IMECE2010-40227.

5.Sheehan, J. R., Kim, D.H., and Bar-Cohen, A., 2009, "Thermal Imaging of Cooled Microgap Channel Wall", *ASME/Pacific Rim Technical Conference and Exhibition on Packaging and Integration of Electronic and Photonic Systems, MEMS and NEMS,* IPACK2009-89238.

Paper presentations:

- "Study of Microgap Coolers Performance" at ASME IMECE, Houston TX, Nov. 2012, IMECE2012-93015
- "Effects of Orientation on Microgap Coolers" at ASME IMECE, Houston TX, Nov. 2012, IMECE2012-93017
- "Spatial and Temporal Wall Temperature Fluctuations in Two-Phase Flow in Microgap Coolers" at ASME IMECE, Vancouver, CA, Nov. 2010, IMECE2010-40227.
- "Thermal Imaging of Two-Phase Cooled Microgap Channel Wall" at the ASME InterPACK, San Francisco, CA, July 2009.
- "Factoring in Ethics into Engineering" at ASME IMECE, Boston, Massachusetts, November 2008.
- "Single Crystal Quartz a Replacement for Diamond Optical Windows" ASME IMECE, Boston, MA, Nov. 2008

Poster presentations:

- "Presence of Lateral Variations in Microgap Coolers" at ASME IMECE, Houston, TX, Nov. 2012, IMECE2012-93016
- "Evaporative Microgap Cooling for High Heat Density Electronics" at ASME IMECE, Vancouver, CA, Nov. 2010.
- "Local and Global Dryout in Two-Phase Microgap Coolers" at ASME IMECE, Vancouver, CA, Nov. 2010.
- "IR Thermography of Two-Phase Microgap Cooler" at ASME IMECE, Vancouver, CA, Nov. 2010.
- "Thermal Imaging of Ebulliently-Cooled Microgap Channel Wall" ASME InterPACK, San Francisco, California, July 2009.
- "IR Imaging of Thin Film Evaporation in Microgap Channels" at UMD Engineering Research Day, 2010.
- "Two-Phase Microgap Coolers" at University of Maryland Engineering Research Day, March 13, 2009.
- "Two-Phase Microgap Coolers" at University of Maryland Engineering Research Day, 2008.

Future Work

Additional work to further understanding of the complex physics governing microgap coolers is necessary. It would be beneficial to better understand the flow regime transitions and flow patterns within the channel to understand the affects this has on performance, and ultimately the affects the various parameters study have on flow within the channel. This could be achieved by collecting data using a high wavelength camera that would utilize the inherent fluid properties of FC-72 being opaque at higher wavelengths, thus permitting IR thermography of the liquid within the channel. Coupling this with the original data and a high speed camera would provide great insight to the flow patterns and flow transitions occurring in the channel. Future work should also include greater refinement of the inverse two-phase heat transfer method, hopefully to include analysis down to the pixel level. A secondary inverse method of imposing IR measured temperatures to the surface instead of iterative h values should be explored. In

addition, further study of environmental effects (i.e. orientation, vibration, elevation) should be conducted to determine channel behavior in practical application situations. Further examination of the edge effects is necessary to fully understand the influence on channel behavior and potential advantage of local behavior. Additional information about the thin liquid film behavior would greatly increase understanding of local dryout and recovery, which could be achieved using an additional IR camera at a higher wavelength.

REFERENCES

[1] iNEMI, "Electronics Manufacturing Initiative Technology Roadmap," 2006.

[2] Silk, E.A., Kim, J.H., and Kiger, K. (2006) “Spray cooling of enhanced surfaces: Impact of structured surface geometry and spray axis inclination” *International Journal of Heat and Mass Transfer,* 49, 4910-4920.

[3] El-Genk, M. S. (2012) “Immersion cooling nucleate boiling of high power computer chips” *Energy Conversion and Management,* 53, 205-218.

[4] Do, K.H. and Jang, S.P. (2010) “Effect of nanofluids on the thermal performance of a flat micro heat pipe with a rectangular grooved wick” *International Journal of Heat and Mass,* 53, 2183-2192.

[5] Kim, D.W., E. Rahim, A. Bar-Cohen, B.T. Han, 2010, "Direct Submount Cooling of High Power LED's," IEEE Transactions on Components and Packaging Technologies, Volume: 33 Issue 4, pp 698 - 712, DOI: 10.1109/TCAPT.2010.2040618 July 2009

[6 Kim, Dae Whan. (2007) “Convection and Flow Boiling in Microgaps and Porous Foam Coolers “ PhD Dissertation, Mechanical Engineering Department, University of Maryland.

[7] Sheehan, J. R., Kim, D.H., and Bar-Cohen, A., 2009, “Thermal Imaging of Cooled Microgap Channel Wall”, *ASME/Pacific Rim Technical Conference and Exhibition on Packaging and Integration of Electronic and Photonic Systems, MEMS and NEMS,* IPACK2009-89238.

[8] Rahim, E., Revellin, R., Thome, J. and Bar-Cohen, A. “Characerization and prediction of two-phase flow regimes in miniature tubes” International Journal of Multiphse Flow, 37, 12-23.

[9] Rahim, E. (2011) “---------- “ PhD Dissertation, Mechanical Engineering Department, University of Maryland.

[10] Andre, Ali. (2011) “-------- “ PhD Dissertation, Mechanical Engineering Department, University of Maryland.

[11] Bar-Cohen, A., E. Rahim, 2009, "Modeling and Prediction of Two-Phase Microgap Channel Heat Transfer Characteristics," Heat Transfer Engineering, Volume 30, Issue 8, pp 601-625

[12] Garimella, S. Killion, J.D., and Coleman, J.W. (2002) “An experimental validated model for two-phase pressure drop in the intermittent flow regime for circular channel” *Journal of Fluid Engineering*, 124, 205-214.

[13] Kattan, N., Thome, J.R., and Favrat, D. (1998) “Flow boiling in horizontal tubes: Part 1-development of a diabiatic two-phase flow pattern map” *Journal of Heat Transfer*, 120, 140-147.

[14 Qu, W. and Mudawar, I. (2004) “Measurement and correlation of critical heat flux in two-phase microchannel heat sinks” *International Journal of Heat and Mass Transfer*, 47, 2045-2059.

[15] Thome, J.R. (2004) “Boiling in microchannels: a review of experiment and theory” *International Journal of Heat Fluid Flow*, 25, 128-139.

[16] Lee, J. and Mudawar, I. (2005) “Two-phase flow in high heat flux microchannel heat sink for refrigeration cooling application: Part i-pressure drop characteristics” *International Journal of Heat and Mass Transfer*, 48, 928-940.

[17] Triplett, K.A., Ghiaasiaan, S.M., Abdel-Khalik, S.I., Lemouel, A., and McCord, B.N. (1999) “Gas-liquid two-phase flow in microchannels part i: two-phase flow patterns” *International Journal of Multiphase Flow*, 25, 377-394.

[18] Triplett, K.A., Ghiaasiaan, S.M., Abdel-Khalik, S.I., Lemouel, A., and McCord, B.N. (1999) “Gas-liquid two-phase flow in microchannels part ii: void fraction and pressure drop” *International Journal of Multiphase Flow*, 25, 395-410.

[19] Bar-Cohen, A. and E. Rahim (2009) “Modeling and Prediction of Two-Phase Refrigerant Flow Regimes and Heat Transfer Characteristics in Microgap Channel” *Heat Transfer Engineering*, **30** (8), 601 – 625.

[20] Hetsroni, G. (1982) Handbook *of Multiphase Systems*, Hemisphere Publishing Co.: New York.

[21] Eckert, E.R.G. and Drake, R.M. (1972) *Analysis of Heat and Mass Transfer*, McGraw-Hill Book Company: New York.

[22] Carey, V.P. (2008) *Liquid-Vapor Phase-Change Phenomena*, Taylor & Francis: New York.

[23] Brewster, M. Q. (1992) *Thermal Radiative Transfer and Properties*, John Wiley & Sons, Inc.: New York.

[24] 3M (2000) “3M Flurinert Electronic Liquid FC-72” *Product Information*, 1-4.

[25] Creighton, J.R., Breiland, W.G., Koleske, D.D., Thaler, G., and Crawford, M.H. (2008) “Emissivity-correcting mid-infrared pyrometry for group-III nitride MOCVD temperature measurement and control” *Journal of Crystal Growth*, **310**, 1062-1068.

[26] Innocenzi, M.E., Swim, R.T., Bass, M., French, R.H., Villaverde, A.B., and Kokta, M.R. (1990) “Room-temperature optical absorption in undoped a-Al2O3” *Journal of Applied Physics*, **67** (12), 7542-7546.

[27] Siegel, R. and Howell, J.R. (1992) *Thermal Radiation Heat Transfer*, Hemisphere Publishing Corporation: Washington.

[28 Greskovich, E.J. and Shrier, A.L. (1972) "Slug Frequency in Horizontal Gas-Liquid Slug Flow" *Industrial and Engineering Chemistry Process Design and Development*, **11** (2), 317-318.

[29] Woods, B.D., Fan, Z., and Hanratty, T.J. (2006) "Frequency and development of slugs in a horizontal pipe at large liquid flows" *International Journal of Multiphase Flow*, **32**, 902-925.

[30] Flir Systems (2004) "ThermaCAM^{TM} Research User's Manual" 1-158.

[31] Eckert, E.R.G. and Drake, R.M. (1972) *Analysis of Heat and Mass Transfer*, McGraw-Hill Book Company: New York.

[32] Sheehan, J.R. and Bar-Cohen, A., 2010, "Spatial and Temporal Wall Temperature Fluctuations in Two-Phase Flow in Microgap Coolers", *ASME International Mechanical Engineering Congress and Exposition*, IMECE2010-40227.

[33] Yang, Y., and Fujita, Y., Flow Boiling Heat Transfer and Flow Pattern in Rectangular Channel of Mini-Gap, Proc. 2nd International Conference on Microchannels and Minichannels, New York, USA, Paper no. ICMM2004-2383, 2004.

[34] Cortina-Diaz, M., and Schmidt, J., Flow Boiling Heat Transfer of n-Hexane and n-Octane in a Minichannel, Proc. the 13th International Heat Transfer Conference, Sydney, Australia, 2006.

[35] Sheehan, J. R. and Bar-Cohen, A., 2011, "IR-Based Inverse calculation of two-phase Heat Transfer Coefficients in Microgap Channels ", *ASME/Pacific Rim Technical Conference and Exhibition on Packaging and Integration of Electronic and Photonic Systems, MEMS and NEMS,* INTERPACK2011-52238.